Enhancement of Inductive Power Transfer Technology

Iron-based Nanocrystalline Ribbon Cores

Daniel Efrén Gaona Erazo

Supervisor: Dr. Teng Long

Advisor: Dr. Tim Flack

Department of Engineering Division B
University of Cambridge

This dissertation is submitted for the degree of
Doctor of Philosophy

Girton College

May 2021

Declaration

This thesis is the result of my own work and includes nothing which is the outcome of work done in collaboration except as declared in the Preface and specified in the text. It is not substantially the same as any that I have submitted, or, is being concurrently submitted for a degree or diploma or other qualification at the University of Cambridge or any other University or similar institution except as declared in the Preface and specified in the text. I further state that no substantial part of my thesis has already been submitted, or, is being concurrently submitted for any such degree, diploma or other qualification at the University of Cambridge or any other University or similar institution except as declared in the Preface and specified in the text. It does not exceed the prescribed word limit for the relevant Degree Committee.

Daniel Efrén Gaona Erazo
May 2021

Enhancement of Inductive Power Transfer Technology

Daniel Efrén Gaona Erazo

Abstract

Inductive power transfer (IPT) has been studied extensively during the last decades, particularly for electric vehicle chargers (EV). Inductive chargers offer several advantages over standard plug-in ones. First, they reduce user interaction increasing comfort and mitigating safety concerns. Furthermore, they allow for the automation of the charging process and the implementation of opportunity charging schemes. Thus, distributed charging points can be deployed in strategic locations — such as traffic lights, public and private parking places, etc.— and EVs can be charged more frequently. This reduces the depth of discharge of the battery and increases its lifespan. Furthermore, IPT systems with bidirectional power flow can facilitate the adoption of vehicle-to-grid schemes (V2G).

IPT technology is reaching a mature state. Nevertheless, several aspects of the technology can still be improved. First, the state-of-the-art systems are sensitive to misalignments between the transmitter and receiver pads. Second, the complete standardization of the pad's design has not yet been achieved. Consequently, the interoperability of systems designed by different manufacturers is not yet guaranteed. Third, the detection of foreign objects between the pads is a problem that has not been completely solved. Last, the power density of the pads can still be improved. Pads are generally large and heavy which hinders the adoption of this technology.

This dissertation addresses some of these problems in an attempt to enhance the state-of-the-art of IPT technology. The largest portion of this thesis is dedicated to the study of alternative core materials for IPT charging pads. In particular, nanocrystalline ribbon cores are considered a promising material. This material offers a higher saturation flux density, a higher permeability, superior thermal performance, and mechanical robustness compared to the standard MnZn ferrites commonly used in IPT systems. A feasibility analysis of this material was carried using intricate finite element models and experimental measurements. The analysis concluded that higher power densities can be effectively achieved with nanocrystalline ribbon cores. However, eddy-current losses on the outer/lateral faces of the cores were identified as problematic. This motivated a new design approach in which the unique properties of this material were considered during the design stage.

Guidelines for the design of nanocrystalline ribbon cores were derived. These were applied to the design of a WPT3, 11 kW pad. These pads showed superior performance as compared to identical pads with ferrite cores. Pads with nanocrystalline cores were 2% more efficient and achieved an 11% higher coupling factor. Likewise, up to 25% lower flux leakage was obtained. Moreover, their performance concerning temperature variation outperformed the one from

ferrite cores both in heat dissipation and thermal stability. Finally, the pads were tested near magnetic saturation. Nanocrystalline cores were able to transfer more power before reaching this point. Thus, higher power densities were achieved with this material. Finally, methods for reducing the eddy-current losses in the system were tested. Ferrite shielding, in particular, was found to be an effective method to improve efficiency and homogenize the temperature distribution within the core. As a minor contribution, a control strategy that uses the dual-resonant frequency characteristic of LCCL-compensated pads is also presented. This strategy was validated experimentally, and it can be used to increase the power transfer capability of pads under misaligned conditions. Moreover, this strategy can ease the interoperability of IPT pads designed by different makers which have different ratings and dimensions.

I would like to dedicate this thesis to my loving parents, Miguel and Monica, for their unconditional love, support, and encouragement. Thank you for always being beside me all these years. I would not be where I am today without you both. I would also like to dedicate this thesis to my beloved sister. Her caring soul and joyful character lightened my days and eased my journey. You make me want to be a better person. I also want to dedicate this thesis to Marina. Thank you for your support, your care, and for being there for me in both the good and the difficult times. Finally, I would like to dedicate this thesis to the rest of my family – cousins, aunts, uncles, and grandparents- for believing in me and inspiring me to follow my dreams.

Acknowledgements

I would like to thank the following people, without whom I would not have been able to complete this thesis:

First, I would like to thank the University of Cambridge, the Department of Engineering, and Girton College for providing an outstanding atmosphere for research and learning. Being part of the Cambridge community has been one of the greatest experiences of my life.

I would also like to thank the Cambridge Commonwealth, European & International Trust for financing my Ph.D. program. The mission and vision of the Trust are outstanding.

I would also like to thank the Engineering and Physical Sciences Research Council (EPSRC) for funding research projects like mine all across the UK.

Thank you to my supervisor Dr. Teng Long, for providing guidance and feedback through this project. Thank you for making sure I had all the resources I needed. Also, thank you for always being supportive and encourage me to think outside the box.

Thank you to all the members of the Applied Power Electronics Group for your friendship and camaraderie. I will cherish the time I work alongside you all. In particular, I would like to thank Noam Ezra, Saikat Ghosh, and Luke Shillaber. The long hours of work in the laboratory seemed shorter when we worked together. Thank you for your friendship and support.

A big thank you to Dr. Ghosh and Dr. Jiang for your assistant with technical matters throughout the length of my Ph.D. program. Your expertise and help were invaluable for this project.

Table of contents

List of figures

List of tables

Chapter 1

Introduction

1.1 Motivation

In an attempt to fulfill the goals established during the Paris Climate Summit, European countries have agreed on accelerating the development of low-emission technologies for transportation. This includes the reduction of CO_2 emissions of vehicles powered by combustion engines, in the short term, and the transition to zero-emission (e.g. electric vehicles) technologies, in the long term. Currently, the UK as well as other EU countries have already determined deadlines for this transition. The Modern Transport Bill of 2016 estimates a complete transition to electric vehicles (EV) by the year 2050 for the UK. Other EU countries have set even tighter deadlines: Germany (2030), Sweden (2030), France (2040) [4].

The EV market continues growing every year as depicted clearly in Fig.1.1. In 2017, more than 50000 electric cars were sold in the UK. Even though this represents only $2-2.5\%$ of the total automotive market size, the EV market share is expected to sustain exponential growth in the next decades. The sustained growth in sales is parallel to the technology development shown by the rapidly increasing number of scientific publications regarding EV technology shown in Fig.1.2a. Most of the research projects have the same three main objectives: increasing the power density, increasing or maintaining high efficiency, and minimizing costs ($/kW). According to the *Power Electronics, Electrical Machines, and Electrical Energy Storage Roadmap* created by the Automotive Council UK and Advance propulsion Centre UK, the cost of power electronics for EV's is expected to drop by 40% by 2035. At the same time, power ratings are expected to increase fivefold while components are expected to become more efficient reaching values of up to $\eta \sim 98\%$ [3]. Likewise, the cost of the electric motor is expected to decrease to half of its current cost. The power density of e-motors is expected to triple in the same period [1]. Following the same trend, the battery's capacity is expected to quadruple while its price is expected to drop to 40% of its current value [2]. The advances

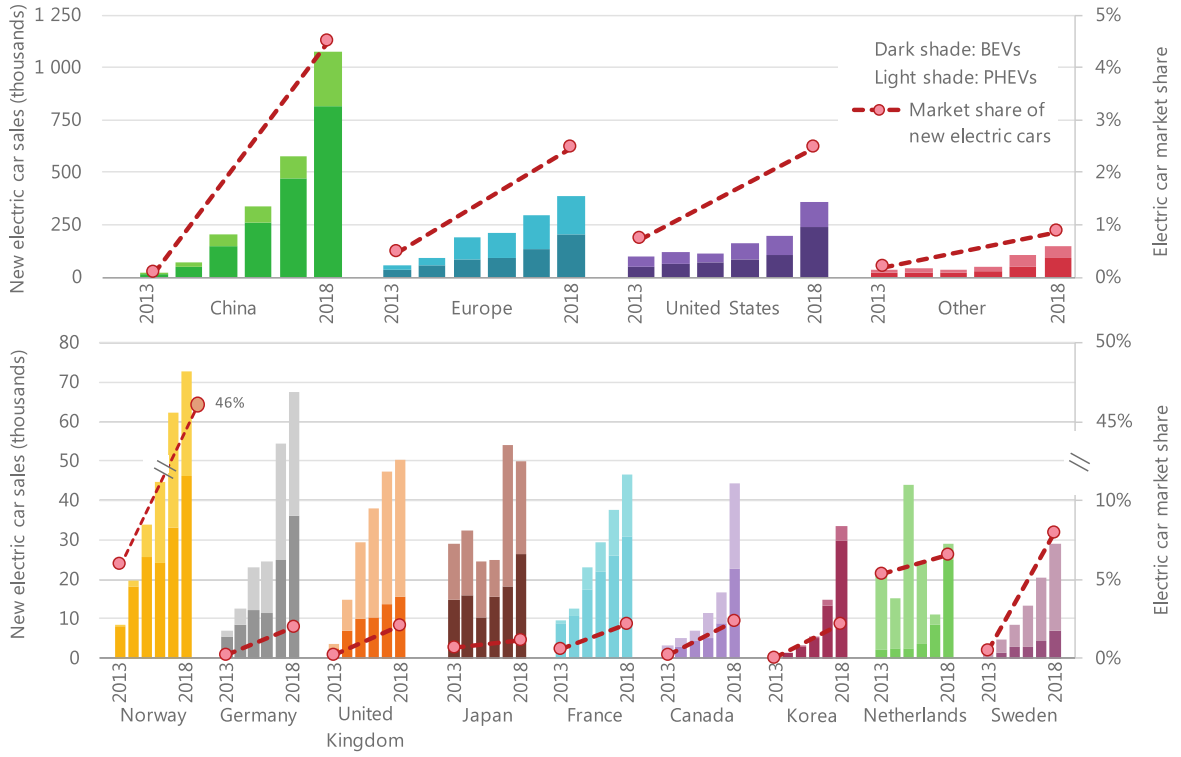

Fig. 1.1 Cumulative market for battery electric vehicles and plug-in vehicles. [4]

in battery technology are crucial to accelerating the adoption of EVs which is currently hindered by the battery capacity. EV's battery capacity has rapidly increased over the last decade reaching ranges of up to $\sim$ 540km/charge [77]. Nonetheless, having a limited range still concerns users particularly due to the sparse charging facilities in place as of today, and the long charging times.

As the battery capacity increases, charging stations with higher power ratings are needed to reduce the charging time. This has motivated the development of different charging schemes and topologies at different power levels: Level 1 (domestic, low power rating), Level 2 (specialized, distributed, medium power rating), Level 3 (charger stations, centralized, high power ratings). Moreover, two charging schemes are been proposed: centralized and decentralized. The former seeks to implement Level 3 stations placed in a few strategic locations within the city and highways (charging hubs) as to not impair the electric grid. This scheme is mostly unidirectional, and it can be understood as the equivalent of a fuel station. On the other hand, decentralized approaches seek to deploy a vast amount of Level 2 chargers in many strategic points within the city following the concept of charge-on-the-go. This decentralized scheme is particularly interesting for visionary grid developments such as Vehicle-to-grid (V2G) integration and smart-grids. Within this scheme, inductive power charger technologies

are particularly relevant as they present several advantages over plug-in chargers [11]. First, the elimination of the galvanic connection allows the implementation of automatic charging reducing the user involvement making it ideal for autonomous vehicles and fleets. Second, inductive chargers eliminate the risks associated with users handling high voltage connections. Additionally, it allows for automation of the charging process which, in turn, permits the implementation of opportunity charging schemes (OCs). OCs change the paradigm from sporadic (high-power) to frequent (low-power) charging. Thus, by placing chargers in strategic locations (traffic lights, parking areas, bus stations, etc.) the charging process occurs frequently and automatically. As a result, the depth of discharge of the battery is decreased drastically which increases its lifespan. As well, OCs reduce the battery capacity requirement for EVs [11]. This can lead to a reduction of the EV's weight and volume. Opportunity charging can be easily applied to public transportation methods such as buses, shuttles, etc. given that their trajectory is known, and their stops are recurrent. Massive adoption of IPT chargers could also facilitate Vehicle-to-grid (V2G) concepts which aim to use the car battery as an energy storage unit for the grid. V2G could ease the stress on the grid and facilitate the integration of renewable energy systems, peak shaving of electricity consumption, and the development of Smart-grids [54].

The benefits of inductive power transfer (IPT) technology have inspired R&D teams worldwide as evidenced by the rapid increase in the number of publications in this field shown in Fig. 1.2b*b*). The IPT technology has been widely studied in the last decades by different research groups and R&D companies worldwide such as Conductix-Wampfler, Momentum Dynamics, Bombardier, WiTricity, and Qualcomm Halo. Conductix-Wampler, Bombardier, and Momentum Dynamics focus on wireless solutions for the public transport sector (buses, railways) with power ratings ranging from 3.3kW up to 20kW (Level 3) and with efficiencies $> 90\%$. On the other hand, WiTricity and Qualcomm Halo, focus on IPT systems for Level

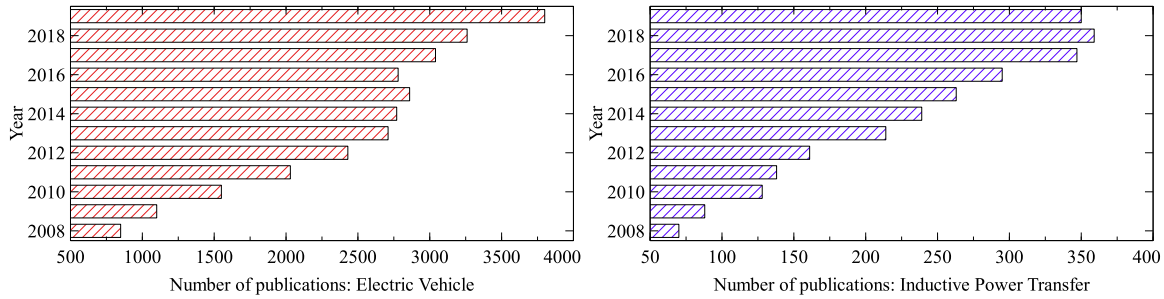

(a) EV's publications (b) IPT's publications

Fig. 1.2 Number of publications for EV and IPT technologies as per Google Scholar from 2008 until 2019.

2. The former, an MIT spin-off company, utilizes the concept of resonant coils to achieve wireless power transfer with efficiencies of up to 94% [86]. Due to its high efficiency and reliability, WiTricity attracted the interest of several industrial partners such as Delphi Inc. and several other car manufacturers such as Toyota and Mitsubishi [74]. Nowadays, WiTricity's inductive chargers are available in the market for current hybrid/electric vehicles. Qualcomm Halo, on the other hand, has developed different prototypes in partnership with the University of Auckland. Their designs range from 3.3kW to 20kW with efficiencies $> 90\%$. Its principle of operation relies on the compensation of the coil leakage inductance to improve the power transfer capability of the system and its power factor. Apart from its compensation techniques, Qualcomm Halo has also patented the "Double D" coil which delivers more power and more efficiently as compared to standard circular charging pads. In 2019, Witricity acquired Qualcomm Halo in an attempt to increase its market share and acquire technology. As a result, Witricity is nowadays one of the key players in the wireless charging market for EVs. The latter is expected to grow up to $1478 million by 2025 with a CAGR of 22.4% [71]. This growth is motivated by the rise in the EV and autonomous vehicle markets. Domestic chargers with power ratings between 11 and 50 kW are expected to experience the fastest growth. This is because IPT chargers are more attractive at medium power levels. For higher power levels, a galvanic connection is preferred to reduce power losses and the cooling requirements.

IPT is a promising technology that provides an efficient, cost-effective, and safer charging alternative. IPT promotes the adoption of EV technology and facilitates opportunity charging, vehicle-to-grid, and autonomous charging schemes. Its potential is matched by the expected growth of the wireless charging market for EVs. However, according to [71], this growth is dependent on the companies being able to provide strong and lightweight prototypes. Apart from being compact and light, IPT chargers are also required to achieve adequate efficiency ($\geq 88\%$) and performance even when the transmitter and the receiver are not perfectly aligned. Thus, even when first products can already be found in the market, inductive power transfer technology is still under development, and opportunities for improvement are not scarce. First, the robustness of the system to misalignment between the transmitter and receiver must be improved. When primary and secondary coils are perfectly aligned, efficiencies $> 90\%$ can be achieved; however, when the primary and secondary are not aligned, the efficiency and power transfer capability of the pad deteriorate drastically. For a circular pad, for instance, the coupling factor and therefore the power transfer capability drops to zero when the pads become misaligned by around 40% of the pad's diameter [19]. As the power transferred to the secondary decreases, so does the efficiency. On the other hand, following the current trend of power electronics and electrical machines, IPT volumetric and gravimetric power densities must be increased without compromising efficiency. Moreover, the mechanical robustness

of the pad ought to be increased without compromising reliability, weight, or costs. Every improvement must consider the constraints regarding volume and size available, thermal, and stray flux limits as well as material and energy costs. Foreign object detection is another clear area of improvement. Detecting metallic objects in between the pads is vital to ensure safety during operation. Finally, the inter-operation of different chargers is another area of research. Given the diverse topologies, dimensions, and ratings of IPT pads, methods to ensure compatibility are required. In this context, this thesis seeks to contribute to the enhancement of IPT technology by studying some of the aforementioned problems. The specific objectives are detailed in the next section.

1.2 Research Objectives

As discussed in the previous section, this thesis seeks to improve the state-of-the-art of inductive power transfer technology for EVs. In particular, this thesis focuses on the following points.

- **Core material:** Different coil topologies have been introduced in the last decades to increase the performance of IPT systems. However, the core material within the pads has not received the same attention. In particular, the optimal amount of ferrite needed and the optimal placement of the core bars within the pad have not been fully studied. Moreover, little effort has been put into researching different materials that can outperform ferrite cores. In this thesis, nanocrystalline ribbon cores − such as Finemet from Hitachi Metals and Vitroperm from Vacuumschmelze − are studied as a possible replacement of ferrite cores. Their superior properties can potentially increase the power density, coupling factor, and robustness of the system. A detailed analysis is presented in this thesis.

- **Interoperability of pads:** The standard SAE J2954 sets guidelines for the design of IPT pads for EV applications. However, there is still a certain degree of freedom when it comes to designing the pads in terms of topology, power rating, and ground clearance. Nonetheless, pads should not be manufacturer-specific. In fact, they should be able to operate regardless of their maker and rating. Another issue that affects the interoperability of the IPT system is the change in power transfer capability caused by the misalignment between transmitter and receiver pads. A multi-frequency control strategy that has the potential to ameliorate these issues is presented in this thesis. This strategy makes use of the multiple resonant frequencies found in LCL and LCCL compensated systems. A proof-of-concept of this strategy is presented and validated experimentally.

Chapter 2

Literature Review: State-of-the-Art and Fundamentals

2.1 Inductive Power Transfer

Inductive power transfer (IPT) technology transmits energy from one system to another through varying magnetic fields which couple power between transmitter (Tx) and receiver (Rx) pads without physical contact. Many IPT systems have been successfully developed for a diverse range of applications from medical devices (low power) to (high power) battery charging stations. Different circuit topologies, compensation strategies, and control algorithms are tailored to each particular case [54]. In this thesis, the focus is on IPT systems for EV charging stations rated at medium to high power levels. This section discusses the main theoretical concepts required concerning such systems.

The standard IPT schematic is shown in Fig.2.1. In a simplified manner, an IPT system can be understood as a large-gap transformer operating at high frequencies. The first stage of the system is the rectification of the low-frequency AC grid voltage. For this purpose, uncontrollable single- or 3-phase rectifiers are required. A boost-PFC circuit is used for power factor correction in applications with unidirectional power flow. Alternatively, active rectifiers are employed in applications requiring bidirectional power flow such as in vehicle-to-grid implementations. In the next stage, high-frequency AC voltages/currents are synthesized using dedicated DC/AC converters. Additionally, different compensation circuits (resonant tanks) are used between the converter and the coil in both the transmitter and receiver sides for reactive power compensation and power flow regulation. Some compensation circuits can also help the system sustain adequate performance when the transmitter and receiver pads are misaligned. This is discussed further later in this chapter. During operation, the AC

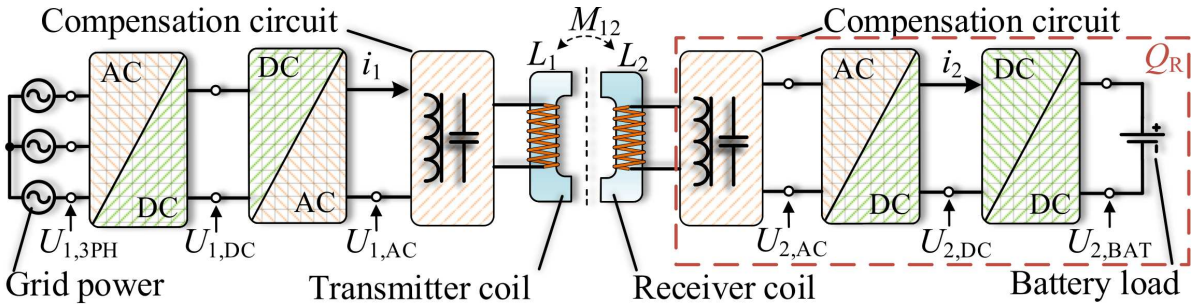

Fig. 2.1 General structure of an IPT system.

current exciting the primary coil induces a voltage in the secondary pad according to Faraday's Law. The induced voltage in the secondary is rectified and used to charge the EV battery in a controllable manner [93]. Depending on the control strategy, the rectifier can be uncontrolled or active and, in some cases, it can be followed by a DC/DC converter stage. This stage is used to control the impedance of the receiver pad and to regulate the power flow. A more in-depth description of the system's components and control strategies is discussed in the next sections.

2.1.1 Main power electronics converters

On the primary (transmitter) side, the main power converters state is the AC grid rectifier. A power-factor-correction module like the one shown in Fig.2.2.*a* is used at the primary side to comply with the grid code. A similar topology is used in 3-phase IPT systems. Although this stage is important, the main power electronic components of the IPT system are surely the DC/AC and AC/DC converters on the primary and secondary sides, respectively. A voltage source H-bridge (VSI) shown in Fig.2.2.*b* is the preferred topology for the primary side in voltage-controlled IPT systems. Contrarily, push-pull converters, like the one shown in Fig.2.2.*c* are commonly used in current-controlled systems [36]. VSI converters are used throughout this thesis; hence, push-pulled converters are not discussed any further, but more information can be found in [36]. On the secondary side, a full bridge rectifier is commonly used in unidirectional power flow systems. Alternatively, a MOSFET-based active bridge can be used for bidirectional power flow or impedance matching. This is discussed in more detail in this chapter when discussing the different control strategies for power flow regulation. Silicon carbide is the preferred semiconductor technology given the requirement for high switching frequency and low power losses. The most common voltage rating is 1.2kV. The current rating depends on the power level; modules of over 325A have been presented for high-power levels, $>$ 100kW [24].

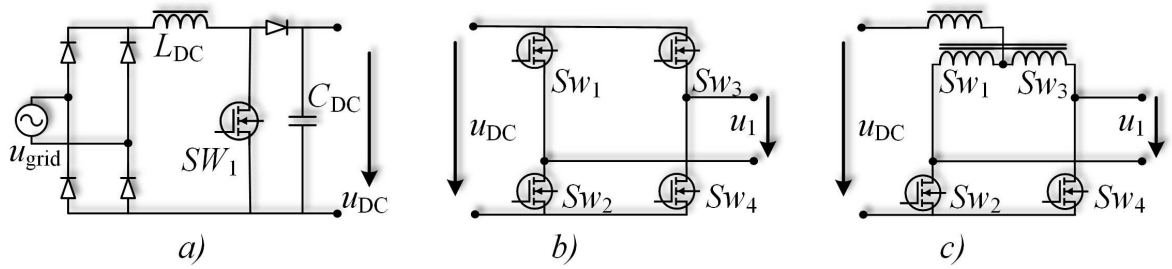

Fig. 2.2 Illustration of the main power electronics circuits required for IPT systems in the transmitter side. a) Power factor correction (PFC) b) Full-bridge inverter. c) Push-pull inverter.

2.1.2 Operating frequency

A high frequency of operation f is desirable as the induced voltage in the secondary coil and the power transfer capability of the pad are both proportional to f. Additionally, high frequencies result, generally, in smaller magnetic couplers [47] and higher power densities. Operating at high frequency, however, presents several challenges. First, not all semiconductor technologies can operate at high frequencies. Moreover, unless the switches are operated in ZCS or ZVS mode, switching losses increase with the switching frequency. Furthermore, skin and proximity effects within the coil positively correlate with the frequency. As a result, thinner Litz wire strands are required which increases the cost of the pad. Higher operating frequencies also result in higher hysteresis losses in the core which can affect the efficiency of the system. Finally, higher frequencies result in higher voltages across the coils which result in coils with higher VA ratings. IPT systems with operating frequencies ranging from few kilohertz to megahertz have been developed in the last decades. Nonetheless, in the last years, the standard SAE J2954 [72] has set a frequency of 85 kHz for EV applications. Consequently, this frequency is the one used in the latest scientific publications and throughout this thesis.

2.1.3 Current harmonics

During normal operation, the VSI H-bridge converter of a typical IPT system synthesizes a square-wave voltage signal at the desired frequency of operation (e.g. 85 kHz). This is achieved by switching both legs of the converter with a 180 phase shift. The magnitude of the n-th harmonic in a square signal is given by $u_i(n) = \frac{4U_{DC,i}}{\pi n}$. Although harmonics decrease with the frequency at a rate of $\sim$20 dB/dec, the harmonic content of this voltage signal is relatively high. To reduce the harmonic content of the voltage, multilevel converters can be implemented at the expense of more components and complexity. Pulse-width-modulation (PWM) is another alternative. PWM, however, will require switching frequencies in the order of MHz which increases the system's intricacy and the switching losses. Fortunately, such

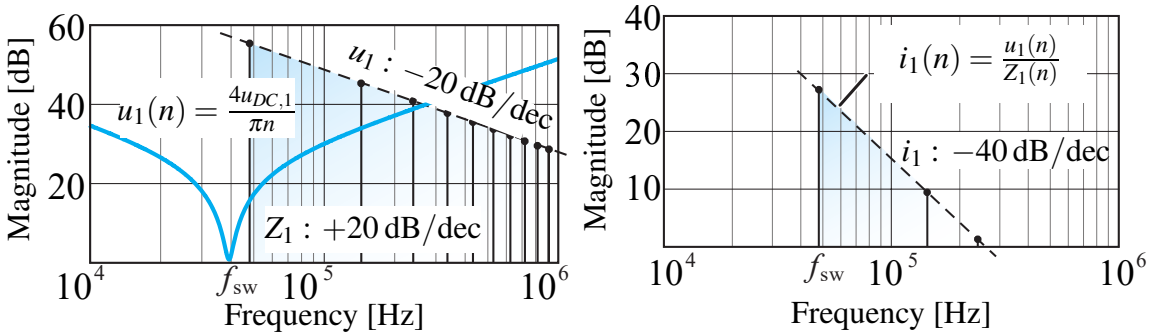

(a) Bode plot: voltage and impedance

(b) Bode plot: current

Fig. 2.3 Frequency response of the a) primary converter voltage and impedance as well as the c) primary converter current. Adapted from [8].

complex solutions are not required for most IPT systems. This is because the impedance of the pads limits the harmonic content of the voltage from being passed into the current [8]. The load equivalent impedance of a series-compensated IPT system is depicted in Fig.2.3a. Due to the resonant circuit between the coil and the converter, the impedance reaches a minimum at the resonant frequency (frequency of operation) and increases at a rate of $\sim$20 dB/dec elsewhere. The frequency response of the current is calculated from the ratio between the voltage and the impedance at each specific frequency. Hence, the magnitude of the current harmonics decreases rapidly at a rate of 40 dB/dec as shown in Fig. 2.3b. Consequently, the harmonic content of the square voltage waveform produces almost negligible current harmonics. As a result, the inverter can be represented as an ideal voltage source for most practical purposes. The same principle applies to the converter on the receiver side.

2.1.4 Equivalent Load

Just as the primary converter can be approximated by its fundamental components, the secondary converter and load can be approximated by an equivalent impedance. Since in an uncontrolled bridge rectifier the converter voltage (u_2) and current (i_2) are in phase, the equivalent impedance is purely resistive. The selection of the appropriate equivalent resistance depends on whether the receiver is driven as a current or a voltage source as shown in Fig.2.4. The equivalent resistance values are given by (2.1)

$$\text{Square } i_2 \text{ waveform}: \quad R_{L,eq} = \frac{\pi^2 u_{DC,2}^2}{8P_2} \qquad \text{Square } u_2 \text{ waveform}: \quad R_{L,eq} = \frac{8u_{DC,2}^2}{\pi^2 P_2} \tag{2.1}$$

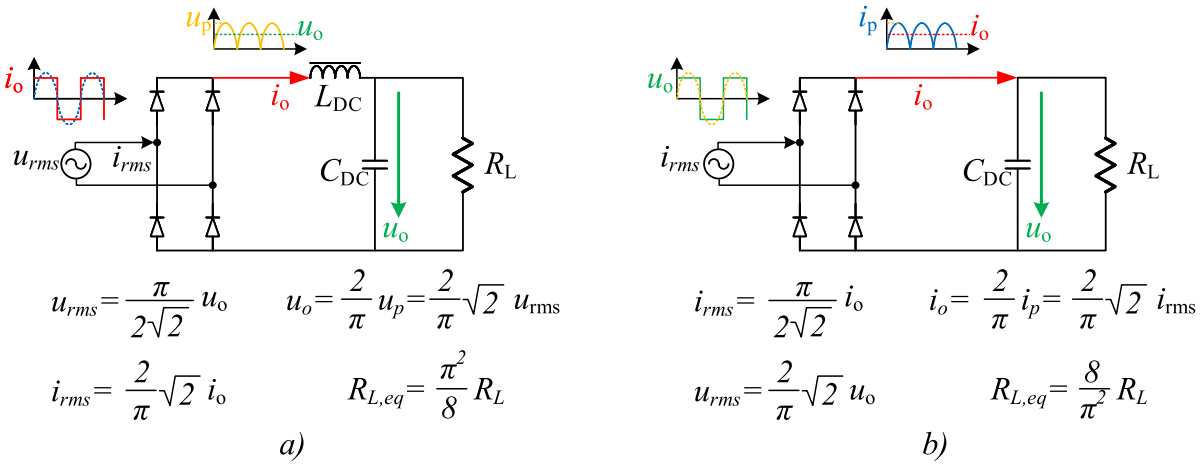

Fig. 2.4 Equivalent resistance model for a a) voltage and b) current driven source respectively. Adapted from [73].

where, P_2 is the power at the receiver estimated as the product between the DC output voltage $u_{DC,2}$ and current $i_{DC,2}$ respectively. This expression is only valid for uncontrolled converters. If the receiver side is active, the equivalent load will be controlled by the converter.

2.1.5 IPT Equivalent Models

In general, the magnetic pads in IPT systems can be represented as a pair of loosely coupled inductors with self-inductances L_1 and L_2 (respectively) and a mutual inductance M. The relation between voltages u_i and currents i_i in the primary and secondary coils is given by

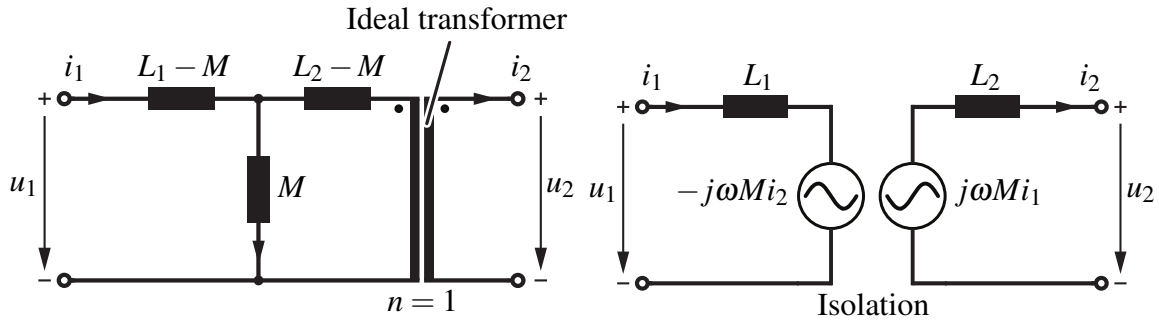

(a) One Circuit (b) Two isolated circuits

Fig. 2.5 Equivalent models of the two magnetically coupled coils. a) T-model. b) Isolated-circuit model (M-Model).

(2.2). Here, the subscript $i = 1,2$ stands for the transmitter and receiver sides respectively:

$$u_1 = L_1 \frac{di_1}{dt} - M \frac{di_2}{dt}$$
$$u_2 = L_2 \frac{di_2}{dt} + M \frac{di_1}{dt} \tag{2.2}$$

The ratio between the self- and mutual inductances $k = \frac{M}{\sqrt{L_1 L_2}}$ is known as the "coupling factor" and determines the portion of the magnetic flux linking both pads compared to the total magnetic flux produced by the coils. Power transformers tend to have high coupling factors ~ 1 which ensures high efficiency and minimum leakage inductance. For IPT pads, however, k is between 0.15 to 0.5 depending on the magnetic design of the pad [46]. The coupling factor is particularly sensitive to the coil topology as well as to the ratio of the distance between pads and their size. The coupling factor is considered as a metric of the effectiveness of the pad's design. Higher coupling factors result in better efficiency and less leakage flux.

The magnetic couplers can be graphically represented with different models. The T-model seen in Fig.2.5a is most used [8]. An alternative representation is shown in Fig.2.5b. Here, both pads are represented as isolated circuits each one with one current-controlled voltage source representing the coupling between them. Alternative representations can be found in [8].

2.1.6 Efficiency

The standard SAE J2954 requires magnetic couplers used in EV applications to sustain efficiencies over 85% during operation. Most commercial units report efficiencies greater than 80% −between the grid and the battery −, and often close to 90%. The efficiency achieved with IPT systems is usually around 5% less than that of plug-in chargers. It is worth noting that higher efficiencies ($> 99\%$) are possible for an optimum design; however, efficiency is compromised when interoperability between pad manufacturers and tolerance to pad misalignment are needed.

The power losses in the IPT systems can be attributed to the power electronic components (MOSFETs/diodes, connectors, and passive elements) and the magnetic couplers (copper and core losses). MOSFETS switching losses can be ameliorated by using soft-switching techniques like ZVS or ZCS. Losses in the other power electronic elements, however, are inherent to each component (dissipation factors). Thus, they must be sized appropriately to reduce their impact on the system's efficiency. The same is true for the coil and core in the magnetic couplers. An adequate design is required to ensure high efficiency. This is discussed more in detail in the next sections.

Maximum Efficiency

To understand the effect that the design of the magnetic couplers has on the system's efficiency, an expression of the maximum efficiency $\eta_{\max}$ can be derived. Considering only the magnetic couplers, an equivalent model of an IPT system can be constructed as shown in Fig.2.6. A series-compensation is implemented by adding a series capacitor C_i to each coil. Each capacitor resonates with its respective coil at the desired frequency of operation, i.e., $f = \frac{1}{2\pi}\frac{1}{\sqrt{L_i C_i}}$. The losses in the coil can be modeled by an equivalent resistance connected in series with the coil inductance. Note that this loss equivalent resistance represents both the copper and magnetic losses of the coil. Thus, the power transfer efficiency can be estimated from the ratio: $P_2/(P_2 + P_{loss,1} + P_{loss,2})$, where $P_{loss,1}$ and $P_{loss,2}$ correspond to the losses in the coil as depicted in Fig.2.6. An equation for the maximum efficiency can be calculated from this equivalent circuit:

$$\eta_{max} = \frac{k^2 Q_1 Q_2}{\left(1 + \sqrt{1 + k^2 Q_1 Q_2}\right)^2} \approx 1 - \frac{2}{kQ} \tag{2.3}$$

where Q_i is the quality factor of the individual coils. The quality factor Q_i represents the ratio between the coil reactance and resistance: $Q_i = \frac{\omega L_i}{R_{i,ac}}$. The quality factor can be also understood as the ratio between the power stored by the coil (inductance) and the power loss in the coil. From (2.3), it is clear that the efficiency of the magnetic coupler is mainly dependent on k and Q. The product kQ is one of the *figures of merit* of IPT technology [11]. Quality factors in IPT technology are kept typically over 100 to ensure higher efficiencies.

To improve the pad's efficiency, Q and k must be increased. The quality factor Q can be improved by reducing the overall AC resistance or by raising the frequency of operation. The AC resistance can be reduced by increasing the cross-section of the coil at the expense of

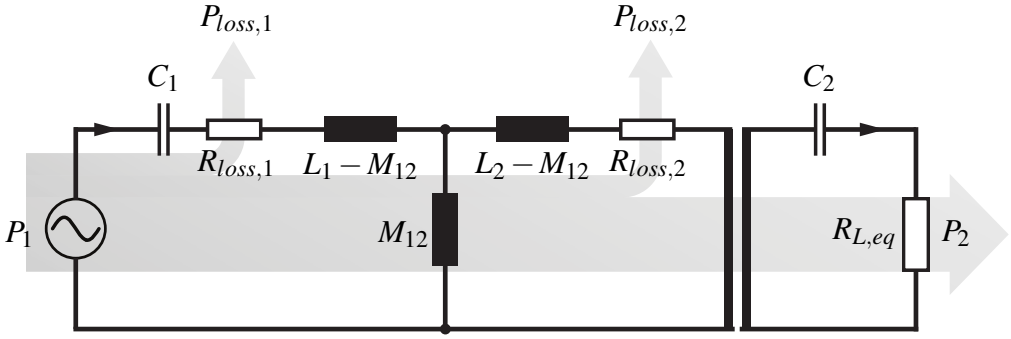

Fig. 2.6 Depiction of the power losses in a series compensated IPT system. Adapted from [8].

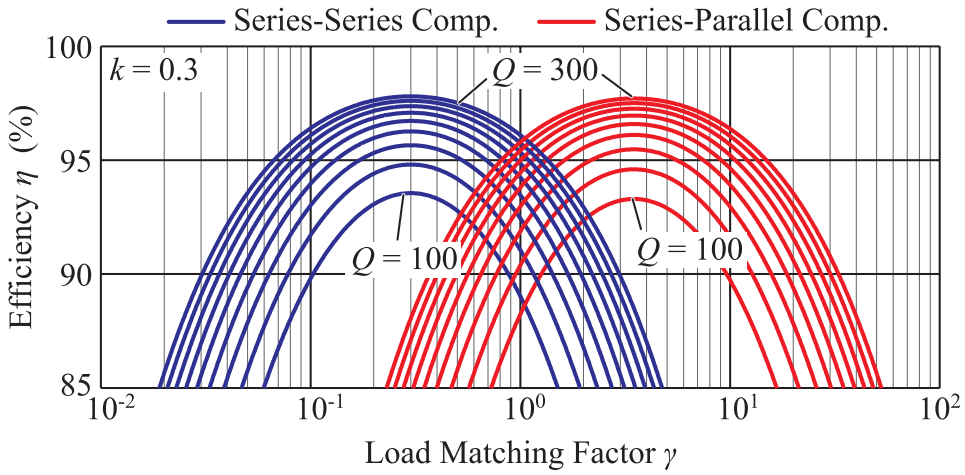

Fig. 2.7 Efficiency of the system as a function of the load (load matching factor, $\gamma = \frac{R_{L,eq}}{\omega L_2}$) for a series-series (SS) and a series-parallel (SP) compensated systems. Q : Quality factor.[8].

more cost, volume, and weight. On the other hand, the coupling factor k can be increased by optimizing the design of the pad. The factor k is particularly dependent on the ratio between the coil area and the distance between pads. Consequently, coils that occupy larger areas yield higher coupling factors. Larger pads imply lower power density as well as an increment in the copper losses due to the extra coil length. A compromise is usually required during the design. On the other hand, k can be also improved by reducing the distance between pads. This is, however, determined by the application. For EVs, the clearance between pads ranges from 75mm to over 200mm [72]. For EVs, typical designs result in coupling factors below 0.3 [24].

Efficiency vs. Load

The maximum pad efficiency given by (2.3) is only achieved for a specific load $R_{L,eq}$. Deviations from this value produce a drop in efficiency. This decay is shown in Fig.2.7 for two different compensation topologies: series-series (SS) and series-parallel (SP). Here, γ represents the equivalent load normalized by the coil reactance, i.e., $\gamma = \frac{R_{L,eq}}{\omega L_2}$. In IPT systems, γ is usually referred to as the "load matching factor".

An optimal pad design must ensure maximum efficiency at the rated load. At any other load, the efficiency of the system will be sub-optimal unless the equivalent impedance of the load is controlled to keep the load matching factor constant at every operating point. For this, an active rectifier or a DC/DC converter stage between the rectifier and the battery is required as seen in Fig.2.1.

2.1.7 Power Transfer

The amount of power transmitted between pads can be estimated from the open-circuit voltage V_{oc}, short-circuit current I_{sc}, and the load quality factor Q_R as in (2.4).

$$P_2 = V_{oc} \cdot I_{sc} \cdot Q_R = \omega^2 \cdot i_1^2 \cdot \frac{M^2}{L_2} \cdot Q_R = P_{su} \cdot Q_R \tag{2.4}$$

Here, Q_R refers to the ratio between the apparent power in the secondary coil VA_2 and the power output P_2. In a series compensated system, Q_R is equivalent to the ratio between the secondary coil reactance (ωL_2) and the equivalent load resistance ($R_{L,eq}$); i.e., $Q_R = \frac{\omega L_2}{R_{L,eq}}$. In parallel compensated systems, Q_R is given by: $\frac{R_{L,eq}}{\omega L_2}$. Higher Q_R values result in higher power transfer. In practice, however, this value is usually limited to 10.

P_{su} in (2.4) refers to the uncompensated power and only considers the magnetic circuit independently of the load and power electronics. For this reason, P_{su} is used as a metric when comparing different designs of magnetic couplers. P_{su} can be also written as in (2.5):

$$P_{su} = (\omega \cdot L_1 \cdot i_1) \cdot i_1 \frac{M^2}{L_1 L_2} = u_1 \cdot i_1 \cdot k^2 = \mathrm{VA}_1 \cdot k^2 \tag{2.5}$$

where VA_1 represent the apparent power of the unloaded primary pad. Effectively, the VA rating of the magnetic couplers is inversely proportional to the coupling factor. Lower VA ratings are preferred as they lead to lower losses and lower component voltage/current stress [66].

2.2 Magnetic Couplers: Coil and Core

The magnetic coupler comprises the winding, core, and shield. Its design determines the performance of the pad in terms of efficiency, VA rating, and power transfer capability. In the next sections, the most relevant aspects of these magnetic components are discussed.

2.2.1 Magnetic Coil

Topologies

The coils are excited with high-frequency currents and they are responsible for the generation of the magnetic fields involved in the transfer of power. Different topologies have been introduced in the last decade. They can be classified into two groups: single-winding (circular) and multi-coil pads (Double-D, Double-D Quadrature, Bipolar, and Tripolar). Detailed

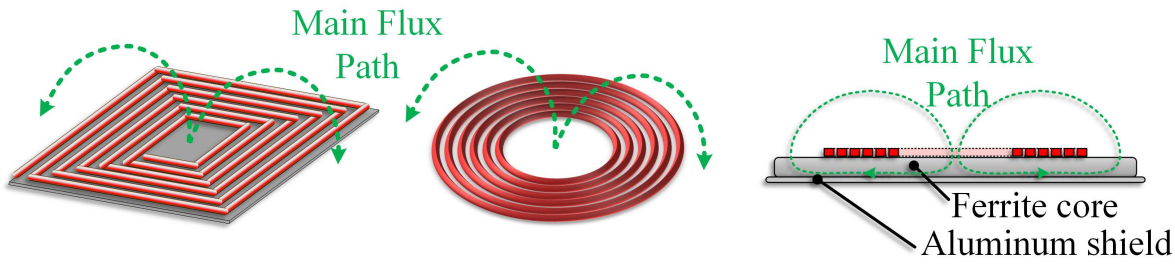

Fig. 2.8 General structure of non-polarized pads with square or circular winding.

descriptions and design methodologies for each topology can be found in [16], [9], [15],[91], [45, 44], respectively. A comparative study is presented in [50].

Non-polarized pads, usually known as circular pads (Fig. 2.8), are formed uniquely by one coil which produces a single magnetic pole per pad. Its structure is simple and requires less amount of copper; however, its performance is inferior compared to polarized pads. First, its power transfer capability P_{su} is lower. Second, it is less robust to pad misalignment and changes on the distance between the transmitter and receiver pads [16]. A polarized pad can be 18% smaller compared to a circular pad. Moreover, it can transfer twice as much uncompensated power and with higher efficiency with 28% less ferrite [50]. Moreover, they are more tolerant to misalignments which results in an operational area three times larger than that of circular pads [40]. Despite their inferior performance, circular pads are still used due to their simplicity of design and implementation, attributed to their radial symmetry. A detailed description of the optimal design of circular pads can be found in [12, 16].

Multi-winding pads require two or more coils per pad. These coils can be connected in series or parallel or independently controlled depending on the application at hand. Multiple coils can generate more than one magnetic pole; hence, they are commonly referred to as polarized pads. The Double-D coil was introduced in 2013 [15]. Its general structure can be seen in Fig.2.9a. A set of two coils are placed horizontally next to each other. The coil's middle section, also known as the flux pipe, creates two magnetic pole pairs. Having two pole pairs helps to constrain the flux to the pad's area more effectively. Consequently, the stray (leakage) flux is largely reduced [10]. The flux created by a DD pad reaches about one-half of the pad's length for DD pads [15]. The ferrite core bars underneath the coils enhance the flux pipe and improve the magnetic coupling. For circular pads, the flux extends only one-quarter of the pad's diameter. As a result, DD pads outperform circular pads in applications when large air gaps are required. Regarding the robustness to pad misalignment, DD coils are more robust to displacements in the y-axis as compared to circular coils. In the x-axis, however, DD pads reach a null point ($P_{su} = 0$) when the misalignment reaches approximately 34 % of

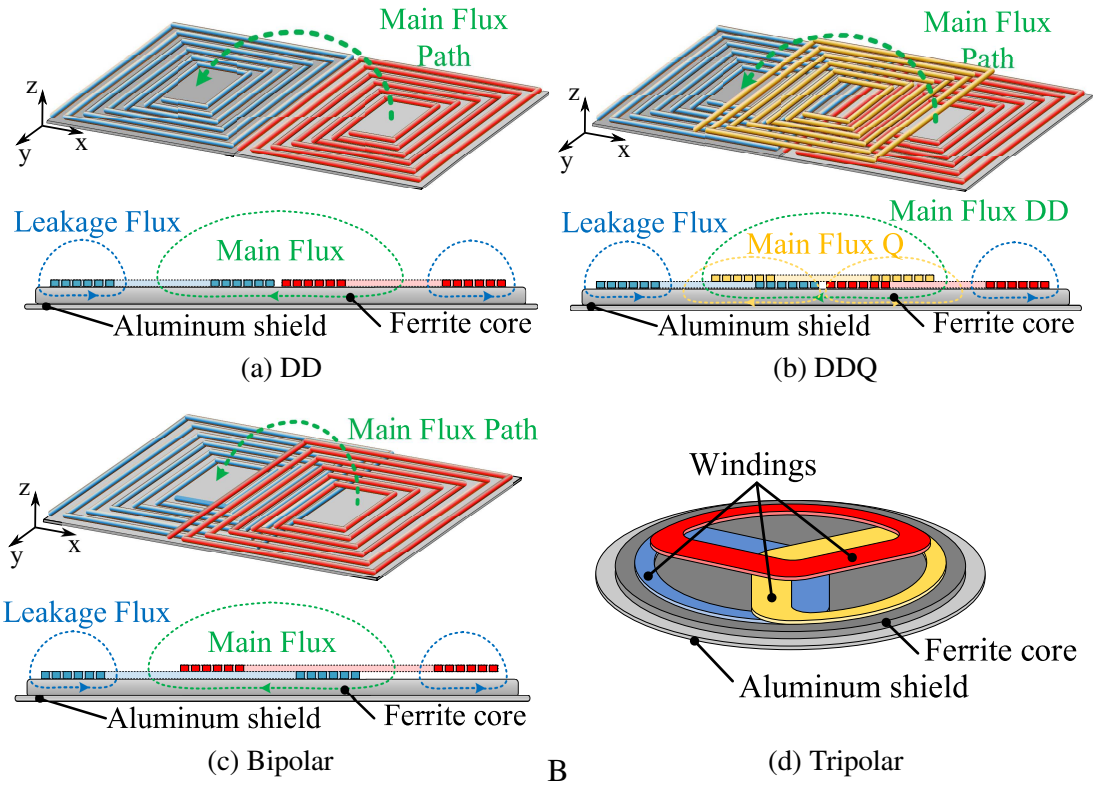

Fig. 2.9 Structure of different polarized topologies as well as their main and leakage fluxes. *a*) Double-D *b*), DDQ *c*) Bipolar BPP and *d*) tripolar.

the pad's length. A quadrature coil is often added to the receiver side to cope with this issue. This arrangement is referred to as Double-D-Quadrature (DDQ) topology and it is shown in Fig.2.9b. The Q coil improves the performance at misaligned conditions at the expense of a higher pad's weight, thickness, and volume [15]. A more in-depth description can be found in [12, 16, 15].

Both coils in a DD pad are magnetically coupled to each other. This coupling is irrelevant in some applications as the coils are connected in series forming one coil with an equivalent lumped impedance. For other applications, however, each coil is connected to a respective compensation circuit or power module and controlled independently from each other. In such cases, the magnetic coupling between the coils is undesirable. This requirement has motivated the development of bipolar pads, like the one shown in Fig.2.9c. Bipolar (BP) pads achieve zero coupling factor between adjacent coils by partially overlapping them, as seen in Fig.2.9c [91]. As a result, each coil is magnetically independent of the other. Thus, each coil can be excited with a different current to generate a variety of magnetic fields. In fact, bipolar pads can operate as polarized or non-polarized pads if needed [51]. Apart from the independence between coils, several other advantages have been found. Bipolar pads can achieve similar ro-

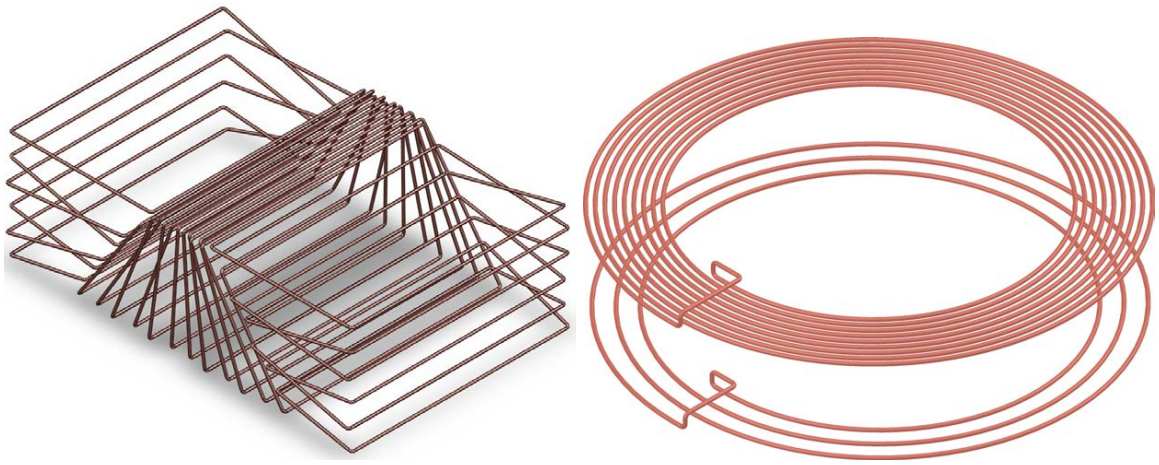

(a) Ferrite-less Pad (b) Ferrite-less Pad

Fig. 2.10 Example of coil topologies for ferrite-less pads. a) polarized b) non-polarized (circular) pad.

bustness to misalignment than DDQ pads while requiring $\sim 25.17\%$ less copper. Additionally, bipolar pads can increase not only the coupling factor but also its robustness to misalignment. Moreover, isolated control of each coil in a BP pad can lead to higher overall efficiencies [91].

The concept of bipolar pads can be extended to three or more sets of pads resulting in tripolar (TPP) or quadpolar, DDQ^2, etc [65]. Using a TPP primary pad can increase the "effective coupling factor" k_{eff} between pads in such a way that power can be transferred with 45% less VA in the primary [45]. Here, k_{eff} is defined as the ratio between apparent power in the secondary and primary, i.e., $k_{eff} = \frac{S_2}{S_1}$. It is useful to determine the power transfer capability of multi-coil systems [44]. The higher k_{eff} found in TPP attest to its superior power transfer capability. The TPP can adjust the magnetic field according to the misalignment and, consequently, are more robust than other pads. Moreover, the TPP has shown less leakage flux which facilitates the compliance of safety codes. However, it is worth noting that multi-winding pads require extra materials, switches, and compensation circuits as compared to single winding systems. The TPP will not be discussed further in this thesis.

Ferromagnetic materials are necessary to improve the magnetic coupling and constrain the trajectory of the magnetic flux. The most common materials used as cores are ceramic. Hence, they are brittle and behave poorly in harsh environments: high temperatures and vibrations. In recent years, several authors have started to look for ferrite-less pads as a way of improving the mechanical robustness of the pad, reducing cost, and simplify the design. As shown in Fig.2.10, different coil topologies have been introduced: using the concept of Halbach array [56] or reflection windings [76, 68, 66, 67]. Ferrite-less pads are an attractive solution for

roadway IPT systems. However, it is worth noting that higher VA ratings are required as compared to ferrite-based IPT systems [65].

Conductors

The high-frequency currents used to excite the coils make the conductors prone to skin and proximity effects. Skin effect refers to the change in the current distribution within the cross-sectional area of a coil as a function of the operating frequency. The proximity effect, on the other hand, refers to the change in current distribution seen in stacked conductors due to the magnetic field of adjacent ones [78]. Both effects tend to increase the AC resistance of the coil. To mitigate the undesired effects of proximity and skin effects, Litz wires are commonly used. Litz wire is a stranded coil designed for high-frequency operation. The diameter of the individual strands is selected according to the skin depth δ of the conductor. The skin depth can be understood as "the depth below the surface of the conductor at which the current density J has fallen to e^{-1} of the current density at the surface J_{surf}" [78] and can be approximated, for round conductors, as in (2.6):

$$\delta = \sqrt{\frac{1}{\pi f \sigma \mu}} \tag{2.6}$$

where f is the frequency of operation, μ is the permeability of the conductor, and σ, its conductivity.

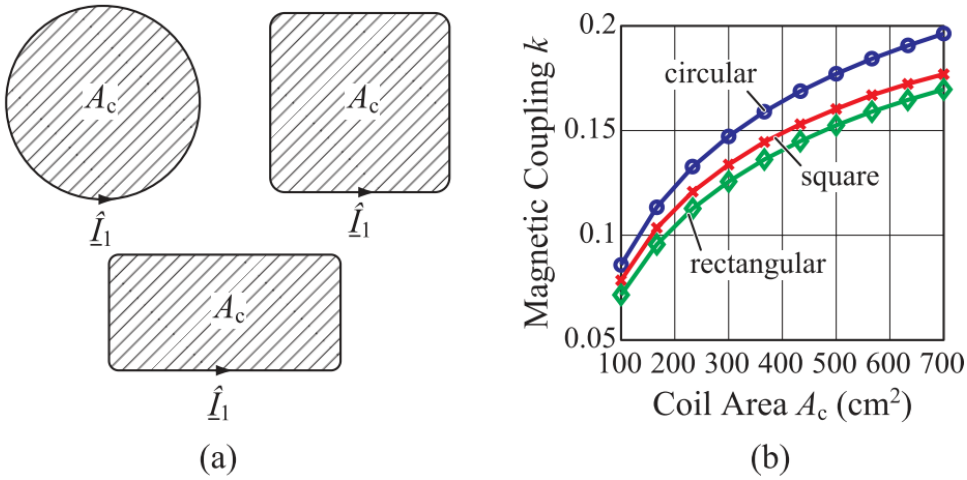

Fig. 2.11 Coil area versus magnetic coupling k for different cross-section geometries of Litz wire. Taken from [12].

Even with Litz wire, winding losses could account for up to $\sim 70\%$ of the overall losses of the magnetic coupler [12]. These losses depend on the cross-sectional area of the conductor. Thicker coils result in lower current densities, higher coil quality factors, and lower copper losses. However, they increase the weight and cost of the pad. According to [9], "a current density of approximately $J = 4\,\mathrm{A/mm^2}$ provides a good balance between copper losses and copper utilization". This value can be used to determine the required cross-sectional area of the coil. Alternatively, the AC resistance of the coil can be analytically calculated. There are different methods to estimate the resistance of a coil in an IPT system. For circular pads, the effective AC coil resistance of the Litz winding can be estimated employing (2.7) [78]:

$$R_{ac+dc} = R_{dc}\left(2 + \frac{\pi^2\omega^2\mu_0^2 N^2 n^2 d_c^6 \gamma_c}{768\rho_c^2 b_c^2}\right) \tag{2.7}$$

where, R_{dc} is the DC resistance of the coil, N is the number of turns, n the number of strands per turn, d_c the strand diameter, b_c the breadth of the window area of the coil and γ_c a factor accounting for the effects of the magnetic field (usually 1) [78]. Another method is presented in [62]. This method is used in this thesis and it will be presented in the next chapter. Litz wire can also have rectangular or square cross-sections. However, coils with circular cross-sections yield higher coupling factors as seen in Fig.2.11. Square and rectangular coils yield lower values of k due to the distortion of field distribution around the corners of the coil. Since the efficiency of the pad is proportional to k, circular cross-sections are preferred.

2.2.2 Magnetic Core

Soft-magnetic materials are added to the IPT pads to improve their magnetic performance. The addition of magnetic cores results in higher P_{su} and k, and lower VA ratings. High resistivity, permeability, and saturation point are some of the requirements for the core material. High resistivity is required to limit eddy-currents induced in the core while a slim hysteresis loop is required to ensure minimum magnetic losses. For IPT applications, manganese-zinc powder ferrites, such as the N87 from EPCOS or K2004, are the most used materials. Ferrite is used due to its adequate magnetic properties, large availability, and low cost. Ferrite cores, however, are brittle and make the implementation of small-scale or geometrically complex cores impractical. Ferrite cores have a relatively low magnetic saturation point, limiting the power rating of the magnetic coupler. Moreover, the performance of ferrite deteriorates rapidly as the operating temperature rises. Ferrite-less pads or alternative materials are the current focus of research.

For non-polarized coils, three core designs are the most recurrent in literature: plates (Fig.2.12c), unidirectional bars (Fig.2.12a), and radially oriented bars (Fig.2.12b). Unidirec-

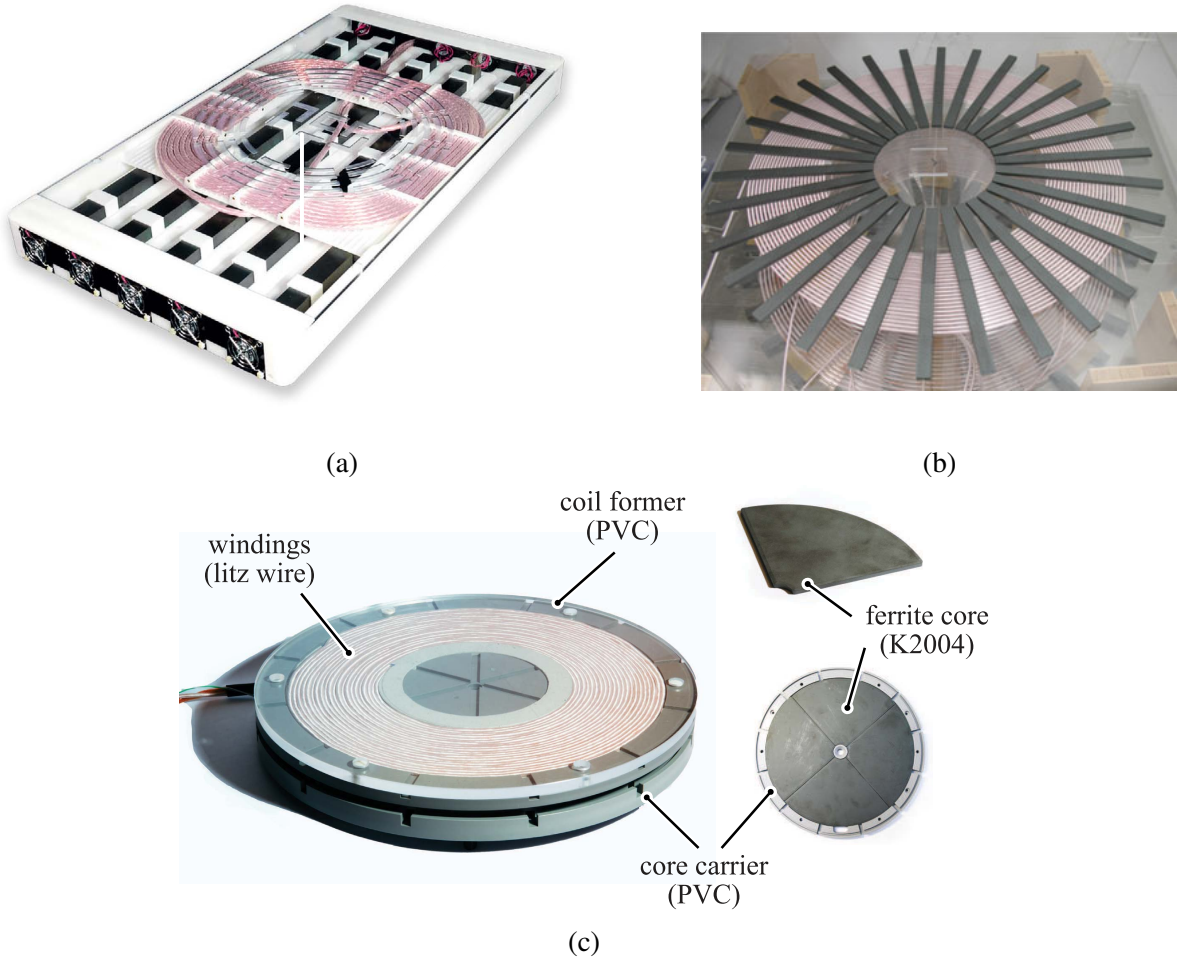

Fig. 2.12 Core designs used in polarized coils: *a*) unidirectional bars [9] *b*) radial core bars [23] and *c*) complete core (plate) [12].

tional bars are a viable alternative for polarized coils as the flux is unidirectional. When both the transmitter and receiver pads are non-polarized, plates or radially oriented bars are preferred. According to [16], discrete core bars achieve similar performance to a continuous core (plate). The optimal size and placement of the core within the pad area have been prominent topics of research in the last years. In [16], the analysis of the optimal placement and size of radially oriented bars is presented. In [89], a particle-swarm-based optimization of 2D-axis-symmetrical circular pads is introduced. In both cases, optimum placement patterns are identified; however, the implementation of these intricate patterns is limited by the scarce options of commercially available geometries [89, 16]. In [22], ferrite nano-particles on a base of polymer were introduced to improve the mechanical performance of the pads and reduce the amount of ferrite. Although the obtained permeabilities are lower, the mechanical robustness of the material was effectively increased.

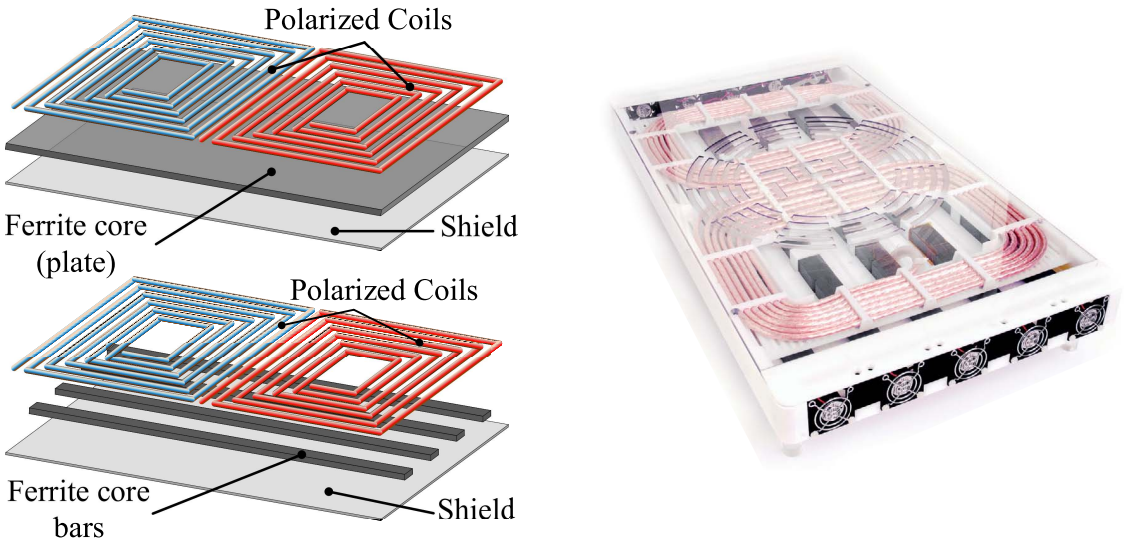

Fig. 2.13 Core designs used in polarized coils: *a*) full core (plate) [60] *b*) core bars [12].

For polarized pads, both ferrite bars and plates are used as shown in Fig.2.13a. In [15], guidelines for Double-D pad design are presented using I93 core bars. Since only discrete core bars were considered, the design process was limited to obtain the optimum separation between bars. The optimum spacing was determined to be twice the core bar thickness. The thickness of the bars was determined according to the maximum allowed flux density within the core. The maximum flux density is constrained by the saturation limit of the material. In most cases, the maximum flux is restricted below the saturation point to reduce the losses in the core. The optimal utilization of ferrite cores within a continuous ferrite plate was studied in [59]. As shown in Fig.2.14c and Fig.2.14d, adjusting the core bar thickness proportionally to the flux density results in better utilization of core material. However, this results in a complicated geometry (thicker in the middle section, flux-pipe) which reduces the pad's manufacturability and robustness. In [65], the effect of reducing the amount of ferrite was analyzed when considering a uniform ferrite plate below the pad. Fig.2.14a shows the primary VA required for a $P_{su} = 1$kVA while the leakage flux with a fully displaced secondary is shown in Fig.2.14b. The leakage flux is measured at 800 mm away from the center of the secondary pad. As the amount of ferrite in the pad decreases, so does the leakage flux. At the same time, however, the required VA and current in the primary pad increase. The increase in VA seems to reduce after the flux pipe is filled with material.

Ferrite plates are considered both in [65] and in [59]. It is worth noting that large ferrite plates are not commercially available and bespoke designs are required. Moreover, large ferrite pieces are difficult to manufacture due to the brittleness of the material. Thus, ferrite

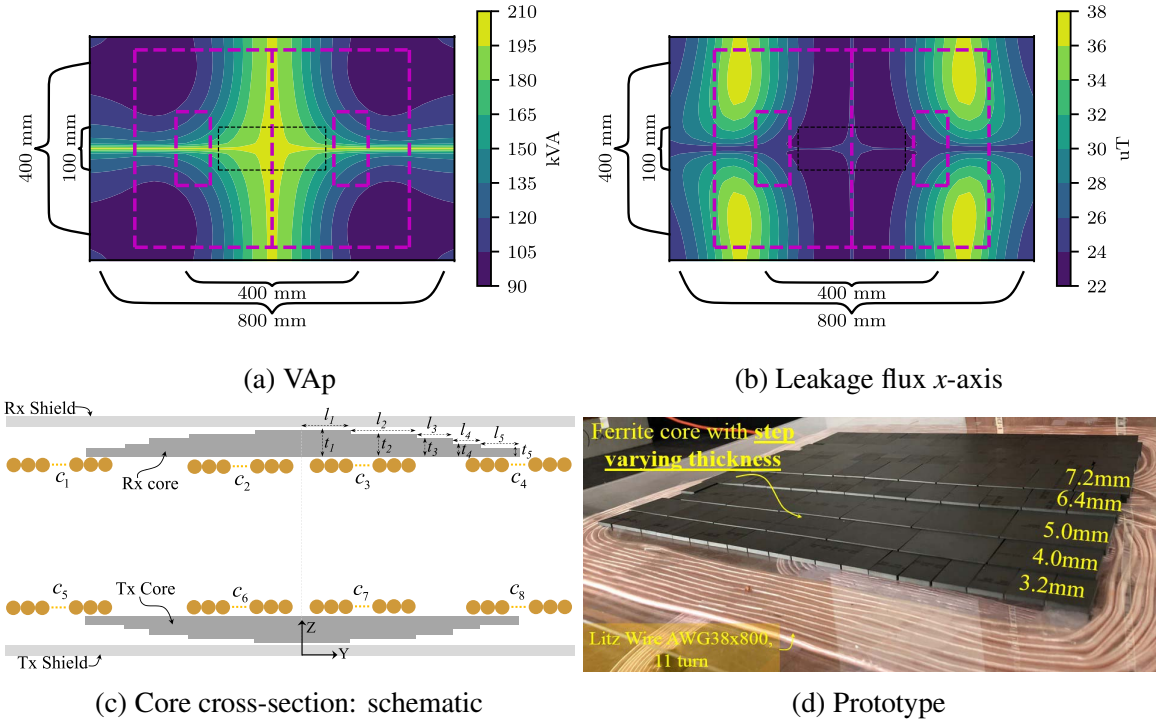

(a) VAp

(b) Leakage flux x-axis

(c) Core cross-section: schematic

(d) Prototype

Fig. 2.14 Optimization of ferrite in DD pads assuming a ferrite plate. $a)$ shows the primary VA required for a $P_{su} = 1$kVA while the leakage flux with a fully displaced secondary is shown in $b)$. The leakage flux is measured at 800 mm away from the center of the secondary pad. Plots taken from [65]. $c)$ and $d)$ show the core topology discussed in [89]. The core cross-section is shaped to minimize core losses.

plates are usually formed by several smaller units. The interface between units leads to several problems such as partial saturation and localized heating in the cores. These problems are more probable as the number of units used in the core increases. In [14], introducing gaps in between units is suggested to mitigate these issues. However, this comes at the expense of higher reluctance in the core which translates into lower coupling factors and inductances. Due to these limitations, ferrite bars are preferred, particularly for high power applications [10]. The spacing between bars is commonly used for cooling as shown in Fig.2.13b.

Core losses

Power losses within the magnetic core are mainly of two types: eddy-current and hysteresis losses. The former results from the circulation of induced currents within the core while the latter results from the stiffness of the magnetic domains [78]. Both are proportional to the magnitude and frequency of the magnetic field density B. In general, power losses in the core can be estimated employing the Steinmetz equation (2.8)

$$P_v = C_m C(\vartheta) f^{\alpha} B_{pk}^{\beta} \tag{2.8}$$

where C_m, α, and β are constants obtained heuristically for each material; f stands for the frequency of the magnetic field, B_{pk} for the peak magnetic flux density while $C(\vartheta)$ is a correction factor due to changes in temperature (ϑ). It is worth noting that (2.8) units are kW/m^3. Thus, to calculate the total losses, volume integration is required. This is commonly done with FEM packages after solving for the magnetic field distribution within the core.

Ferrite losses can be also estimated directly from FEM simulations by specifying the permeability as a complex quantity. Complex permeability (μ') can be understood as follows. When an AC excitation $H = H_m e^{j\omega t}$ is applied to a ferromagnetic material, a flux density $B = B_m e^{j(\omega t - \delta)}$ is obtained. Here, δ represents the phase angle between H and B and it is related to the power loss in the material due to the AC magnetization. The complex permeability can be defined as the ratio between B and H as in (2.9) [26]:

$$\mu' = \frac{B}{H} = \mu_r + j\mu_i = \frac{B_m}{H_m} cos(\delta) - j\frac{B_m}{H_m} sin(\delta) \tag{2.9}$$

The complex permeability μ' reflects the combined effect of eddy-current, hysteresis, and relaxation losses [26]. Complex permeability values can be obtained from the material datasheets. The measurement of complex permeability is commonly performed by using toroidal cores. Thus, the measured values considered unidirectional uniform flux. When the core is exposed to traverse fluxes, alternative methods of estimating losses are required, particularly for anisotropic and/or laminated cores. These methods are discussed in this thesis in Chapter 3.

2.2.3 Stray flux regulations and Shield

According to the International Commission of Non-Ionizing Radiation Protection's guidelines (ICNIRP), the general public should not be exposed to more than B_{rms} =27 μT of magnetic flux for frequencies between 3 kHz and 10 MHz. This value is slightly relaxed for occupational exposure to about B_{rms} = 100 μT [38]. For many IPT systems, the general public limit is considered and, therefore, a limit of B_{rms} = 27.3 μT is usually selected. [10, 13].

Contrary to the ICNIRP, the IEEE.C95 standard defines a limit of 205 μT_{rms} for exposure of head and torso and 1130 μT_{rms} for limbs [39]. The lack of agreement between these two standards is attributed to differences in statistical and biological models, stated objectives, and specification of safety limits in specific body parts [70]. In literature, limits vary across research institutes. In recent years, however, more authors seem to favor the pacemaker limit of

15 μT_{rms} as it considers a worst-case scenario [72]. To ensure code compliance, the magnetic flux is measured in different points around the pad and the safe zone is defined accordingly [72, 9]. A distance of ~800 mm from the center of the receiver pad is usually considered as the limit of the safety area (considering the vehicle width as 1.6 m), as shown in Fig.2.15.

The magnitude of the flux leakage depends on the frequency of operation, the primary apparent power, and the coupling factor between pads [50]. High power ratings complicate the compliance of safety codes as the flux leakage increases with the power level. Therefore, most IPT systems use magnetic shielding to reduce leakage flux. Two main shielding methods can be found in literature: metallic shielding and reflection coils [43]. A metallic shield is a metal sheet placed in strategic locations within the pad, usually below the pad. The magnetic flux reaching the shield induces currents which, in turn, creates a magnetic field that opposes the main one [43]. The currents in the shield produce losses that can be estimated with FEM simulations as is done in [11]. A reflection coil, on the other hand, is an additional winding placed below the pad. When excited, it produces a magnetic field that cancels the flux generated by the main windings. The reflection coil can be active (driven by a power source) or passive (driven by the main winding). Active coils require more power electronics and control units but are more versatile and easier to design as compared to passive coils.

2.2.4 Magnetic pad design

The optimum design of an IPT charger is not straightforward. There are many variables to be defined and a similar number of constraints to be satisfied. The design variables refer to the geometric and intrinsic characteristics of the coil (number of turns N, coil diameter, coil area, the separation between coils, etc.) and core (material, size, placement, etc.). Several metrics are used to evaluate and constraint the design; namely, the power density, efficiency η,

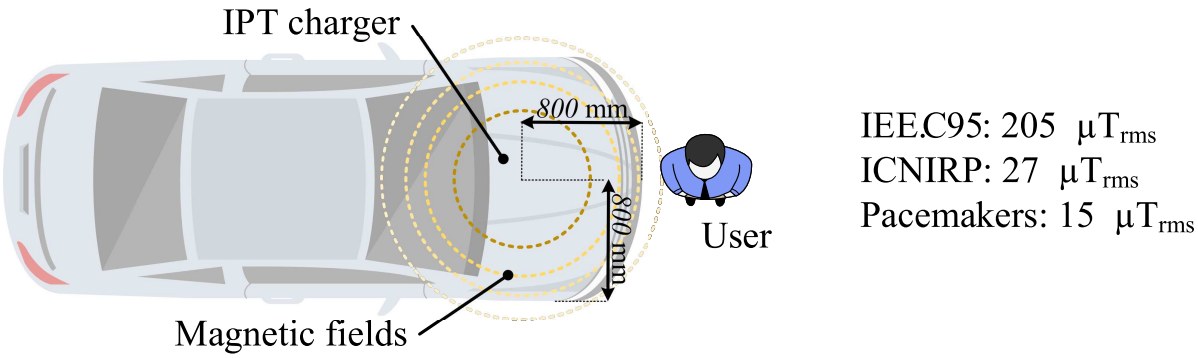

Fig. 2.15 Depiction of the distance at which the stray flux is measured considering a vehicle width of 1.6 m. The limits according the different standards are listed as well: IEEE.C95 [39], ICNIRP [38], and pacemaker [72].

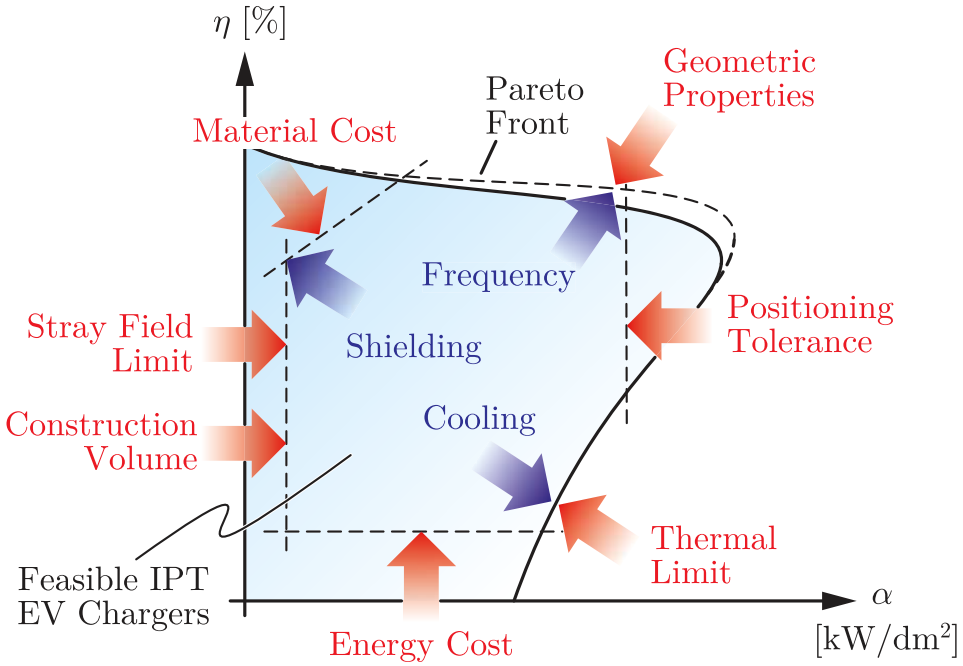

Fig. 2.16 Pareto front delimiting the design space for IPT pads [11].

cost, tolerance to pad misalignment, and maximum leakage flux. Each design variable relates intricately to a metric. Moreover, metrics are closely linked. Thus, adjusting a design variable to improve one metric can have a detrimental effect on the others. As a result, the design of an IPT system requires balancing opposing requirements [12].

Given that IPT receiver pads are installed under the EV's chassis, the volume and weight of the pad should be as minimum as possible. Moreover, the area occupied by the pad must be also reduced as it is directly correlated to the volume, weight, and leakage flux. The power density per unit area is defined for IPT systems as α_A; i.e., the rated power divided by the surface area of the pad in kW/dm^2. More compact pads have a higher power density; however, they are less robust to misalignment between pads. Moreover, their efficiency tends to be lower as the coupling factor is proportional to the pad area. Lower efficiency can lead to thermal and reliability problems. On the other hand, larger pads are more efficient but result in higher leakage flux outside the vehicle, higher cost, and weight. As shown in Fig.2.16, there is an inherent trade-off between metrics; particularly, between α_A and η. This trade-off defines a Pareto-front which can be used for the design of IPT systems [12]. A design framework based on this Pareto-front is presented in [12] and it is briefly summarized next.

The first step during the design phase is to determine all the design requirements. These are set by the power converters (maximum voltage, current, power rating, etc). Second, a range of feasible values for all the design variables (pad width, the pad length, number of turns, etc.) is

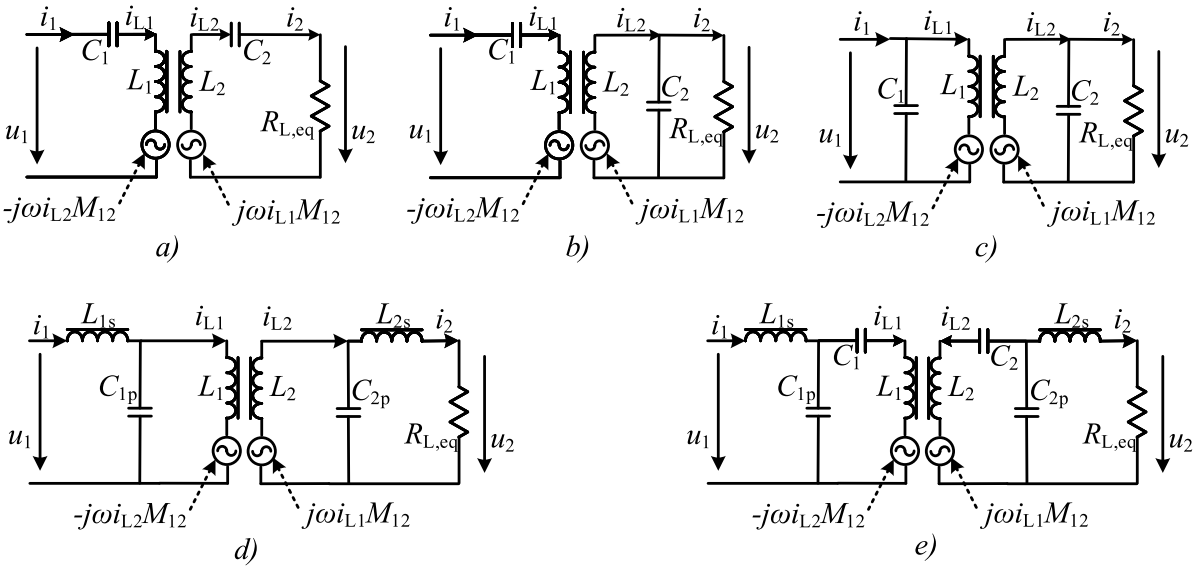

Fig. 2.17 Different compensation topologies. *a*) series-series, *b*)series-parallel, *c*) parallel-parallel, *d*) LCL-LCL, and *e*) LCCL-LCCL.

defined. Thereafter, FEM simulations are used to sweep the design variables for a specific coil topology and core material. The models that comply with design requirements are considered as part of the design space. Analytic models and FEM results are used to calculate metrics that evaluate the effectiveness of a specific design. Usually, efficiency and power density are used as metrics. These metrics will define a Pareto-front from which the final design will be selected depending on manufacturability, availability of materials, among other factors [10].

2.3 Compensation circuit

Compensation circuits are essential elements in an IPT system [40]. Due to the large air gaps, the leakage flux of the coils is considerably high. Thus, the power factor of an uncompensated IPT system is low. Moreover, large reactive currents cause unacceptable losses. Resonant tanks are therefore used for reactive power compensation to achieve a unity power factor [23]. Several compensation circuits have been analyzed during the last decades. The number of components (capacitors and inductors) as well as their performance regarding power flow control, robustness to misalignment, and current sharing are different for each topology. The most commonly used compensation topologies for non-polarized pads are the series-series, series-parallel, LCL-LCL, and LCCL-LCCL, as shown in Fig.2.17. For polarized pads, these same resonant tanks, as well as combinations of them, are considered. The operation of these topologies is discussed next.

Analysis Framework

The analysis of any compensation topology follows the procedure depicted in Fig.2.18. First, the equivalent impedance of the secondary side is obtained by combining the load and compensation circuit into one single impedance $Z_{2,eq}$. The capacitance and inductance values in the secondary compensation tank are defined so its resonant frequency is $\omega = 2\pi f$; where f is the desired operating frequency. As a result, the expression of $Z_{2,eq}$ can be significantly simplified when considering resonance.

The current in the secondary coil i_{L2} is calculated as in (2.10):

$$i_{L2} = \frac{j\omega M_{12} i_{L1}}{Z_{2,eq}} \tag{2.10}$$

In some compensation topologies, the secondary coil current and the load current i_2 are the same. However, this is not always the case. In these cases, the load current i_2 can be calculated using Kirchhoff's current law and i_{L2}. The load current is required to compute the power transfer to the load as given by (2.11):

$$P_2 = i_2^2 R_{L,eq} \tag{2.11}$$

Once i_{L2} is defined, the secondary circuit can be reflected into the primary side as an equivalent impedance by means of (2.12):

$$Z_{\text{ref}} = \frac{-j\omega M_{12} i_{L2}}{i_{L1}} \tag{2.12}$$

The equivalent input impedance $Z_{1,eq}$ is then estimated by combining Z_{ref}, L_1, and the compensation circuit in the primary coil. The input current i_1 and the primary coil current i_{L1} are estimated from this equivalent circuit. The power can be also calculated as a function of the voltage in the primary converter u_1: $P_2 = u_1 \cdot i_1^*$.

Following this procedure, expressions for the converters and coil currents can be defined. Moreover, explicit expressions for the power transfer can be found. Finally, the values of the capacitors and inductors required to achieve resonance can be mathematically defined. Table 2.1 lists the most important equations for the commonly used compensation circuits. Details of every compensation model are introduced in the next sections. It is worth noting that in this analysis, the coil resistance is not considered. Thus, the coils are considered as loss-less to facilitate the analysis of the compensation topologies. Nevertheless, the analysis can be extended to lossy conductors following the same procedure.

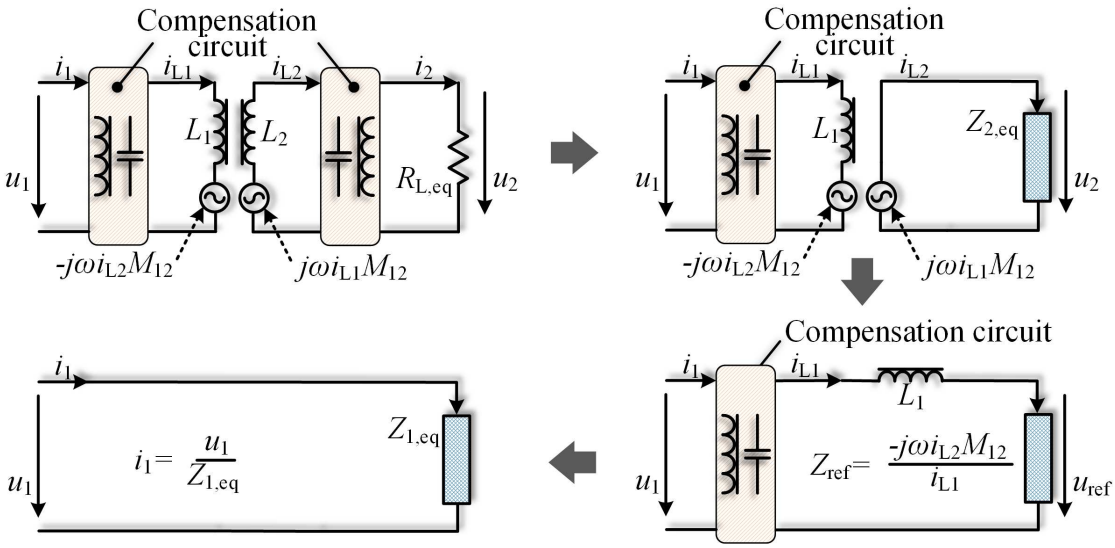

Fig. 2.18 Depiction of the process used when analyzing compensation circuits as part of IPT systems.

2.3.1 Series-Series (CL)

This compensation is depicted in Fig.2.17.*a* and its most important equations are listed in Table 2.1. The main advantage of this topology is its simplicity and low component count; only one extra capacitor per pad is necessary. Additionally, the resonant conditions are independent of the coupling factor.

At the resonant frequency, the voltage u_1 defines the current in the secondary $i_2 = i_{L2}$. The input current $i_1 = i_{L1}$, on the other hand, is proportional to the load $R_{L,eq}$. Assuming no losses in the pad, the power transferred is given by (2.13) as a function of the input and output voltages.

$$P_2 = \frac{U_1 \cdot U_2 \cdot \sin(\theta)}{\omega} \frac{1}{M_{12}} \tag{2.13}$$

In (2.13), θ is the phase difference between the RMS converter voltages U_1 and U_2. For a passive secondary converter (e.g. diode bridge), θ is always $\frac{\pi}{2}$ when operated at the resonant frequency. In active converters, θ can be controlled to regulate the power flow [23]. The power transfer in (2.13) is inversely proportional to the mutual inductance M_{12}. As M_{12} reduces due to pad misalignment or due to the increase in the clearance between pads, the power transfer capability of the pad increases at the expense of lower efficiency. The extreme case is an operation without a receiver. In this scenario, the current in the primary will increase uncontrollably. Thus, an open-secondary operation is not possible with this topology. Another disadvantage attributed to this compensation method is the load dependency of the voltage

Table 2.1 Relevant expressions for the most important compensation circuits.

	Series-Series	Series-Parallel	LCL-LCL	LCCL-LCCL
		Secondary		
Resonant condition	$C_2 = \frac{1}{\omega^2 L_2}$	$C_2 = \frac{1}{\omega^2 L_2}$	$C_2 = \frac{1}{\omega^2 L_2}$ $L_{2s} = L_2$	$C_{2p} = \frac{1}{\omega^2 L_2"}$ $L_{2s} = L_2"$ $L_2" = L_2 - \frac{1}{\omega^2 C_2}$
Secondary imp. $Z_{2,eq}$	$R_{L,eq}$	$\frac{j\omega L_2}{1+j\frac{R_{L,eq}}{\omega L_2}}$	$\frac{\omega^2 L_2^2}{R_{L,eq}}$	$\frac{\omega^2 L_2"^2}{R_{L,eq}}$
Load current i_2	$\frac{j\omega M_{12} i_{L1}}{R_{L,eq}}$	$\frac{M_{12} i_{L1}}{L_2}$	$\frac{M_{12} i_{L1}}{L_2}$	$\frac{M_{12} i_{L1}}{L_2"}$
Sec. coil current i_{L2}	$\frac{j\omega M_{12} i_{L1}}{R_{L,eq}}$	$\frac{M_{12} i_{L1}}{L_2}\left(1 + j\frac{R_{L,eq}}{\omega L_2}\right)$	$j\frac{R_{L,eq} M_{12} i_{L1}}{\omega L_2^2}$	$j\frac{R_{L,eq} M_{12} i_{L1}}{\omega L_2"^2}$
Load quality factor Q_s	$\frac{\omega L_2}{R_{L,eq}}$	$\frac{R_{L,eq}}{\omega L_2}$	$\frac{R_{L,eq}}{\omega L_2}$	$\frac{R_{L,eq}}{\omega L_2"}$
Power output P_2	$\frac{\omega^2 M_{12}^2 I_{L1}^2}{R_{L,eq}}$	$\frac{M_{12}^2 I_{L1}^2}{L_2^2} R_{L,eq}$	$\frac{M_{12}^2 i_{L1}^2 R_{L,eq}}{L_2^2}$	$\frac{M_{12}^2 i_{L1}^2 R_{L,eq}}{L_2"^2}$
		Primary		
Reflected imp. Z_{ref}	$\frac{\omega^2 M_{12}^2}{R_{L,eq}}$	$\frac{M_{12}^2}{L_2^2}\left(R_{L,eq} - j\omega L_2\right)$	$\frac{M_{12}^2 R_{L,eq}}{L_2^2}$	$\frac{M_{12}^2 R_{L,eq}}{L_2"^2}$
Resonant condition	$C_1 = \frac{1}{\omega^2 L_1}$	$C_1 = \frac{1}{\omega^2 L_1 (1-k)}$	$C_1 = \frac{1}{\omega^2 L_1}$ $L_{1s} = L_1$	$C_{1p} = \frac{1}{\omega^2 L_1"}$ $L_{1s} = L_1"$ $L_1" = L_1 - \frac{1}{\omega^2 C_1}$
Conv. current i_1	$\frac{u_1 R_{L,eq}}{\omega^2 M_{12}^2}$	$\frac{u_1 L_2^2}{M_{12}^2 R_{L,eq}}$	$\frac{M_{12} R_{L,eq} u_1}{L_2^2 \omega^2 L_1^2}$	$\frac{M_{12} R_{L,eq} u_1}{L_2"^2 \omega^2 L_1"^2}$
Pri. coil current i_{L1}	$\frac{u_1 R_{L,eq}}{\omega^2 M_{12}^2}$	$\frac{u_1 L_2^2}{M_{12}^2 R_{L,eq}}$	$\frac{u_1}{j\omega L_1}$	$\frac{u_1}{j\omega L_1"}$
Power output P_2	$\frac{U_1^2 R_{L,eq}}{\omega^2 M_{12}^2}$	$\frac{U_1^2 L_2^2}{M_{12}^2 R_{L,eq}}$	$\frac{U_1^2 M_{12}^2 R_{L,eq}}{L_2^2 \omega^2 L_1^2}$	$\frac{U_1^2 M_{12}^2 R_{L,eq}}{L_2"^2 \omega^2 L_1"^2}$
Power output P_2	$\frac{U_1 U_2 \sin(\theta)}{\omega M_{12}}$	$U_1 I_2 \frac{M}{L2}$	$\frac{U_1 U_2 M_{12}}{L_1 L_2 \omega}$	$\frac{U_1 U_2 M_{12}}{L_1" L_2" \omega}$

U_i: rms values, u_i: peak values.

transfer ratio; however, this is not an issue when using a load impedance matching converter in the secondary.

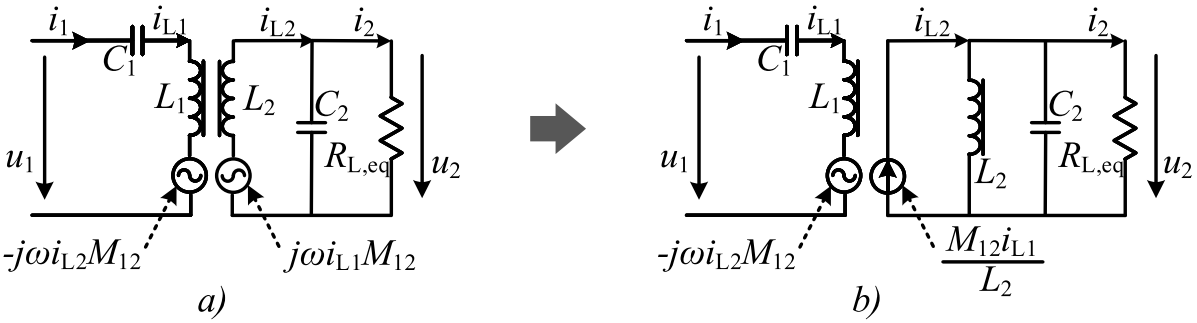

Fig. 2.19 Norton equivalent circuit of a parallel compensated IPT pad. *a*) Before and *b*) after the transformation.

When designing a pad with this resonant circuit, the pad is designed to transmit maximum rated power at the position with the highest coupling factor, $k = k_{\max}$. At this condition, the value of M_{12} can be estimated from (2.13) and the system can be designed accordingly. Alternatively, the equivalent load can be calculated using (2.1): $R_{L,eq} = \frac{\pi^2 u_{DC,2}^2}{8P_2}$. Thereafter, the required self-inductances of the transmitter and receiver pads can be estimated as in (2.14).

$$L_2 \approx \frac{R_{L,eq}}{\omega k} \quad L_1 \approx L_2 \left(\frac{u_{DC,1}}{u_{DC,2}}\right)^2 \tag{2.14}$$

It is worth noting that 2.14 requires a predefined desired (target) value of k. More information on how to design series compensated pads can be found in [12].

2.3.2 Series-parallel (SP or CP)

The series-parallel topology is shown in Fig.2.17.*b* while the most important equations are listed in Table 2.1. This topology can be more easily analyzed by replacing the secondary circuit with its Norton's equivalent as seen in Fig.2.19. As opposed to the series-series compensation, the primary converter voltage u_1 determines the value of u_2. Thus, a constant voltage ratio can be achieved independently from the load. This is an advantage over the series-series topology. However, as opposed to series compensation topology, the capacitance value at the primary side required for resonance depends on the coupling factor. This compromises the actual implementation as the coupling factor changes with the position of the pad. Moreover, parallel topologies usually require a filter inductor at the load side rectifier to force a continuous sinusoidal current flow. To achieve this, a boost converter stage is placed after the rectification. A current-based converter is required since a voltage source and a capacitor cannot be connected in parallel. As explained in previous sections, the equivalent load for

current-source converters is given by (2.1): $R_{L,eq} = \frac{8u_{DC,2}^2}{\pi^2 P_2}$. $R_{L,eq}$ can be used to determine the required values of L_1 and L_2 as show in (2.15).

$$L_2 = R_{L,eq}\frac{k}{\omega\sqrt{1+k^2}} \quad L_1 \approx L_2\left(\frac{8}{\pi^2 k}\frac{u_{DC,1}}{u_{DC,2}}\right) \tag{2.15}$$

2.3.3 Series-series vs series-parallel

From Fig.2.7, it can be seen that for series-parallel topologies, the maximum efficiency is achieved at higher load matching factors (γ), compared to a series-series system. Thus, for a given load, frequency of operation, and coupling factor, a series-parallel needs lower inductance value. Hence, this topology is popular for low-power applications in which the size of the secondary's pad is critical. In high power applications, however, low inductance values are hardly realizable as the pad size is larger. Thus, the series-series topology is preferred. Moreover, the resonant frequency of series-series compensated systems is independent of the coupling factor. This makes the IPT system more robust to misalignments. At the same time, the series-series compensation does not require a filter inductor in the secondary rectifier which can reduce the converter size. For these reasons, series-series compensation is one of the most used topologies for medium and high power IPT systems in the literature. In commercial systems, however, LCCL-LCCL resonant tanks are dominant.

2.3.4 Parallel-series and parallel-parallel

When using a parallel compensation in the primary side, the equivalent impedance seen by the primary converter is given by (2.16)

$$Z_{1,eq} = \frac{\omega^2 L_1^2}{Z_{\text{ref}}} + \frac{1}{j\omega C_1} \tag{2.16}$$

where Z_{ref} is the reflected impedance of the secondary pad. The converter sees a capacitive impedance; therefore, a voltage-source inverter cannot be used in the primary as it would imply connecting a capacitor and a voltage source in parallel. A current-source inverter such as the push-pull converter is used [36]. Topologies with a parallel compensation on the primary side are less commonly used and they will not be discussed further in this thesis.

2.3.5 LCL-LCL and LCCL-LCCL

The LCL topology, introduced by Wang in 2004 [80], is shown in 2.17.*d*. Its main equations are summed up in Table 2.1. The analysis of the LCCL-LCCL topology is done by substituting the voltage sources with current sources using Norton's theorem as shown in Fig.2.20. Assuming no losses in the pad, the power transfer P_2 is given by (2.17).

$$P_2 = \frac{u_1 \cdot u_2 \cdot \sin(\theta)}{\omega} \frac{M_{12}}{L_{1s} L_{2s}} \tag{2.17}$$

where θ is the phase of the voltage imposed by the secondary converter with respect to the voltage waveform of the primary converter. Thus, the power transfer is directly proportional to the voltage magnitude and the mutual inductance, and inversely proportional to compensation inductances L_{1s} and L_{2s}. Higher power transfer can be achieved by reducing L_{1s} and L_{2s}. However, to preserve the resonant frequency constant, the values of L_1 and L_2 must be also reduced while keeping M_{12} constant. Achieving this by adjusting the geometry or number of turns of the coil is challenging. Alternatively, capacitors can be added in series with the main coils L_1 and L_2. These capacitors reduce the equivalent inductance without changing the actual inductance values. This topology is known as LCCL-LCCL and behaves almost exactly as the LCL-LCL when operated at the resonant frequency.

The primary coil current is independent of the load as seen in Table 2.1. When pads are misaligned or the clearance between pads increases, the mutual inductance M_{12} drops, leading to lower power transfer. This condition allows the safe operation of the pad even with an open-secondary. This behavior is contrary to the series-series compensation and is a clear advantage over the series-series topology. The improved performance, however, comes at the cost of higher complexity and component count.

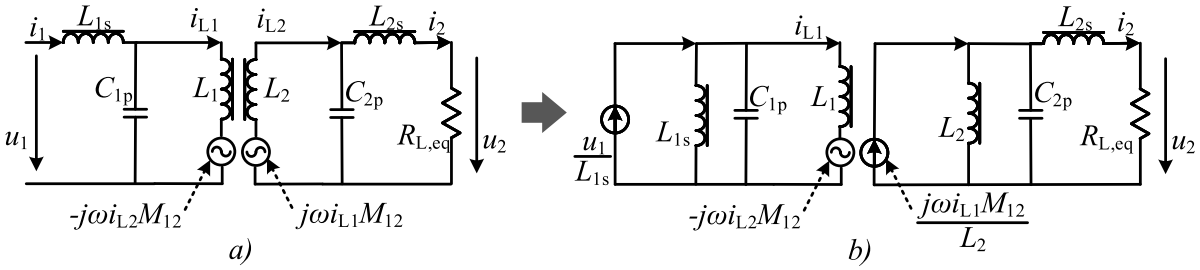

Fig. 2.20 Norton equivalent circuit of an LCL compensated IPT pad. *a*) Before and *b*) after the transformation.

2.3.6 Compensation topologies for polarized pads

For polarized pads, since the number of coils is equal to or greater than two, each coil can be compensated in a different manner which gives rise to hybrid topologies. Hybrid topologies are based on the previously discussed compensation networks and seek to improve the performance of the pad in response to misalignment or increments in the clearance between pads [93]. In [93], for instance, a hybrid compensation topology is presented in which a series-series and an LCL-LCL compensation are combined in parallel. Constant power is transmitted despite when the pads are misaligned. Similar results are achieved by other authors with different topologies [95, 94]. Hybrid topologies have been applied to pads with two coils (Double-D, bipolar) as well as pad as three coils (DDQ) [92, 28]. In general, the number of components required by these topologies is higher. However, several methods for reducing these elements have been presented. One of these methods results from including the resonant inductors as part of the main magnetic coupler [69].

2.4 Control Strategy

There are different control strategies used for power flow regulation in VSI-based systems. The main control strategies are described below:

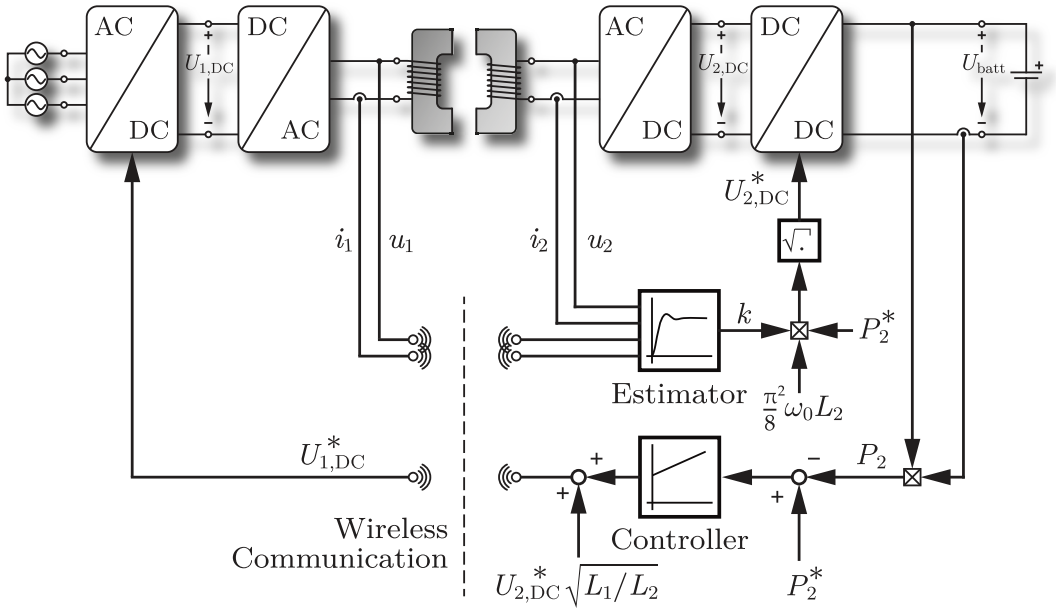

Fig. 2.21 Control strategy: Maximum efficiency control. Adapted from [8].

- **Maximum Efficiency Control with DC-link Voltage control-VC):** For a series-series compensated system, the power output is given by (2.18):

$$P_{\text{out}} = \frac{U_1 U_2}{\omega M} \sin(\theta) \tag{2.18}$$

where U_1 and U_2 corresponds to the fundamental RMS voltages synthesized by the primary and secondary converters, and θ is the phase angle between the AC converter voltages. If the converters produce square voltage signals, (2.18) can be expressed as a function of the DC-link voltages in the transmitter and receiver pads as shown in (2.13) and repeated in (2.19):

$$P_{\text{out}} = \frac{8}{\pi^2} \frac{u_{DC,1} u_{DC,2}}{\omega M} \sin(\theta) \tag{2.19}$$

This expression is only valid when square voltage waveforms are considered. Considering (2.19), the power flow can be controlled by adjusting the DC-link values. The DC-link voltage in the secondary $u_{DC,2}$ can be adjusted via a DC/DC converter in the secondary, between the rectification and the battery. Another DC/DC converter stage can be used to regulate the DC-link voltages in the primary. The PFC converter used in the input is not enough to regulate $u_{DC,1}$ since both step-down and step-up capabilities are needed and the PFC only permits boosting capability.

If the DC-link voltages are regulated, the primary converters (DC/AC in the primary and AC/DC in the secondary) are operated at a constant duty-cycle of 50% and constant frequency (85 kHz). As a result, soft switching can be always achieved. Consequently, this control strategy achieves high efficiency but requires a larger number of power electronic components and stages [8].

The overall scheme is shown in Fig.2.21. For a required power output, the DC-link voltage in the secondary is adjusted to ensure that the equivalent load $R_{L,eq}$ yields the maximum efficiency (impedance matching). If both DC-link voltages are reduced or increased proportionally, then the maximum efficiency is always maintained. The load matching is corrected only when there are changes in the coupling factor due to movements (misalignment) in the pads. Wireless communication is needed for the secondary to estimate the value of k in real-time. The value of k and the reference power $P_{\text{out}} = P_2^*$ is then used to determine the command $u_{DC,2}$. A controller (PI, for instance) is used to regulate the value of $u_{DC,1}$ to provide the required power [8].

- **Maximum efficiency control with duty-cycle control:** The previous method achieves high efficiencies by ensuring soft-switching at all times. In [23], however, Diekhans and De Doncker showed that high efficiencies can be also achieved by using dual-side power controllers and hard-switching when wide-bandgap switches are used. To this goal, the passive rectifier in the secondary is replaced by an active VSI converter as shown in Fig.2.22.*a*. The power flow, given by (2.18), is then regulated by adjusting the magnitude of the fundamental AC voltages u_1 and u_2 while the DC-link voltages are kept constant. Here, (2.18) corresponds to a series-series compensation; however, this method can also be applied to other compensation circuits.

  The fundamental AC voltages of a full-bridge with firing-angle control are given by (2.20):

$$\begin{aligned} u_1 &= \frac{4 \cdot u_{DC,1}}{\pi} \sin\left(\frac{\alpha_{f,1}}{2}\right) \\ u_2 &= \frac{4 \cdot u_{DC,2}}{\pi} \sin\left(\frac{\alpha_{f,2}}{2}\right) \end{aligned} \tag{2.20}$$

  where α_f is the firing angle of the converter as shown in Fig.2.22.*b* and Fig.2.22.*c* for two exemplary cases. Substituting (2.20) into (2.18), the power transfer in the system is given by (2.21):

$$P_{\text{out}} = \frac{8 \cdot u_{DC,1} u_{DC,2}}{\pi^2} \sin\left(\frac{\alpha_{f,1}}{2}\right) \sin\left(\frac{\alpha_{f,1}}{2}\right) \frac{1}{\omega M} \sin(\theta) \tag{2.21}$$

  This methodology relaxes the requirements for DC/DC converter stages and reduces the number of power electronics components. The firing angles are adjusted depending on the coupling factor and the load. Since the duty cycle is not constant, soft switching cannot always be guaranteed, only at rated load when $\alpha_{f,1}$ and $\alpha_{f,2}$ are both equal to π. It is worth noting that the use of active converters in both transmitter and receiver sides

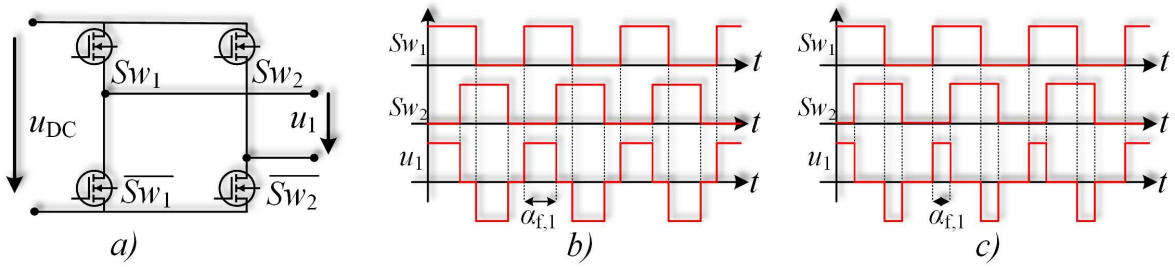

Fig. 2.22 Illustration of the firing angle control of an VSI H-bridge converter.

also allows for bidirectional power flow. This can be easily achieved by making θ equal to $-\frac{\pi}{2}$.

- **Switching frequency control (FC):** Frequency control is widely used in the operation of resonant converters. If the frequency of operation is shifted from resonance into the inductive region, the impedance of the system increases, and the power flow is reduced. For IPT systems in EV applications, however, the nominal frequency of operation is set to 85 kHz (between 81.38 and 90 kHz) by the standard SAE J2954. Hence, this control method is not ideal for EV charging. Particularly, since the efficiency of the system is reduced when operating out of the resonant point [8].

- **Self-oscillating Control (SOC):** Self-oscillating control is a combination of frequency control and duty cycle control of the receiving stage. A current sensor with its dedicated signal conditioning circuit is used to estimate the zero-crossing of the converter current. This signal is used to coordinate the converter switches. Thus, the system oscillates at its natural frequency and no predetermined frequency is imposed beforehand. Once the zero-crossing is determined and the sign of the current (positive or negative) is known, the controller can inject/remove power in/from the system or enter in a free-wheeling state. Power injection is guaranteed by matching the polarity of the converter voltage and current for a specific duty cycle. Since the zero crossing is known, soft switching can be achieved. Nonetheless, due to the high frequency of operation, SOC can be difficult to implement [8].

- **FC vs SOC and VC:** For FC and SOC, the current in the primary is higher than the current in the secondary at partial load. Unequal current sharing produces higher power losses as seen in Fig.2.23. Controlling the voltage in primary and secondary, VC yields higher efficiency values at partial load. However, this strategy requires extra components and power converter stages. Similarly, controlling the AC voltage by changing the firing angle reduces the losses at partial load [23]. However, the efficiency is lower compared to VC due to the higher switching losses produce by hard switching. Nonetheless, having an active secondary reduces the number of converter stages and components and can facilitate bidirectional power flow. The selection of the best control strategy depends on the application at hand.

- **Universal charger control strategy:** In [52], the control strategy known as *universal control* is presented. The main objectives of this design are 1) limit/eliminate the need for wireless communication between charging pads and 2) facilitate the interoperability of different pad designs. The control method is briefly described next.

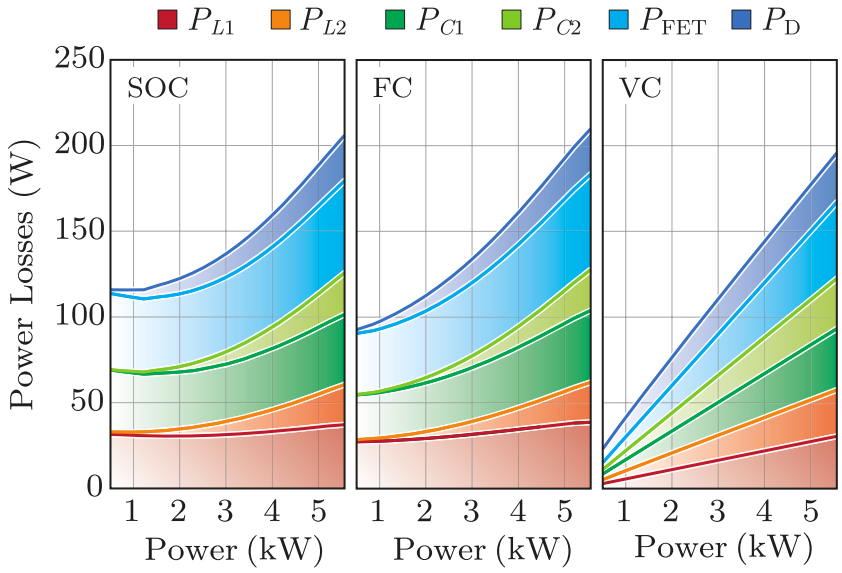

Fig. 2.23 Comparison of power losses for different control strategies: Self-oscillating control (SOC), Frequency control (FC), and Voltage control (VC). Adapted from [8]. P_{L1} : power losses in primary coil; P_{L2} : power losses in secondary coil. P_{C1} : power losses in primary compensation capacitor. P_{C2} : power losses in secondary compensation capacitor. P_{FET} : Switching and conduction losses in the MOSFETs. P_D : Losses in the rectification diodes.

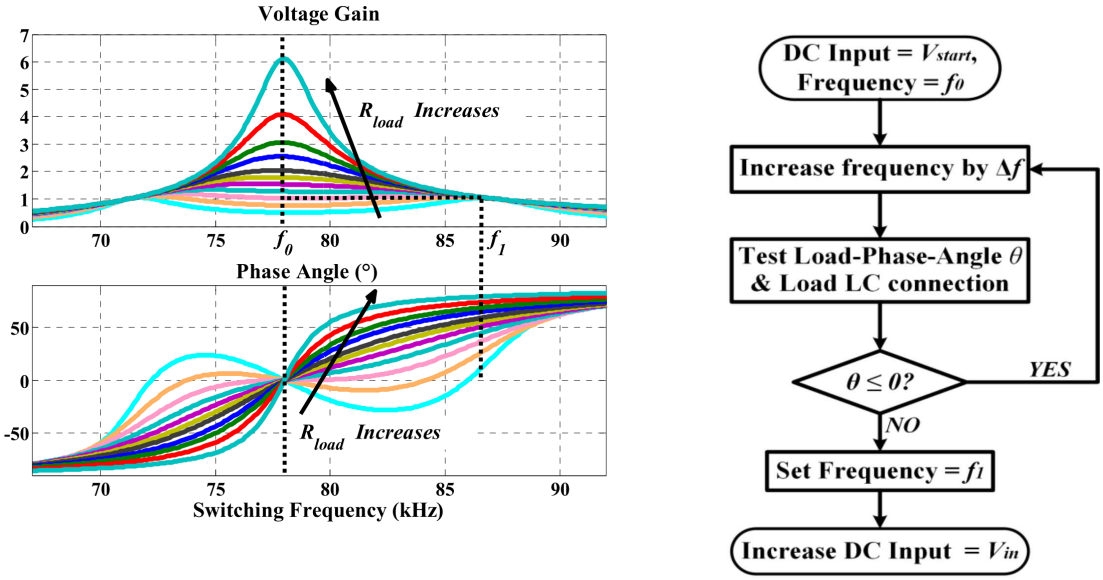

(a) (b)

Fig. 2.24 *a*) Frequency response $\frac{u_2(s)}{u_1(s)}$ for a series-series IPT system. *b*) Method of detecting f_1. Adapted from [52].

In Fig. 2.24a, the frequency response $\frac{u_2(s)}{u_1(s)}$ is plotted for a series-series compensated pad. At the resonant frequency f_0, the voltage increases along with the load $R_{L,eq}$ due to the current-source behavior of the primary. Nevertheless, if the system operates at f_1 instead of f_0, the voltage gain remains constant, and it is equal to 1 regardless of the load. This facilitates the interoperability between different designs as the system is impervious to changes in the load. However, it is worth noting that the impedance seen by the primary at f_1 is inductive for heavy loads (high R_{load} in Fig.2.24). On one hand, an inductive equivalent impedance guarantees ZVS. On the other hand, a lower power factor is expected. For light loads, however, the power factor at f_1 is close to one, as seen in Fig.2.24a. In fact, this is the strategy used in [52] to find f_1 during operation. This strategy is depicted in Fig.2.24b. Although this method of operation can be practical for applications where the load varies drastically, finding f_1 requires extra circuitry. An extra voltage sensor and a current sensor at the output of the primary inverter and as well as a phase estimation circuit are required. These requirements hinder the implementation of this control strategy, particularly in commercial units.

2.5 Summary

This section presents the fundamentals as well as some more advanced concepts related to IPT technology. The objective of this chapter was to present a theoretical background that facilitates the analyses presented in the upcoming chapters. First, the basic operation of an IPT system was discussed along with the most important mathematical models used for its representation. The main components of the magnetic couplers were presented. Different coil topologies, core materials, and methods for the calculation of power losses were described. Additionally, different compensation circuits and their behaviors were introduced along with mathematical expressions that define their performance. Finally, different control strategies used in power flow regulation were discussed.

Chapter 3

Nanocrystalline Ribbon Cores for IPT Applications

MnZn based ferrites such as the EPCOS [16, 10] or K2004 [10, 8] are commonly used as magnetic cores in IPT systems. However, the brittleness of these materials makes the IPT system prone to mechanical breakage and hinders the implementation of large-scale and/or complex geometries. Moreover, ferrite cores have a lower flux density saturation point, which presents challenges for compact and high-power IPT systems.

In recent years, reducing the amount of core material has become a popular topic of research. Optimizing ferrite utilization is crucial to increase the power density and reliability of the system. In [59], the core bars are reshaped to obtain a uniform flux density throughout the entire bar. On the other hand, in [89], an optimum 2-D axis-symmetric placement of the core for a polarized pad was studied. In both cases, optimum designs are intrinsically limited by the poor mechanical (Young's modulus, yield strength, and manufacturability) and magnetic (magnetic saturation and permeability) properties of ferrite [58, 89]. The need for new magnetic materials becomes evident. In this chapter, nanocrystalline-ribbon cores are presented as an alternative core material for IPT systems. Their performance in IPT systems is evaluated experimentally and with FEM simulations.

3.1 Magnetic Core Materials

Ideal magnetic materials for optimum IPT designs ought to have the following properties: high saturation flux density, high permeability, high resistivity, lower power loss, high thermal stability, and low-cost [82]. No material can satisfy all these conditions and, therefore, compromises are required. A list of magnetic materials commonly used in power electronic

applications is shown in Table 3.1. To ease the comparison, the magnetic saturation flux density, permeability, and core losses are depicted in Fig.3.1 for the most common materials.

MnZn ferrites have low saturation flux density and permeability values; however, they are reasonably priced and have high resistivity and moderate core losses [82]. Silicon steels (FeSi) on the other hand have a higher flux saturation density B_{sat} with moderate values of permeability. These materials are prone to eddy-currents which makes them lossy. They are usually laminated to mitigate these losses. The lamination thickness ranges between 0.1 mm to 0.65 mm. The content of Si can be also increased to reduce the conductivity of the material. However, this makes the core more brittle. Thus, the percentage of Si is usually kept under 4 % [61]. Due to the losses, the operation of this material is restricted to low frequencies (<kHz).

Different alloys are also used in magnetic cores. The Nickel-Iron alloy (NiFe), known as Permalloy, offers higher permeability and B_{sat} than silicon-steels. The properties depend on the specific composition [57]. Nickel-rich alloys have higher permeability but low saturation flux density while iron-rich alloys have the opposite behavior. Iron-cobalt alloys such as Permendur, exhibit high saturation flux density (2.54 T) but lower permeability than NiFe alloys [18]. The high cost of cobalt limits its application. These alloys are used in the form of powder which is then sintered to the required core shapes [18].

Amorphous alloys are also used as magnetic cores material. Amorphous alloys have higher permeability and resistivity than the aforementioned crystalline structures [20]. They commonly contain Fe, Co, Ni, Si, B, and small quantities of Nb, Cu, Mn, and C. They are mainly divided into two groups: Fe-based alloys and Co-based alloys. The former has higher saturation flux density while the latter has lower magneto-restriction which translates into lower losses [32, 20]. While amorphous materials are devoid of a lattice structure, crystalline and nanocrystalline materials have a well-defined grain structure. Nanocrystalline grains range between 1 to 50 nm, much finer than other crystalline structures [88]. Nanocrystalline materials exhibit very high permeability and saturation flux density and low magneto-restriction (low hysteresis losses). For these reasons, they have been widely used in high-frequency applications [82].

Powder iron cores exhibit higher losses and low permeability which makes them not ideal for IPT applications. Iron and silicon steel have lower losses but low permeability values. This is also true for powder-based cores. Permalloy, Sendust, and FE-based amorphous materials can count as possible replacements for ferrite in IPT pads due to their higher saturation point. However, their magnetic properties are inferior to that of the nanocrystalline ribbon cores [20]. Thus, nanocrystalline ribbon cores are a viable replacement for ferrite cores. A detailed comparison of nanocrystalline ribbon core versus ferrite is presented next.

Table 3.1 Properties of Commonly Used Magnetic Materials.

Material Type	Manufacturer	Material	B_{sat} [T] @25 °C	μ_r @20 kHz	Cont. Temp.	Resist. [$\mu\Omega$·m]	Ther. Cond. [W/mK]	Density [g/cm^3]	Core Loss [kW/m^3]
Ferrite (MnZn)	Ferroxcube	3C95	0.53	3000	140	5E+06	3.5-5	4.8	350
Ferrite (MnZn)	EPCOS	N87	0.49	2200	140	10	3.5-5	4.85	110
Powder Core (NiFeMo)	Magnetics	Molypermalloy	0.75	14-550	200	-	-	8.2	45
Powder Core (AlSiFe)	Magnetics	KoolMu 26	1.05	26-125	200	-	-	6.8	83
Powder Core (NiFe)	Magnetics	High Flux	1.5	14-160	200	-	-	7.7	116
Powder Core (FeSi)	Chang Sung	Mega Flux	1.6	26-90	200	-	11.4	6.8	186
Powder Iron (C=OFe)	Micrometals	Mix-26	1.38	75	<75	-	4.2	7	630
Powder Iron (C=OFe)	Micrometals	Mix-30	1.38	22	<75	-	2	6	835
Amorphous (FeSiB)	Metglas	2605SA1	1.56	600	150*	1.37	10**	7.18	70
Amorphous (FeSiB)	Metglas	S605SA3	1.41	35000	150*	1.38	10**	7.29	17
Silicon Steel (FeSi)	JFE Steel	10JNHF600	1.88	600	150*	0.82	18.6**	7.53	150
Silicon Steel (FeSi)	JFE Steel	10JNEX900	1.8	900	150*	0.82	18.6**	7.49	180
Nanocrys.(FeSiNbBCu)	Vaccumsch.	Vitroperm 500F	1.2	13200	120*	1.15	10**	7.3	5
Nanocrys.(FeSiNbBCu)	Hitachi	Finemet FT-3M	1.23	15000	155*	1.2	10**	7.3	5
Nanocrys.(FeSiNbBCu)	AT&M	Antainano	1.25	300-30000	155*	1.2	10**	7.2	5

$*$:laminated. $**$: thermal conductivity along laminations

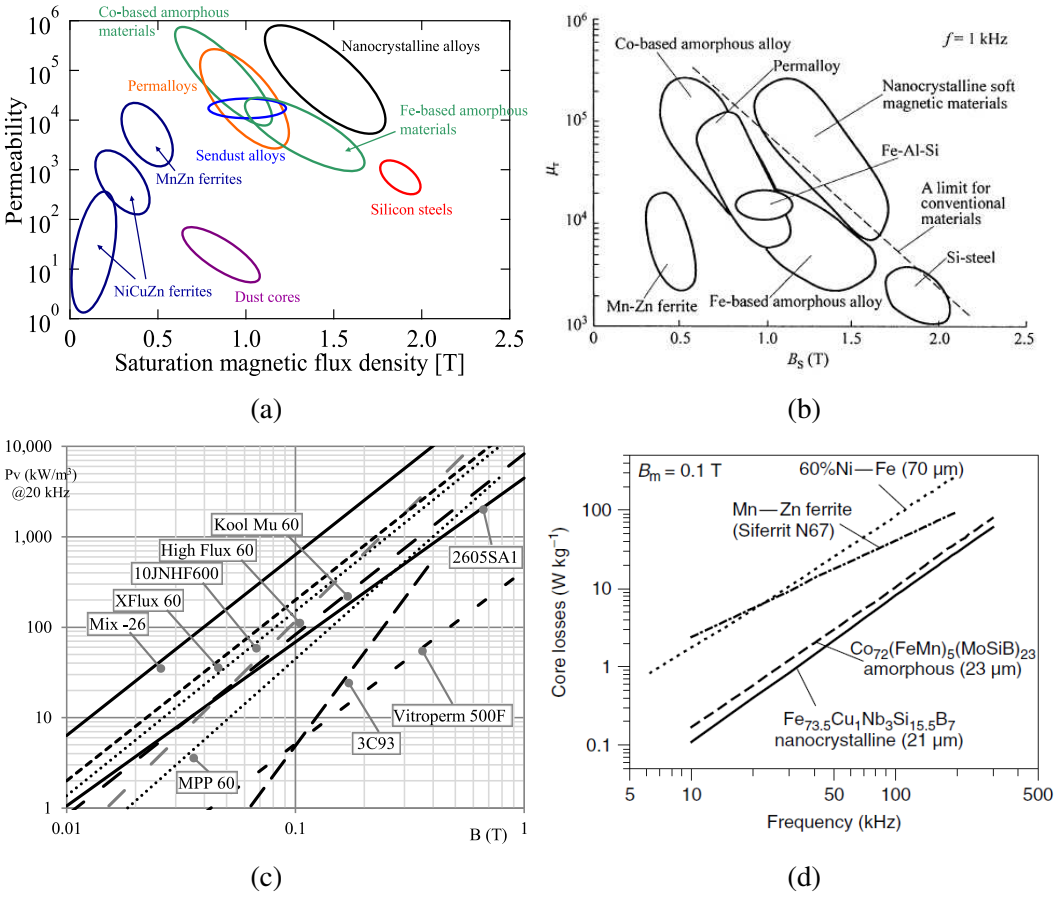

Fig. 3.1 Comparison of the electromagnetic properties of commonly used magnetic materials. $a) - b)$ Permeability versus Saturation flux density [32, 90], $c)$ Saturation flux density vs core losses [84], and $d)$ frequency vs core losses [32] for different magnetic materials.

Ferrite versus nanocrystalline

Fig. 3.2 compares a typical nanocrystalline alloy versus other standard materials for IPT cores such as ferrite and other MnZn alloys. Nanocrystalline materials show several advantages that make them attractive for IPT applications. First, their relative permeability can be tuned during the manufacturing process from 120 000 up to 300 000 as shown in Fig. 3.2.*a*. These values are several orders of magnitude higher than that of ferrite. Higher permeability has the potential to increase the coupling coefficient k which is evaluated in the next section. Moreover, higher permeability constrains more effectively the magnetic flux, reducing the flux leakage to shields or other metallic surfaces. It is important to notice that the permeability of the ribbon decays significantly as the frequency increases as shown in Fig.3.2.*a*. However, this is only problematic for frequencies ≥ 100 kHz which are out of the desired range for high-power IPT applications.

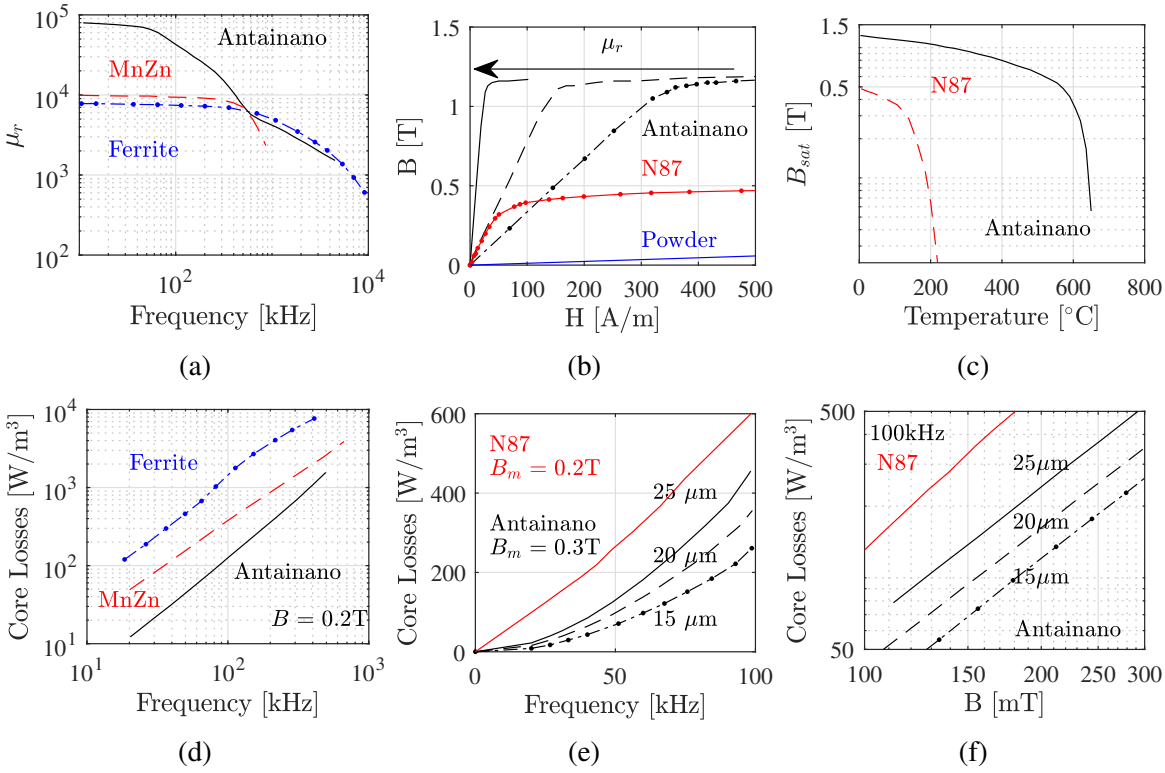

Fig. 3.2 Comparison of the electromagnetic properties of MnZn Ferrite N87 [64, 75] and nanocrystalline ribbon cores (Antainano) [5]. The power losses for the latter consider a stacking factor of 0.88.

A seen in Fig.3.2.*b*, nanocrystalline alloys such as Antainano saturate at $\geq$1.25 T; more than twice the saturation point of standard ferrite N87. A higher saturation point B_{sat} is crucial to achieving high power density. Nanocrystalline powders can achieve similar saturation levels; however, their relative permeability is restricted to values below 100. Thus, nanocrystalline powders do not outperform ferrite as core materials. The saturation flux density of the nanocrystalline ribbon is more stable to temperature deviations. As seen in Fig. 3.2.*c*, nanocrystalline Curie temperature is close to $T \geq$600 °C which is three times higher than that of ferrite N87. Moreover, the decay of B_{sat} as a function of the temperature is gradual for nanocrystalline. Hence, it can operate at higher temperatures without compromising the performance of the system. Moreover, the metallic nature of nanocrystalline ribbon cores yields higher thermal conductivity than the ceramic-based ferrite cores. Consequently, the requirements for cooling can be relaxed which simplifies its design and reduces its cost and size. In contrast, B_{sat} decays rapidly with temperature for ferrite N87 as seen in Fig.3.2.*c*. As a result, the operation is strictly restricted to the low-temperature range.

In general, nanocrystalline exhibits lower magnetic losses as compared to ferrite and MnZn as shown in Fig. 3.2.*d*. Magnetic losses are minimal due to the soft characteristic of the material which ensures a slim hysteresis loop. Nonetheless, the eddy-current losses can be problematic as the conductivity of nanocrystalline materials is high: σ =833 333 S/m. Fortunately, eddy-current losses are limited since the thickness of the nanocrystalline ribbon is between $14-30\mu$m thick. As seen in Fig.3.2.*e*, as the thickness of the ribbon decreases, so do the power losses. IPT systems for EVs operate at a fixed frequency ∼85 kHz; thus, losses are then only dependent on the magnetic flux as shown in Fig.3.2.*f* for a frequency of 100 kHz. From Fig3.2.*e* and Fig3.2.*f*, the Steinmetz coefficients can be obtained which can be used later in the estimation of the overall core losses. Finally, nanocrystalline ribbons have a higher yield strength which makes the bar considerably more robust compared to other ceramic materials such as ferrite.

Nanocrystalline cores are formed by stacking ribbons together using an organic binder. Each ribbon is galvanically isolated from others. Laminated cores are therefore anisotropic; that is, their properties are different in each axis. In most applications, the magnetic flux is unidirectional and the anisotropy is inconsequential. However, it can problematic in applications with multi-directional flux, such as in IPT systems. Moreover, anisotropy can also lead to extra losses in gap inductors [83].

3.1.1 Fabrication Method

MnZn Ferrite cores: The standard manufacturing process of MnZn ferrite cores is depicted in Fig.3.3.*a*. The process begins with a mix of high purity raw materials in the form of powders. Water is usually used as a medium. Next, the mix is preheated in a process known as pre-sintering. Here, the temperature is increased up to 75% of the final sintering temperature. The impurities in the mix are evaporated and oxides are formed. A grinding process follows next to make sure that the particle size meets the requirements, usually between 2 and 16μm. Thereafter, a binder is added to the mix and the pressing process takes place. Through this process, the core is given the required shape (E, C, I, U cores, etc.). Next, the cores are sintered. This process is crucial to ensure the electromagnetic properties of the material. Sintering occurs in a controlled environment with regulated temperature and atmosphere content. During this stage, impurities, binders, and lubricants are burnt out and the final microstructure of the material is achieved. As shown in Fig.3.4.*a*, the final microstructure of ferrite is formed by domains whose size is in the order of tens of micrometers. To finalize the process, the cores are machined (e.g. with a diamond wheel) to ensure the final dimensions. Quality control and inspection then conclude the fabrication cycle.

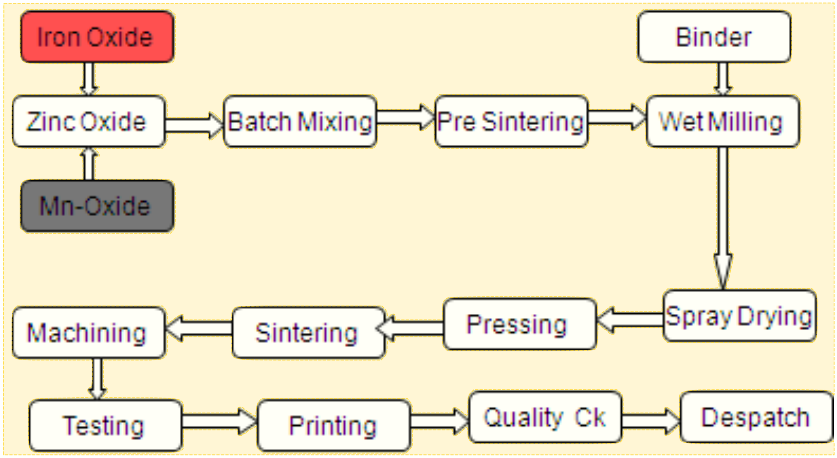

(a)

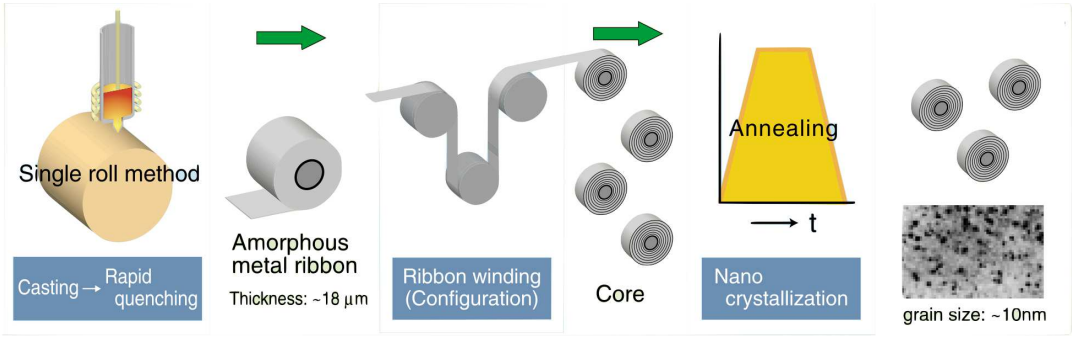

(b)

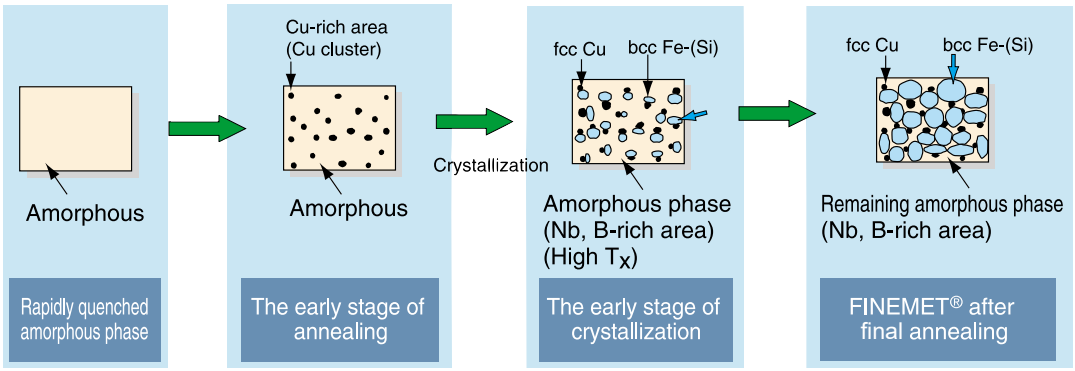

(c)

Fig. 3.3 Fabrication process of nanocrystalline and ferrite cores. *a*) Fabrication process of MnZn ferrite cores [21]. *b*) Manufacturing process of the nanocrystalline ribbon [33]. *c*) Detail of changes in the micro-structure as result of the annealing process [33].

Nanocrystalline alloy ribbon cores: The fabrication method of MnZn ferrite cores and nanocrystalline alloy cores is substantially different. The manufacturing process is depicted in Fig.3.3.*b*. The process starts with a high-temperature melt consisting of Fe −as the main

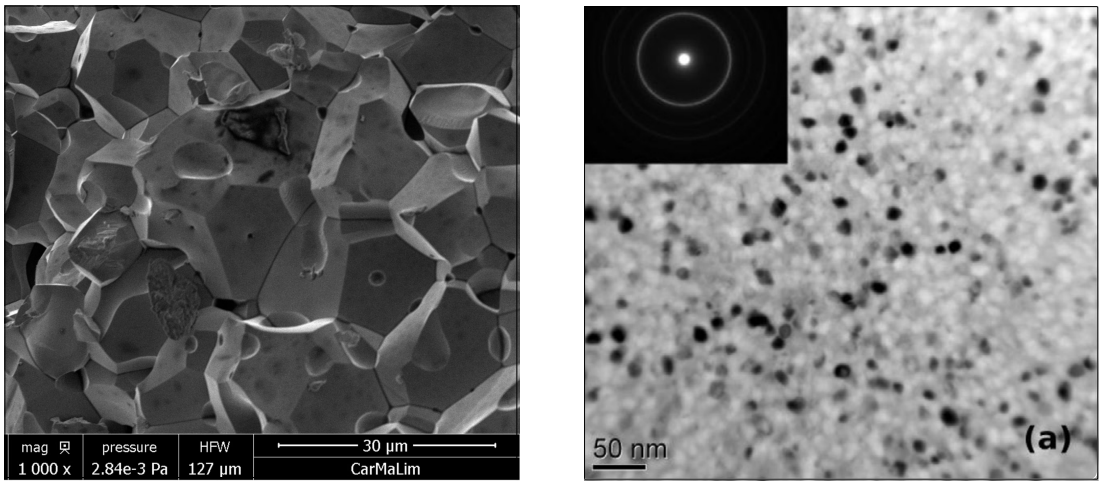

(a) (b)

Fig. 3.4 Microstructure of nanocrystalline and ferrite cores. *a*) Ferrite microstructure SEM [48]. *b*) Nanocrystalline alloy microstructure TEM [53].

phase−, Si, B, Cu, and Nb. This melt is quenched rapidly as it is poured onto a rotating wheel forming an amorphous metal ribbon. This method is known as single-roll. The wheel speed and the material injection rate define the thickness of the ribbon, which is usually between 14 and 25 µm. This amorphous ribbon is the precursor of the nanocrystalline one. The former is wound into single units which are then annealed. The annealing process is critical as it defines the microstructure of the material as well as its macro-scale properties such as its magnetic permeability. The annealing process is depicted in Fig.3.3.*c*. In the early stages of annealing, clusters of copper are formed. These clusters multiply the nucleation centers of iron (Fe). The nucleation derives into a crystallization phase of Fe-(Si). These crystalline structures continue growing until an equilibrium is reached. Equilibrium is achieved because the crystallization temperature of the remaining amorphous phase increases and becomes more stable due to the enrichment of Niobium (Nb) and Boron (B) [33]. The presence of Niobium also inhibits the growth of the grain [41] during crystallization and keeps the size of the crystalline grain in the order of nanometers, as seen in Fig.3.4.*b*. In the last stage of fabrication, the ribbons are impregnated with resins (binders) which are responsible for binding the ribbons together. It is critical to ensure that the resin forms an even and thin layer between the ribbons. After the impregnation, the core is cured under controlled conditions. Should tooling be required, special care must be also paid to prevent damaging the ribbons and the insulation between them.

3.2 FEM Simulation of IPT systems

3.2.1 Fundamentals

It is a common practice to model the electromagnetic and thermal behavior of IPT systems via FEM simulations. The values of self and mutual inductance, coupling factors, open-circuit voltage, and short-circuit currents can be obtained from FEM simulations. Moreover, power losses in the different components can be also calculated. In the literature, different authors use different FEM software programs. Common options are JMAG, Ansys Maxwell, Opera, and COMSOL. The latter is used throughout this thesis. To ensure the accuracy of the simulations, several IPT systems were simulated and the results were compared against previously reported values in [16, 10]. The results matched with a difference of less than 5%. The accuracy of the simulations was also validated against experimental results shown later in this chapter. Deviations of less than 8% are measured. Details regarding the modeling of all IPT components are presented in the next sections.

2D vs 3D modeling

For IPT pads using circular non-polarized coils and core plates (Fig.2.12c), 2D-axis-symmetric simulations can be used as the system has radial symmetry. When discrete core bars are used as opposed to plates, the radial symmetry is disrupted, and 3D models are necessary. The same is true for every polarized coil (DD, DDQ, BPP, etc.) as well as for non-polarized coils with square coils. 3D models are used in this dissertation.

Time-domain vs frequency-domain simulations

As explained in Section 2.1.3, the harmonic components of the excitation current in the coil are low and, therefore, the excitation current can be considered as sinusoidal for all practical purposes. As a result, *frequency domain* simulations can be used considering the fundamental current component at 85 kHz. The multi-physics environment within COMSOL permits heat transfer simulations to be performed as well as simulating the IPT pad as a part of an electric circuit. However, for the characterization of the IPT pad, electromagnetic simulations within the frequency domain are usually sufficient.

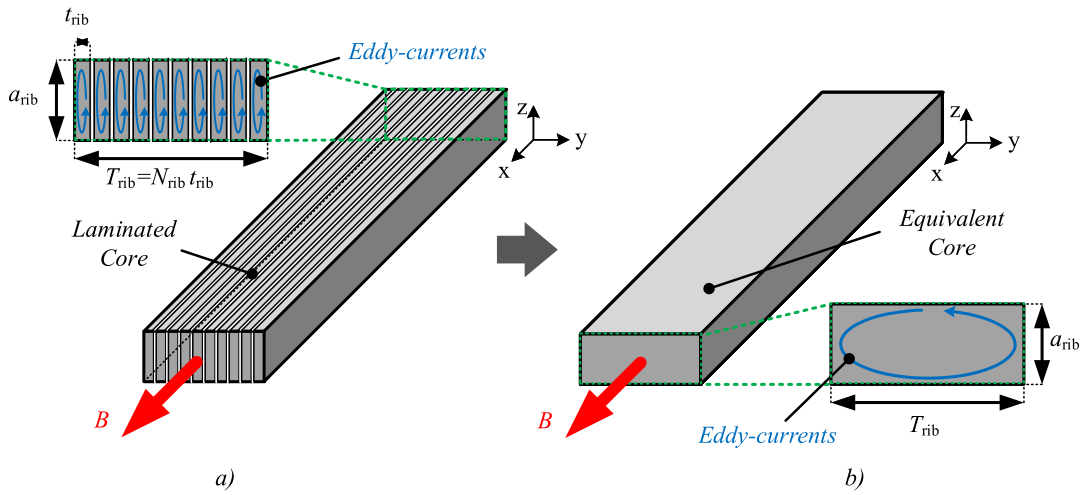

Fig. 3.5 Illustration of the homogenization method. *a*) Laminated Core. *b*): Equivalent Core.

3.2.2 Magnetic Core Modeling

Modeling of Solid and Laminated Cores

Ferrite is an isotropic material whose properties are homogeneous and oblivious to the material orientation in space. Thus, they can be modeled with uniform electromagnetic properties. Nanocrystalline bars, on the other hand, are formed by ribbons stacked together with a binder material. As a result, the core bars are anisotropic; i.e., their electromagnetic properties (permeability and conductivity) are different in each axis.

The effect of laminations in numerical FEM simulation has been extensively researched in the last century by Steinmetz, Bertotti, and more recently by Hanhne *et al.*, Bermudez [7] and Wang [37]. One of the most popular methods is the *homogenization method* since it permits a decrease in the complexity of the FEM simulations with an acceptable compromise of accuracy. Accuracy values over 95% can be achieved [83]. Thus, a laminated core, shown in Fig. 3.5*a*, can be represented as a non-laminated one with equivalent conductivity σ_{eq} and permeability μ_{eq} values as shown in Fig.3.5*b*). The equivalent parameters can be isotropic or anisotropic depending on the flux distribution. In transformers with laminated cores, for instance, the equivalent conductivity can be isotropic as the flux is mainly unidirectional. For cuboid-shaped magnetic cores in IPT applications, however, the flux paths are multi-directional. Consequently, anisotropic properties must be considered; i.e., the equivalent permeability (μ_{eq}) and conductivity (σ_{eq}) must be considered as tensors [82].

Several methods of calculating the equivalent properties for laminated cores are reported in literature [7], [37], [81], and [35]. They vary in terms of accuracy, assumptions, and complexity. In [7], (3.1) was introduced for the equivalent conductivity in the y-axis ($\sigma_{eq,y}$), for a

Table 3.2 Equivalent Electromagnetic Properties of the Nanocrystalline ribbon cores using the homogenization method: Antainano (AT&M) and Finemet (Hitachi Metals).

Material	a_{rib}	$\mu_{eq,x} = \mu_{eq,z}$	$\mu_{eq,y}$	$\sigma_{eq,x} = \sigma eq,z$	$\sigma_{eq,y}$
Antainano 1k107	8 mm	$78000\mu_0$	$4.54\mu_0$	6.5×10^5 S/m	6.67 S/m
Antainano 1k107	16 mm	$78000\mu_0$	$4.54\mu_0$	6.5×10^5 S/m	1.66 S/m
Finemet F3CC0050	9.5 mm	$2000\mu_0$	$5\mu_0$	6.67×10^5 S/m	0.46 S/m
Finemet F3BC342425	4 mm	$17710\mu_0$	$4.34\mu_0$	6.41×10^5 S/m	21.9 S/m

stacking factor of 1 ($F = 1$). The stacking factor defines the portion of the core width filled by the ribbon in relation to the binder. In other words, F indicates how closely packed the ribbons are.

$$\sigma_{eq,y} = \sigma \left(\frac{T_{\text{rib}} - 2\delta}{N_{\text{rib}}(a_{\text{rib}} + t_{\text{rib}} - 2\delta) - a_{\text{rib}}} \right)^2 \tag{3.1}$$

In (3.1), σ is the conductivity of the bulk material, t_{rib} and a_{rib} represent the ribbon thickness and width respectively, T_{rib} is the core width (see Fig.3.5), and δ is the skin-depth defined as $\delta = (\sqrt{\pi f \mu_0 \mu_r \sigma})^{-1}$ with f as the frequency of operation (85 kHz). In [81], simplified equations are presented which include the stacking factor F. The equivalent conductivity tensor is given by (3.2) [81]. This expression is used in this thesis due to its simplicity and the fact that the stacking factor is considered.

$$\sigma_{eq,z} = \sigma_{eq,x} = F\sigma, \quad \sigma_{eq,y} \approx \frac{\sigma}{F} \left(\frac{t_{\text{rib}}}{a_{\text{rib}}} \right)^2 \tag{3.2}$$

On the other hand, the estimation of the equivalent anisotropic permeability is straightforward as only the stacking factor is considered as shown in (3.3) and (3.4) [83].

$$\mu_{eq,x} = \mu_{eq,z} = \frac{\mu\mu_0}{F\mu_0 + (1-F)\mu} \tag{3.3}$$

$$\mu_{eq,y} = F\mu + (1-F)\mu_0 \tag{3.4}$$

Here, μ refers to the bulk permeability whilst μ_0 refers to the permeability of the free space. A nanocrystalline ribbon core made with Antainano 1k107 (AT&M), has the following properties: $\mu = 100000$, $\sigma = 8.33 \times 10^5$ S/m, t_{rib} =20 μm, and $F = 0.78$. Finemet F3CC0050, on the other hand, has the following properties: $\mu = 2500$, $\sigma = 8.33 \times 10^5$ S/m, t_{rib} =20 μm, and $F = 0.8$. Finemet F3BC342425 has the following properties: $\mu = 23000$, $\sigma = 8.33 \times 10^5$

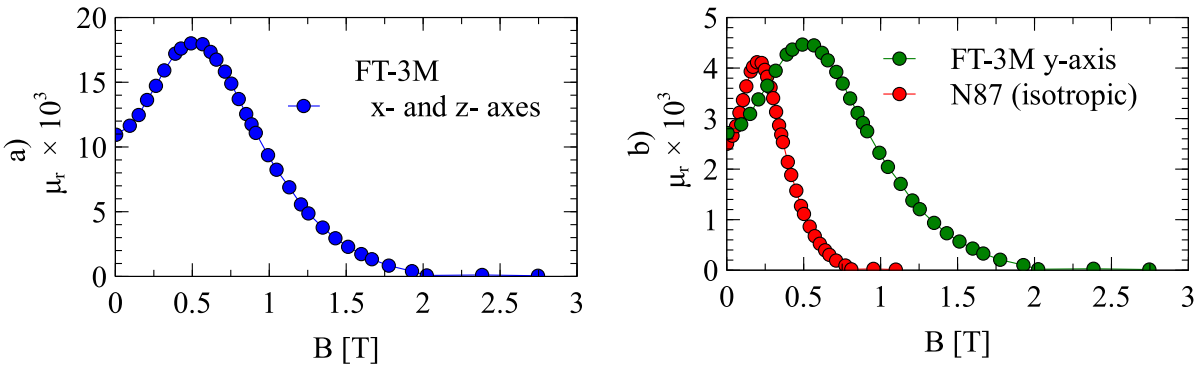

Fig. 3.6 Relative permeability as a function of the flux density for ferrite (isotropic) and nanocrystalline ribbon cores (anisotropic). *a*) Nanocrystalline ribbon cores in the x and z axes. *b*) Ferrite and nanocrystalline ribbon cores in the y-axis. Finemet FT-3M is considered as the nanocrystalline material for this example.

S/m, $t_{\text{rib}} = 18\,\mu$m, and $F = 0.77$. The equivalent permeability and conductivity tensors are shown in Table 3.2.

Depending on the design, saturation can be reached in some parts of the core. To account for saturation, the BH curve of the material is required. For an anisotropic material, the BH-curve of the bulk material is scaled using (3.3) and (3.4) depending on the specific axes, as seen in Fig.3.6 [96]. For ferrite, only one curve is required while two are needed for a nanocrystalline ribbon core.

Lamination Orientation

In power transformers, the flux path is unidirectional; thus, as long as the flux travels along the lamination, the lamination orientation has no relevance. Thus, orientation is selected only based on manufacturability. In IPT systems, however, the flux is multi-directional and, *a priori*, the orientation of the ribbons is not intuitive as the flux enters all sides of the bar except the bottom side attached to the shield. To analyze the effect of the orientation, FEM simulations are performed for two different orientations shown in Fig.3.7a and Fig.3.7d. Two identical circular pads were considered. The pad dimensions were based on the design presented in [16]. The outer radius of the pad is 42cm. The coil consists of 12 turns of 4mm-diameter Litz wire. The mean radius of the coil is 23.8cm. For the core, eight I-cores ($118 \times 30 \times 10$mm) are considered, all placed radially and uniformly in the pad area. Fig.3.7 shows the values of L_1, M_{12}, k, and P_{su} for different distances between transmitter and receiver pads.

The eddy-currents induced in the core affect the overall magnetic circuit. They decrease L_1 and M which in turn decreases P_{su} and k. Their effect is stronger for small air gaps between pads as the magnetic core plays a more important role over the overall magnetic circuit. For

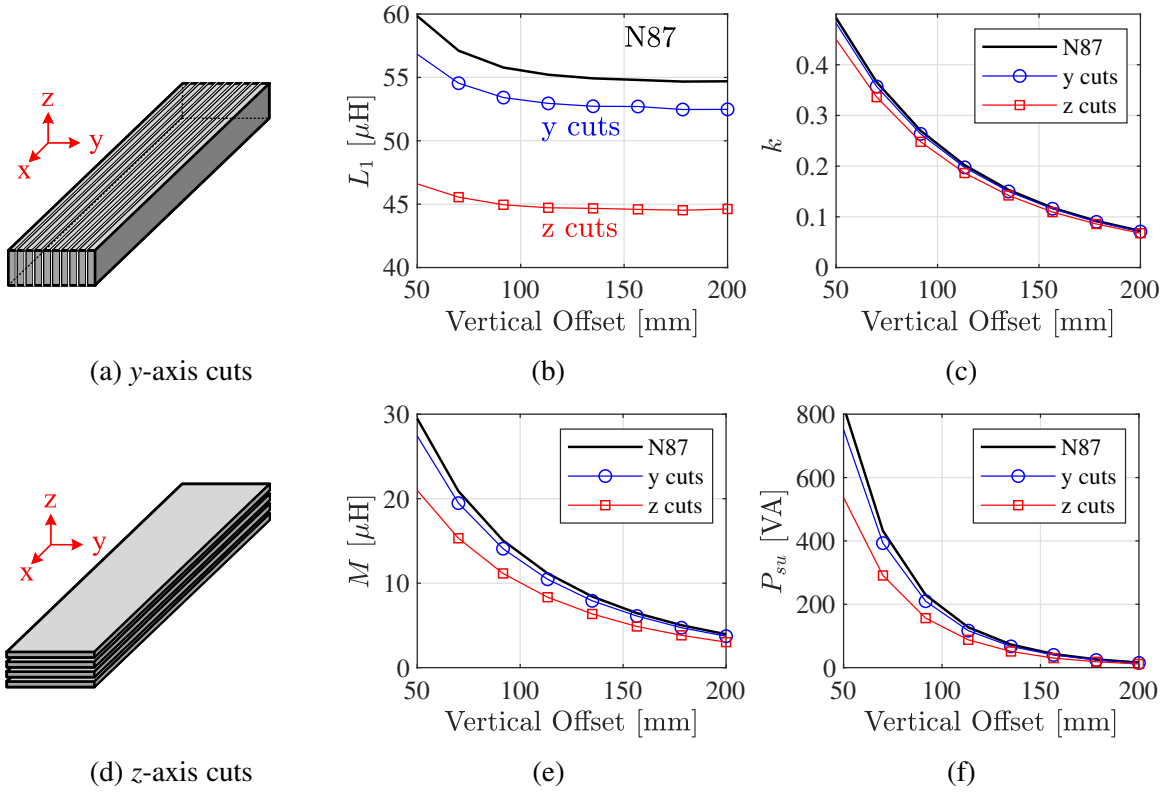

(a) y-axis cuts (b) (c)

(d) z-axis cuts (e) (f)

Fig. 3.7 Effect of the orientation of the nanocrystalline ribbons on the magnetic performance of the pad. $a)-c)$ y-axis cuts (z-axis orientation): $\sigma_x = \sigma_z = 6.6\times10^5$S/m, σ_y =0.79 S/m, $\mu_y = 5\mu_o$, $\mu_x = \mu_z = 240000\mu_o$. $d)-f)$ z-axis cuts (y-axis orientation): $\sigma_x = \sigma_y = 6.6\times10^5$S/m, σ_z =0.26 S/m,$\mu_z = 5\mu_o$, $\mu_x = \mu_y = 240000\mu_o$.

large air gaps, the leakage flux dominates the magnetic circuit. As seen in Fig.3.7, a core laminated in the z-axis is more affected as compared to a core laminated in the y-axis. Thus, the latter is preferred, and it will be used throughout this thesis.

Core Losses

As explained in Chapter 2, power losses in the cores can be computed either using the concept of complex permeability or following the traditional Steinmetz method. The complex permeability model can be easily defined for isotropic materials, but it complicates the FEA computations for anisotropic ones. Consequently, the Steinmetz method is used for nanocrystalline ribbon cores. This method is standard for core loss estimation in IPT designs as reported in [10, 8, 16, 13]. The power loss per unit volume is given by (3.5):

$$P_v = C_m f^{\alpha} B^{\beta} \tag{3.5}$$

Table 3.3 Steinmetz coefficients for different the magnetic materials used in this thesis [75, 5, 34].

Material	**Thickness**	C'_m [W/m^3/T$^\beta$]	β
Nanocrystalline	15 μm	$2.27 \times 10^6 \times F$	1.93
Antainano from	20 μm	$3.01 \times 10^6 \times F$	1.93
AT&M	25 μm	$4.48 \times 10^6 \times F$	1.93
Finemet F3BC342425 $F = 0.77$	18 μm	$4.45 \times 10^6 \times F$	1.87
N87		2.5×10^7	2.7

F : Stacking Factor

where, C_m, α, and β are obtained from the datasheets of each material. In principle, given the switching mode characteristic of the power electronics, the Modified Steinmetz Equation (MSE) or the Generalized Steinmetz Equation (GSE) could be used to increase the accuracy. However, if a compensation circuit is in place, the current harmonics are minimum, and the excitation current can be considered as purely sinusoidal [11]. As a result, the standard Steinmetz equation is sufficient to estimate losses with adequate accuracy. For a fixed frequency, the Steinmetz equation can be rewritten as in (3.6):

$$P_v = C'_m B^\beta \tag{3.6}$$

The coefficients C'_m, B, and β, are listed Table 3.3 for ferrite and Antainano [5, 75] and Finemet F3BC 342-4-25. From Table 3.3, it is clear that nanocrystalline ribbon cores generate fewer losses than ferrite cores for the same flux traveling along the ribbon. Traverse flux (perpendicular to the ribbon), however, induces eddy-currents in the ribbons which in turn increases the overall power losses. In fact, even in nanocrystalline U-shaped inductors with small air gaps, gap losses can account for up to 40 % of the total losses at high flux densities [83]. In [83, 82], the estimation of losses via FEM simulations was successfully validated with an accuracy of 95 %. Using the same approach, the eddy-current and the hysteresis losses, hereafter referred to as P_{elec} and P_{mag} respectively, can be estimated for nanocrystalline ribbon cores.

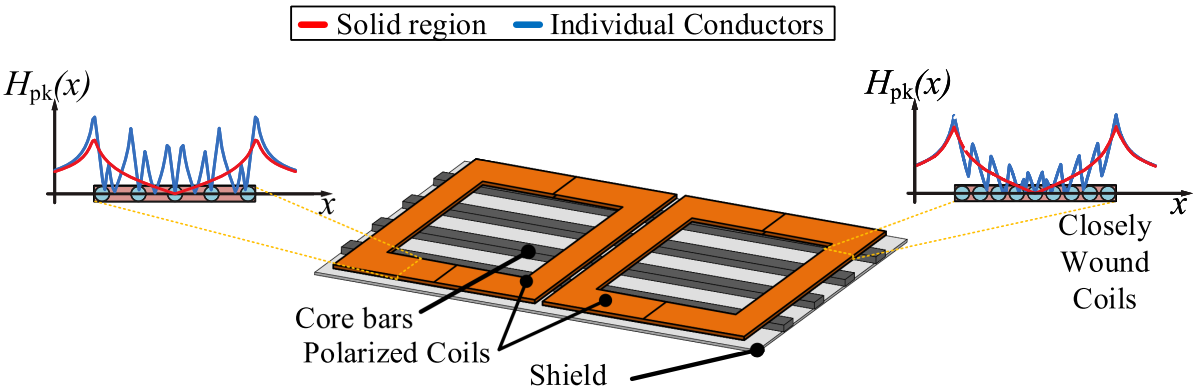

Fig. 3.8 Illustration of the modeling of a Litz-wire winding as a solid structure. The magnetic field strength is depicted when considering individual conductors and a solid region for closely and loosely wound coils.

3.2.3 Winding Modeling

Equivalent Winding Model

In FEM simulations, a multi-turn winding can be represented considering each individual turn, or as a lumped solid region. Using individual conductors has several advantages. First, the accuracy of the simulation is higher. Second, with a fine mesh inside the conductor, proximity and skin effects can be modeled. As a result, accurate estimations of the losses in the winding can be obtained. However, constructing 3D models of individual conductors is more complicated than using solid regions. Furthermore, individual conductors increase the complexity of the FEM model and the number of elements in the mesh. Third, simulating proximity and skin effects require fine meshes. For large geometries (e.g. IPT pad), fine meshes result in an extremely large number of elements. Such models are impractical for design purposes due to the long computation times. Thus, modeling the individual conductors is a valid option for 2D-axis-symmetric models but not for 3D models.

A better approach is to model the winding as a solid region as shown in Fig.3.8. In general, the following three conditions make the use of solid regions possible. 1) Since Litz wires are used, proximity and skin effects are minimized. As a result, the current distribution within the conductors is relatively homogeneous and, therefore, its impact on the overall magnetic field is negligible. 2) The difference between the magnetic flux generated by a solid region and the one generated by individual conductors is minimum when the coils are closely packed. The discrepancy increases as the distance between coils enlarge. For closely wounded coils, like the ones in IPT systems, errors of less than 2% are expected when using this approximation [12]. 3) The estimation of coil losses is not performed directly using FEM tools but rather employing analytic methods.

Winding Losses

When using the solid region approximation for a winding, the copper losses cannot be directly calculated from the FEM simulations as the proximity and skin effects are not considered during the simulation. Thus, other methods are required. In [62], a method for estimation of losses in a Litz wire winding is presented. This method has been validated for IPT systems in [12] and it is used in this dissertation to estimate copper losses. The method considers skin effect and the proximity effects separately: $P_{cu} = P_{skin} + P_{prox}$. DC losses are included in P_{skin}. Expressions to compute P_{skin} and $P_{prox.}$ are derived next. The geometric parameters used during the derivation are depicted in Fig.3.9.

Skin Effect The skin effect losses are due to the AC current through each conductor. The self-induced eddy-current losses change the distribution of the current in its cross-sectional area. In a Litz wire, the skin effect losses are reduced due to the narrow diameter of the strands. These losses can be estimated using (3.7) [62]:

$$P_{skin,L} = n \cdot R_{DC} \cdot F_R(f) \cdot \left(\frac{i_{pk}}{n}\right)^2 \quad [\mathrm{W/m}] \tag{3.7}$$

where r_i is the strand radius as depicted in Fig.3.9, i_{pk} is the peak excitation current, n is the number of strands per coil, $R_{DC} = \frac{1}{\sigma \pi r_i^2}$ is the DC resistance of a strand per unit length, and $F_R(f)$ represent the increment of the resistance as a function of the frequency of operation. $F_R(f)$ is given by (3.8) [62]:

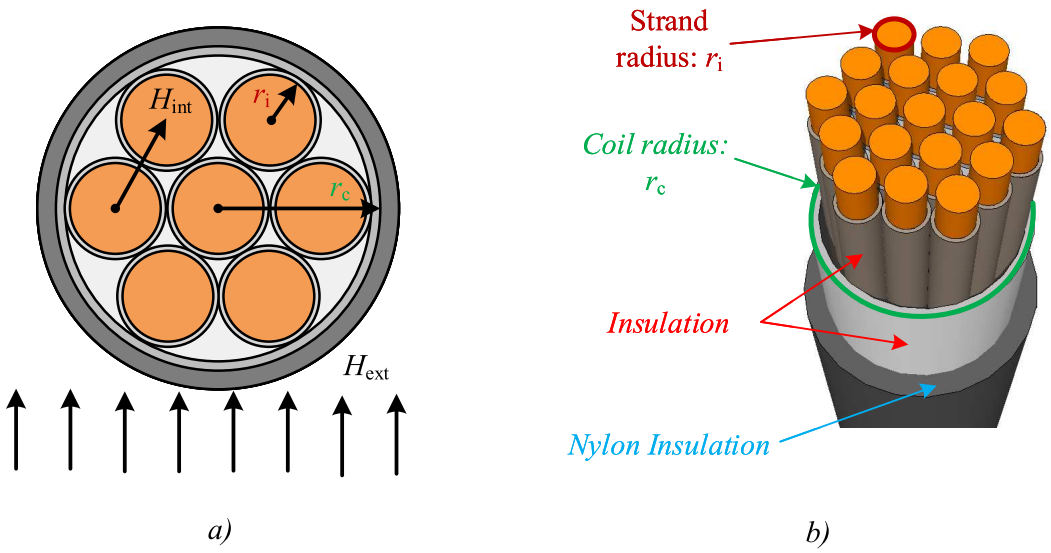

Fig. 3.9 Illustration of the structure of a Litz-wire coil. a) Cross-section of the Litz wire coil. b) Isometric view of the Litz wire coil.

$$F_R = \frac{\xi}{4\sqrt{2}}\left(\frac{\mathrm{ber}_0(\xi)\mathrm{bei}_1(\xi)-\mathrm{ber}_0(\xi)\mathrm{ber}_1(\xi)}{\mathrm{ber}_1(\xi)^2+\mathrm{bei}_1(\xi)^2} - \frac{\mathrm{bei}_0(\xi)\mathrm{ber}_1(\xi)+\mathrm{bei}_0(\xi)\mathrm{bei}_1(\xi)}{\mathrm{ber}_1(\xi)^2+\mathrm{bei}_1(\xi)^2}\right) \tag{3.8}$$

where ξ represents the ratio between the skin depth δ_{cu} of copper and the strand diameter:

$$\xi = \frac{2\cdot r_i}{\sqrt{2}\delta_{cu}} \qquad \text{with} \qquad \delta_{cu} = \frac{1}{\sqrt{\pi\mu_0\sigma_{cu}f}} \tag{3.9}$$

Likewise, ber_x and bei_x correspond to real and imaginary parts of the Kelvin functions of order x. The Kelvin functions are the solution to the x^{th}-order Bessel functions of the first kind ($J_x(z)$) when the argument z is considered as real. In other words:

$$\mathrm{ber}_x(\xi) = \Re(J_x(\xi e^{j\frac{3\cdot\pi}{4}})) \tag{3.10}$$

Despite the complexity of (3.8), it can be solved easily with specialized math software like MATLAB. Both $\mathrm{ber}_x(\xi)$ and $\mathrm{bei}_x(\xi)$ can be calculated directly using MATLAB once ξ is known.

Proximity Effect Proximity effect losses in one strand are a consequence of the alternating magnetic fields which are produced by other strands in the same and neighboring coils. The magnetic field that leads to proximity losses results from the sum of the external field H_e and the internal field H_i. The former is the field induced by neighboring conductors while H_i is produced from its neighboring strands in the same conductor. Consequently, the total proximity losses can be calculated using (3.11) [62]:

$$\begin{aligned} P_{prox,L} &= P_{prox,L,ext} + P_{prox,L,int} \quad [\mathrm{W/m}] \\ &= n\cdot R_{DC}\cdot G_R(f)\cdot\left(H^2_{ext,pk}+H^2_{int,pk}\right) \quad [\mathrm{W/m}] \end{aligned} \tag{3.11}$$

where G_R defines the increment of the proximity effect as a function of the frequency and it can be calculated as in (3.12) [62]:

$$G_R = -\frac{\xi\pi^2 2r_i^2}{\sqrt{2}}\left(\frac{\mathrm{ber}_2(\xi)\mathrm{ber}_1(\xi)+\mathrm{ber}_2(\xi)\mathrm{bei}_1(\xi)}{\mathrm{ber}_0(\xi)^2+\mathrm{bei}_0(\xi)^2} + \frac{\mathrm{bei}_2(\xi)\mathrm{bei}_1(\xi)-\mathrm{bei}_2(\xi)\mathrm{ber}_1(\xi)}{\mathrm{ber}_0(\xi)^2+\mathrm{bei}_0(\xi)^2}\right) \tag{3.12}$$

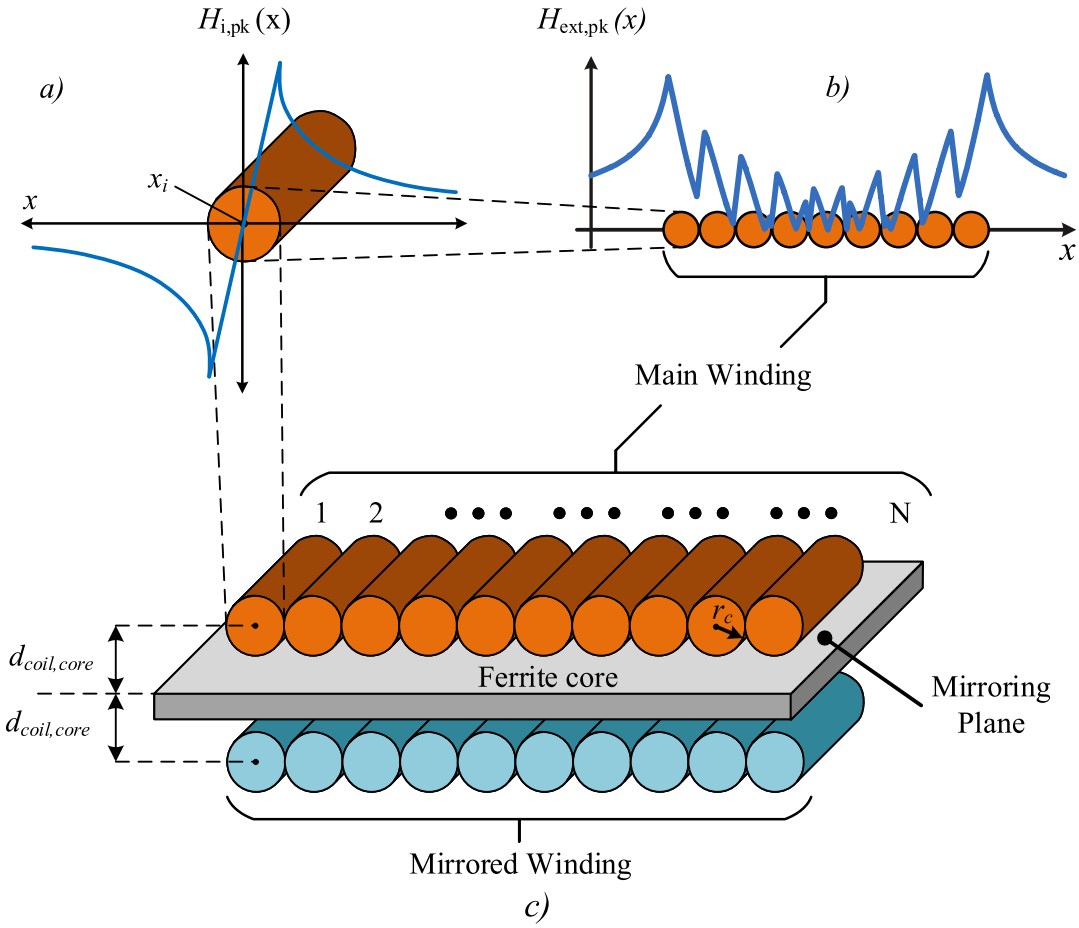

Fig. 3.10 Illustration of the technique used in the estimation of copper losses of IPT coils. *a*) Magnetic field intensity produced by one conductor with uniform current density. *b*) Magnetic field intensity of a group of conductors. *c*) Illustration of the mirroring technique.

where r_i, ber_x, and bei_x were defined in the previous section. The internal field strength H_{int} can be approximated by (3.13) [62]:

$$H_{int,pk} = \frac{i_{pk}}{2 \cdot \sqrt{2} \cdot \pi \cdot r_c} \tag{3.13}$$

where r_c is the Litz wire radius as depicted in Fig.3.9.

The estimation of the external field $H_{ext,pk}$ is more complicated as all the coils in the winding must be considered. H_{ext} can be obtained from FEM simulations or it can be estimated analytically [10] as explained next. The magnetic field intensity $H_{i,pk}(x)$ generated by the i-th coil with uniform current density J [A/m^2] is depicted in Fig.3.10.*a*. The assumption of a uniform current distribution is valid for Litz wire coils. $H_{i,pk}(x)$ can be analytically calculated

as a function of the position using (3.14):

$$H_{i,pk}(x) = \begin{cases} \frac{i_{pk}(x-x_i)}{\pi \cdot r_c}; & |x| \leq r_c \\ \frac{i_{pk}}{2 \cdot \pi \cdot (x-x_i)}; & |x| > r_c \end{cases} \tag{3.14}$$

where x_i is the position of the center of the i-th circular conductor and r_c is the conductor radius. The total magnetic field intensity $H_{ext}(x)$ of the group of coils forming the winding is generated from the superposition of field generated by every individual coil as shown in Fig.3.10.*b*. Mathematically, $H_{ext}(x)$ can be described as in (3.15):

$$H_{ext,pk}(x) = \sum_{i=1}^{N} H_{i,pk}(x) \tag{3.15}$$

where N is the total number of conductors. The total $H(x)$ is intensified by the presence of the magnetic cores in the vicinity of the coil. To include this effect, the *method of images* also known as *mirroring technique* is used. The method is depicted in Fig.3.10.*c*. The boundaries of the ferromagnetic material are used as mirror planes. Since the distance between pads is large ($100-200$mm), the core in the receiver pad is usually not considered during mirroring but it can be included to increase the estimation accuracy.

Total Losses The total losses are calculated considering (3.7) and (3.11). These expressions are in per unit length; thus, they need to be multiplied by the length of the entire coil. A more detailed explanation of the methodology can be found in [10] and [62].

3.2.4 Boundary Conditions and Geometric Symmetry

Two types of boundary conditions are commonly considered for solving electromagnetic FEM problems: The Magnetic Insulation (MI) and the Perfect Magnetic Conductor (PMC) boundary conditions. MI (Dirichlet condition) can be understood as the boundary to a domain with infinity conductivity. Mathematically speaking, it defines the field as zero at the boundary. This condition is the equivalent to encapsulate the model inside a sphere of very high conductivity. PMC, on the other hand, enforces a Neumann condition. Mathematically, it defines the derivative of the field as zero at the boundary. That is, no current can be induced, and the normal component of the field is zero. This condition is equivalent to encapsulate the model inside a sphere of infinite permeability.

In practice, the mismatch in the results obtained using one condition or the other decreases rapidly as the radius of the boundary (sphere) increases. A radius of 3 times the IPT system size is considered an acceptable compromise. Moreover, the boundary, shown in Fig.3.11, is

defined as an "infinite element" in COMSOL. The software then internally performs a coordinate stretching to ensure high accuracy.

3.2.5 Meshing

Regarding meshing, a compromise between accuracy and computation burden is necessary. Although automatic meshing of finite element domains usually leads to accurate inductance estimations, it was not enough to guarantee the high accuracy of the estimated core losses. A refinement of the mesh was performed.

To ensure the high accuracy of the eddy-current analysis it is suggested that the mesh size should be no larger than half of the skin depth [63]. For nanocrystalline ribbon cores at 85 kHz, the skin depth is 0.9 mm. Thus, a mesh size between $0.3 - 0.4$mm was considered at the critical boundaries within the core as shown in Fig.3.11. The meshing in the core can be uniform (for core bars or small cores) or it can follow a non-uniform distribution; i.e., it can

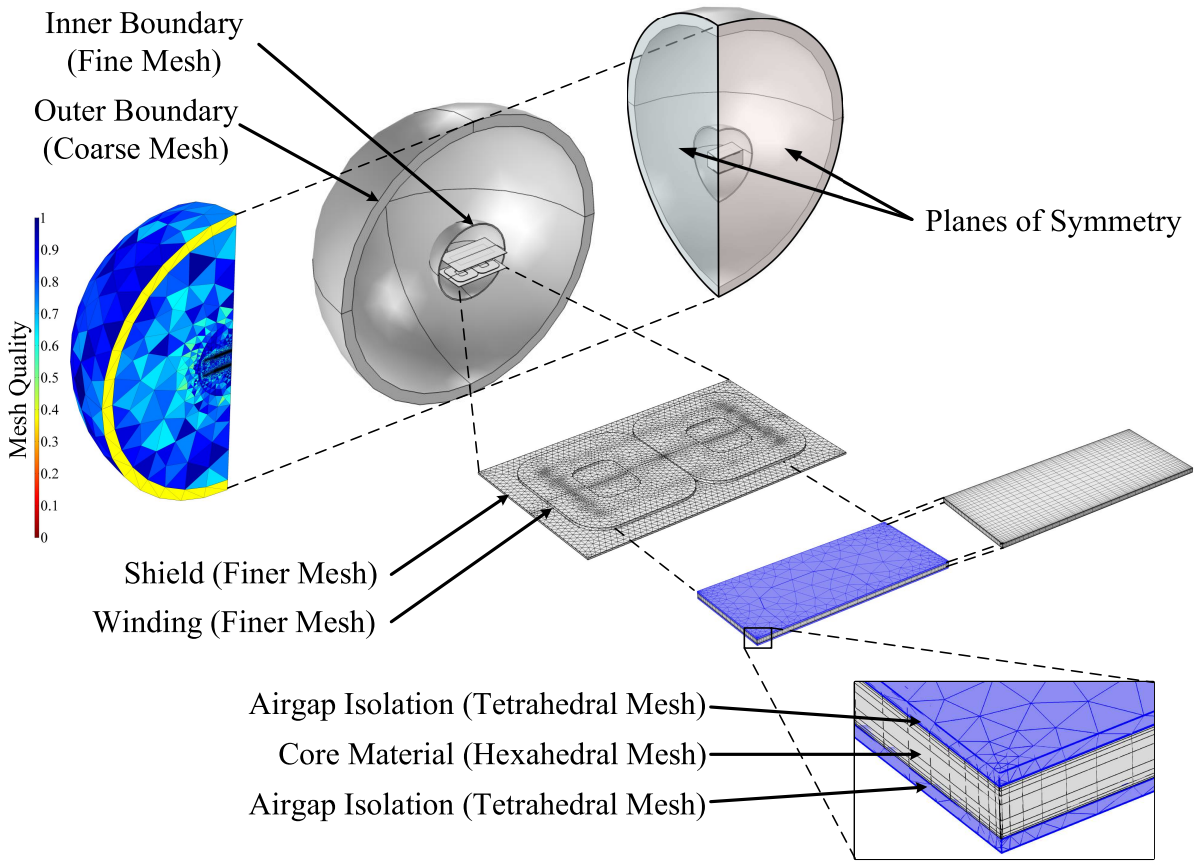

Fig. 3.11 Illustration of the meshing of the different components of the system as well as the planes of symmetry used to simplify the mode. The meshing quality is also shown.

be finer near the edges and coarser elsewhere. This meshing strategy, shown in Fig.3.11, is optimum for bigger cores (e.g. core plates) as it reduces the number of elements. The effect on the accuracy is negligible as the eddy-currents mainly occur at the lateral faces of the core bars. In any case, the maximum element size was set to 5mm to keep the mesh quality high.

Tetrahedral and hexahedral meshes are combined to improve the accuracy of the FEM model. Hexahedral meshes are used within the core as they have proved to reduce the number of meshing elements and lead to a more accurate representation of laminated cores [82]. Tetrahedral meshing is used elsewhere. To ease the meshing process, the core-to-shield and core-to-coil clearances are meshed after the cores. They are meshed independently from the rest of the components to ensure adequate quality. A slightly coarser mesh is used for shield, winding, and surroundings as shown in Fig.3.11. Since accurate estimations of the copper losses are not of interest, a fine meshing of the windings is not necessary. Regarding the surroundings, outer and inner boundaries are considered. Within the inner boundary, a fine mesh is used while a coarse mesh is used in the space between outer and inner boundaries. The quality of the elements is shown in Fig.3.11. Mesh quality here is defined as the maximum ratio between two sides of the tetrahedral normalized between 1 (good quality) and 0. Within the inner boundary, the quality is close to 1. The mesh quality is lower for the outer boundary; however, it is kept at values greater than 0.4 as to not compromise the accuracy.

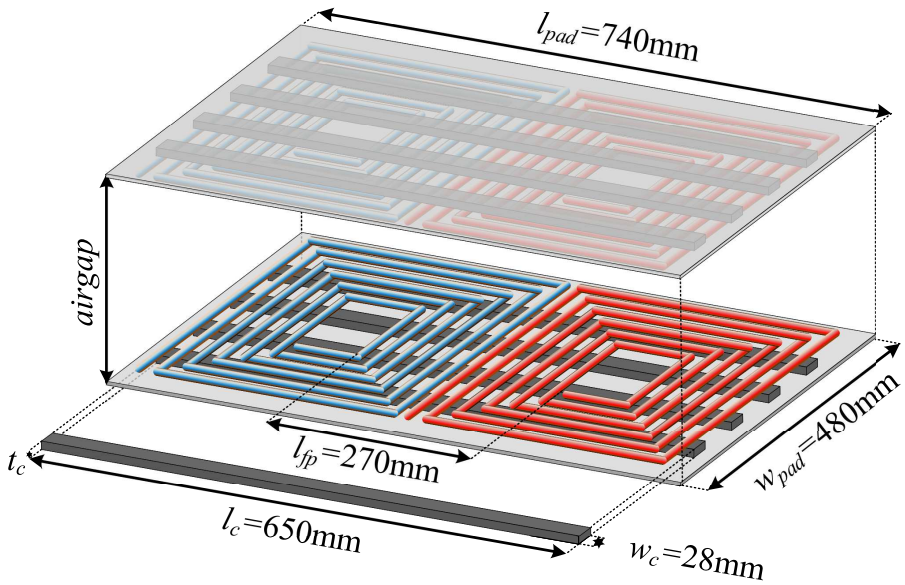

Fig. 3.12 Dimensions of the Double-D pad used for the FEM analysis and experimental validation. The coil is made of 22 turns of Litz wire with a 5.5 mm^2 cross-section.

Geometric Symmetry

To reduce the computation time, the symmetry of the pad was exploited whenever possible. This is only possible when simulating the coils at their nominal position; i.e., without misalignments in the x or y axes. Under this condition, the pad can be represented effectively by one-quarter of its volume. This volume along with the planes of symmetry are depicted in Fig.3.11. The plane of symmetry in blue is set with a *perfect magnetic conductor* (PMC) condition whereas a *magnetic insulation* (MI) condition is used for the other plane.

3.3 Simulation Results: Ferrite vs. Nanocrystalline ribbon cores

Following the FEM methodology described in the previous section, a FEM-based comparative study of nanocrystalline ribbon cores and ferrite cores is performed. Different electromagnetic properties are evaluated. In particular, the effect of the higher permeability and conductivity values are studied. The specific dimension of the pads, winding, and cores are shown in Fig.3.12. Since the transmitter and receiver pads are identical, their self-inductance is the same, i.e. $L_1 = L_2 = L$. The core is made up of four bars, each of 650mm$\times$28mm$\times$16mm. N87 ferrite is considered for the ferrite cores while Antainano 1k107 (20μm ribbon) is used for the nanocrystalline ribbon cores. The coil comprises 22 turns of Litz wire with a cross-section of 5.5 mm^2.

3.3.1 Effect of the core permeability on the self L_1 and mutual M inductances

Fig. 3.13 compares the self-inductance L_1, mutual inductance M, and coupling factor k when using ferrite and nanocrystalline ribbon cores respectively in an IPT pad. The cores are considered as loss-less materials (i.e. $\sigma = 0$) to isolate the permeability from the conductivity. An air gap of 200 mm between pads is considered.

Given that the mutual inductance is inversely proportional to the magnetic reluctance $\mathfrak{R}$, the higher magnetic permeability of the nanocrystalline ribbon is expected to lower $\mathfrak{R}$ and yield higher values of self and mutual inductances. As seen in Fig.3.13, a small increment of L, k, and M is observed when using nanocrystalline ribbon cores as compared to ferrite cores. An increment of only 5% to 9% (depending on the air gap) was observed even though the permeability of the nanocrystalline material is more than 100 times higher than that of the ferrite N87 used in this comparison. The reason for this relatively small increment is the fact

that the air gap between pads dominates the magnetic circuit. Thus, a lower core reluctance has an insignificant effect on the overall magnetic flux. Thus, the benefits of higher permeability are relatively less important for large air gaps between pads. The impact of the permeability increases as the clearance (air gap) between pads decreases. However, for IPT systems used in EVs, the clearance is large ($>$ 100mm) and thus the benefits of having a higher permeability are less important.

3.3.2 Effect of the core conductivity on the self L_1 and mutual M inductances

Core bars, as opposed to plates, are commonly used to constrain effectively the magnetic flux while reducing magnetic material, cost, weight, and fragility [15]. When using core bars, a considerable portion of the flux enters through the lateral faces of the bars and induces eddy-currents in the cores. For ferrite, the eddy-currents induced in the core are very small due to the high resistivity (10 Ωm) of the material. The eddy-currents induced in the core are practically negligible. In contrast, the resistivity of nanocrystalline material, 1.2×10^{-6}Ωm, is considerably lower than that of ferrite. Thus, the eddy-currents induced in the cores are not negligible. The lateral faces of the core bar operate effectively as a shield. The shielding effect results in magnetic fields that oppose the main field reducing the overall self and mutual-inductance and increasing the power losses [8, 30]. As seen in Fig.3.14$a) - b$), the self and mutual inductances obtained from nanocrystalline ribbon cores are only 1.5% to 3% higher than that

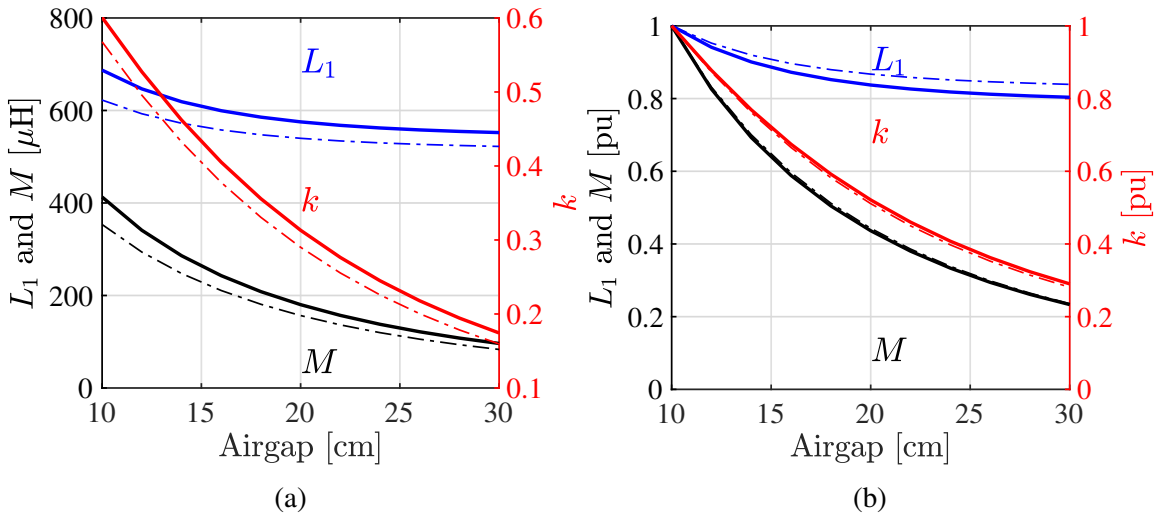

Fig. 3.13 a) Coupling factor k, self L, and mutual M inductances for nanocrystalline ribbon ($-$) and ferrite N87 ($.-$) cores with $\sigma_{x,y,z} = 0$. b) Normalized parameter variation as a function of the airgap.

of ferrite cores. Thus, the overall inductance is only marginally higher than the one obtained with ferrite cores. The increment on the inductance obtained due to the higher permeability (see Fig.3.13) is counterbalanced by the opposing field created by the eddy-currents induced in the cores. The overall effect will depend on the exact design of the pad; i.e., the number of cores, core dimensions, etc.

From these results, one can conclude that there is only a marginal improvement in the magnetic performance of the pad when using nanocrystalline ribbon core bars as compared to ferrite bars.

3.3.3 Comparison of Flux Distribution in the Core

The anisotropic characteristic of the permeability along with the eddy-currents induced in the magnetic cores influences the distribution of magnetic flux within the core. A comparison of the flux distribution in the core is shown in Fig. 3.15 for N87 and nanocrystalline ribbon materials.

Ferrite Cores

Due to the isotropic properties of the material, the flux distribution in the cross-sectional area of the N87 cores is practically uniform as depicted in Fig.3.15.*a*. The flux density reaches its maximum value at the center of the coil (with respect to the *x*-axis) since that section

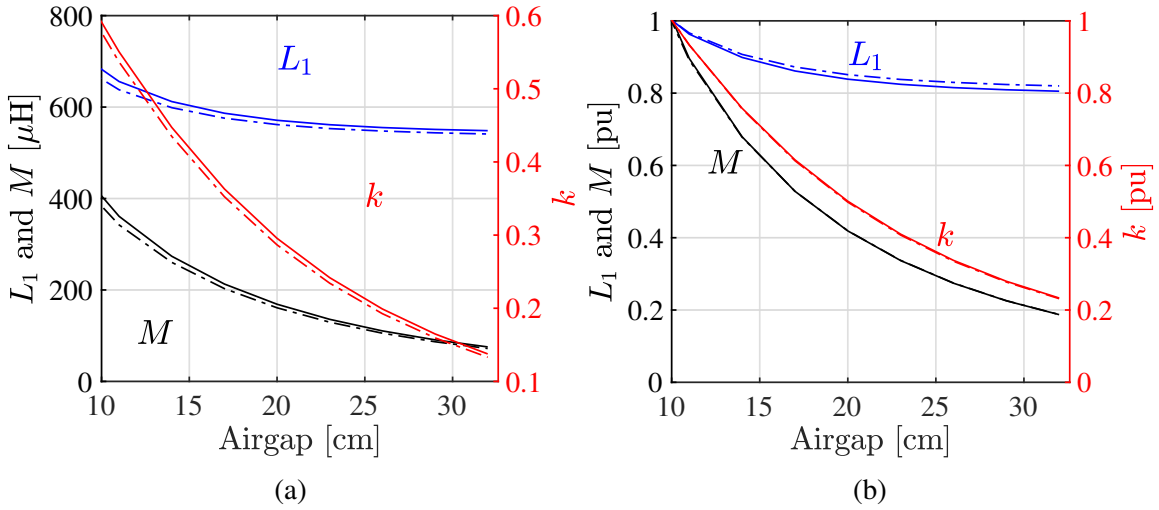

Fig. 3.14 *a*) Coupling factor k, self L, and mutual M inductances for nanocrystalline ribbon ($-$) and ferrite N87 ($.-$) cores with $\sigma_{x,y,z} \neq 0$. *b*) *b*) Normalized parameter variation as a function of the airgap.

offers a shorter flux path between two coils; i.e., nearly all flux paths cross the center of the core. The flux density value is directly proportional to the coil excitation current and inversely proportional to the clearance between pads. For large air gaps ($\geq$50 mm), the leakage flux accounts for the majority of the linkage flux. Here, the leakage flux is defined as the portion of flux linking only the transmitter or receiver pads but not both. Therefore, the flux density remains approximately constant, as seen in Fig.3.15.*c*. As a result, the self-inductance L does not change greatly with the misalignment. As a result, during the design of an IPT pad, once the operating point (air gap and excitation current) is determined, the thickness of the ferrite core can be selected to ensure that saturation does not occur at any point within the core. This will be further discussed in the next section.

Nanocrystalline Ribbon Cores

Similar to a pad with ferrite cores, the middle section of the nanocrystalline ribbon core bars (x-axis) shows larger flux density as this region is below the pad flux pipe. As opposed to the ferrite core, the flux distribution in the cross-sectional area of the core bar is not uniform. Due to the anisotropic characteristic of the bar (see Section 3.2.2), the parallel direction (x-axis) is the preferred magnetic path for the flux. The perpendicular direction (y-axis) represents a high reluctance path due to the binder between ribbons. Thus, the flux entering the lateral face of the bar will only reach a ribbon once the prevailing ones are close to saturation. As a result, the core lateral faces show the highest flux density. From the lateral face to the middle of the core bar (y-axis), the flux density decreases.

A model of this effect is shown in Fig.3.16. Here, ψ represents the total flux entering the lateral faces of the core bar. Since the reluctance $\Re_{\text{adh}} >> \Re_{\text{nano}}$, the first lamination will uptake most of the flux. The subsequent ribbons will carry decreasing amounts of flux. A high magnetic flux ψ, can cause saturation of the ribbons close to the lateral face of the bar. The extent of the saturated region depends on the actual design of the bar (thickness, width, etc.) and the operation point of the pad. For the exemplary case shown in Fig.3.15.*b*, the saturation region represents only a small portion of the total core volume. The higher flux density at the lateral faces implies higher hysteresis losses. Thus, high temperatures during operation are expected to occur at the lateral walls of the core.

Additionally, the flux perpendicular to the ribbons induces eddy-currents in the lateral faces of the core which changes the distribution and increases the power losses. From [82], higher flux density is expected in the upper part of the core closer to the coil as shown in Fig.3.15.*d*.

Despite the localized effects at the faces of the bar, the flux density in most of the bar is like that obtained with ferrite cores and therefore far from the saturation point of the nanocrys-

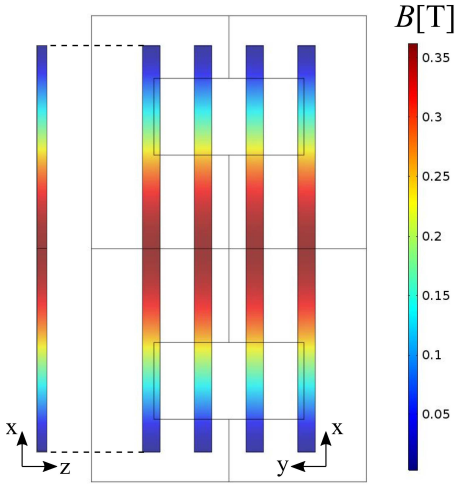

(a) N87

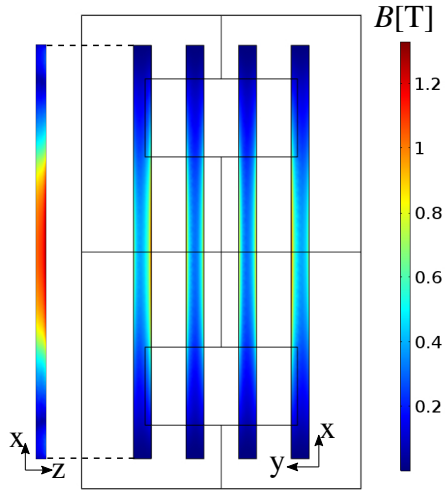

(b) Nanocrystalline, electrical conductivity $\sigma_{eq} = 0$

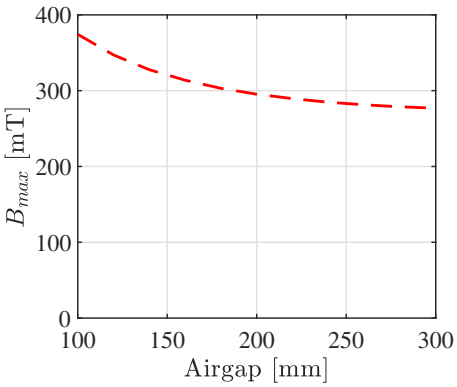

(c)

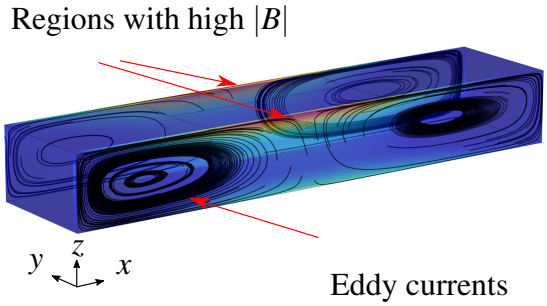

(d) Nanocrystalline, electrical conductivity $\sigma_{eq} \neq 0$

Fig. 3.15 Flux density distribution for *a*) N87 *b*) nanocrystalline ribbon cores at an air gap of 100 mm. *c*) Flux density in the middle of the ferrite core as a function of the air gap. *d*) Eddy-currents induced in the nanocrystalline ribbon core. Result obtained from pad shown in Fig.3.17.

talline material. This suggests that the thickness of the bar can be further reduced resulting in higher power densities. Nonetheless, the effect that eddy-currents have on the losses and efficiency must be considered.

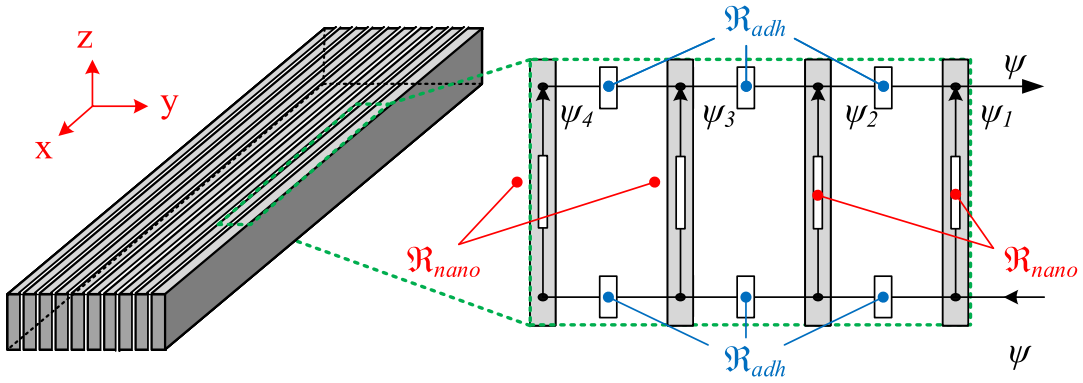

Fig. 3.16 Representation of the transverse flux magnetic ψ entering the lateral faces of the cuboid core bars. $\Re_{nano}$ and $\Re_{adh.}$ represent the magnetic reluctance of the nanocrystalline ribbon and binder between ribbons, respectively. $\Re_{adh.} >> \Re_{nano}$. $\psi_1 >> \psi_2 >> \psi_3 >> \psi_4$

3.4 Experimental Results

3.4.1 Experimental Setup

Inductive Couplers

Two identical Double-D pads were manufactured to validate the simulation results: one with nanocrystalline ribbon cores and the other with N87 cores. The dimensions of the pad, winding, and cores are shown in Fig. 3.17a. The dimensions are based on a previous publication [15] to have a reference for comparison.

The winding consists of 22 turns of Litz-wire which is made of 850 strands of AWG36, giving a total cross-sectional area of 5.5 mm^2. The coil is coated with a double-nylon layer for protection. This coating is capable of handling high voltages and high temperatures.

The core consists of 4 bars. For the pad with ferrite cores, each core bar is made of 7 I93 ($93 \times 28 \times 16$ mm) cores from TDK (EPCOS). The cores occupy approximately 30 % of the surface area of the pad. The 16 mm core thickness ensures a maximum flux density of 350 mT during operation. For the pad with nanocrystalline ribbon cores, each core bar is a single unit. Each bar is formed by ribbons with a stacking factor of 0.78. The thickness of each thin ribbon is 20 μm. Due to the selected orientation discussed in Section 3.2.2, the width of the ribbon determines the thickness of the bar. Ribbons of two different widths have been used: t_{c1} =16 mm and t_{c2} =8 mm. The core cross-sections are shown in Fig.3.17b. The cores are held in place with double-sided tape (3M®). Kapton®tape is used to isolate the cores from the shield and the coil. Transparent and perforated acrylic sheets are used to hold both the coil and core in position. Fig.3.17b shows images of the pads after construction.

Power Electronics

A bespoke power converter, shown in Fig.3.18, was designed to control the power flow between pads. The H-bridge uses Silicon carbide MOSFETs C3M0065100K from CREE as switches. They are rated for 1000 V and 35A and have a low $R_{DS(on)}$ of 65 mΩ. This secures low conduction losses. To increase the current rating of the converter, two MOSFETs (connected in parallel) are used for every switch. The PCB layout is completely symmetrical to secure equal current sharing between MOSFETs as well as symmetric turn-on and turn-off times. From simulations, the DC-link voltage capacitor size was estimated as 300 μF. Six film capacitors EPCOS 50 μF are used for this purpose. The board allows the connection of an extra aluminum capacitor if needed.

A diode bridge rectifier is also connected to the same DC-link bus. This way, the device can operate actively or passively. SiC diodes (On Semiconductor, 512-FFSH40120ADNF155) are used. Additionally, the board incorporates gate drive circuits for each switch. The gate

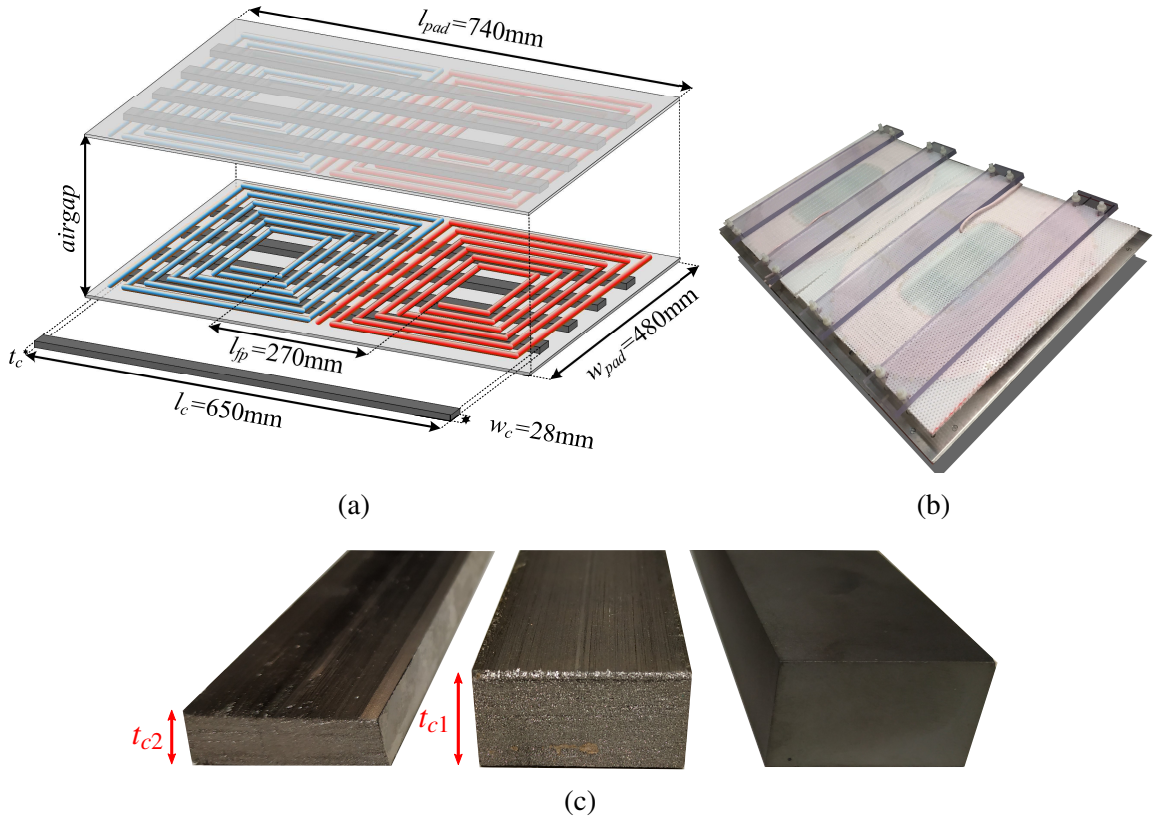

Fig. 3.17 Illustration of the pad constructed for the experimental testing. a) Dimension of the Double-D pad. $b) - c$) Image of the pad after construction. d) From left to right, Nanocrystalline ribbon core with t_{c2} =8 mm, nanocrystalline core with t_{c1} = 16 mm, and ferrite core $t_{fe} = t_{c1}$.

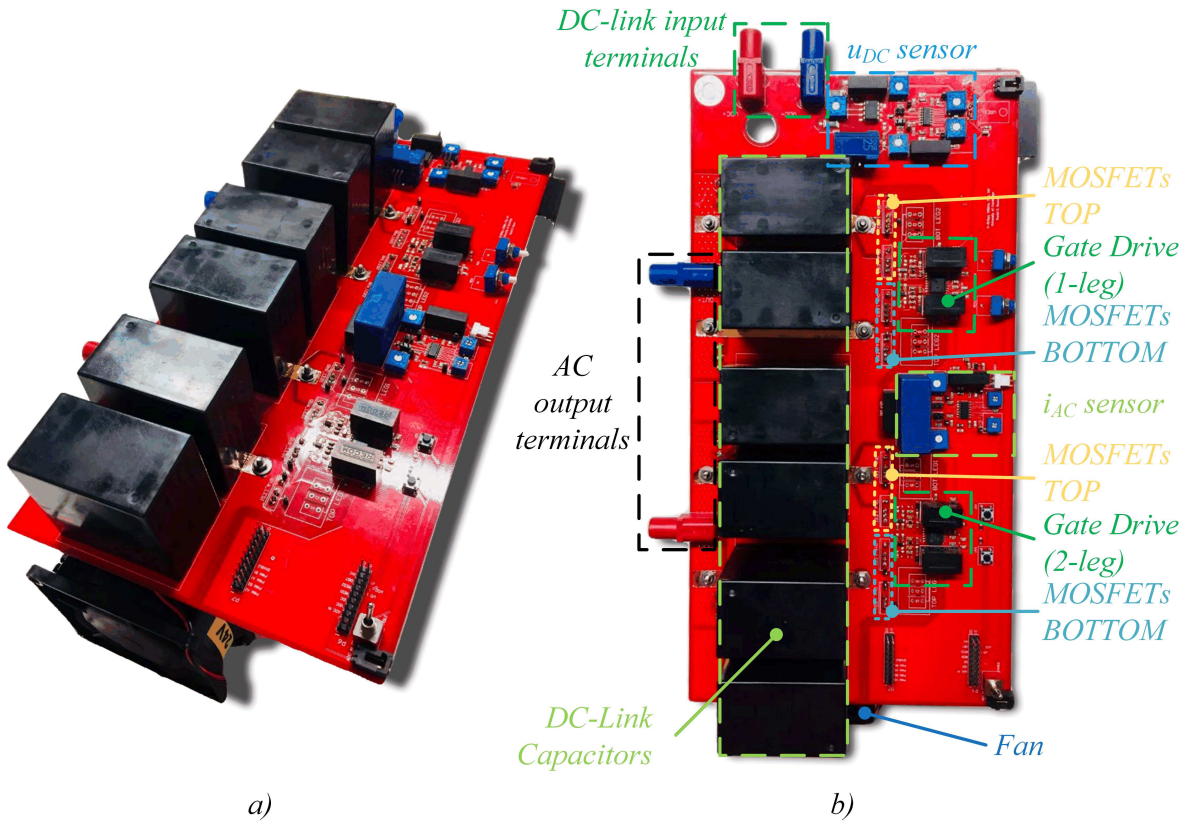

Fig. 3.18 Illustration of the power electronics converters designed to test IPT systems. *a*) 3D-view of the H-Bridge Power Converter. *b*) Description of the components of the power electronic board (PCB).

signals are generated from a Texas Instrument DSP controller (LAUNCHXL-F28379D) which can be easily stacked into the board.

Several measurement circuits are also included on the board. The DC-link voltage and the AC load current are measured employing dedicated sensors. The AC current is measured using a LEM hall effect sensor. The DC-link voltage, on the other hand, is measured directly through an isolated voltage divider circuit. Signal processing circuits are used to scale the voltage and to reduce noise. These signals are fed back into the micro-controller and they can be for closed-loop control. Additionally, the board contains auxiliary control features such as push buttons, toggle buttons, and knobs to facilitate the safe operation of the system. Specific schematics of these circuits are shown in Appendix A.

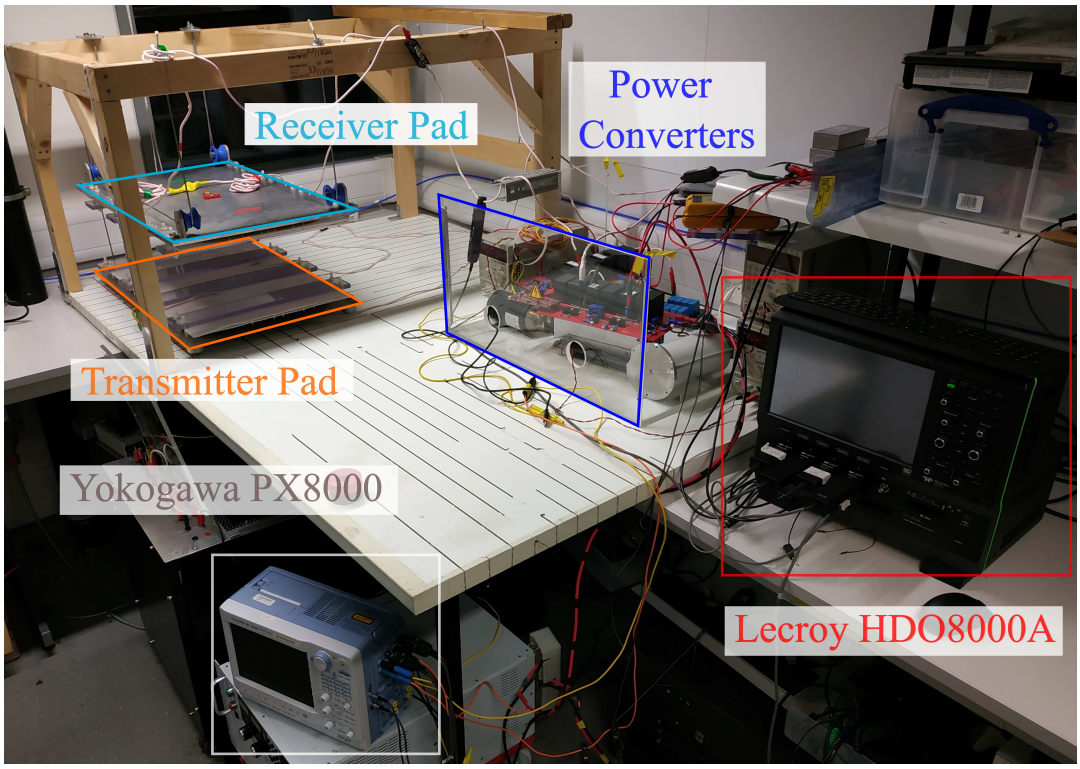

Fig. 3.19 Photography of the test-rig constructed for the experimental validation. The components of the test-rig and measuring equipment are highlighted.

Testbench and Instrumentation

A test rig has been designed and constructed to facilitate the movement of IPT pads. As shown in Fig. 3.19, the transmitter pad has wheels below the shielding that allow it to move freely in the *xy*-plane. A pulley system allows the secondary to be moved up and down (*z*-axis). As a result, the pad can be misaligned in every direction. The setup can operate for pads of different sizes and ratings. The test rig includes dedicated power converters −which are placed in an enclosure for safety purposes−, and three instrumentation devices: a power analyzer Yokogawa PX8000, an oscilloscope LeCroy HDO8000A, and a network analyzer N4L PSM3750. The latter is used to measure inductance, coupling factors, and frequency responses.

3.4.2 Measurement of Impedance

To validate the FEM simulation results, the impedance of a pad with three different cores is measured. These measurements were conducted under small-signal conditions, i.e. low power excitation. Self and mutual inductances are shown in Fig.3.20$a) - c)$ at different clearances

between pads (air gap) and pad misalignments. The inductance values match FEM results with a difference of less than 8% for all pads using different cores. Only the FEM results for the pad with the nanocrystalline ribbon cores of thickness t_{c1} are depicted in Fig.3.20 to avoid information overload. As predicted by FEM models, pads with nanocrystalline ribbon cores yield slightly higher self and mutual inductance values compared to pads with ferrite cores. This is attributed to their higher relative permeability, μ_r. Fig.3.20$d) - f)$ depicts the equivalent resistance of the pad measured with an impedance analyzer. The equivalent impedance considers a series-connected resistor and inductor as shown in Fig.3.21b.. The equivalent resistance R consists of both the high-frequency ohmic resistance of the coil (Litz wire) and the core losses which are seen as a real impedance from the impedance point of view.

Conventionally, the equivalent model of a pair of coupled coils (e.g. transformer) considers a resistor in parallel with the magnetizing inductor to model the eddy-current and hysteresis losses as shown in Fig.3.21.a. The value of the resistance represents the eddy-current loss. When using the equivalent model in Fig.3.21.a, the resistor value is inversely proportional to the conductivity of the magnetic core. Higher conductivities result in a lower resistor value and a higher eddy-current loss. When using the series model, Fig.3.21.b, higher core conductivity results in a larger resistance in the equivalent circuit. For the pads with nanocrystalline ribbon cores, this resistance is between 7.6 and 20 times larger than that of ferrite's pads depending on the pad misalignment and the core thickness. The pad with slimmer nanocrystalline ribbon cores yields lower resistance. This is explained by the fact that the eddy-currents in the lateral faces of the core decrease proportionally to the area of the exposed surface.

Nanocrystalline alloy's higher equivalent resistance reduces the effective pad's quality factor Q as shown in Fig.3.20$g) - i)$. While Q ranges from $500 - 570$ for the pad with ferrite cores, it reaches a maximum value of 50 and 75 for the one with nanocrystalline ribbon cores when the ribbon thickness is 16 mm and 8 mm, respectively. As discussed in Section II, the efficiency of the pad is proportional to Q. Hence, pads with nanocrystalline ribbon cores are expected to have a lower efficiency as compared to pads with ferrite cores for the same core dimensions. This is analyzed with more detail in the next sections.

3.4.3 Measurement of Power Losses and Efficiency

To measure the power losses of the pad during normal operation, the set-up in Fig.3.19 is used. Series compensation circuits are used for simplicity in both transmitter and receiver sides. The resonant circuit is tuned for an air gap of 200 mm and perfect alignment between the transmitter and the receiver pads.

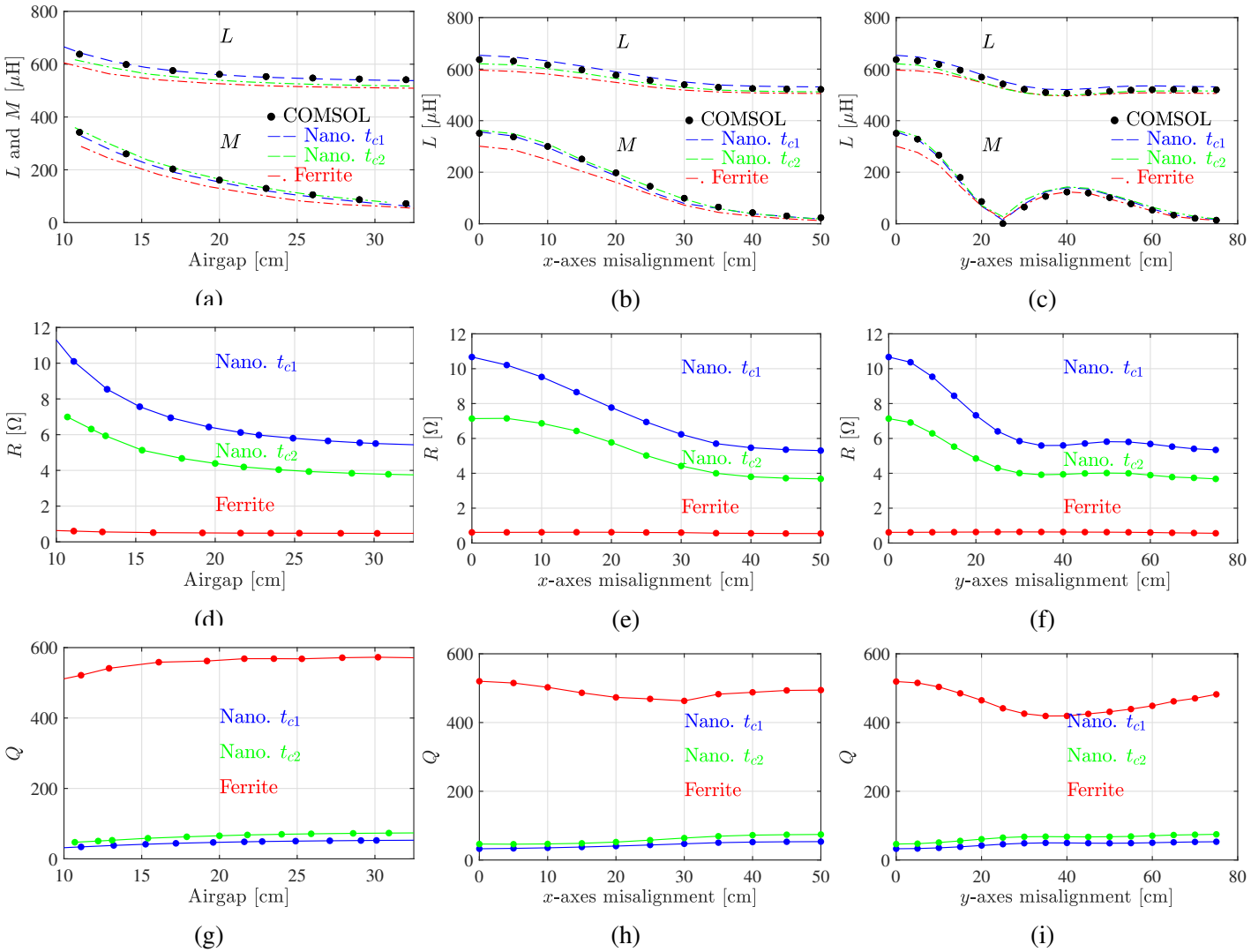

Fig. 3.20 Measurement of inductances, equivalent resistance, and quality factor of a Double-D pad with nanocrystalline and N87 cores at different pad misalignments. $a)-c)$ Measured self $L_1 = L_2 = L$ and mutual M inductances. $d)-f)$ Measured pad's AC equivalent resistance R at 85 kHz. $f)-i)$ Coil quality factor $Q = \omega L_1/R$. $t_{c1} = 16$ mm. $t_{c2} = 8$ mm. COMSOL is the FEM estimation of the nanocrystalline t_{c1}.

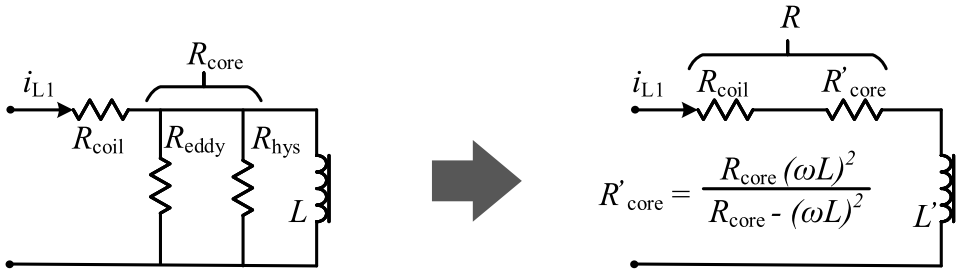

Fig. 3.21 Equivalent circuit of the coupled coils of an IPT system. On the left, a traditional model of the eddy-current and hysteresis losses in the core as parallel resistors, R_{eddy} and R_{hys} respectively, is depicted. On the right, the equivalent circuit is considered as a series impedance. $L' \approx L$ as R_{core} is large. The DC resistance of the coil was measured as 148 mΩ.

At these conditions, $L_1 = L_2 = L$ =515 μH, M =130 μH, and $C_S = 1/(\omega^2 L_1)$ =6.8 nF. The latter is achieved by connecting ten TDK capacitors of 68 nF in series.

It is well known that the efficiency of the pad depends on the load [8]. In the case of identical transmitter and receiver pads, the maximum efficiency of the system is achieved when the currents in both coils are equal. This operating point occurs when the equivalent AC load on the receiver side is $R_{L,ac} = \omega M = 69.4\,\Omega$. This AC resistance is equivalent to a DC resistance of approximately 85 Ω after the receiver rectifier stage. The maximum efficiency point is independent of the voltage magnitude [12]. Therefore, the power transfer can be regulated by adjusting the input DC-link voltage while maintaining maximum operational efficiency.

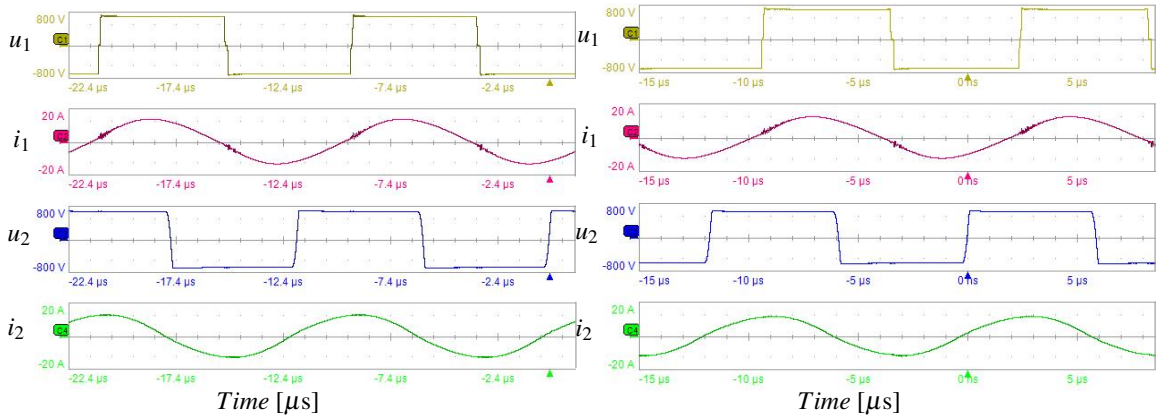

(a) With ferrite cores (b) With nanocrystalline ribbon cores

Fig. 3.22 Measured current and voltage waveforms at the primary converter, u_1 and i_1 as well as at the secondary converter, u_2 and i_2. Double-D pad with *a*) ferrite N87 and *b*) nanocrystalline ribbon t_{c2} cores, respectively. Air gap between pads: ∼ 200 mm.

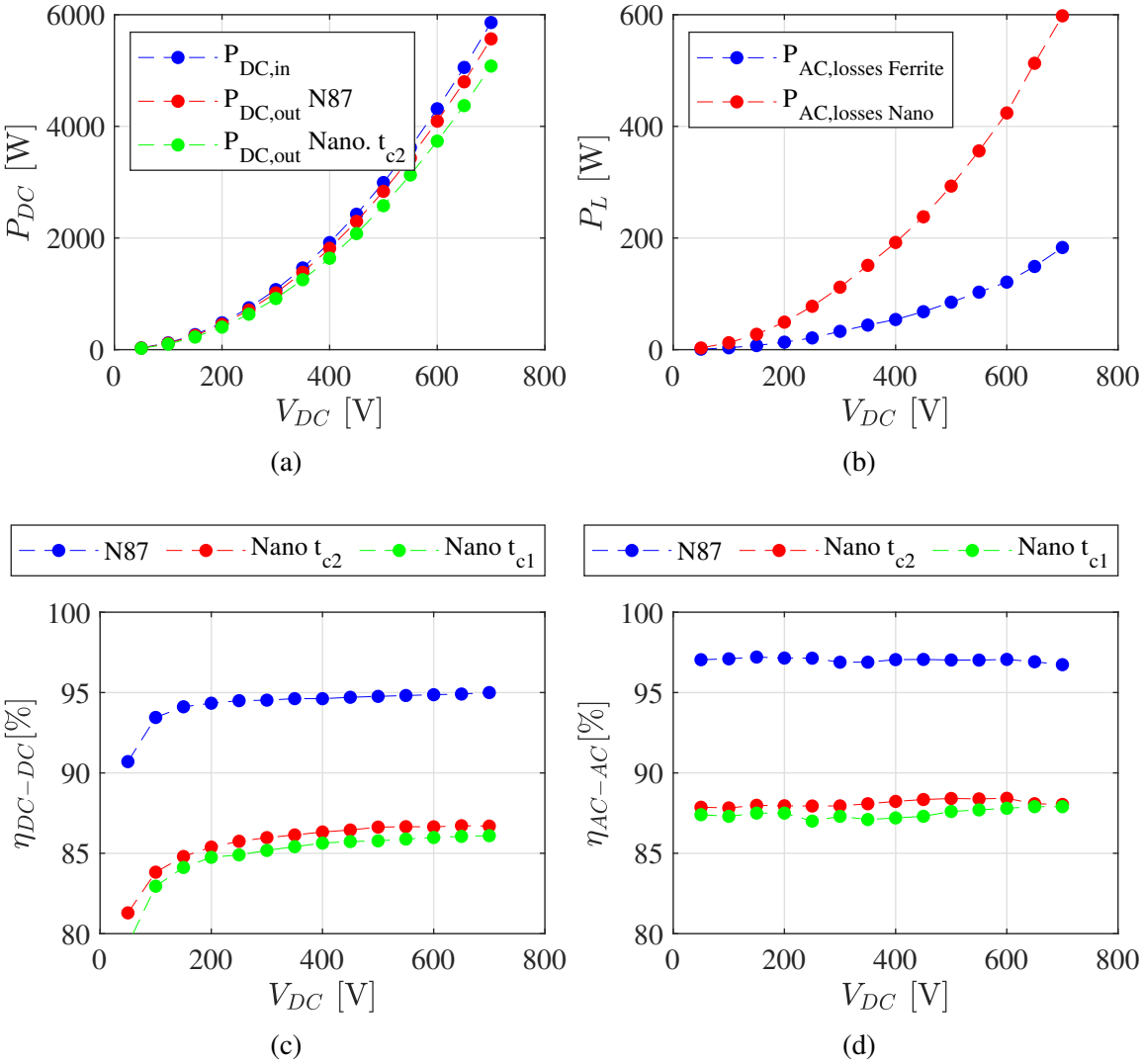

Fig. 3.23 Measured power losses for the Double-D pad with nanocrystalline and N87 cores, respectively. *a*) Power DC input. *b*) Measured power losses in the coils (core and copper losses). *c*) Overall system efficiency. *d*) efficiency of the pad (without considering converter losses).

A LeCroy HDO8000A −equipped with a 120 MHz differential voltage probe and a 100 MHz Hall-effect current probe− is used to acquire AC waveforms and measured AC power. Fig.3.22 shows the voltage and current waveforms at the converter terminals for an operating point of 5 kW. A Yokogawa PX8000 is used at the DC sides to measure the overall system efficiency. The power and efficiency measurements are shown in Fig.3.23 for the different pads.

Fig.3.23 shows the power input of both pads, the power losses in the pads as well as the pad's and system's efficiencies. The lower efficiency of the pads with nanocrystalline ribbon cores is evidenced in Fig.3.23*d*). At about 5 kW, the power losses in the system with

ferrite and nanocrystalline ribbon cores are approximately 200 W and 600 W, respectively. The pad efficiency is approximately 89 % when using nanocrystalline ribbon cores and 97 % when using ferrite cores. The power converter efficiency for both cases remains constant at approximately 98 % since the operating conditions for the converter are the same. As a result, the overall system efficiency with nanocrystalline ribbon cores is approximately 87.5 %. This efficiency is higher than the minimum efficiency required by the standard SAE J2954 of 85 % but lower than the ferrite counterpart which achieves a system's efficiency of 95 %. The system with nanocrystalline ribbon cores with thickness t_{c1} is about 1% less efficient than the one with t_{c2} even though more material is used. Using more core material results in lower flux densities within the core. Thus, lower hysteresis losses are expected with thicker cores. However, the reduction of hysteresis losses is counterbalanced by the higher eddy-currents at the lateral faces of the cores. The overall result is a reduction in efficiency.

For ferrite cores, due to their isotropic behavior, a reduction of efficiency is observed as a result of a decrease in core thickness. The minimum core thickness is limited by saturation. Apart from the increase in power losses, operation in saturation implies non-linear system performance which is undesirable. Thus, nanocrystalline ribbon cores offer an alternative for high power density and high-power rating IPT applications. Nevertheless, without further changes in core geometry, the lower efficiency of the pad can be problematic and limit the application of nanocrystalline ribbon cores for IPT applications. Methods for reducing these losses will be discussed in the next chapter.

Estimated vs. Measured Power Losses

The measured losses can be segregated in terms of components using the methodology for estimation of core and coil losses detailed in Section 3.2). Fig.3.24 shows the overall and breakdown losses for both materials where P_{cu} corresponds to the copper loss, P_{cap} to the capacitor loss, P_{shield} to the loss in the aluminum shield, and P_{elec} and P_{mag} to the eddy-current and hysteresis losses in the core, respectively.

The losses in the compensation capacitors P_{cap} are calculated from (3.16):

$$P_{L,cap} = \frac{\tan(\delta(f_0))}{4 \cdot \pi f_0 C} \cdot i_{pk}^2, \qquad f_0 = 85\,\text{kHz} \tag{3.16}$$

where C corresponds to the capacitance value while $\tan\delta(f_0) = 1.85 \times 10^{-3}$ is the dissipation factor. The latter is identified from the datasheet of the TDK's Metallized Polypropylene Film Capacitors (MKP) Series B32651. The losses in the coil and core are calculated using the methodologies presented in Sections 3.2.3 and 3.2.2, respectively.

Ferrite cores: For the pads with ferrite cores, the majority of the loss, 40.9 %, corresponds to the compensation capacitors. Magnetic loss accounts for a third of the total loss while the copper loss corresponds to only 22.6 % of the total loss. This is due to the high number of strands used in the coil. On the other hand, the loss due to stray flux coupled in the shield accounts for only 1.5% of the total loss. The difference between the measured and estimated total loss is less than 8%.

Nanocrystalline ribbon cores: Similar accuracy has been obtained when estimating the power loss of the pad with nanocrystalline ribbon cores. A difference of less than 6% has been achieved. While the losses in the shield and the capacitors are similar to the ones seen

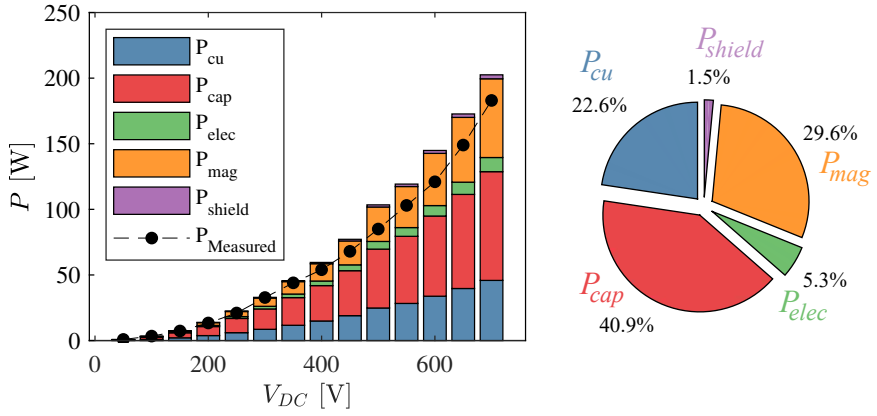

(a) Ferrite

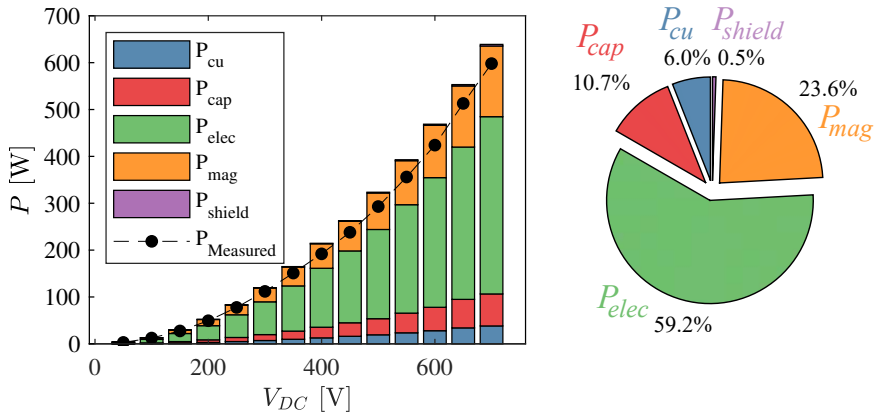

(b) Nanocrystalline t_{c2}

Fig. 3.24 Breakdown of the calculated losses in the system for different DC-link voltages. *a*) ferrite-based Double-D pad. *b*) nanocrystalline-based Double-D pad. P_{cu}: Copper losses. P_{cap}: Capacitor losses. P_{elec}: Eddy-current losses in the core. P_{mag}: Hysteresis Losses in the core. P_{shield}: Power losses in the aluminum shield.

in the system with ferrite cores, the eddy-current and the hysteresis losses are higher. eddy-current loss accounts for almost 60 % of the total loss. On the other hand, the hysteresis loss accounts for 23.6% of the total loss and it is approximately 2.5 times higher than that of the pad with ferrite cores. All things considered, the total loss is 3 times higher than that obtained with ferrite cores.

The higher losses of the nanocrystalline ribbon cores are mainly a result of the higher conductivity of the core bars and the transverse flux. The 2.5% increment of the hysteresis losses P_{mag} is negligible compared to the larger increment of eddy-current losses P_{elec}. Thus, mitigating the latter is crucial to take advantage of the higher power density achievable by nanocrystalline ribbon cores.

3.5 Summary and Conclusions

In this section, a feasibility analysis of using nanocrystalline as a core material for IPT systems is presented. The chapter begins by discussing different magnetic materials that are used in components for power electronics. A detailed comparison between ferrite and nanocrystalline ribbon cores is then presented, highlighting the benefits of the nanocrystalline ribbon cores. Next, a FEM simulation methodology for IPT systems with laminated cores is detailed. This section covers all aspects of the simulation process. Simulation and experimental results are used to validate the following conclusions:

1. The higher permeability of the nanocrystalline ribbon cores results in a slight improvement of L, M, and k. However, its high conductivity tends to counterbalance this effect by decreasing L, M, and k. The overall effect would depend on the core dimensions.

2. Due to the anisotropy of the material, the flux distribution in the nanocrystalline ribbon cores tends to accumulate at the lateral walls of the core bars. However, the flux density in the majority of the bar is lower than the saturation point, which allows for miniaturization of the IPT pad.

3. The losses in the nanocrystalline ribbon cores are higher than the ones obtained from ferrite cores. The dominant contribution of the loss originates from the eddy-current loss at the core's lateral walls.

4. The analytic calculations of power losses closely match the experimental results. This methodology can be used for other ultra-thin laminated cores for IPT applications.

Nanocrystalline ribbon cores are studied as a possible core material for IPT systems. Higher power densities can be achieved. The eddy-current losses, however, result in lower efficiency. Methods for reducing these losses are discussed in the next Chapter.

Chapter 4

Improved Utilization of Nanocrystalline Ribbon Cores

In Chapter 3, a comparison of nanocrystalline ribbon cores versus ferrite cores was presented. IPT pads with nanocrystalline ribbon cores achieved a slightly superior coupling factor, higher power density but lower efficiency. This is due to the eddy-current losses induced by the magnetic flux perpendicular to the ribbon. A reduction of the eddy-current losses is required to unleash the full potential of nanocrystalline alloys. The IPT pad analyzed and tested in Chapter 3 was originally designed for ferrite cores. Later, the cores were replaced by nanocrystalline ribbon ones of the same dimensions. The design of the pad was therefore optimized only for ferrite. For this material, brittleness, temperature, and availability of geometries are the most important design constraints. For nanocrystalline ribbon cores, however, the constraints are different: anisotropy, manufacturability, and reduction of eddy-current losses. Consequently, a new design method that considers the unique characteristics of this material is necessary.

In this Chapter, the optimum utilization of nanocrystalline ribbon cores is studied. First, the effect of the core dimensions on the power transfer capability, saturation flux density, and core losses is analyzed in general, for any core material. Next, the effect of dimensions of the nanocrystalline ribbon cores on the performance of the system is studied. Guidelines for the optimum sizing of nanocrystalline ribbon cores are presented in the context of a WPT3 (11.1 kW) pad. The pad is evaluated via FEM simulations and experiments and compared against an identical one with ferrite cores. Finally, the Chapter introduces different methods for reducing eddy-current losses. Among them, the shielding of the nanocrystalline ribbon cores with ferromagnetic material is identified as a promising method and it is evaluated via FEM simulations and experimental measurements.

4.1 Double-D Pads: Core Design versus Pad Performance

Regardless of the core material, the dimension of the core bars (thickness t_c, width w_c and length l_c), the number of core bars per core n_c, as well as their location within the pad have an impact on the power transfer capability of the system. In the next section, the optimal sizing and positioning of the core bars are studied for Double-D pads. A similar analysis for circular coils can be found in Appendix B. For this analysis, isotropic and linear magnetic properties are considered without loss of generality. This analysis seeks to identify design trends that ensure optimum core utilization.

4.1.1 Optimum Core Location

In this section, the optimal location of the core bars is studied for coils with different turns N, and different number of cores N_c. For all the cases, the length and thickness of the core

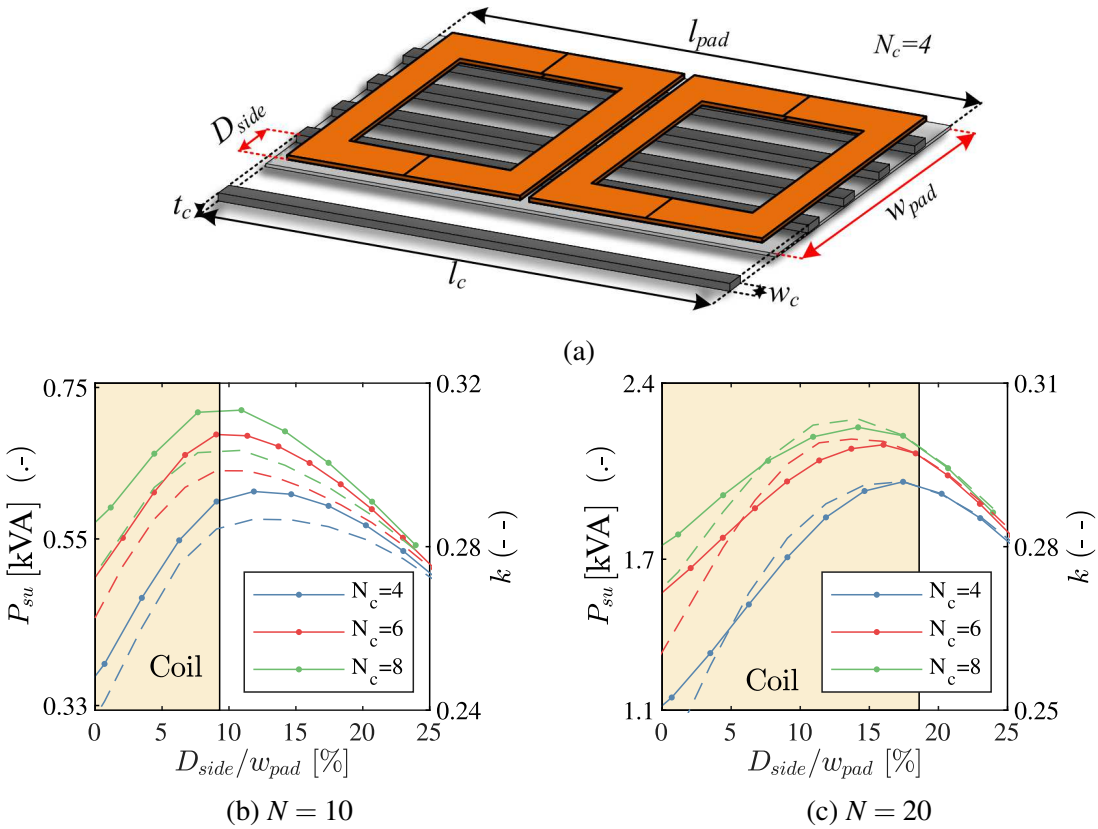

Fig. 4.1 Location of cores with respect to the edge of the pad/coil for different number of cores N_c and number of turns N. For all cases, the area of the core covered by core material is constant at 30%; w_c is adjusted according to the number of cores. Shaded area depicts the coil footprint. l_{pad} =740 mm.w_{pad} = 430 mm.

bars are kept constant. Similarly, the percentage of pad's area covered by core (A_c) is kept at 30%. Thus, the core width w_c is adjusted depending on the number of cores (N_c). Since the core bars are equally spaced and centered in the pad area, the only degree of freedom is the distance D_{side} between the edge of the pad/coil and the first core bar as shown in Fig. 4.1a.

As shown in Fig. 4.1, there is an optimal core location for every (N, N_c) combination. For $N_c = 4$, for instance, the optimal location lies near the edge of the coil. When more cores are used, D_{side} reduces slightly. Increasing D_{side} after the optimum point reduces the core material in the flux pipe and therefore leads to lower P_{su} values. Reducing D_{side} from its maximum, on the other hand, reduces the amount of core material covering the flux pipe. Moreover, it increases the leakage flux but not the linkage flux. This results in lower P_{su} and k values. The optimal position of the coil can be found via FEM simulations for a specific design. However, for an initial design, setting D_{side} as approximately 10% of the coil width yields an adequate performance.

Another interesting finding is that the magnetic performance of the pad increases as the core is segregated in a larger number of bars (N_c). This is due to the reduction of the reluctance in the flux path. Using more cores also results in a more uniform flux density in the air gap which yields higher power transfer.

4.1.2 Optimum Core Dimensions

As shown in Fig.4.2, the power transfer capability of the pad P_{su}, the maximum flux density in the core B_{max}, and the core losses P_{loss} depend on the volume and dimension of the core bars. The core dimensions −core length l_c, width w_c, thickness t_c, number of cores N_c − were varied in order to understand the impact that each of these variables has on the system. The percentage of pad covered by the core material (A_c) is presented as a metric instead of the bar width w_c. The analysis considers the pad tested in Chapter 3. The main findings are listed below:

- P_{su} increases with the volume of the core material. However, for a given core volume, different core dimensions lead to higher or lower P_{su} values, as seen in Fig.4.2a.
- For the same volume of core material, the segmentation of the magnetic core in a higher number of uniformly distributed core bars produces a higher P_{su}. This is due to the more uniform flux patterns. This effect decreases when a large portion of the pad is covered with core material (i.e., higher A_c values).
- There is an optimum core length. As shown in Fig. 4.2a, P_{su} increases with the core length l_c until it reaches a value of $\sim 88\%$ of the pad's length. Longer cores increase

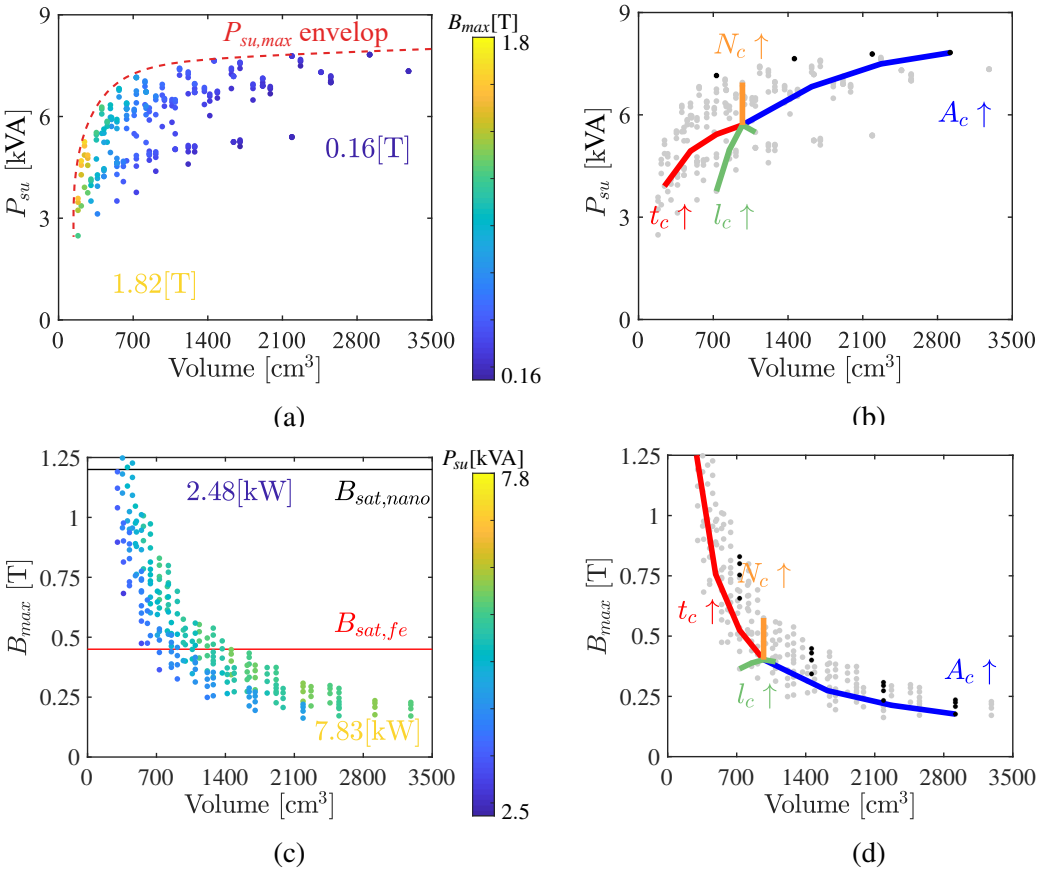

Fig. 4.2 Power transfer capability P_{su} and maximum flux density in the core B_{max} versus volume of core material for different values of l_c, w_c, and N_c. Pad dimensions shown in Fig.3.12. $i_{1,rms} = 23$A. f_0 =85 kHz. The lines results from the change of one specific dimension (l_c, N_c, A_c or t_c) while the others remain fixed.

the leakage flux in the transmitter without increasing the mutual inductance; therefore, decreasing both k and P_{su}.

- P_{su} increases along with A_c and the bar thickness t_c. As A_c increases, however, the influence of t_c reduces. For $A_c \geq 60\%$, the thickness of the bar has an almost negligible impact on P_{su}. Increasing t_c, nonetheless, reduces the flux density within the core; i.e., B_{max}. Consequently, t_c can be selected to prevent saturation in the core as it is done in [9, 15, 10].

- The maximum flux density B_{max} is inversely proportional to the core volume as seen in Fig.4.2c.

From Fig.4.2, guidelines for design can be obtained. An optimal core design should lie on the $P_{su,max}$-envelop shown in Fig.B.2a. The core designs forming the Pareto-front are then

ones that with large cores ($l_c \approx 88\%$ of l_{pad}) and ample area coverage ($A_c > 60\%$). It is worth noting that this envelope does not decrease linearly with the core volume. Contrarily, $P_{su,max}$ is fairly constant and only decays for low volumes of the core material. Thus, to optimize the utilization of core material, the design should be near the knee point of $P_{su,max}$. At the knee point, P_{su} is around 90% of that achieved with a full ferrite plate below the coil. Given that B_{max} is inversely proportional to the core volume, for some designs, the knee point can exceed the saturation point of magnetic material. If ferrite is used in the cores, B_{max} is limited to $0.45T$ at ambient temperature. If nanocrystalline ribbon cores are used, B_{max} can reach up to $1.25T$. Consequently, higher power densities can be achieved with nanocrystalline ribbon cores. However, from Chapter 3, it is known that eddy-current losses are a limiting factor for nanocrystalline ribbon cores. The effect of the core dimensions on the eddy-current losses is analyzed in the next section.

4.1.3 Core Loss versus Core Dimensions for Nanocrystalline Ribbon Cores

The dimensions of the core have an impact on the power transfer capability of the pad but also the hysteresis and eddy-current losses. This is analyzed via FEM simulation. Different values of A_c (percentage of the pad's area covered by core material), core thicknesses t_c, and the number of cores N_c are considered. The coil tested in Chapter 3 is considered for the analysis. Both ferrite and nanocrystalline ribbon cores are compared. The results are shown in Fig.4.3. The most important conclusions are discussed next.

P_{su} is practically identical for both systems using nanocrystalline and ferrite cores. Nanocrystalline ribbon cores result in marginally higher P_{su} values due to their higher permeability. As discussed in the previous section, P_{su} increases along with A_c. The rate of increase is higher when more cores (N_c) are used. Increasing N_c also reduces the eddy-current losses. This can be explained as follows. Even though the number of faces exposed to transversal flux increases linearly with N_c, the magnitude of the transversal flux entering each bar decreases. As a result, the overall eddy-current losses reduces (compare P_{elec} in Fig.4.3.*a* and Fig.4.3.*b*).

Regarding hysteresis losses, nanocrystalline ribbon cores exhibit higher hysteresis losses P_{mag} than ferrite cores despite their lower Steinmetz coefficients. As explained in Chapter 3, this is due to the higher magnetic flux density at the lateral faces of the core bars. However, the hysteresis losses decay as the area coverage (A_c) increases. This is true for both materials and it is due to the reduction of the flux density in the core. A similar reduction of flux density and associated losses can be achieved by using thicker cores. However, the thickness of the core increases the eddy-current losses as discussed next.

Although almost negligible for ferrite cores, eddy-current losses are considerably high for the nanocrystalline ribbon cores. To reduce these losses, the flux entering the lateral faces

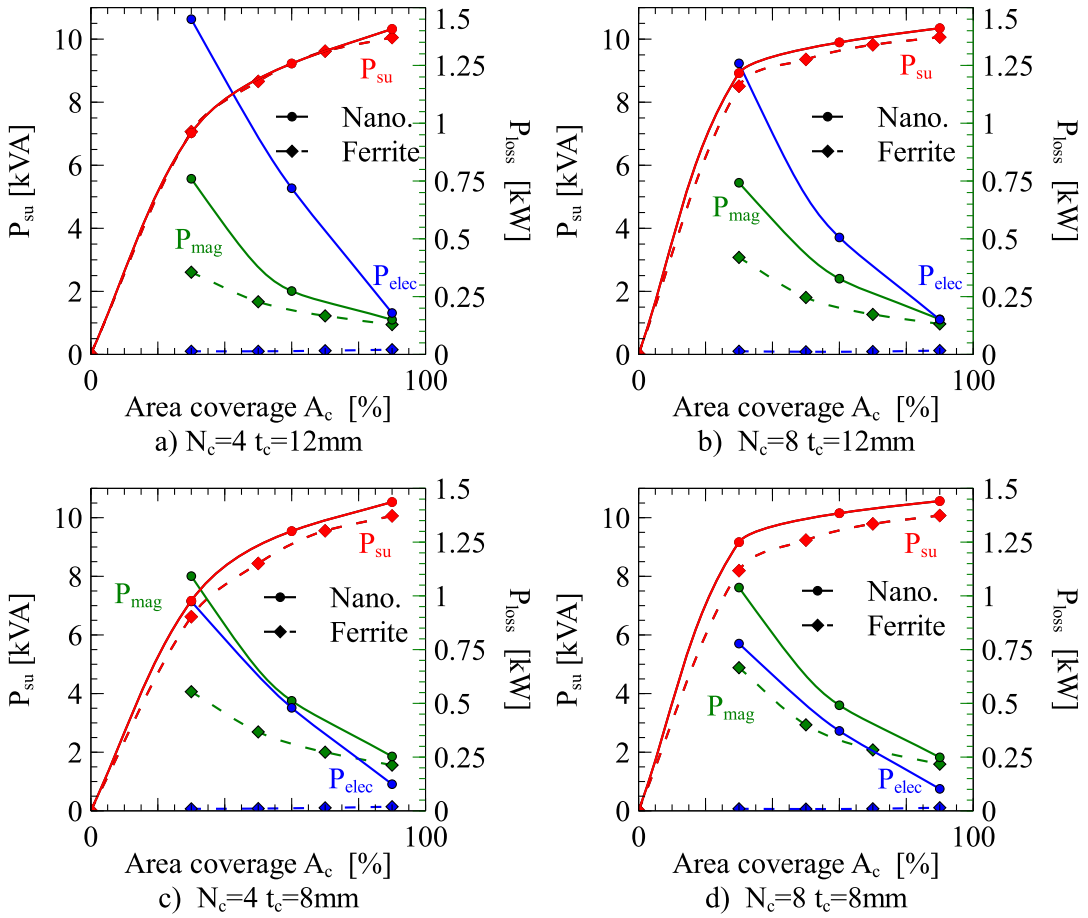

Fig. 4.3 Magnetic performance and core loss in nanocrystalline ribbon cores for different core dimensions. Self-inductance L_1, mutual inductance M, eddy-current losses P_{elec} and hysteresis losses P_{mag} for a Double-D pad with different percentages of surface area covered by core material (Area coverage: A_c), different coil thicknesses t_c, and number of cores N_c.

of the bars must be reduced. As shown in Fig.4.3, this can be achieved by increasing N_c or A_c. Thus, for nanocrystalline ribbon cores, higher values of A_c are required to mitigate eddy-current losses. The increment of the core material required by larger area coverage can be compensated with a reduction of core thickness. Thinner cores also result in lower losses (compare P_{elec} in Fig.4.3.*a* and Fig.4.3.*c*) since the area exposed to transversal flux is proportional to the thickness of the core.

4.1.4 Summary of Design Guidelines for nanocrystalline ribbon cores

From the analysis of the flux density distribution in the core and the effect of core dimensions on the pad performance (power transfer and core losses), it is possible to determine design guidelines to be used for IPT systems with nanocrystalline ribbon cores.

The core length has the largest impact on the power transfer capability of the pad. Core lengths between 80% and 88% of the pad's length are recommended. To reduce eddy-current losses, the core ought to cover a large portion of the pad's area. Larger areas yield lower power losses. In fact, full plates are a recommended option. To limit the core volume while using large core areas, the core thickness can be reduced accordingly. The thickness of the core (t_c in Fig.4.1a) can be as small as possible but sufficiently large to avoid magnetic saturation. The thickness of the core bar (t_c) is determined by the width of the nanocrystalline ribbon. Manufacturability constraints the minimum attainable width. Commonly, the minimum width of the ribbon commercially available is three to four millimeters [79] [34], [33]. Thus, nanocrystalline ribbon cores are best suitable for high-power IPT systems as low power systems would require slimmer cores. Finally, the first and last core bars ought to be placed near the inner border of the winding. As a rule-of-thumb, the distance D_{side} between the coil and core should be around 10% of the coil width. The optimum point can be estimated for every specific case via FEM simulations.

4.2 Optimum Design of a WPT3/Z1 Pad

The design guidelines discussed in the previous section are applied here in the design of a WPT3/Z1 (11.1 kW/100 mm air gap) IPT system. The design methodology of a series compensated IPT system presented in [12, 10] is used in this section.

4.2.1 Coil Design

The design process starts by selecting the DC-link voltages in the primary and secondary sides: $u_{DC,1}$ and $u_{DC,2}$. A voltage of 650 V is selected for both DC-links. Next, the mutual inductance required to transfer a given power P_2 of 11.1 kW is calculated. The power transfer equation for a series compensated IPT system is shown in (4.1):

$$P_2 = \frac{4 \cdot u_{DC,1} u_{DC,2}}{\pi^3 \cdot f_0 \cdot M_{12}} \tag{4.1}$$

Thus, the value of M required to transmit 11.1 kW is $\approx 57\mu$H. Next, the coil dimensions and the number of turns N need to be selected. For this purpose, FEM simulations are performed to obtain the design space considering full coverage of the core plate underneath the coil. From the analysis presented in Section 4.1.2, core designs near the knee of the Pareto-front $P_{su,max}$ result in values of mutual inductance of approximately 90% of the ones obtained with full core coverage. Assuming that L_2 and M change in the same proportion in response to changes in the ferrite core, we can say that M at the knee of the Pareto front decreases to

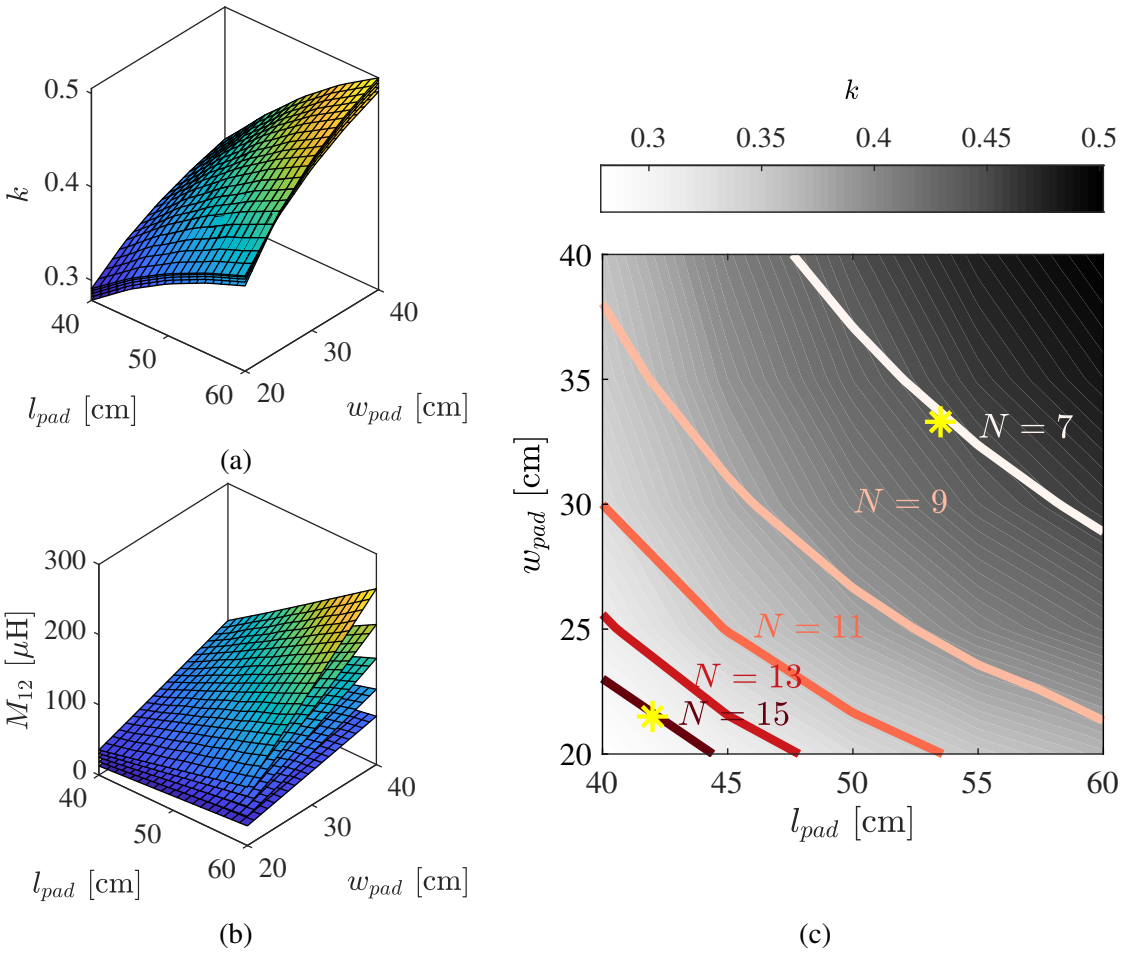

Fig. 4.4 Design space for the WPT3/Z1 system of >11 kW for different pad's lengths l_{pad}, widths w_{pad}, and number of turns N. *a*) Coupling factor k *b*) mutual inductance M. The contour lines in *c*) define the pad size required to obtain the target mutual inductance of 64 μH. $*$: Selected designs.

approximately 90% of its value with full core coverage. Thus, when sizing the pad, FEM simulation with full core coverage can be used as long as a value of M of 64 μH is considered as opposed to 57 μH.

Fig.4.4a and 4.4b show the coupling factor k and mutual inductance M respectively, for different pad dimensions and number of turns. The coupling factor increases with the area of the pad and it is practically unaffected by the number of turns. On the other hand, M is directly proportional to both the pad area and the number of turns N. For every value of N, one can determine different pad dimensions that result in the required value of M. These are depicted as contour-lines in Fig.4.4c. Every design on the line would result in the same value of M and P_2. At first, two pads with different power densities are considered: 1) a 53 cm×34 cm pad

with $N = 7$; and 2) 42 cm$\times$21 cm pad with $N = 15$. These two pads are considered during the design of the core shown in the next section.

4.2.2 Core Design

Fig.4.5$a) - d)$ show the core's design space for the two pads selected in the previous section. The design space considers different core dimensions: length l_c, width w_c, thickness t_c and number of cores N_c. The smaller pad requires less core material. However, the flux density in the core will be higher as compared to the larger pad. Consequently, the saturation point of the material becomes a limiting factor in the design of smaller pads with minimum core material. This can be more easily seen in Fig.4.5$c)$ and Fig.4.5 $f)$ where the blue (x) and red (•) markers represent the designs achievable with nanocrystalline and ferrite cores, respectively. Designs with nanocrystalline bars require less core material and can achieve higher power densities. This is particularly important for smaller pads as designs near the knee point of $P_{su,max}$-envelope are not possible with ferrite cores. Thus, the smaller pad is used in this dissertation to exploit the advantages of the nanocrystalline material. Selecting a smaller footprint has a detrimental impact on the ferrite design as it makes it operate outside its acceptable specification. Giving that the pad was optimized for nanocrystalline cores, the performance of an identical system that uses ferrite cores will be inevitably sub-optimal. This will be shown later on during the experimental comparison.

From the possible designs at the knee point of Fig.4.5$e)$, one design is selected following the guidelines of core design presented in Section 4.1.4. The final core design has the following properties: A_c =60 % (which corresponds to a total core width of 150mm), l_c =342 mm ($\sim$ 82% of the pad length), and t_c =4 mm. The thickness of 4 mm was deliberately selected as this is the minimum ribbon width commercially available. Lower widths are currently restricted by the manufacturing process. The core can be one single-plate or divided into N_c bars. This is analyzed next.

Solid core plate vs core bars

Superior core-utilization factors can be achieved when the core material covers a large portion of the pad area. The same area coverage, however, can be achieved with a single-core plate or by using more core bars with different spacing between them. Fig.4.6 illustrates the effect that core segmentation has on the power transfer capability of the pad P_{su} and the core losses when using nanocrystalline ribbon cores.

In Fig.4.6.a, the total core width is constant while the spacing between the cores is increased. This results in a reduction in the volume of the core material. Four bars are consid-

ered for this analysis. As the spacing increases, P_{su} decreases rapidly while the hysteresis P_{mag}

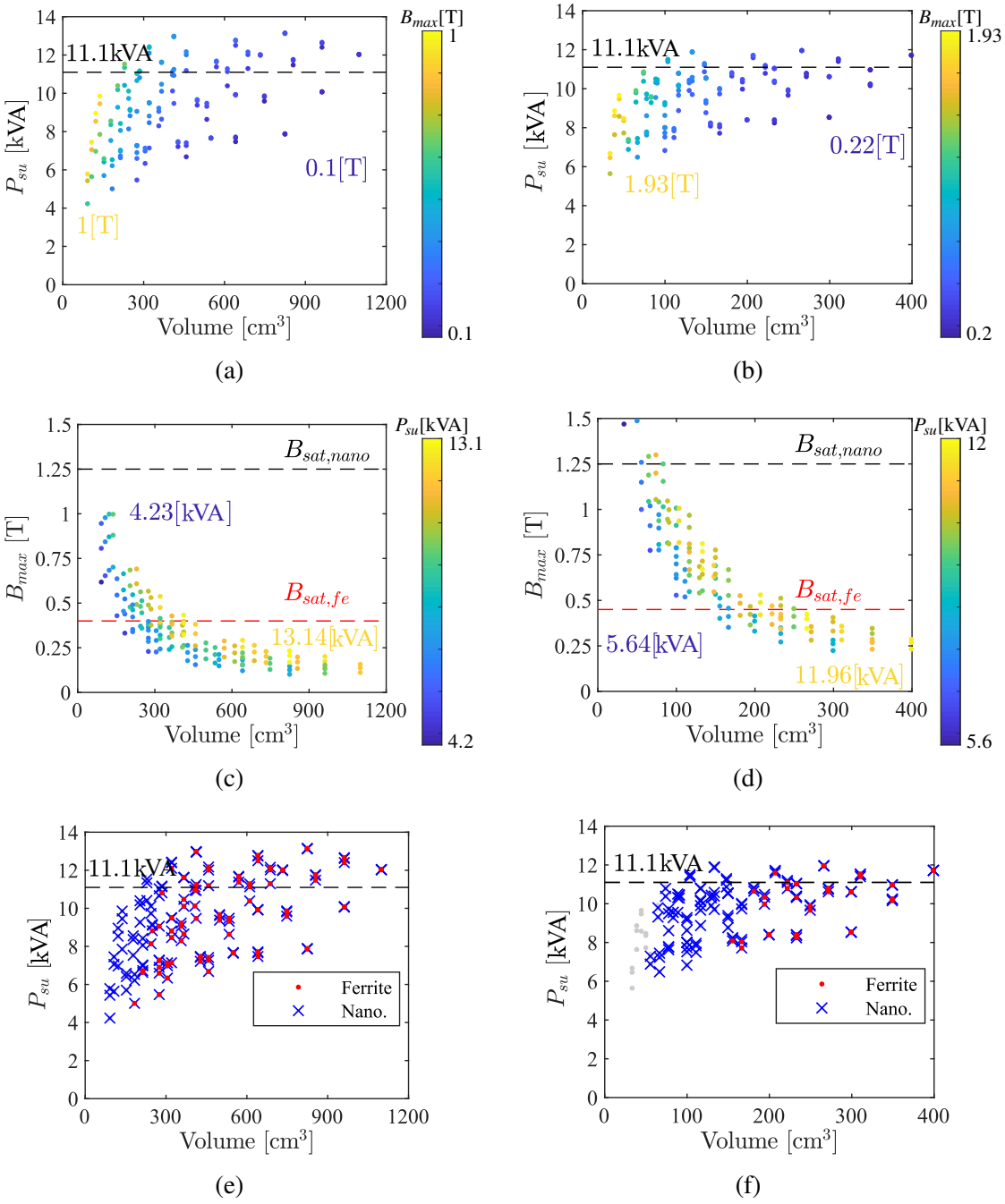

Fig. 4.5 Power transfer capability P_{su} and maximum flux density B_{max} within the core for different core dimensions. *a*), *c*) and *e*) correspond to a 53 cm $\times$34 cm pad with $N = 7$. *b*), *d*), and *f*) correspond to a 42 cm$\times$21 cm pad with $N = 15$. In *e*) and *f*), (x) and (•) indicate the designs that are achievable with nanocrystalline and ferrite cores respectively. P_{su} is calculated considering an excitation current of $i = 30\text{A}_{rms}$.

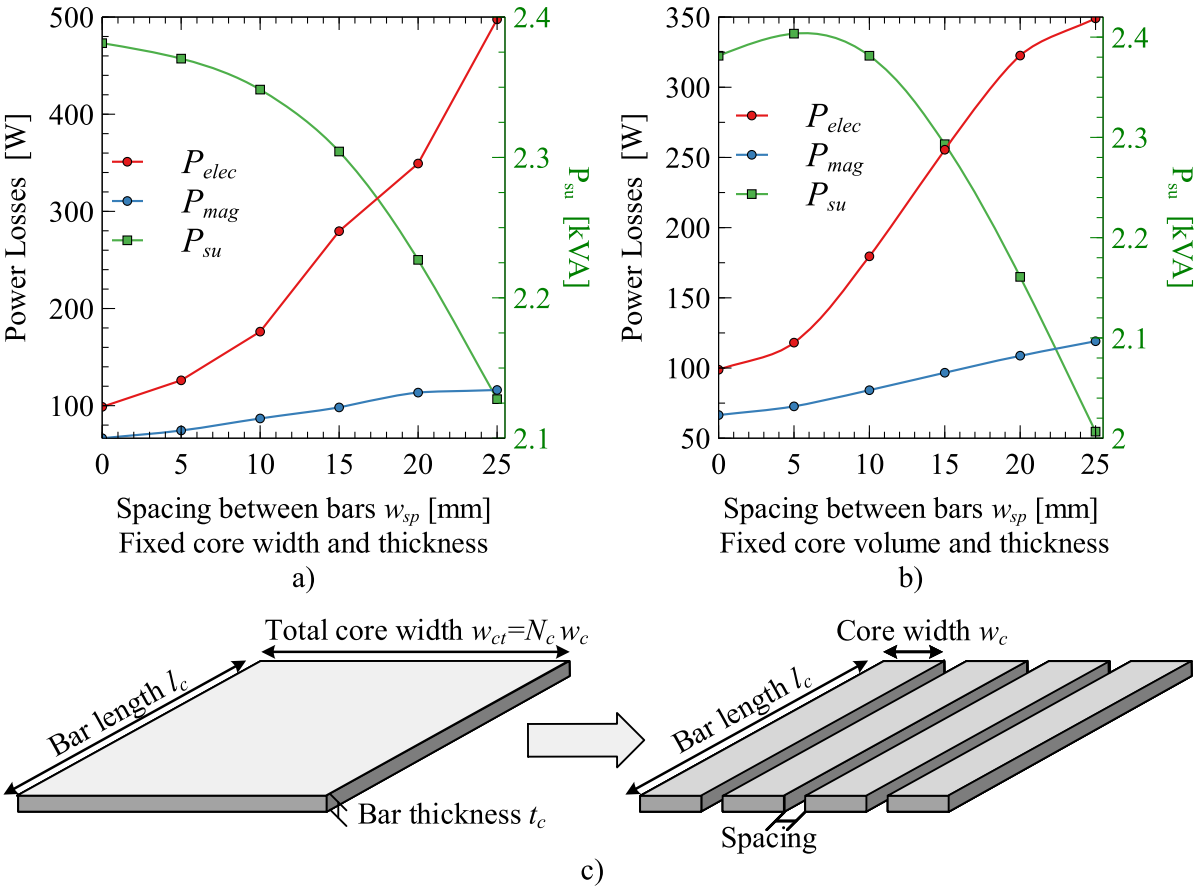

Fig. 4.6 Simulation results showing the effect of the spacing between core bars on the power transfer capability of the pad P_{su}, eddy-current losses P_{elec}, and hysteresis losses P_{mag}. In a) the total core width is constant while in b) the core volume is constant. c) Illustration of the core segregation. Excitation current $i_{1,pk} = 21$ A.

and eddy current P_{elec} losses increase. Eddy-current losses increase drastically from 98 W for an entire ferrite plate to 497 W when the bars are 25 mm apart from each other.

In Fig.4.6.*b*, the volume of the core material is kept constant while the distance between the bars is increased. At a spacing of 5 mm, the power transfer capability of the pad P_{su} reaches a maximum, increasing 1% compared to that at zero spacing. However, at this point, the eddy-current losses are already 18% higher than those of a solid plate (zero spacing). Eddy-current losses increase continuously with the spacing. At the same time, the power transfer capability of the pad P_{su} reduces as less core material is present in the flux pipe region of the DD pad.

In both analysis, Fig.4.6.*a* and Fig.4.6.*b*, the hysteresis losses increase with the distance between bars. This increment results from the higher flux density at the lateral faces of the core bars. Another effect of the separation of the core bars is that more flux leaks to the shield. This deteriorates the performance of the pad even further. For these reasons, solid plates are

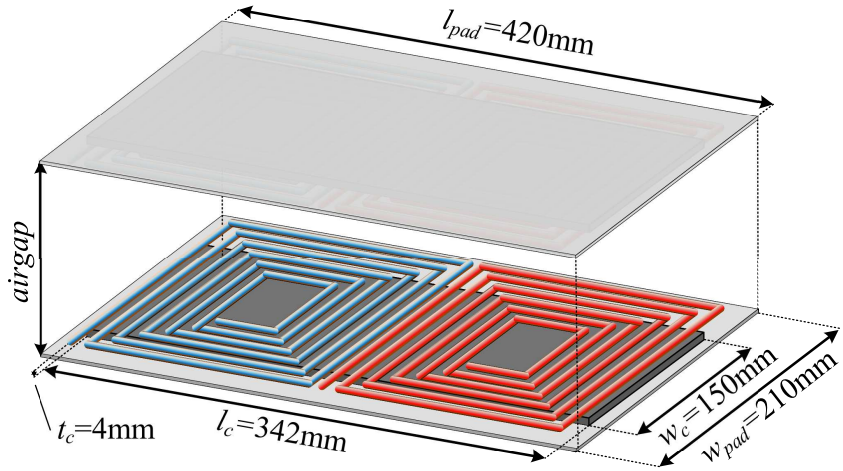

Fig. 4.7 Dimensions of the final design of the WPT3/Z1 IPT system.

preferred for nanocrystalline ribbon cores used in IPT systems. For ferrite cores, simulation results also showed that solid plates can improve the performance of the system as compared to segregated bars. However, the increment in power loss caused by the segregation is less important than for the nanocrystalline ribbon counterpart.

Final Pad design

The final dimensions of the pad and the core are shown in Fig.4.7. The coil is made of 15-turns of Litz wire.

4.2.3 Flux Distribution and Power Losses

Flux Distribution: Fig4.8 shows the distribution of the flux density B in the core for the pad designed in the previous section. Both ferrite and nanocrystalline ribbon cores are considered. Given that ferrite is an isotropic material, the flux distribution is uniform in the y-axis. The flux density is limited to the saturation value of 0.45 T [27]. The anisotropic behavior of the nanocrystalline ribbon core results in a more convoluted distribution. The edge of the core in the y-axis are zones of higher flux density due to the perpendicular flux entering the lateral wall of the core [27]. The other two areas of higher flux density are found in the flux-pipe region (center of the core) and are due to both the anisotropic permeability of the core and the geometry of the winding.

Power Losses: Fig.4.8c shows a break-down of the core losses for a 6.6kW power transfer, for both nanocrystalline ribbon and ferrite cores. The hysteresis losses in the nanocrystalline

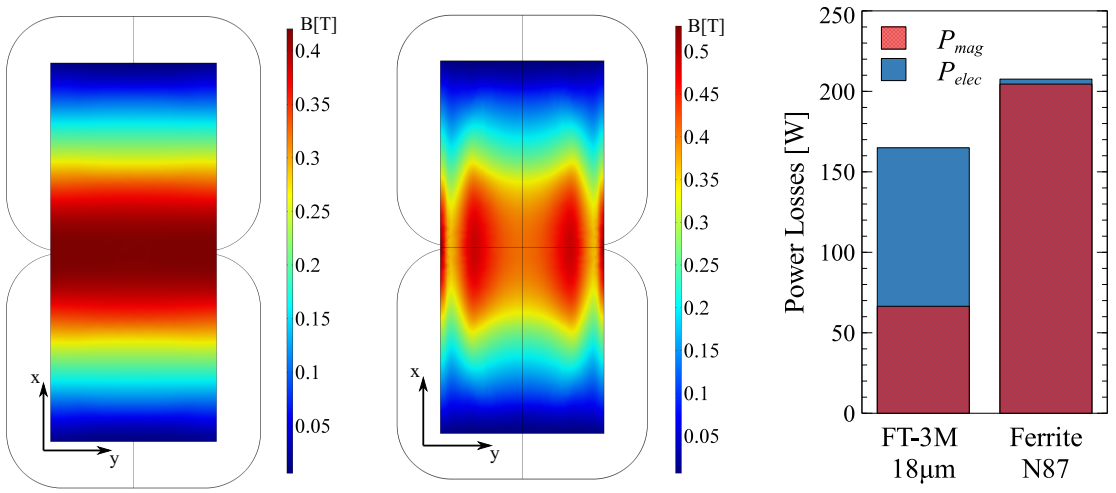

(a) N87 (b) Nanocrystalline (c)

Fig. 4.8 Flux distribution and power losses in the system when using ferrite and nanocrystalline ribbon cores, respectively. Flux density distribution within the core when using *a*) ferrite N87 and *b*) finemet's FT-3M cores. Air gap: 10 cm. I_{pk} =40 A. *c*) Estimation of core losses at 6.6 kW.

ribbon cores are much lower than those obtained with ferrite cores due to the lower Steinmetz coefficients. The eddy-current losses are higher in the nanocrystalline ribbon cores but they are compensated by the lower hysteresis losses. As a result, nanocrystalline ribbon cores have about 21% lower core losses as compared to the classic ferrite cores for the same power transfer. This ensures a higher power transfer efficiency and relaxes the cooling system's requirements.

4.3 Experimental Validation

Two identical DD coils were built for the transmitter and receiver pads as shown in Fig.4.9a. The pad's dimensions are shown in Fig.4.7. The coil comprises 15 turns of Litz wire, made of 850 0.1 mm-diameter strands, giving a total cross-sectional area of 6.5 mm^2. For the core material, nanocrystalline ribbon cores and ferrite cores are considered. In the case of ferrite, two structures are used. The first one considers a core made of an array of 54 pieces of 38.1 mm×25.4 mm×4 mm ferrite N87, as shown in Fig.4.9b. The second configuration uses only 11 tiles as shown in Fig.4.9c. Three pieces of 150 mm×100 mm×4 mm DMR44 fill most of the core surface area. Additionally, 8 pieces of 38.1 mm×25.4 mm×4 mm DMR44 are located at the edges of the core to fill the desired surface area.

(a) (b) (c) (d)

Fig. 4.9 Photography of the pad and the cores used for the experimental validation. *a*) Constructed pad (the dimension of the pad are shown in Fig.4.7). *b*) N87 ferrite core (54 tiles). *c*) DMR44 ferrite core (11 tiles). *d*) Finemet's FT-3M nanocrystalline ribbon core.

The nanocrystalline ribbon core, on the other hand, comprises 6 nanocrystalline ribbon bars, each of 342 mm×25.4 mm×4 mm as seen in Fig.4.9d. Hitachi's FT-3M nanocrystalline 18 μm ribbon is used. The ribbons are coated with insulation material and bonded using an organic resin. The overall core has a stacking factor of approximately 0.77.

The same power electronics, measurement equipment, and test-rig used in Chapter 3 are also used for these pads. Series compensation circuits are used on both transmitter and receiver sides. The capacitors used for the resonant tank correspond to the series KEMET PHE450 with a voltage rating of 3kV-DC. These capacitors have a dissipation factor of approximately 0.15% at 100kHz. Several capacitors are combined in series and/or parallel to achieve the required capacitance and voltage rating. The electromagnetic properties of the cores are discussed next.

4.3.1 Nanocrystalline Ribbon vs. Ferrite: Material Structure and Properties

The fabrication method of nanocrystalline ribbon cores was presented in Chapter 3. A summary of the process is depicted in Fig.4.10a. After the annealing process, the ribbons are wound into the required geometry. The ribbons are covered with a resin material and wound around molds which can be toroidal or U-shaped. The winding process continues until the core achieves the required thickness. The final result is a core race track like the one shown in Fig.4.10b. The core is then cured, to ensure the adhesion of the ribbons, and then segmented.

For inductors, the core race track is split into two C-shaped cores. For the bespoke cores designed in this dissertation, on the other hand, the core is divided into two U and two I cores, as seen in Fig.4.10c.

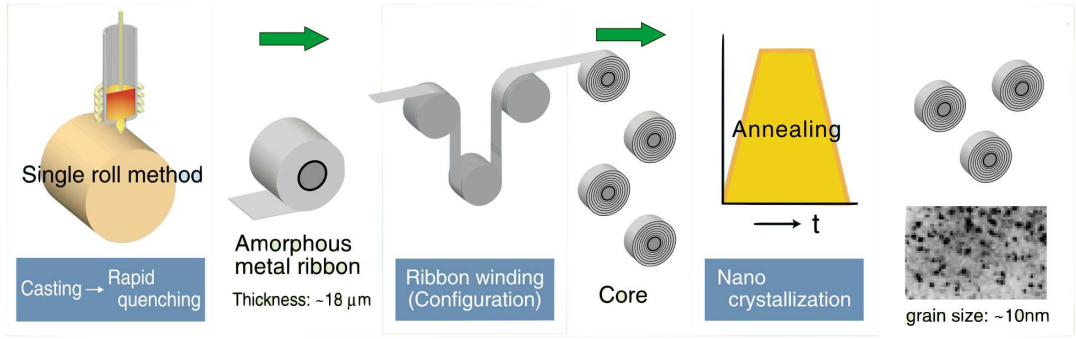

(a)

(b)

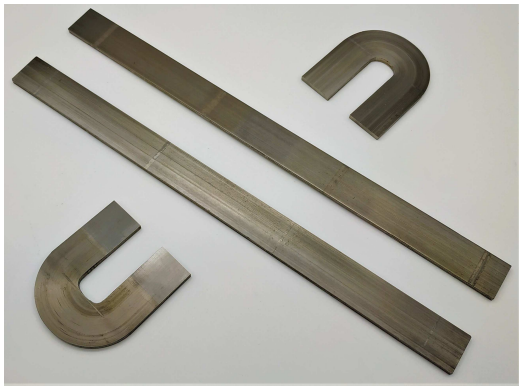

(c)

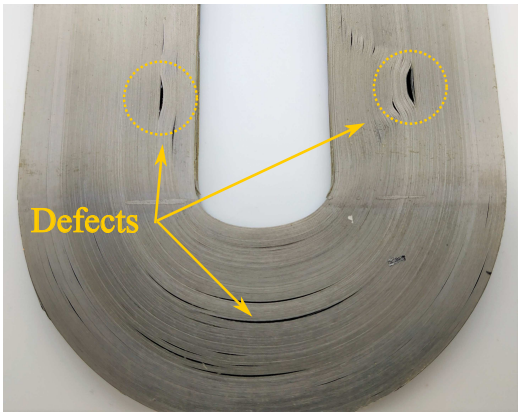

(d)

(e)

Fig. 4.10 Fabrication process of the nanocrystalline ribbon cores. *a*) Manufacturing process of the laminated nanocrystalline alloy. *b*) Core race track after impregnation, cure and before cutting. *c*) Cut cores. *d*) Defects found in discarded bars. *e*) Location of the fixtures used during annealing and curing.

During the winding, curing, and tooling processes, mechanical defects can be introduced to the bars. During winding, large air gaps between laminations −like the ones shown in Fig.4.10d− can be formed. These defects are particularly problematic as they can lead to localized heating. Also, during curing, the mechanical fixtures used to hold the core in place can damage the core surface as shown in Fig.4.10e. Moreover, during tooling, cutting in particular, the ribbons can be damaged, bent, or short-circuited. Usually, etching treatments are necessary after cutting to ensure the ribbons are electrically isolated from each other to prevent eddy currents.

Microscopic defects can also be introduced during fabrication, depending on the quality of the manufacturing process. This is clear when comparing the nanocrystalline alloy core bars of two different manufacturers. Fig.4.11 shows microscope images of the cores manufacture by Hitachi Metals (*.a*-*.c*) and AT&M (*.d*-*.f*). Fig.4.11*.a* and Fig.4.11*.d* correspond to TOP views of the cores. Hitachi's bars depict in a better way the separation between ribbons as compared to the ones from AT&M. The same conclusion can be drawn when comparing the sides of the

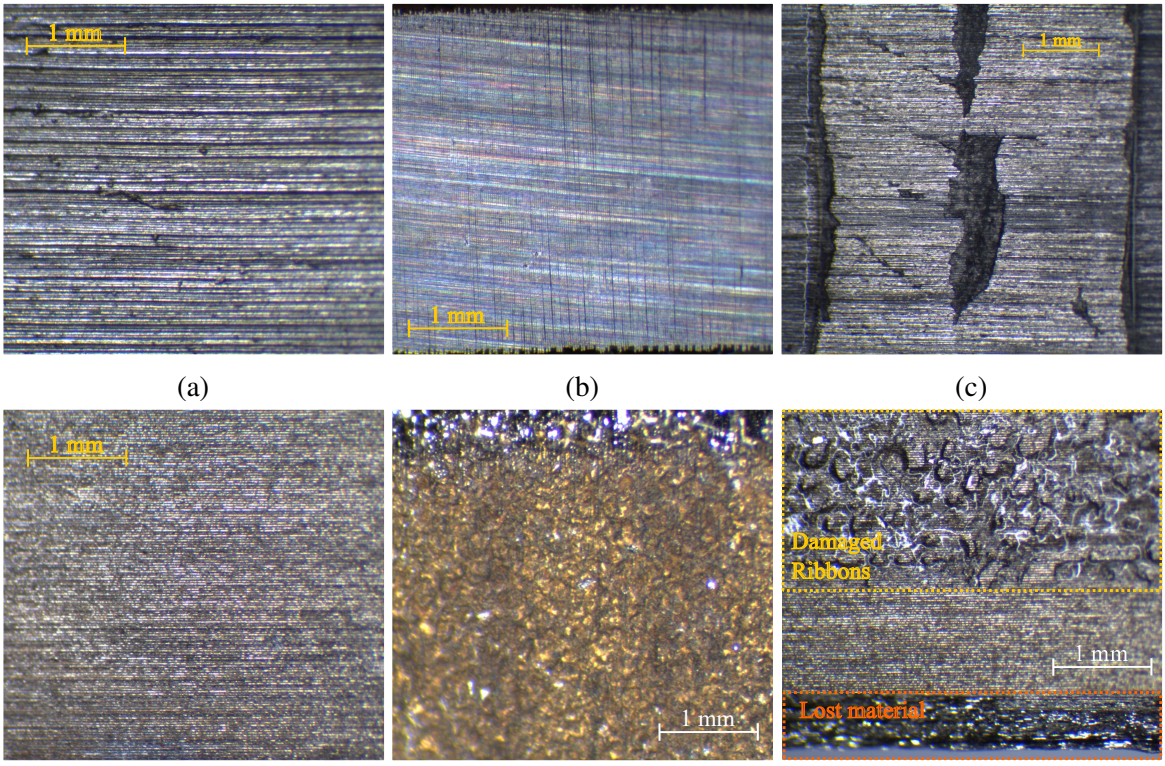

Fig. 4.11 Images of the nanocrystalline ribbon cores taken with a microscope AMPScope MA500. Nanocrystalline ribbon cores from $a)-c)$ Hitachi Metals and $d)-f)$ AT&M. $a)-d)$ Top view. $b)-e)$ Side view (edge). $c)-f)$ Manufacture defects in the bar.

Table 4.1 Electromagnetic properties of Finemet's FT-3M, Ferrite N87, and DMR44.

Parameter at 85 kHz	**Nanocrystalline Finemet**	**Ferrite N87**	**Ferrite DMR44**
Density w/o resin	$7300\,\mathrm{kg/m^3}$	$4850\,\mathrm{kg/m^3}$	$4800\,\mathrm{kg/m^3}$
Density with resin	$5717\,\mathrm{kg/m^3}$	NA	NA
Filling/Stacking Factor F	0.77	1	1
Ribbon thickness t	$18\,\mu\mathrm{m}$	NA	NA
Ribbon width	4 mm	NA	NA
Resistivity $1/\sigma$	$1.2\,\mu\Omega\mathrm{m}$	$10\,\Omega\mathrm{m}$	$2\,\Omega\mathrm{m}$
Relative Permeability (Bulk)	23 000	2300	2400
$\sigma_{eq,z} = \sigma_{eq,x}$	$6.42 \times 10^5\,\mathrm{S/m}$	$0.1\,\mathrm{S/m}$	$0.5\,\mathrm{S/m}$
$\sigma_{eq,y}$	$22\,\mathrm{S/m}$	$0.1\,\mathrm{S/m}$	$0.5\,\mathrm{S/m}$
$\mu_{eq,z} = \mu_{eq,x}$	17652	2300	2400
$\mu_{eq,y}$	4.34	2300	2400
C'_m in (3.6)	4.45×10^6	2.54×10^7	1.51×10^7
β in (3.6)	1.87	2.3	2.06

core bars shown in Fig.4.11.*d* and Fig.4.11.*e*. When measuring the resistance across the bar (y-axis), Hitachi's cores yield higher resistances ($129\,\Omega$) compared to the AT&M cores ($2.75\,\Omega$). This suggests that the insulation between ribbons is not as effective in the latter. This effect is detrimental to the efficiency of the system. Other macroscopic and microscopic defects were found in the bars. In Hitachi's bars, surface damages were observed particularly in places where the fixtures were used to hold the bar during annealing and curing. This is shown in Fig.4.11.*c*. Surface damages were also found in AT&M's bars, as seen in Fig.4.11.*f*. At the edges of these bars, the ribbons were flaking causing a loss of material. Hitachi's bars do not present any signs of flaking which suggests that the manufacturing process is of a higher quality.

Twenty-four bars (12 core race tracks) were manufactured by Hitachi following the same fabrication process. The equivalent relative permeability of the cores along the ribbon was measured to be 17652 ± 2000. The standard deviation is not negligible, about 11% of the mean value. This is attributed to manufacturing tolerances such as temperature differences during annealing, different resin thicknesses, differences in the stacking factors, etc. It is worth noting that manufacturing tolerances are larger for bespoke designs like this one as compared to standard products. Therefore, lower tolerances are expected in mass production.

The electromagnetic properties of this nanocrystalline ribbon material are listed in Table 4.1. The equivalent conductivity and permeability – obtained following the methodology described in Chapter 3 – are also listed along with the Steinmetz coefficients for core loss estimation. These properties are used for FEM modeling. The mesh of the FEM model near

the lateral faces of the cores is restricted to 0.4mm. Coarser meshes are defined elsewhere. Within the core, the maximum element size is set to 5 mm to ensure adequate accuracy.

4.3.2 Nanocrystalline Ribbon vs. Ferrite: Self/Mutual Inductance and Coupling Factor

The self and mutual inductance of pads constructed with nanocrystalline and ferrite cores were measured at 85 kHz using a dedicated piece of equipment: N4L PSM3750. The results are shown in Fig.4.12 for different alignments between transmitter and receiver pads. For the pad with nanocrystalline ribbon cores, the measurement of the inductance matches the FEM simulations with a difference of less than 3%. Nanocrystalline ribbon cores yield higher inductance values (compared to ferrite) due to the higher relative permeability of the bulk material.

For the N87-ferrite cores, the difference between the simulated and measured inductances is higher, approximately 6.5%. This is because the simulation considered the core as a single-piece whereas, in practice, the core is constituted of discrete tiles as shown in Fig.4.9b and Fig.4.9c. Despite being closely packed, there are diminutive air gaps between tiles. These air gaps reduce the magnetic performance of the pad. Fig.4.12 includes simulation results including air gaps of 50μm between the tiles. The measurement results lie between the simulation result with and without air gaps for both ferrite materials: N87 and DMR44.

Table 4.2 shows the inductance and other metrics for the pads without misalignment and with a clearance of 100 mm between pads. Compared with the ferrite core made with 54 tiles, the self-inductance of the pad that uses nanocrystalline ribbon cores is approximately 10% higher. Similarly, the mutual inductance is 23% higher which results in an 11.1% improvement in the coupling factor. This not only improves the power transfer capability of the pad but also its efficiency. The quality factor is higher for the pad with ferrite cores. However, it is important to notice that this factor is measured at very low power due to the limits of the measuring device. The quality factor decreases at higher power as the core losses become

Table 4.2 Inductance measurement for different core configurations and materials

Parameter	Ferrite N87 (54 tiles)	Ferrite DMR44 (11 tiles)	Finemet's FT-3M	Unit
L_1	159.5	165	175.8	μH
L_2	153.2	162.8	170.6	μH
M	46.35	50.53	57.15	μH
k	0.297	0.308	0.33	
$Q = \sqrt{Q_1 Q_2}$	340	435	286	
P_{su}	1.65	1.85	2.25	kVA

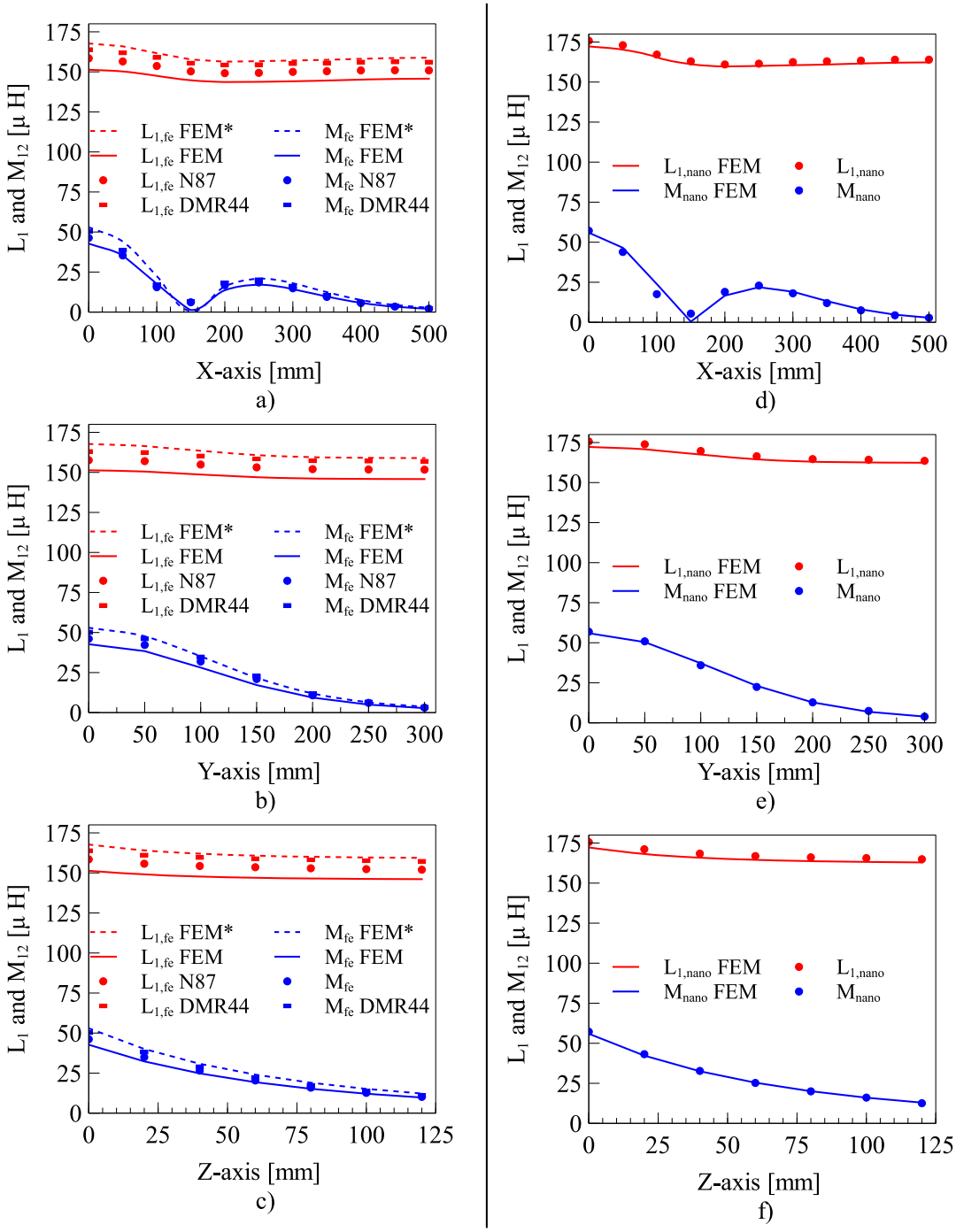

Fig. 4.12 Measurement of self $L_1 \approx L_2 = L$ and mutual M inductances of the designed DD pad with nanocrystalline and N87/DMR44 cores at different clearances (air gaps) between transmitter and received pads. For the ferrite cores, two simulation results are shown. One considering a core made up of N87-ferrite tiles with 0.05mm separation between them and another considering a complete N87-ferrite plate and marked with (*).

more important [65]. The measurement of the quality factor at rated conditions is intricate and it is a current topic of research. To compare pad designs with different cores, efficiency is a better metric. This is discussed further in the next section. The magnetic performance of the pad constructed with 11 ferrite tiles is superior to that of the one obtained with the core made of 54 tiles. This is due to the smaller air gap introduced in the magnetic circuit. However, the pad using nanocrystalline ribbon cores has still a 6.5% higher self-inductance and 13% higher mutual inductance. This results in a 7% improvement in the coupling factor and 22.1% improvement in the power transfer capability of the pad.

Better performances of the ferrite cores could be obtained with a core made of a single piece of ferrite. However, solid ferrite cores of large dimensions are not commercially available and hence must be custom-made. It is worth noting that even in bespoke designs, the small thickness of the core makes the construction of large segments unpractical since they will be very fragile. Moreover, according to [21], the production of ferrite cores of large dimensions entails temperature gradients across the body which result in high stress and ultimately in product cracking. The DMR44 ferrite cores shown in Fig.4.9c were manufactured exclusively for this dissertation; however, their size was restricted to 150 mm due to the aforementioned reasons. On the other hand, the length of nanocrystalline ribbon core bars is less restricted; they can be built as considerably long pieces. Since no air gaps are introduced in the core, superior magnetic performance can be achieved.

4.3.3 Nanocrystalline Ribbon vs. Ferrite: Power Transfer and Efficiency

The efficiency and the power transfer capability of the pads with ferrite and nanocrystalline ribbon cores were evaluated using the power analyzer Yokogawa WT5000. For this, the transmitter and receiver pads were placed at the distance of 100 mm. They were both connected to the same DC-link, in recirculating power mode. Since the transmitter and receiver pads are practically identical, this operating mode allows the system to function at the optimum load matching factor which ensures maximum efficiency (see Chapter 2). Under these conditions, the power transfer is given by (4.2):

$$P_2 = \frac{8U_{DC}^2}{\pi^2}\frac{1}{\omega M_{12}} \tag{4.2}$$

The power transfer increases quadratically with the DC-link voltage as shown in Fig.4.13.*a*. The power transfer is inversely proportional to the mutual inductance. Thus, more power is transmitted with the pad with ferrite cores for the same DC-link voltage. Nevertheless, more power is transferred with the nanocrystalline ribbon cores for the same excitation current.

The efficiency of the system (η_{DC-DC}) is shown in Fig.4.13.*b*. The efficiency was measured at different DC-link voltages and 25 °C. The overall system's efficiency of the IPT system with N87-ferrite cores converges to 93.5% as the power transfer increases. A slightly higher efficiency, 93.9%, is obtained for the pad with DMR44 cores. For the pad with nanocrystalline ribbon cores, an efficiency of 95.5% is achieved. The superior efficiency is attributed to the higher coupling factor (due to fewer air gaps in the core plate) and the lower hysteresis losses of the material.

The efficiency of the pad without considering converter losses is shown in Fig.4.13.*c*. The efficiency remains more or less constant at approximately 96.26% for the pad with nanocrystalline ribbon cores. The efficiency of the pad with N87-ferrite cores, however, starts at approximately 95.5% at low power and decreases for higher power ratings. At rated power, 11.1 kW,

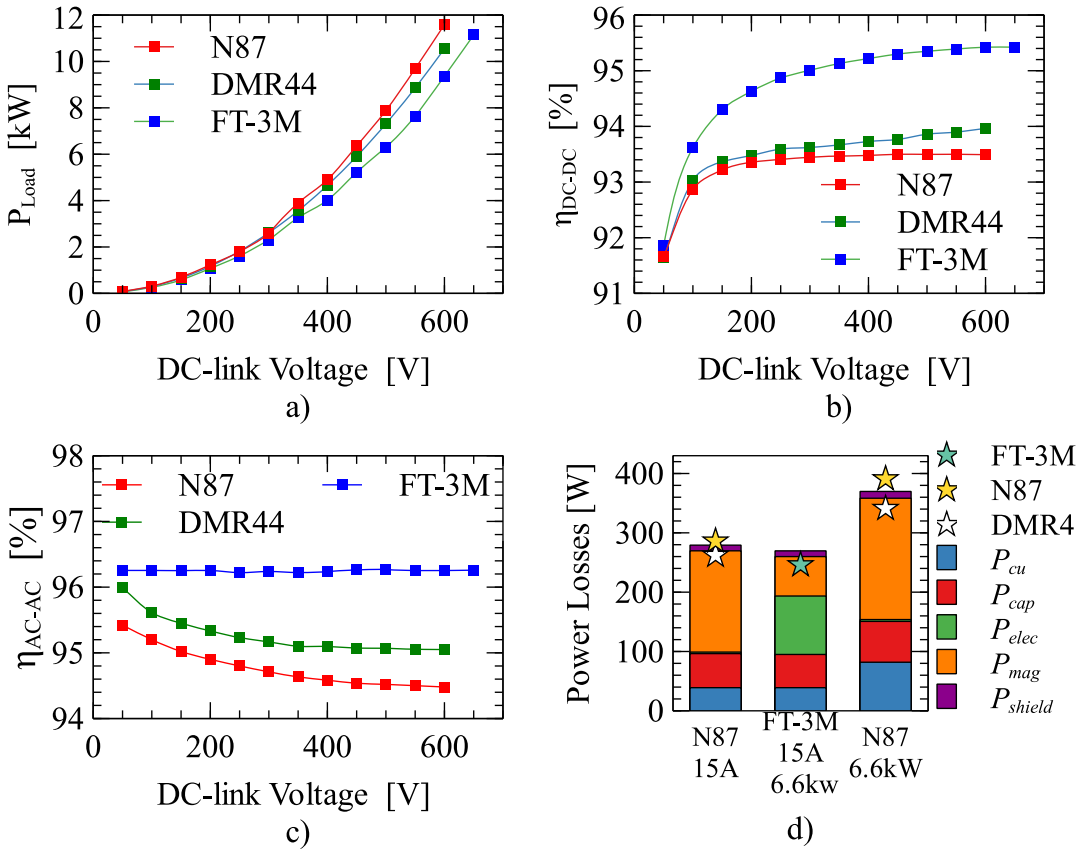

Fig. 4.13 Measured power loss, efficiency, and loss-breakdown for the Double-D pad with N87 cores and nanocrystalline ribbon cores. *a*) Output power to the load. *b*) Overall efficiency of the system η_{DC-DC}. *c*) Efficiency of the pad without considering the power converters. *d*) Breakdown of losses in the pad. P_{cu} : Copper losses, P_{cap} : Capacitor losses, P_{elec} : Eddy-current losses, P_{mag} : Hysteresis losses, P_{shield} : Losses in the shield. Experimental results are shown with ($\star$).

it is about 94.5%. This reduction in efficiency is due to the hysteresis losses in the ferrite material which increases exponentially with the flux density. As a result, the quality factor of the coil also worsens at high power-transfer levels. This behavior matches the analysis of the quality factor at high power presented in [42]. Similar behavior is observed for the pad with DMR44-ferrite cores. However, for this pad, the efficiency converges to 95% at 11.1 kW. This efficiency is superior to the one obtained with the N87-ferrite cores but still 1.26% lower than that obtained with the nanocrystalline ribbon cores. The slight efficiency improvement, compared to the N87, is attributed to the higher coupling factor and slightly lower hysteresis losses.

In Chapter 3, a pad with four nanocrystalline ribbon core bars was evaluated. Its efficiency (88%) was lower than the one achieved with identical ferrite cores (94%). That design did not consider the particular characteristics of nanocrystalline ribbon cores. The results shown in Fig.4.13 demonstrate that pads with nanocrystalline ribbon cores can, in fact, yield high efficiency when designed properly, following the guidelines discussed in Section 4.1.4.

Breakdown of Losses

Fig.4.13.*d* shows a breakdown of the losses in the pad. The copper losses, P_{cu}, are calculated analytically using the methodology presented [27], [62] and [8]. The eddy-current, hysteresis, and shield losses – P_{elec}, P_{mag}, and P_{shield}, respectively – are computed using COMSOL by means of volume integrals. Capacitor losses, P_{cap}, are calculated considering a dissipation factor of 0.15% typical of KEMET PHE450/F450 film capacitors. A detailed methodology of estimation of losses was presented in Chapter 3. For the ferrite core, the estimation of losses shown in Fig.4.13.*d* is calculated considering a N87 ferrite plate core without loss of generality. Experimental results are shown with a ($\star$) for DMR44, N87, and nanocrystalline ribbon FT-3M cores.

In the pad with nanocrystalline ribbon cores, the eddy-current losses are the largest component of the losses, accounting for almost 30% of the total loss. Hysteresis losses correspond to 23% of the total power loss. On the other hand, for the pads with ferrite cores, the majority of the loss corresponds to the hysteresis losses. They account for approximately 58% of the total loss. Hysteresis losses in the pad with ferrite cores are about 2.6 times larger than that of the pad with nanocrystalline ribbon cores. As a result, despite having larger eddy-current losses, the system that uses nanocrystalline ribbon cores shows lower overall losses for the same current. When comparing the power losses at the same power transfer, the results are even more clear. For the same power transfer, the total losses in the pad with ferrite cores are between 38% (DMR44, 11 tiles) and 59% (N87 54 tiles) larger than the losses obtained with the nanocrystalline ribbon cores. This is depicted in Fig.4.13.*d*. As mentioned before,

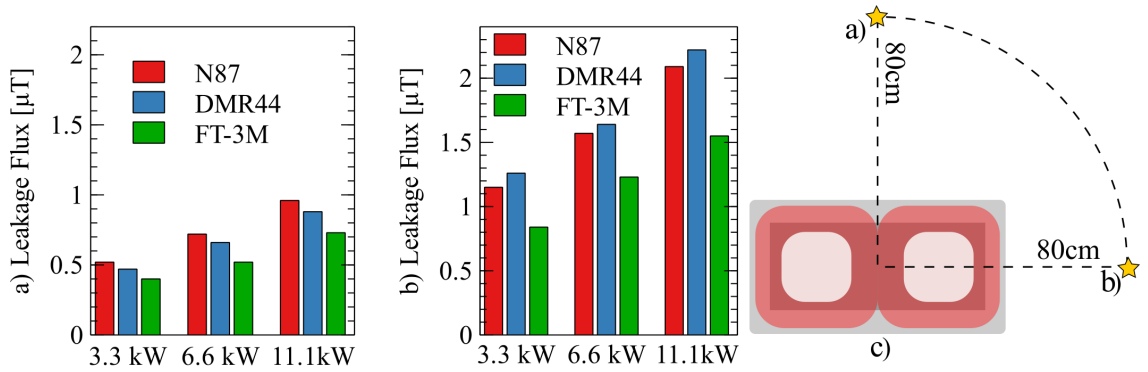

Fig. 4.14 Measured leakage flux at 80 cm from the center of the pad in the *a*) *y*-axis and *b*) *x*-axis. *c*) Depiction of the testing points.

the lower losses achieved with the DMR44-ferrite are due to the higher coupling factor and slightly lower hysteresis losses achieved with this material as compared to the N87-ferrite. Finally, it is worth noting that there is a good agreement between the estimated and measured losses which validates the modeling approach.

4.3.4 Nanocrystalline Ribbon vs. Ferrite: Flux Leakage

The flux leakage was measured for pads using both ferrite and nanocrystalline ribbon cores. For the measurement, a Beehive Electronics' 100C magnetic flux probe and a Rigol's Spectrum Analyzer DSA815 were used. The pads were tested at a clearance of 100 mm between the transmitter and the receiver pads. The leakage was measured at a distance of 80 cm from the center of the pad. Two points on the mid-plane between the transmitter and receiver pads were selected, as shown in Fig.4.14.*c*. These points were considered as simulations show that they corresponded to the maximum leakage flux. This is because both transmitter and receiver pads are identical and the pads are under perfect alignment during the measurement of the leakage flux.

As seen in Fig.4.14.*a* and Fig.4.14.*b*, the leakage flux increases with the power rating. However, due to the smaller footprint of the pad − compared to other commercial units [72]−, the leakage flux remains below 2.5 µT even at the rated power, 11.1 kW. The leakage flux for the system with nanocrystalline ribbon cores is up to 25% lower than for the system with ferrite cores. This is attributed to the higher permeability of the core. Lower leakage fluxes facilitate the compliance of safety regulations at high power ratings.

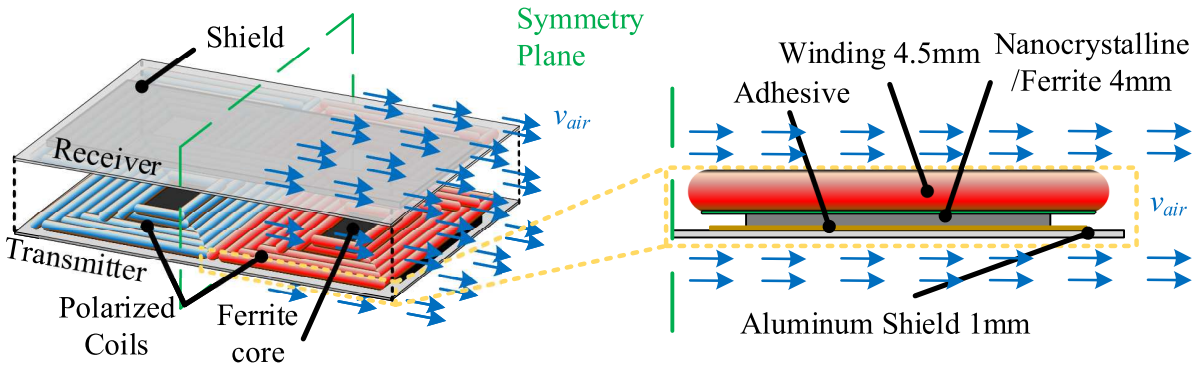

Fig. 4.15 Schematic of heat transfer model used in the FEA.

4.3.5 Nanocrystalline Ribbon vs. Ferrite: Flux Density and Temperature Distribution

The flux distribution within the core cannot be easily measured. However, given that the power losses are correlated to the flux density, thermal images of the core can be used to estimate the flux distribution within them. For this purpose, the shield is removed from the receiver side and thermal images were taken after a 5 min operation at 6.6 kW before the system reached thermal equilibrium. This was done purposely as, at thermal equilibrium, the temperature distribution in the core becomes more uniform. Consequently, the regions of the core with higher flux density −and heat generation− are less evident. Thermal images at the thermal equilibrium were also taken. Heat transfer simulations are also shown for comparison. A brief description of the thermal model is presented next followed by a discussion of the results.

A schematic of the heat transfer model is shown in Fig.4.15. The model considers natural convection. A wind speed of 0.2 m/s is defined to simulate this effect. For the ferrite cores, the thermal conductivity is considered isotropic. Different authors considered different thermal conductivity values, from 3.5 W/mK [64] to 5 W/mK [82, 75]. A value of 4 W/mK is considered here as an average. For the nanocrystalline ribbon core, an anisotropic thermal conductivity is considered due to its laminated structure. Following the thermal analysis of nanocrystalline ribbon cores presented in [82], 10 W/mK for the x and z axes and 0.5 W/mK for the y-axis are selected. To complete the model, the layer between the coil and the core, which corresponds to the fiber insulation of the Litz wire, is set to 0.15 W/mK. With this model, the temperature distribution of the pads at thermal equilibrium was estimated. It is worth noting that this model was not optimized for accuracy as it is only used to have an estimation of the temperatures in the core.

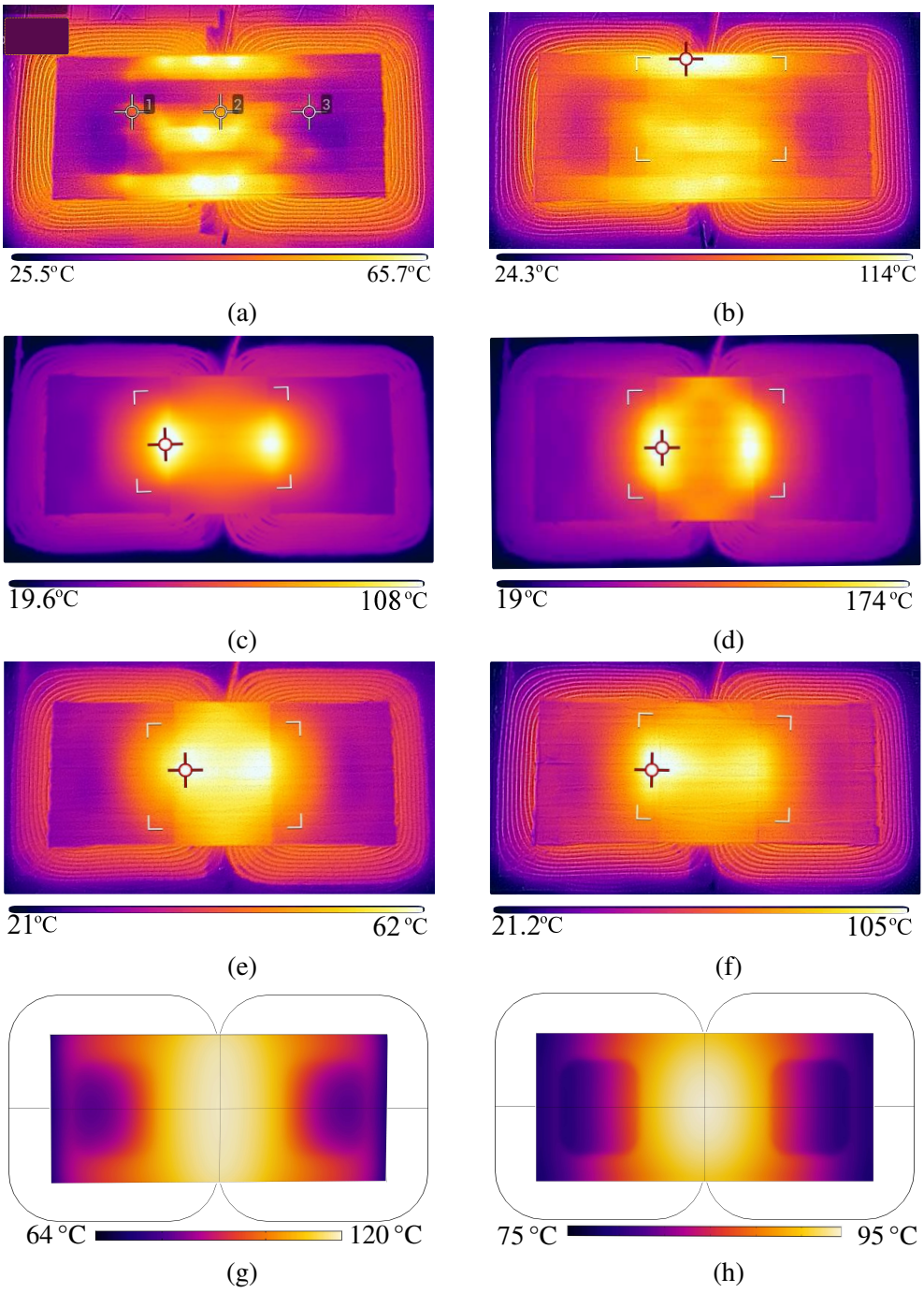

Fig. 4.16 Temperature distribution in the ferrite cores when the system operates at 6.6 kW. N87-ferrite (54 tiles) after *a*) 5 min operation and *b*) thermal equilibrium. DMR44-ferrite (11 tiles) after *c*) 5 min and *b*) 10 min operation. DMR44-ferrite (11 tiles) with a 0.1 mm air gap between tiles after *e*) 5 min and *f*) 10 min operation. Simulation results at thermal equilibrium *g*) without and *h*) with shield.

Ferrite Cores

Fig.4.16a shows the temperature/flux distribution of the N87 ferrite core (54 tiles) after a 5 min operation. The temperature/flux distribution is nonuniform. This is opposed to what is expected from the FEM simulations. The heterogeneous flux distribution is due to the small air gaps between the tiles forming the core. Since the air gaps are not identical nor uniformly distributed, the flux density is higher where the gap between tiles is narrower. Localized heat is therefore found at these spots due to the concentration of magnetic flux. The higher localized temperatures reduce the magnetic performance of the pad, its efficiency, and can lead to failure due to thermal shock. When the pad reaches thermal equilibrium, Fig.4.16b, the temperature distribution is more uniform than at transient and it is closer to the distribution obtained with the FEM analysis shown in Fig.4.16g and Fig.4.16h for the system without and with shield, respectively. The shield helps to spread the heat and reduces the maximum temperature in the pad.

Fig.4.16c, shows the temperature/distribution of the DMR44-ferrite core (11 tiles) after a 5 min operation. Three larger ferrite pieces constitute the center of the core. Due to manufacturing tolerances, the borders of these pieces do not match perfectly. As a result, the flux concentrates in the mid-section of the tiles, resulting in two clear heat spots. After a 5 min operation, the temperature reached 108 °C at the these spots. After only 10 min, the temperature already reached 174 °C as seen in Fig.4.16d. The test was stopped at 180 °C before reaching thermal equilibrium due to safety constraints.

In [14], increasing the spacing between the tiles forming the cores was proposed as a method to mitigate hot spots at the expense of magnetic performance. To evaluate this strategy, a gap of 0.1 mm was added in between the three tiles below the flux pipe. As shown in Fig.4.16e, the two hot spots remain, however, the temperature is more evenly distributed. After a 5 min operation, the maximum temperature in the core was approximately 62 °C, almost 46 °C lower than the one without the air gap between tiles. After 10 min, the maximum temperature of the core reached 105 °C, as seen in Fig.4.16f. This is almost 69 °C lower than without the air gap between tiles. The test was also stopped at 180 °C after approximately 30 min. This confirms that the introduction of air gaps can indeed improve the thermal performance of the pad. However, this improvement comes at the cost of a 9% reduction of the mutual inductance and a $\sim 5\%$ lower coupling factor.

Nanocrystalline Ribbon Cores The flux/temperature distribution for the nanocrystalline ribbon cores after a 5 min operation is shown in Fig.4.17a. The distribution agrees with flux mapping shown in Fig.4.8b. The top and bottom edges of the core show higher temperatures due to eddy-current losses. Additionally, two other regions with higher temperatures are ob-

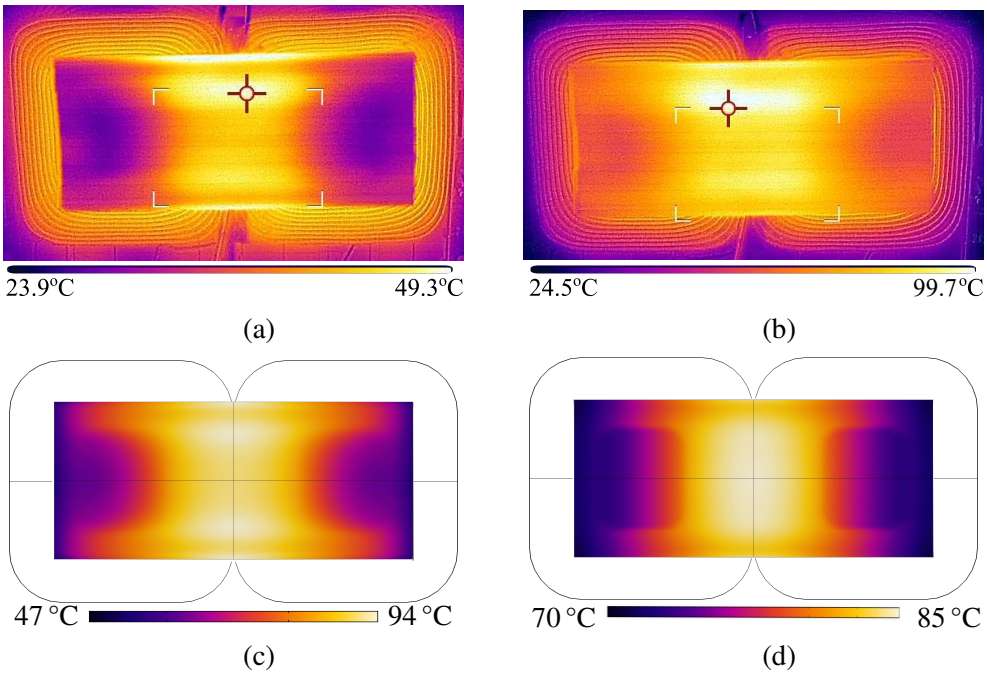

Fig. 4.17 Temperature distribution in the nanocrystalline ribbon cores when the system operates at 6.6 kW after a a) 5 min operation and at b) thermal equilibrium. Simulation results at thermal equilibrium g) without and h) with shield.

served. These regions coincide with the zones of higher flux density and eddy-current losses, according to Fig.4.8b. The upper part of the nanocrystalline ribbon core in Fig.4.17a shows slightly higher temperatures. This asymmetry is attributed to manufacturing tolerances as the separation between bars is slightly larger at the top. Since the nanocrystalline ribbon bars used in this design are bespoke, the manufacture tolerances are more important than that of off-the-shelf products. A deeper analysis of the effect of the manufacture tolerances on the performance of the pad is not presented in this dissertation. Particularly, since in mass production, the tolerances are generally much lower than in bespoke designs.

At the thermal equilibrium, the temperature distribution in the nanocrystalline ribbon core is more uniform than at transient. Its distribution resembles the one obtained via FEM and shown in Fig.4.17c and Fig.4.17d for the system without and with shield, respectively. The estimated temperatures are close to the measured ones. The shield improves the thermal performance and reduces the temperature as well as the temperature gradient. This is true regardless of the core material.

Out of all ferrite core materials and configurations, the ones with N87-ferrite (54 tiles) show the best thermal performance. Despite having several hot spots, the flux distribution is more uniform. Using fewer tiles, as in the case of the DMR44-ferrite core (11 tiles), leads to better magnetic performance. However, this core configuration is more prone to breakage.

Moreover, if the air gap between tiles is not uniform, this configuration can degenerate in a few high-temperature spots with large flux concentrations. This can greatly compromise the thermal performance of the pad. Including air gaps between tiles can improve the thermal performance of the pad but at the expense of lower coupling factor and efficiency values. Using a single ferrite tile is still the preferable solution. However, as discussed in Section 4.3.2, making larger pieces of ferrite is difficult due to the brittleness of the material. Nanocrystalline ribbon core bars, on the other hand, can be manufactured as long pieces without compromising the mechanical robustness of the core.

Fig.4.16b and Fig.4.17b compare the thermal performance of the ferrite and nanocrystalline ribbon cores once thermal equilibrium is achieved. The maximum temperature in the core is lower when using nanocrystalline ribbon cores: 99.7 °C versus 113 °C for ferrite cores. The average temperature in the center of the core is also lower: 98 °C for the ferrite and 86 °C for the nanocrystalline ribbon core. The temperature in the x-axis is less homogeneous in the ferrite core. The maximum temperature difference in the core is approximately 55 °C. This large difference is attributed to the lower thermal conductivity of the ferrite which is worsened by the air gaps between the tiles. Contrarily, the higher thermal conductivity of the nanocrystalline ribbon permits a better heat distribution in the x-axis. This enhances the heat dissipation of the pad. The maximum temperature difference within one nanocrystalline ribbon core bar was measured as 45 °C. The lower temperature gradient in the core is partly due to the lower cores losses as well as due to the higher thermal conductivity of the ribbon.

4.3.6 Nanocrystalline Ribbon vs. Ferrite: Performance vs. Temperature

The performance of the pad versus temperature was evaluated by measuring the power transferred and the efficiency of the pad during operation. For this, the system was tested at a clearance of 10 cm between transmitter and receiver pads. The initial power transfer is fixed at 6.6 kW and the system uses series-series compensation.

Ferrite Cores

Three ferrite core structures were tested: 1) N87-ferrite (54 tiles), 2) DMR44 (11 tiles), and DMR44 with a 0.1 mm air gaps between tiles. For all the materials, similar trends can be seen. First, the increase in the temperature produces a reduction of permeability which translates into lower values of self L and mutual M inductances and coupling factor k. This produces an increment in the power transfer P_2 since the latter is inversely proportional to M (see (4.1)). Moreover, the changes in L also alter the resonant point of the system, and consequently the power being transferred. Thus, as the temperature increases due to the core and coil losses,

the power transfer for a fixed DC-link voltage also increases, as seen in Fig.4.18.*b*. A 2.2% increment is measured for the N87-ferrite core (54 tiles) at thermal equilibrium.

With the increasing temperature, the efficiency of the pad increases. This is expected as the hysteresis losses decrease with temperature for MnZn-ferrites as shown in Fig.4.19.*a*. This change however is non-monotonic; i.e., the losses decrease until the core reaches approximately 100 °C. Thereafter, the core losses increase once again. This can be clearly seen in Fig.4.18.*a*. For the DMR44-ferrite core, this point is achieved rather quickly. The inclusion of an 0.1 mm air gap slows down the temperature increase. However, a similar efficiency drop is observed after the delay. The N87-ferrite core configuration is the only one that can reach thermal equilibrium before the efficiency drop. It also shows the largest improvement in efficiency. Hence, in the next sections of this Chapter, only the N87-ferrite configuration will be discussed as its performance is superior to the others.

For optimum efficiency, ferrite cores should be operated at around 100 °C. However, the decay of the saturation flux density with temperature should be also considered. As seen in Fig.4.19.*b*, the saturation flux density of the material can decay swiftly with temperature. A deeper discussion of magnetic saturation is presented in Section 4.3.7.

Nanocrystalline ribbon cores

Similarly to the previous subsection, the performance of the nanocrystalline ribbon cores was evaluated with respect to time/temperature. The temperature was sensed with a thermocouple placed in the center of the pad. The results for the N87-ferrite cores are also shown for comparison. The measured temperatures are shown in Fig.4.20.*a*. These temperatures are measured

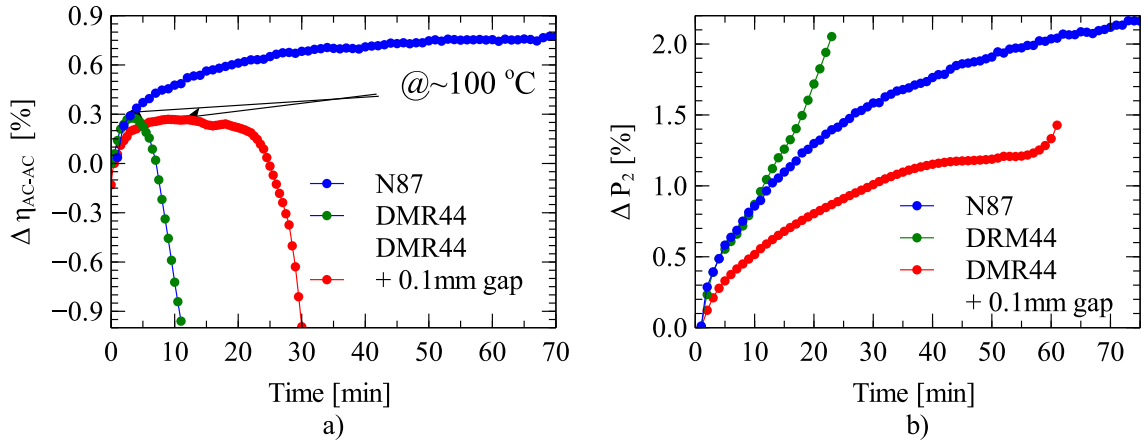

Fig. 4.18 Performance of the pad versus time/temperature when using ferrite cores. *a*) Variation of the efficiency and *b*) power transfer capability of the pad for different configuration and ferrite materials.

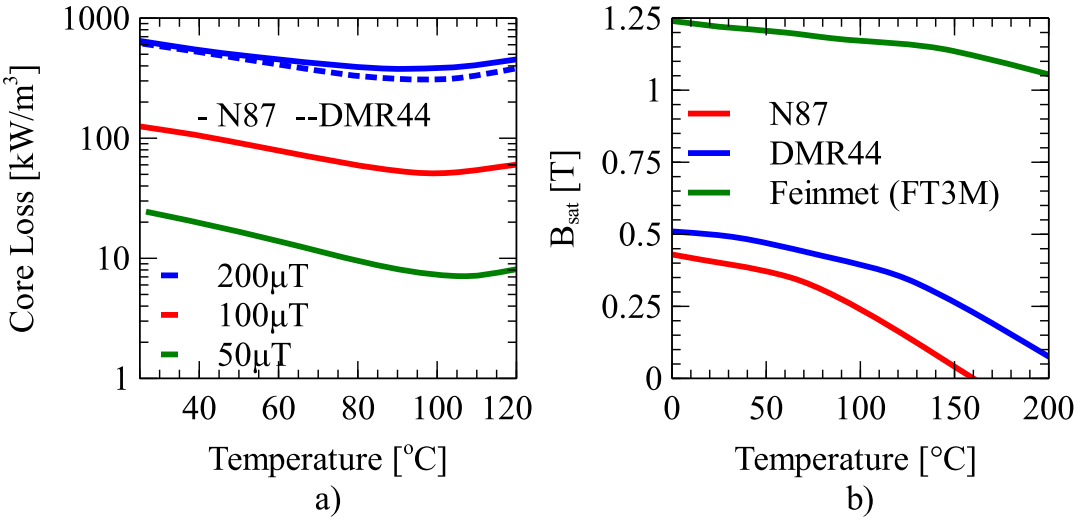

Fig. 4.19 Variation of the core loss and saturation flux density for different magnetic materials. *a*) Core loss vs. temperature for the ferrite N87 and DMR44. *b*) Saturation flux density vs. temperature for the FT-3M nanocrystalline ribbon [34] and typical MnZn ferrites [55].

at the center of the pad and do not consider the irregular temperature distribution in the core discussed in Section 4.3.5.

Fig.4.20.*b* shows the change in the power received in the secondary pad as a function of time. As mentioned before, the power increases with the temperature. A 2.2% variation of power is seen for the system that uses ferrite cores whereas a 1% variation is measured for the one with nanocrystalline ribbon cores. The latter is, therefore, more stable to temperature variations.

Fig.4.20.*c* shows the change in the pad's efficiency versus time. As expected, the efficiency of the pad with ferrite cores increases with the temperature. It changes by approximately 0.85%. The increase is monotonic as the average temperature remains below 100 °C. During the same interval, the efficiency of the pad with nanocrystalline ribbon cores reduces by about 0.3%. Even with this reduction, the efficiency of the pad with nanocrystalline ribbon cores is $\sim 1.2\%$ higher than that of the pad with N87 cores. This is seen more clearly when comparing the power losses in the pad, depicted in Fig.4.20.*d*. These losses consist of the core losses, capacitor losses as well as copper losses, all of which increase with temperature.

The Curie temperature of nanocrystalline ribbon cores is approximately 570 °C. Due to the uneven distribution of temperature in the cores, a temperature-controlled chamber is required to accurately analyze the performance of the pad at high temperatures. This analysis is not presented in this dissertation and it is suggested as future work.

4.3.7 Nanocrystalline Ribbon vs. Ferrite: Magnetic Saturation

Nanocrystalline ribbon cores have a higher saturation point. Therefore, they can operate at higher magnetic loading. To analyze the effect of saturation within the cores, the pads were tested exceeding their nominal rating of 11 kW. The distance between the transmitter and the receiver pads was increased for the system with nanocrystalline ribbon cores until its mutual inductance matched that of the one with ferrite cores. This way, the excitation currents and the power transferred for a given DC-link voltage are the same for both pads. The ferrite cores were tested at an air gap of 10.5 cm whereas the nanocrystalline ribbon cores were tested at 14.5 cm; i.e., a 38% larger air gap. The power transferred between the pads and the efficiency is shown in Fig.4.21.

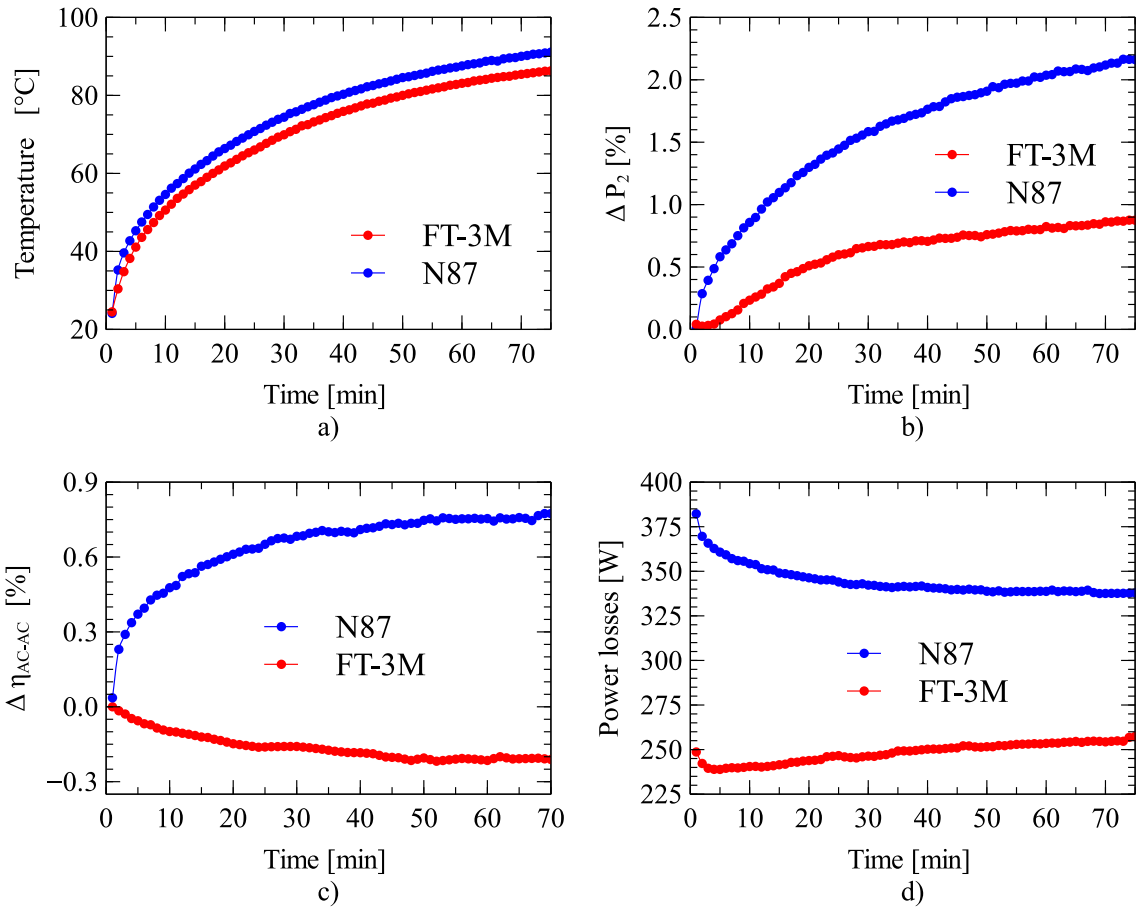

Fig. 4.20 Pad performance versus time/temperature when using nanocrystalline ribbon cores. The performance of the N87-ferrite is also shown for comparison. *a*) Estimated temperature at the center of the pad. Variation of the *b*) power transfer and *c*) efficiency of the pads. *d*) Power losses.

The power increases quadratically with the DC-link voltage for both pads. This is seen more clearly in Fig.4.21.*c* and Fig.4.21.*d* where the square of the voltage is used in the *x*-axis. For the pad with ferrite cores, however, the power transfer is limited to ∼16 kW due to saturation. DC-link voltages which are greater than ∼600 V result in almost no additional

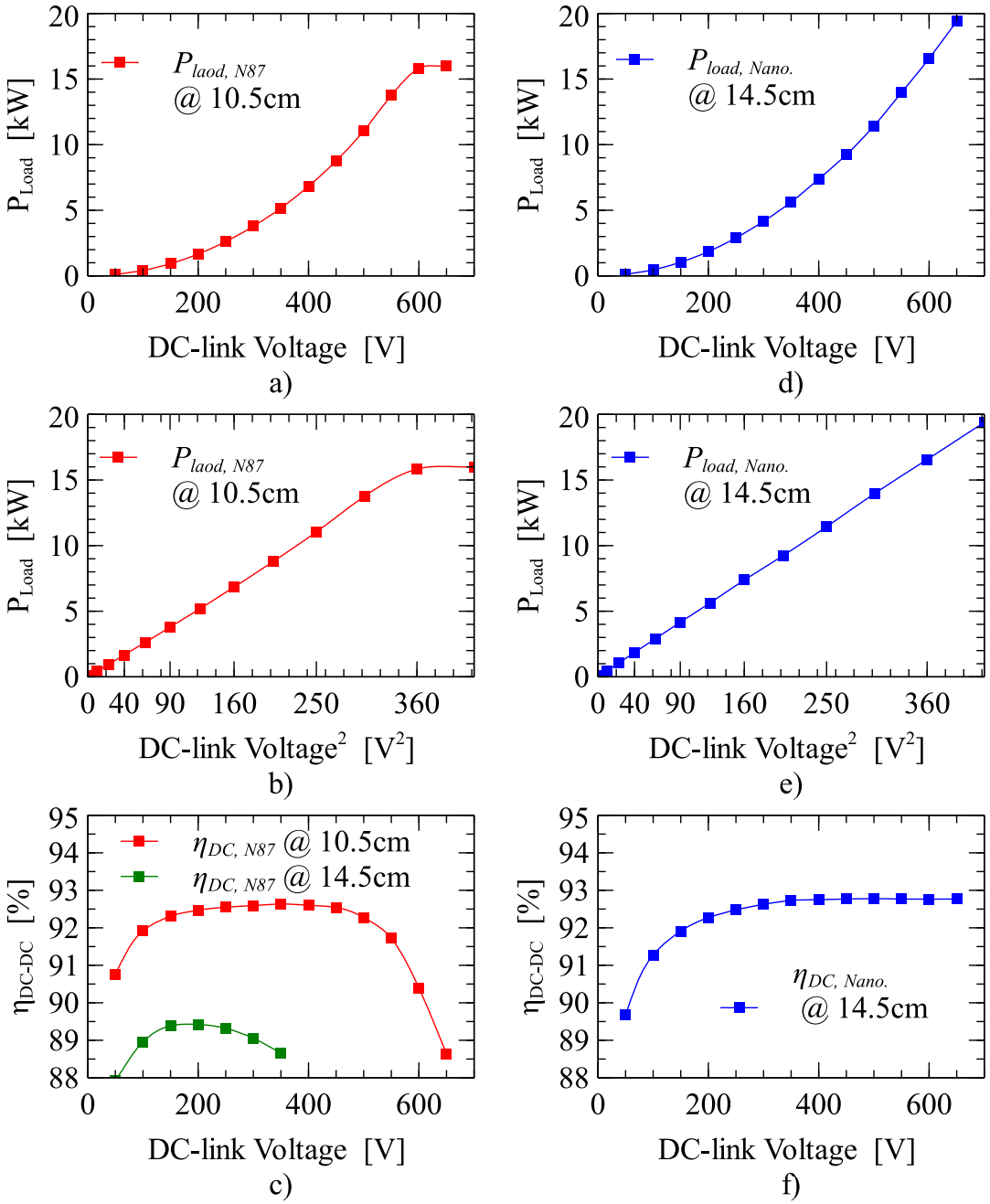

Fig. 4.21 Performance of the WPT3/Z1 pad with $(a)-c)$ N87-ferrite and $(d)-f)$ nanocrystalline ribbon cores at power levels above their rating. $a),e)$ Output power. $b),d)$ Linearized out power. $c),f)$ System's efficiency.

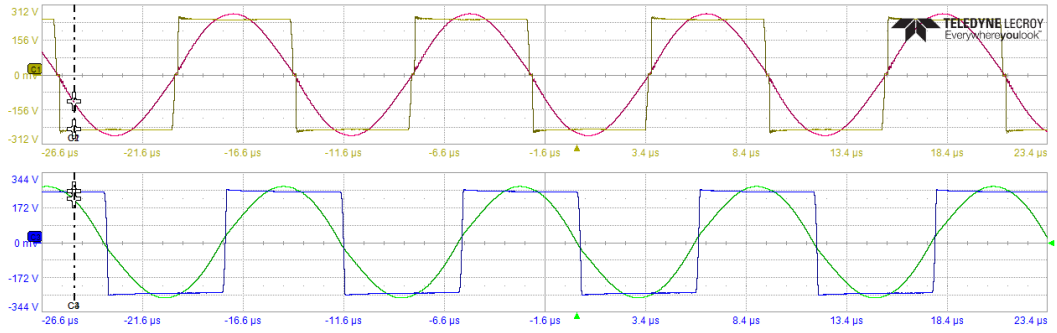

(a) 250*V*

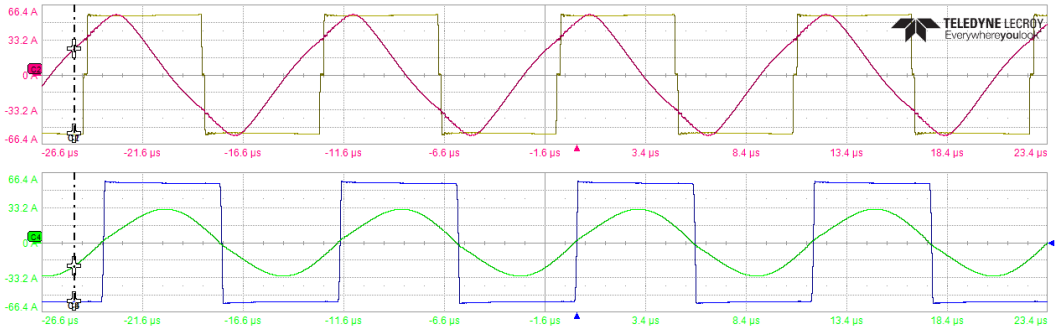

(b) $v_{DC} = 650$

Fig. 4.22 Converter's currents and voltages for the WPT3/Z1 pad with ferrite cores for an *a*) unsaturated and *b*) saturated core. u_1 (yellow), u_2 (blue), i_1 (red), and i_2 (green). *a*)$u_{DC,1} = u_{DC,2}$ =250 V and *a*)$u_{DC,1} = u_{DC,2}$ =650 V. Air gap between pads: $\sim$ 100 mm.

power. For the pad with nanocrystalline ribbon cores, the power increases unrestricted. The measurement was limited to 20 kW due to safety regulations in the laboratory where the test took place. Even at this power rating, the cores remained unsaturated. Thus, more power could be transferred between pads.

For an unsaturated pad, the system's efficiency usually increases along with power transfer and it levels out for higher power transfer values, as shown in Fig.4.21.*f* for the nanocrystalline ribbon cores. At a clearance of 14.5 cm, this pad has achieved an efficiency of approximately 93 %. When the system with ferrite cores was operated at this clearance, its efficiency was less than 90 %, as seen in Fig.4.21.*c*. Due to saturation, the system's efficiency of the system with N87-ferrite cores does not equalize but rather decays as the pad approaches saturation. This is due to the following two reasons. First, saturation produces a change in the effective coil inductance. As a result, the resonant frequency shifts, and the compensation circuit is no longer at resonance. This can be seen in Fig. 4.22.*b*; here, the power factor in the transmitter side is no longer one (unity power factor) for higher DC-link voltages. Second, the current waveform is no longer sinusoidal during saturation. It shows large peaks as seen in Fig.4.22*b*).

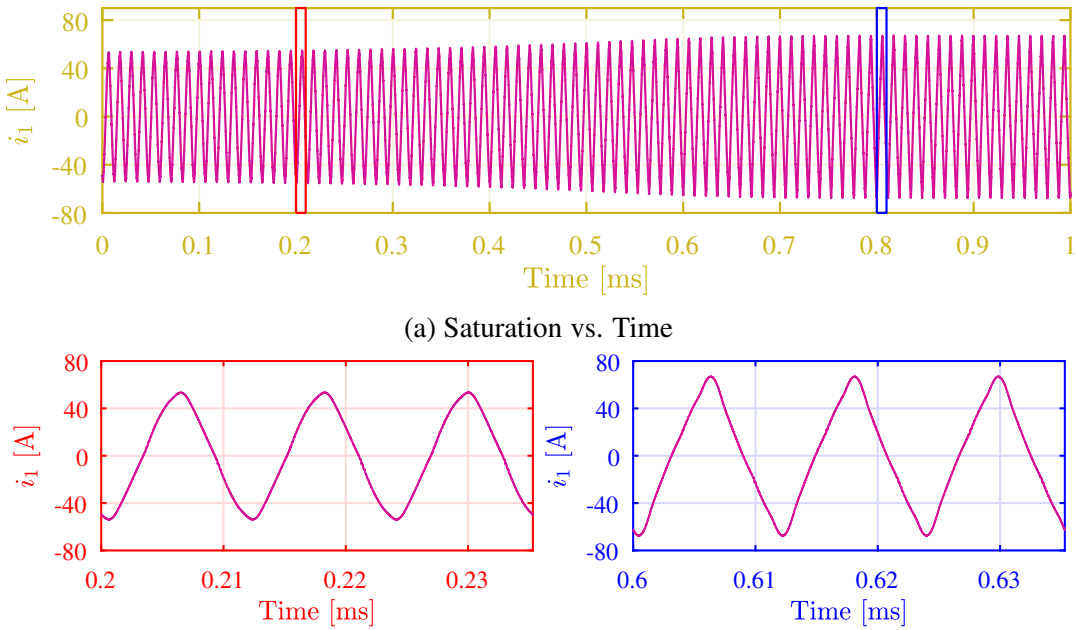

(a) Saturation vs. Time

(b) Before Saturation

(c) After Saturation

Fig. 4.23 Illustration of a stable operating point converging into saturation due to the change in temperature. *a*) Current in the primary coil vs. time. Zoomed in view at at two time instants: *b*)0.2 s and *c*)0.8 s. Air gap:100 mm.

This results in higher copper losses. It is worth noting that these currents increase rapidly as the pad approaches saturation and can exceed the current limits of the converter. This is particularly dangerous as it can cause the failure of the power electronics components. During experimentation, the DC power supply was used to limit the current once saturation was reached to prevent possible faults.

The saturation point of ferrite is temperature-dependent. In fact, it decays rapidly as the temperature increases as shown in Fig.4.19.*b*. The rate of decay varies depending on the composition of the ferrite. For most cases, the saturation point halves for temperatures between 100 and 150 °C. The saturation point of nanocrystalline alloy also decays with temperature. However, its rate of decay is much slower. Even at 200 °C, the saturation point decreases only by less than 20% as seen in Fig.4.19.*b*. Most of the pads with ferrite cores are designed for maximum flux density less than 200 mT and operating temperature below 100 °C [10, 9]. In this context, nanocrystalline ribbon cores have an advantage over ferrite cores since they can withstand operation at high temperatures.

Due to the high rate of change of the saturation point versus temperature, a stable operating point can quickly reach saturation. This is shown in Fig.4.23. Here, the pad was operated close to saturation point $-$ 600V DC-link as seen in Fig.4.21.*a* $-$ for a few seconds. The saturation

can be observed by the rapid increase in the current which happens rather quickly. The DC power supply restricts further increase in the current after the saturation point is reached.

4.4 Nanocrystalline Ribbon Core Segmentation

This section analyses the effect of core segmentation by considering gaps of 5, 10, and 15 mm between core bars. Fig.4.24.*a* shows the 6 bars that constitute the core with different separations between them. Fig.4.24.*b* and Fig.4.24.*c*, on the other hand, compares the system's

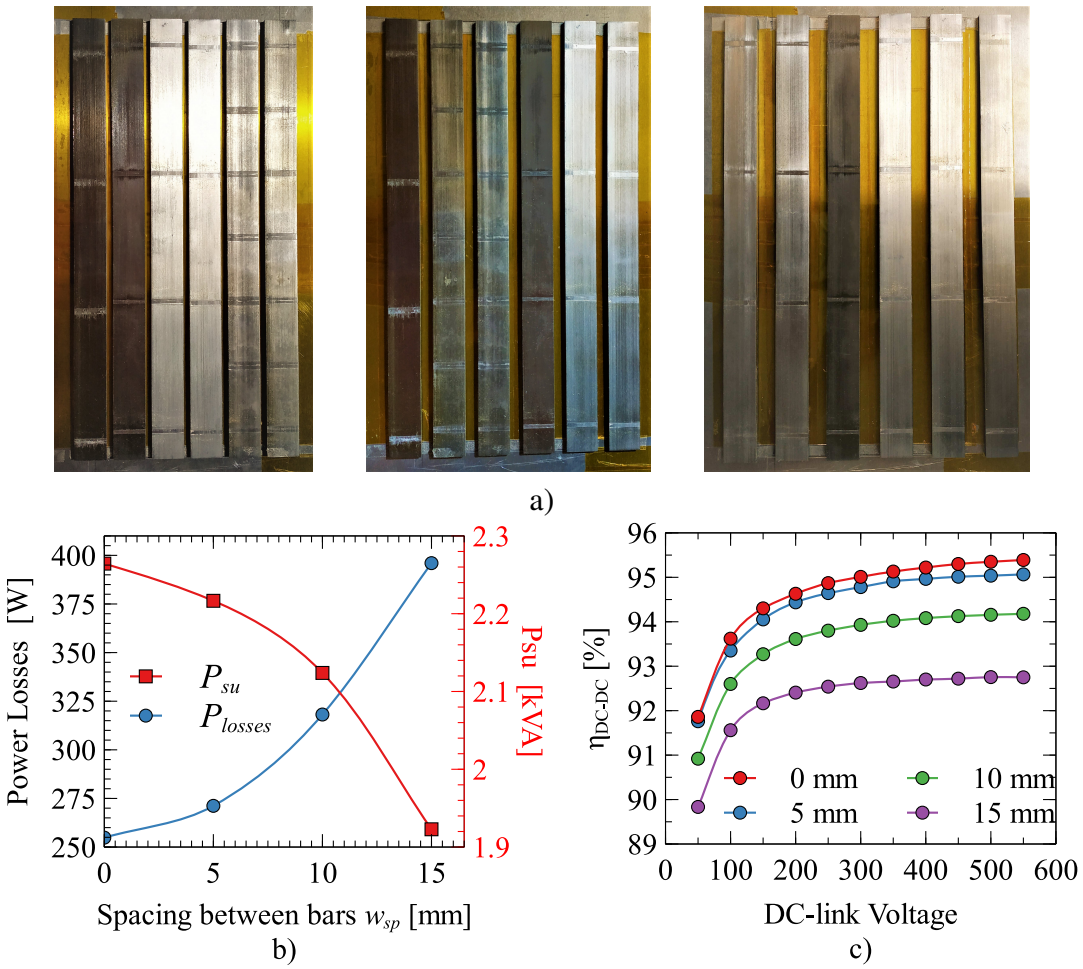

Fig. 4.24 Effect of the spacing between nanocrystalline ribbon core bars on the efficiency and power transfer capability of the pad. *a*) Depiction of the bars with different spacing: 5 mm, 10 mm, and 15 mm. Analysis of the effect of the core segmentation on: *a*) the power transfer capability P_{su}, total system losses P_{losses}, and *b*) the system's efficiency η_{DC-DC}. Six core bars are considered, each of 4 mm×25 mm×342 mm. The efficiency was measured at 25 °C. P_{su} @ $i_{1,pk}$ =21 A.

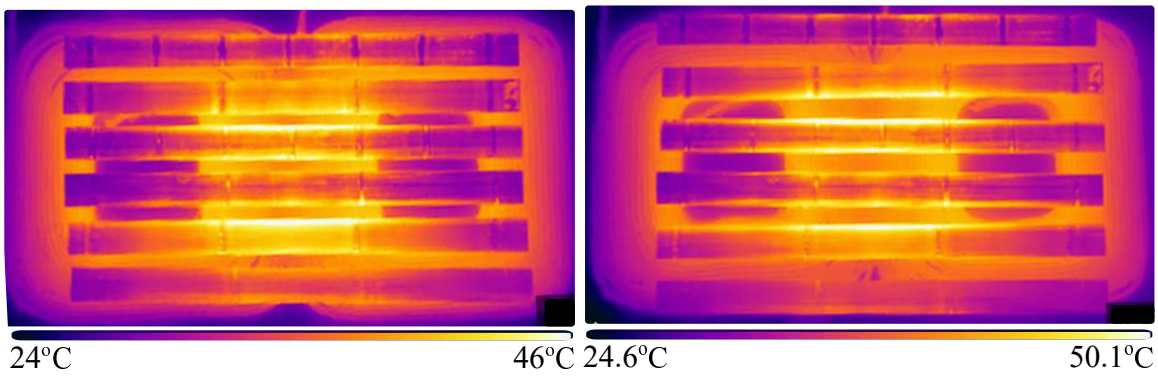

Fig. 4.25 Temperature distribution in the segregated nanocrystalline ribbon core after a 5 min operation at 3.3 kW. Separation between the core bars: *a*) 10 mm and *b*) 15 mm.

efficiency (DC-DC), power loss, and power transfer capability P_{su} for different separations between bars.

The experimental results confirm the conclusions obtained from simulations. Increasing the separation between the cores reduces the power transfer capability of the pad as shown in Fig.4.24.*b*. At the same time, the power losses increase, leading to lower system efficiencies, as seen in Fig.4.24.*c*. The reduction of efficiency increases exponentially with the separation between bars.

Thermal images of the pads are shown in Fig.4.25 for the pads with 10 mm and 15 mm separation between the nanocrystalline ribbon bars. The thermal images were taken after a 5 min operation at 3.3 kW with an ambient temperature of 23 °C. In both cases, the highest temperatures are located at the lateral faces of the core bars. This agrees with the analysis made in Chapter 3 (see Fig.3.15). These are regions where higher eddy currents and magnetic flux densities are present. Higher temperatures are measured for the pad with a 15mm separation. This is due to the higher losses in this configuration.

From these results, one can conclude that the use of segregated bars as cores of an IPT pad with nanocrystalline ribbon cores is not effective. Keeping the core bars together forming one equivalent core plate helps to reduce eddy-current losses. One can argue that using a core plate as opposed to core bars requires more magnetic material. However, this is incorrect as the thickness of the core can be reduced to keep the volume of the core material constant −provided that the core remains unsaturated.

4.5 Screening and Magnetic Shielding

4.5.1 Analysis of Copper screening

In large electrical machines, flux shields (also known as screens) are used to cover the stator end-core laminations. This prevents the non-axial flux generated by the end-windings from reaching the core, avoiding with this, excessive eddy-current losses [29] in the stator. In inductors, copper screens are sometimes used to reduce the air gap fringing flux which causes eddy-current losses in the exposed conductors [25]. This strategy can also be applied to the nanocrystalline ribbon core bars. Covering the lateral faces of the bar with copper or aluminum foils can reduce the power losses.

The effect of the metallic shielding can be mathematically described as follows. A magnetic field B_0 reaching the shield will induce eddy currents in it, which in turn will produce a magnetic field B_e. B_e opposes B_0 (Lenz's law). The overall magnetic field, B_r, results from the superposition of these two fields. B_r can be approximated as in (4.3):

$$B_r = \frac{B_0}{1 + \frac{j \cdot \omega \cdot A_{sh} \cdot K_{Br,i_{sh}}}{R_{sh}}} \tag{4.3}$$

where A_{sh} is the shield area, ω is the frequency of the sinusoidal flux B_0, R_{sh} is the shield resistance, and $K_{Br,i_{sh}}$ is the constant that relates the eddy currents in the shield to the magnetic field produce by them. $K_{Br,i_{sh}}$ depends on the geometry and dimensions of the shield. For large shields of high conductive material, the second term in the denominator of (4.3) is larger than 1. Thus, B_r can be approximated as in (4.4):

$$B_r \approx \frac{B_0 \cdot R_{sh}}{j \cdot \omega \cdot A_{sh} \cdot K_{Br,i}} \tag{4.4}$$

From (4.4), one can see that B_r is proportional to the shield resistance R_{sh}. This resistance depends on the conductivity of the shielding material as well as on the dimensions of the shield. R_{sh} can be calculated using (4.5):

$$R_{sh} = \frac{L_{sh}}{\delta_{sh} \cdot t_{sh} \cdot \sigma_{sh}} \quad \text{with} \quad \delta_{sh} = \sqrt{\frac{1}{\pi \cdot f \cdot \sigma_{sh} \cdot \mu_{sh}}} \tag{4.5}$$

where t_{sh} is the shield sheet thickness, L_{sh} is the shield perimeter, δ_{sh} is the skin-depth, f is the frequency of operation ($\omega = 2\pi f$), and σ_{sh} and μ_{sh} refer to the conductivity and permeability of the shield, respectively. Thick shields of high conductivity materials result in lower resistance values and, therefore, in lower overall values of B_r.

The shielding effect is produced by the formation of eddy currents. These currents generate losses which can be estimated employing (4.6):

$$\begin{aligned} P_{eddy,sh} = \quad i^2_{sh,rms} \times R_{sh} = \quad & \left(\frac{\partial (B_r \cdot A_{sh})}{\partial t} \cdot \frac{1}{R_{sh}} \right)^2 \times R_{sh} \\ = \quad & \left(\frac{j \cdot \omega \cdot B_r \cdot A_{sh}}{R_{sh}} \right)^2 \times R_{sh} = \quad \left(\frac{B_0}{K_{Br,i}} \right)^2 \times R_{sh} \end{aligned} \tag{4.6}$$

Eddy-current losses in the shield are proportional to R_{sh} and the magnetic flux which is imposed by the IPT system. As a result, the losses for a given frequency decrease with the shield thickness. Additionally, eddy-current losses decrease with the conductivity of the shield, proportionally to $\sigma_{sh}^{1/2}$. The resistivity of copper and aluminum is $0.0168\mu\Omega\,\mathrm{m}$ and $0.0265\Omega\,\mathrm{m}$, respectively. These values are two orders of magnitude lower than that of the nanocrystalline ribbon. Using copper or aluminum to cover the nanocrystalline ribbon core bars can lead to a reduction of the eddy-current losses. However, it is worth noting that the shield will have an impact on the flux distribution and reduce the coupling factor as discussed in [30]. This is evaluated via simulation and experimental results.

Simulation results

Fig.4.26 shows the effect of the copper screening on the system. The copper screen reduces the eddy-current losses. A small thickness ($<0.5\,\mathrm{mm}$) is sufficient to completely shield the core. Since the shield prevents the flux from entering the core, the flux density in the core also reduces. As a result, the hysteresis losses are also slightly decreased. By placing a shield, the eddy-current losses are now localized in the copper screen. These losses decrease as the screen thickness increases as shown in green in Fig.4.26.*a*.

As opposed to ferromagnetic shielding, using copper screening reduces the linkage flux of the pad. Consequently, the power transfer capability of the pad, P_{su}, decreases as seen in Fig.4.26.*b*. Thus, more current is required to transfer the same power. The benefit of lower eddy-current losses can be outweighed by the reduction of P_{su}, particularly for thin screens. This is evaluated experimentally in the next section.

Experimental Results

Fig.4.27 shows the core with copper screens on the lateral faces of the nanocrystalline ribbon core plate as well as a table comparing their performance. The experimental results agree with the simulation results. Adding a copper screening reduces the magnetic flux entering the bar.

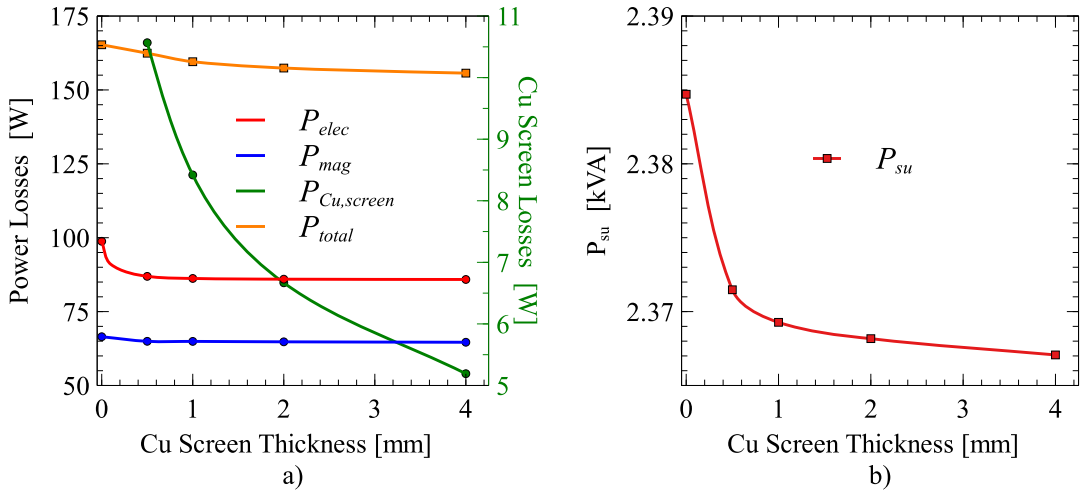

Fig. 4.26 FEM analysis of the effect of copper shielding on the core losses: *a*) eddy-current losses P_{elec} and hysteresis losses P_{mag}, losses in the copper screen, and total losses. *b*) Power transfer capability of the pad, P_{su}.

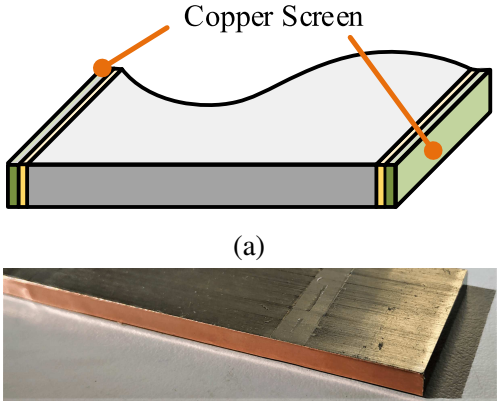

Parameter	w/o Screen	50 μm Screen	350 μm Screen	Units
L_1	176.6	175.7	175.5	μH
M	57.375	56.9	56.7	μH
k	0.33	0.329	0.328	
P_{su}	2.264	2.240	2.231	kVA
η_{DC-DC}	95.4	95.2	95.3	%

c)

Fig. 4.27 Experimental evaluation of copper screening. *a*) Location of the copper screens in the core. *b*) Image of the core with the copper screens. *c*) Table comparing the performance of the pad when using the screens. Clearance between pads around 95 mm. P_{su} @ $i_{1,pk}$ =21 A.

This translates into lower inductance values, coupling factor, and power transfer capability P_{su}. Copper screening is intended to reduce the eddy-current loss. However, the reduction of the eddy-current losses is outweighed by the reduction in power transfer. Consequently, the overall efficiency is diminished. This is seen in Fig. 4.27.*c* when comparing the efficiency with and without screening. Using a thicker screen (350 μm yields a slightly better efficiency as compared to using thin screens (50 μm). Nevertheless, the efficiency is lower than the one obtained without the copper screen. These results suggest that copper screening is not an effective method for improving the efficiency of nanocrystalline ribbon cores in IPT systems.

A better alternative would be to use ferromagnetic shielding. This is discussed in the next section.

4.5.2 Analysis of Magnetic Shielding

Apart from copper screens, ferromagnetic materials can also be used as shielding. This method has been successful at reducing eddy-current losses in transformers constructed with nanocrystalline ribbon cores [6]. As opposed to metallic shielding, ferromagnetic shielding does not necessarily decrease the magnetic performance of the pads.

In IPT systems, ferromagnetic shielding can be used to cover the lateral faces of the nanocrystalline alloy core plate as shown in Fig.4.28. The shield needs to be attached to the cores with an adhesive layer. This results in the equivalent magnetic circuit shown in the same figure. The total magnetic flux, ψ, entering the lateral face of the core is distributed between the ferrite shield and the nanocrystalline ribbon core depending on the value of the reluctance of the magnetic circuit: $\Re_{adh}$, $\Re_{nano}$, and $\Re_{fe}$. These depend, among other things, on the dimensions of the ferrite shield, its permeability, and the thickness of the adhesive layers ($\mu_r = 1$). The reluctance of the ferrite shield remains low during the linear region but increases rapidly once it reaches saturation. Thus, the shielding is only effective if the ferrite shield is not saturated. After this point, the shield no longer prevents the flux from entering the nanocrystalline ribbon core.

One can approximate the reluctance values of the equivalent system shown in Fig.4.28 using the parameters of Table4.1 and the standard reluctance equation: $\Re = \frac{l}{\mu\mu_r A}$. Here, l corresponds to the length of the flux-path and A the flux-path cross-sectional area. The ratio between the reluctance of the ferrite $\Re_{fe}$ versus the total reluctance that comprises the nanocrystalline core and the adhesive gaps is shown in Fig.4.28 for different shield thicknesses. As this ratio decreases, more flux is channeled through the shield and less through the nanocrystalline core.

Fig.4.29.*a* shows the losses in the nanocrystalline alloy as a function of the thickness of the ferrite shield. As the thickness increases, both eddy-current and hysteresis losses in the nanocrystalline alloy core decrease. This is because the amount of the flux entering the lateral faces of the nanocrystalline alloy bar drops. As a result, eddy-current losses decrease and settle at a lower value. Approximately a 17 % reduction of these losses is achieved. Since less flux enters the nanocrystalline alloy core, the flux density also reduces. This translates into a slight decrease in the overall hysteresis losses, as seen in Fig.4.29.*a*.

Power losses in the ferrite shield are shown in Fig.4.29.*b*. They show a non-monotonic profile which can be explained as follows. The losses in the shield depend on both the volume of ferrite and the amplitude of the magnetic flux density. The increase in shield thickness

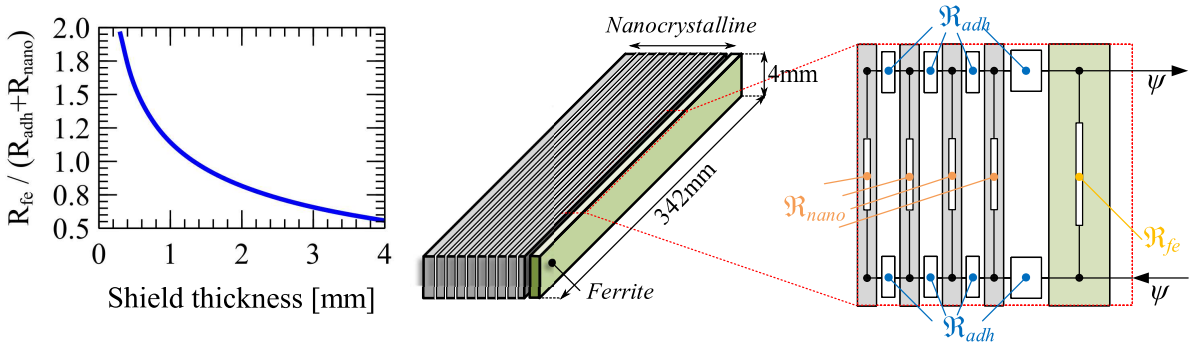

Fig. 4.28 Lumped parameter magnetic circuit illustrating the effect of ferromagnetic shielding. $\Re$: Reluctance. Subscript: *adh.* : adhesive, *fe* : ferrite shield, *nano* : adhesive layer.

reduces its magnetic reluctance. Consequently, more flux is carried by the shield which in turn tends to increase the losses in the shield. Once most of the perpendicular flux is conducted through the ferrite, any increment in thickness translated into a reduction of both the flux density and power losses in the shield.

The overall core losses considering both the losses in the nanocrystalline alloy core and the ferrite shield are depicted in Fig.4.29.*c*. In effect, the ferromagnetic shielding reduces the overall losses for a given excitation current. Moreover, the shield also increases the power transfer capability of the pad (P_{su}), but only until a certain point, as shown in Fig.4.29.*d*. If the shield thickness is increased after this point (∼8 mm in this case), the self-inductance of the pad increases more than the mutual inductance leading to lower P_{su} values and coupling factors. This can have a detrimental effect on efficiency.

Flux distribution

Fig.4.30 shows the distribution of the flux density *B* for a pad with nanocrystalline alloy cores with and without ferromagnetic shielding. The flux distribution of the nanocrystalline alloy core without shielding was previously discussed in Section 4.3.5. The sides of the core plate are zones of higher flux density −due to the magnetic flux entering the lateral faces of the core [27]. The addition of the ferrite shield results in a reduction of the flux density at both sides of the core plate, as seen in Fig.4.30.*b* and Fig.4.30.*c*. The flux density in the ferrite shield can be reduced if the thickness of the shield is enlarged as shown in Fig.4.30.*c*. By doing so, the flux density and hysteresis losses in the shield can be both reduced.

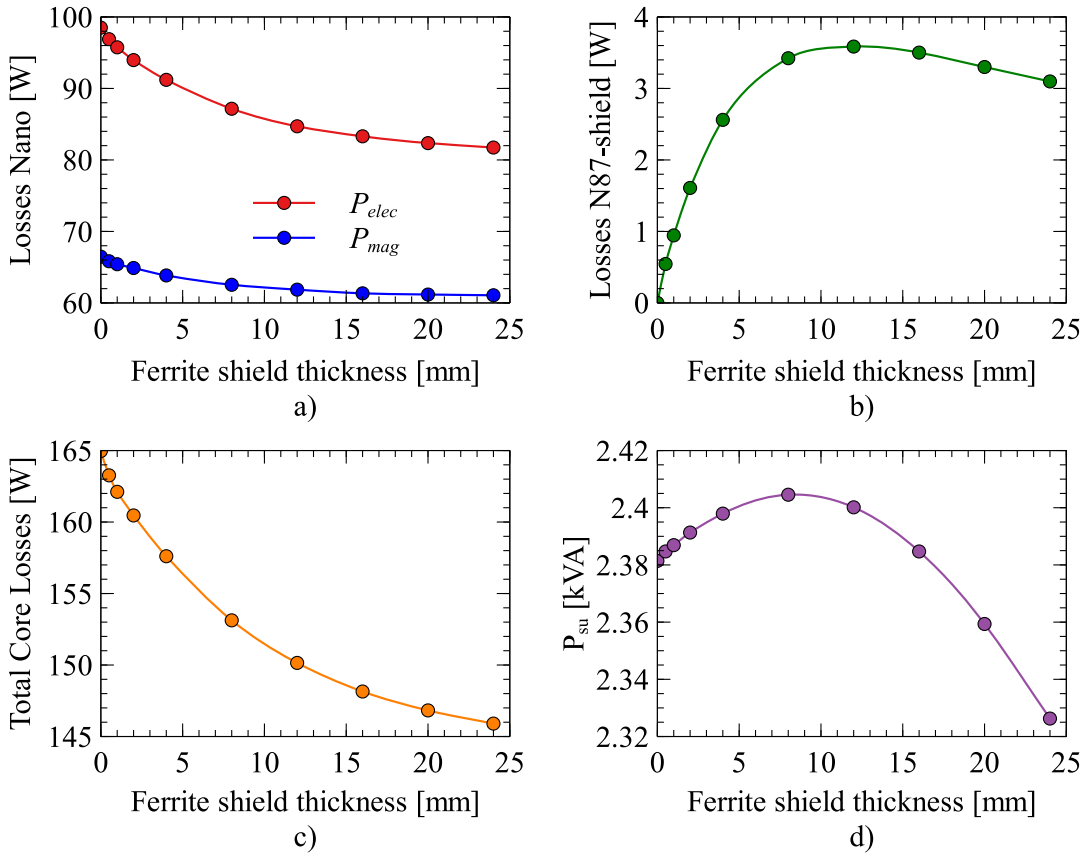

Fig. 4.29 FEM analysis of the effect of ferromagnetic shielding on the core losses: *a*) eddy-current losses P_{elec} and hysteresis losses P_{mag}. *b*) Hysteresis losses in the shield. *c*) Total losses in the core including losses in the shield. *d*) Power transfer capability of the pad also known as uncompensated power, P_{su} @ i_{pk} =21 A.

Power losses

Fig.4.31 shows a detailed comparison of the losses for three different core materials: 1) ferrite N87, 2) nanocrystalline ribbon, and 3) nanocrystalline ribbon with a 4 mm ferrite shielding. As discussed before, nanocrystalline ribbon cores result in $\sim$ 20% lower core losses as compared to that of ferrite cores. When adding a 4 mm shield to the core, the eddy-current losses reduce by nearly 7.5% which brings the overall core losses down by about 4.5%. Nanocrystalline ribbon cores, with a 4 mm shield, are 24 % less lossy than ferrite cores. Magnetic shielding is an effective method to mitigate eddy-current losses in nanocrystalline alloy cores used in IPT systems. Since the amount of ferrite in the pad is minimum, any impact on the mechanical robustness of the pad can be considered negligible. Experimental results are shown next.

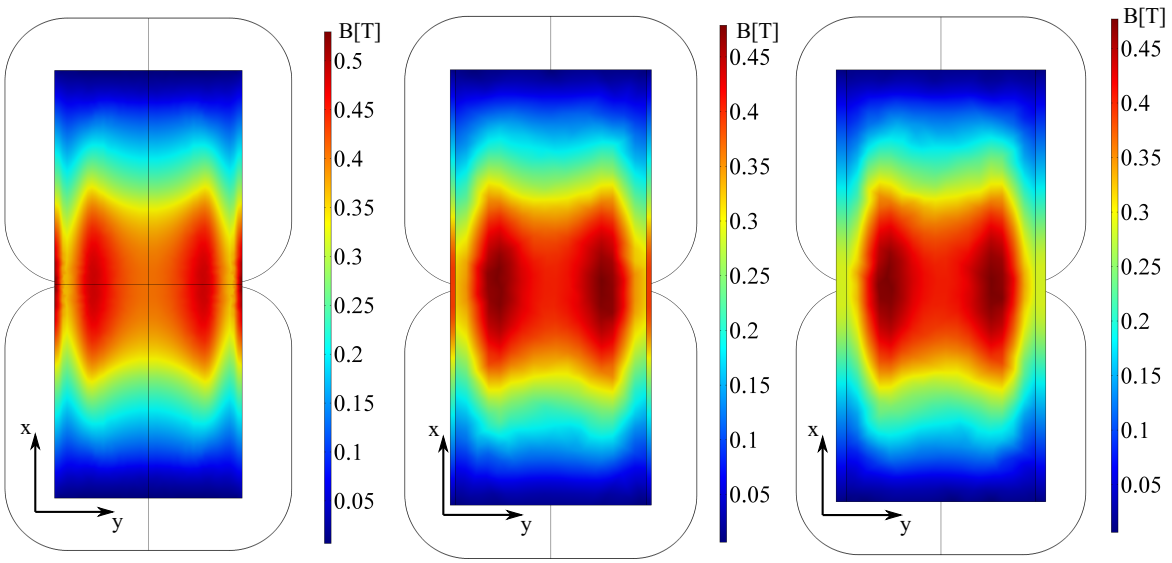

(a) Nanocrystalline (b) Nano. + 4mm shield (c) Nano. + 8mm shield

Fig. 4.30 Flux density distribution within the core for *a*) nanocrystalline ribbon cores without shielding, *b*) with a 4 mm and a *c*) 8 mm shielding for an exemplary operating point at I_{pk} =40 A and with and air gap of 100 mm.

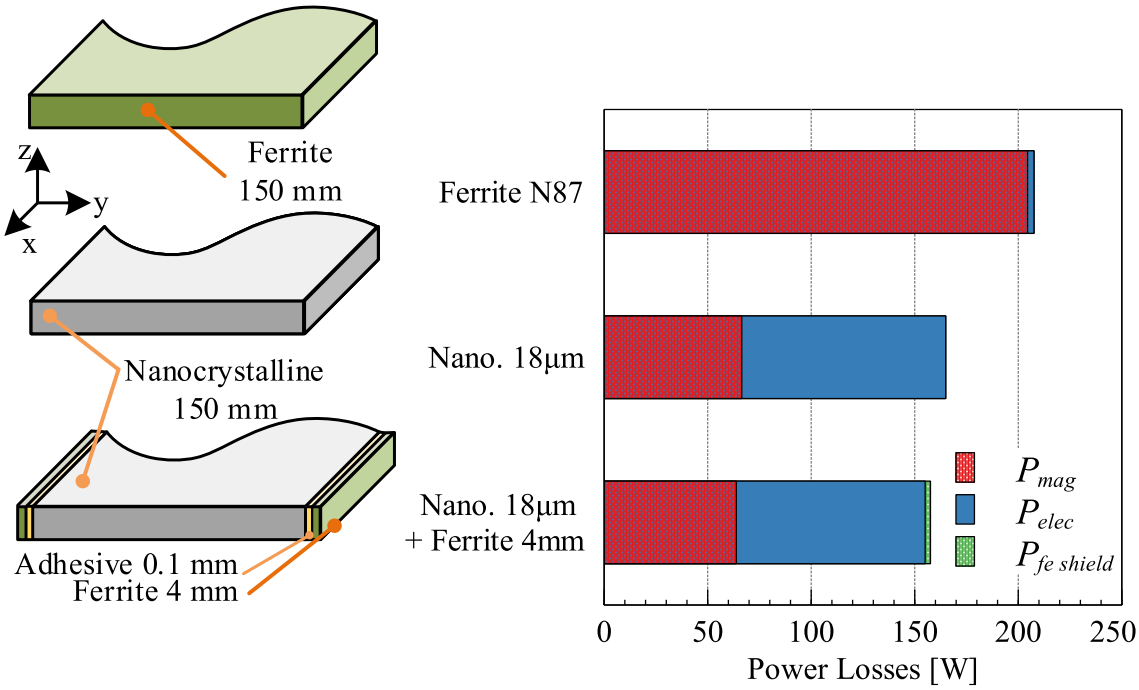

Fig. 4.31 Estimation of core losses in the ferrite and nanocrystalline ribbon cores with and without ferromagnetic shielding (4 mm) at 6.6 kW.

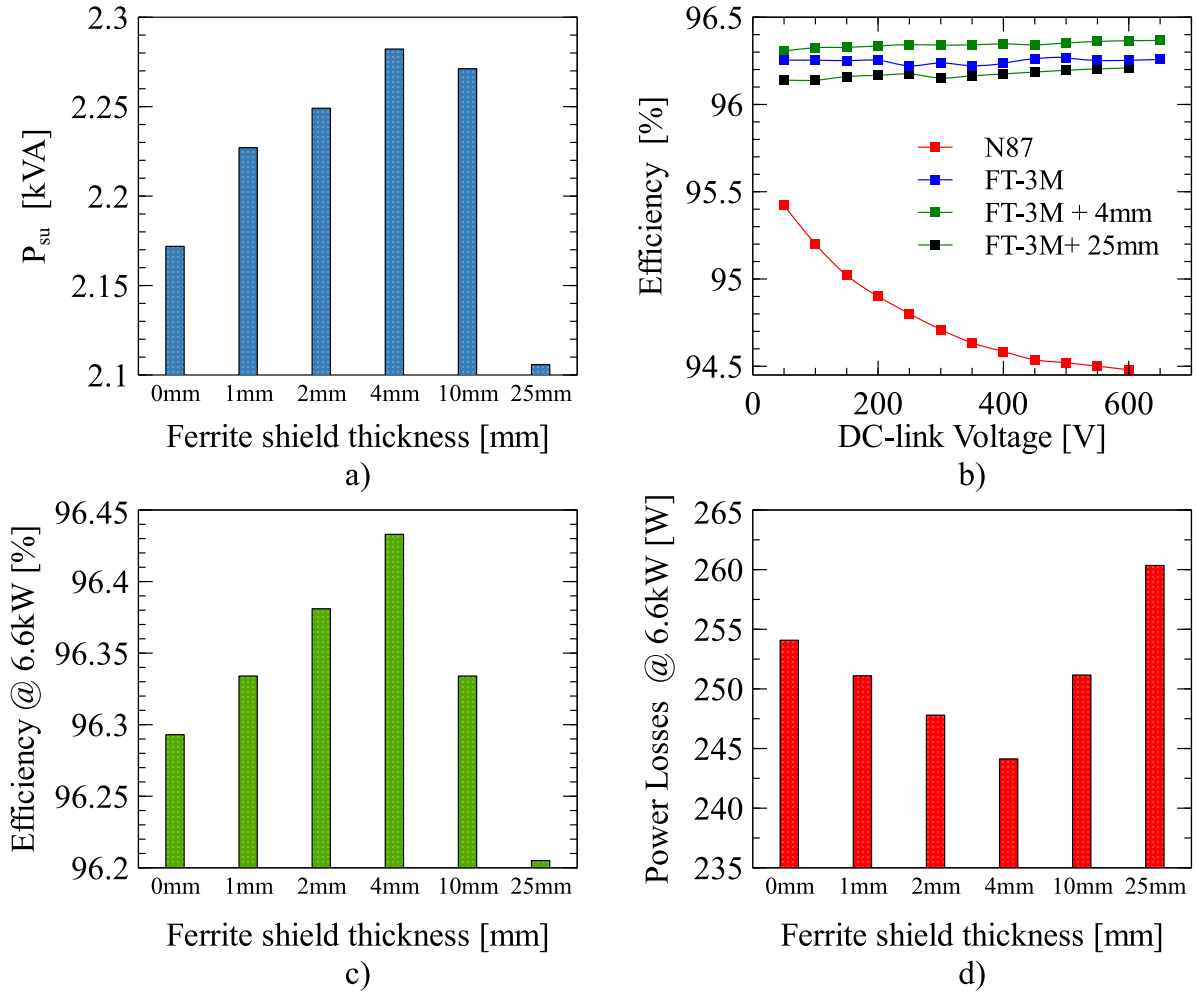

Fig. 4.32 Experimental validation of ferromagnetic shielding. *a*) Efficiency of the pad with different core materials. *b*) Power transfer capability of the pad considering vs. shield thickness. *c*) Efficiency of the pad at 6.6 kW vs. shield thickness. *d*) Power losses at at 6.6 kW vs. shield thickness. P_{su} @ $i_{1,pk}$ =21 A.

Experimental Power Measurement

The nanocrystalline ribbon core plate was shielded with closely packed ferrite tiles of different thicknesses: 1 mm (DMR44), 2 mm (DMR44), 4 mm (DMR44), 10 mm (N87), and 25 mm (N87). The shields cover the entire lateral walls of the nanocrystalline core plate, each of 342mm×4mm as shown in Fig.4.28. The experimental results are shown in Fig.4.32. Fig.4.32.*a* shows the power transfer capability of the pad P_{su} for different shield thicknesses. The experimental results agree with the simulations. The addition of the shield improves P_{su} but only until a certain thickness ($\sim$ 4 mm). For larger thicknesses, P_{su} decreases as the leak-

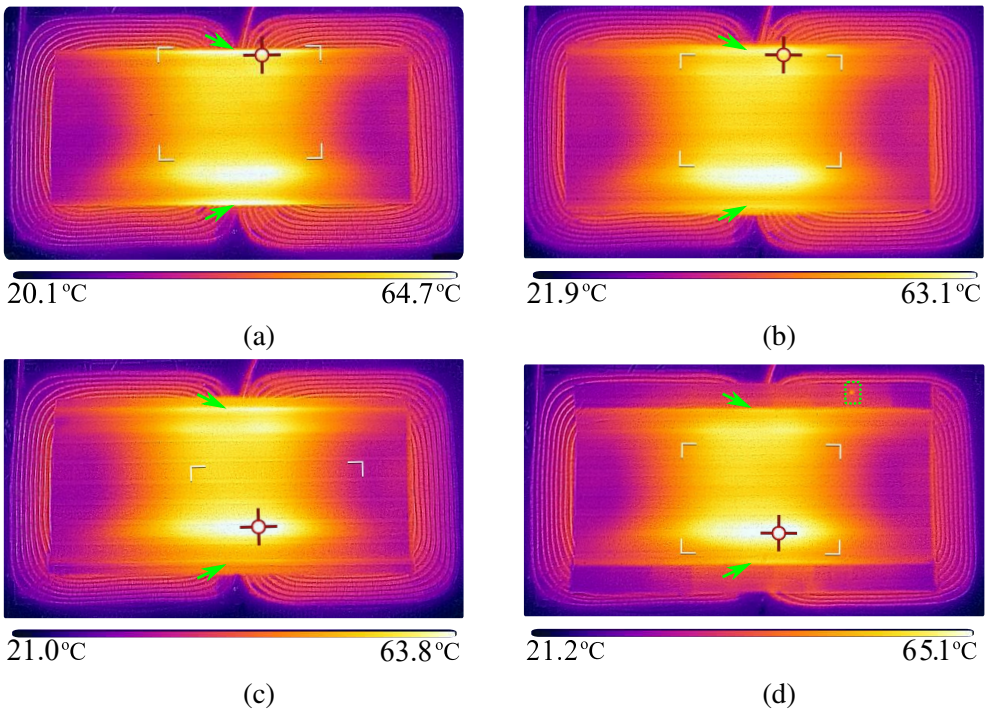

Fig. 4.33 Temperature distribution in the nanocrystalline ribbon cores after a 5 min operation at 6.6 kW for different shield thicknesses: *a*) no shield *b*) 4 mm shield, *c*) 10 mm, and *d*) 25 mm

age flux becomes more important. The reduction of P_{su} decreases the efficiency as discussed next.

Fig.4.32.*b* shows measurements of efficiency for different DC-link voltages and different core configurations. Compared to the N87-ferrite core (54 tiles), nanocrystalline ribbon cores with and without shielding yield higher efficiency. Higher efficiency values can be obtained when using the shield. However, the improvement of efficiency is non-monotonic. An optimum point was determined, for this particular design, at a thickness of approximately 4 mm. This can be seen more clearly in Fig.4.32.*c* where the efficiency of the pad is compared at an operating point of 6.6 kW. This power level was selected to achieve adequate accuracy. At the highest efficiency, the power losses decrease by about 10 W. This represents approximately a 4 % reduction in losses. With this, the total efficiency of the pad reaches a value of 96.44%. This confirms that shielding can effectively improve the pad performance.

In the simulation, the maximum point took place at a shield thickness of approximately 10 mm. In the experiment, this point was achieved at 4 mm. The difference is attributed to the different materials used for shielding: N87 has slightly higher hysteresis losses than the DMR44. Moreover, due to the limited commercial availability, 38 tiles were used for the 10 mm-thick shield, whereas only 7 were required for the shields with DMR44. The higher the

number of tiles, the lower the effective permeability of the shield. Better performance could be obtained with a single-piece shield; however, the fabrication of such a piece is constrained by the brittleness of the material.

Experimental Flux/Temperature Distribution

Temperature images of the core after are used to determine the effect of the shielding on the flux distribution and losses. Fig.4.33 shows the temperature distribution of the nanocrystalline ribbon core with and without shielding after a 5 min operation at 6.6 kW. The clearance between pads was approximately 10.5 cm.

Comparing the temperature distribution with and without shielding, the effect of the shield can be observed. With the shield, the temperature at the top/bottom edges of the core plate decreases and becomes more uniform. Shielding improves the thermal performance of the pad by removing the localized losses (hot spots) at the edges of the bar. The maximum temperatures are in the same range for all the cases. However, slightly lower temperatures are obtained when the shield thickness is around 4 mm. This is attributed to the improvement in efficiency. In this contribution, individual ferrite tiles whose lengths lie between 18 mm and 38 mm were used and packed closely. Better performance is expected when using single-piece shields. Particularly since localize heat-spots can be produced at the border between tiles. An example of such case is shown in Fig.4.33d with a □. Moreover, the small air gaps between the tiles can reduce the effectiveness of the shield. This can be seen in Fig.4.33c when comparing the temperature at the top and bottom of the core: lower temperatures are achieved at the bottom which suggests a more effective shielding in that edge.

4.6 Other Methods for Reduction of eddy-current losses

The mitigation of eddy-current losses in laminated cores has been a continuous topic of research, both in Academia and Industry. Apart from the shielding, other strategies have been applied to the design of inductors, transformers, and electric machines. Some of these methods can also be applied to nanocrystalline alloy cores used in IPT applications. The most relevant methods are described below. Their feasibility in IPT applications is also discussed.

4.6.1 Modification of the cross-section of the core

Eddy currents are a product of the flux entering perpendicular to the nanocrystalline ribbon. Thus, they can be mitigated by limiting the number of ribbons exposed to perpendicular (transversal) flux. This can be achieved by modifying the cross-section of the core bars. Two

exemplary cases are shown in Fig.4.34. In Fig.4.34a, the ribbons at the lateral walls of the cores are placed radially. This way, the side of the ribbon is not exposed to the flux. This geometry is convoluted and therefore difficult to manufacture. A simpler alternative is shown in Fig.4.34b. Here, the core bar is chamfered into a trapezoidal geometry. Thus, the exposed planar surface of the ribbon is reduced. According to FEM simulations, a reduction of 54% and 16% of the eddy current and the hysteresis losses, respectively, can be expected when using these cores as compared to cuboid-shaped bars like the ones used in Chapter 3.

In principle, bars with trapezoidal cross-sections can be constructed stacking ribbons of different widths. However, the minimum width commercially available is 3.2 mm [79]. Additionally, stacking ribbons of different widths is not possible with the current technology and novel equipment would be required. An alternative manufacturing method is to cut a rectangular bar into a trapezoidal one. This method was attempted. However, the results were less than promising. Normal cutting methods such as turning or waterjet cutting are too strident for the cores. They damage ribbons, break pieces of the core, and ruin the insulation between them. Thus, more delicate methods, such as electro-discharge machining (EDM), are required. One of the 8 mm bars used in Chapter 3 was cut using this method. EDM did not compromise the integrity of the core bar; however, it damaged several ribbons, particularly the ones at the edge of the bar. This is shown in Fig.4.35a and in Fig.4.35b. Several ribbons were bent, and flaking was detected along the edge of the bar. Moreover, due to the cutting, the insulation between ribbons was damaged which could result in short circuits between ribbons. The defects introduced by this method along with the high cost of the EDM and a large amount of wasted material make this methodology sub-optimal for loss reduction. Thus, this method was not pursued further.

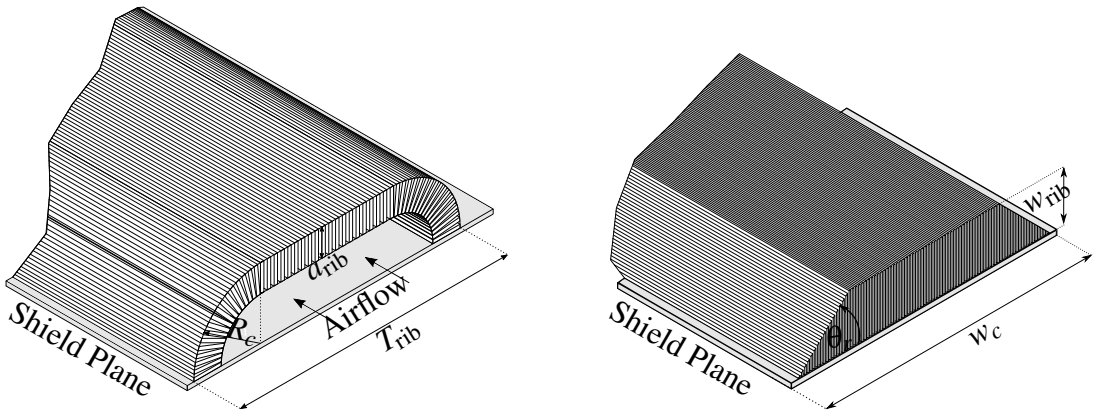

(a) (b)

Fig. 4.34 Proposed core cross-sections to mitigate the eddy-current losses in nanocrystalline ribbon cores. w_c: Core width. w_{rib}: Ribbon width. R_c: radius of curvature.

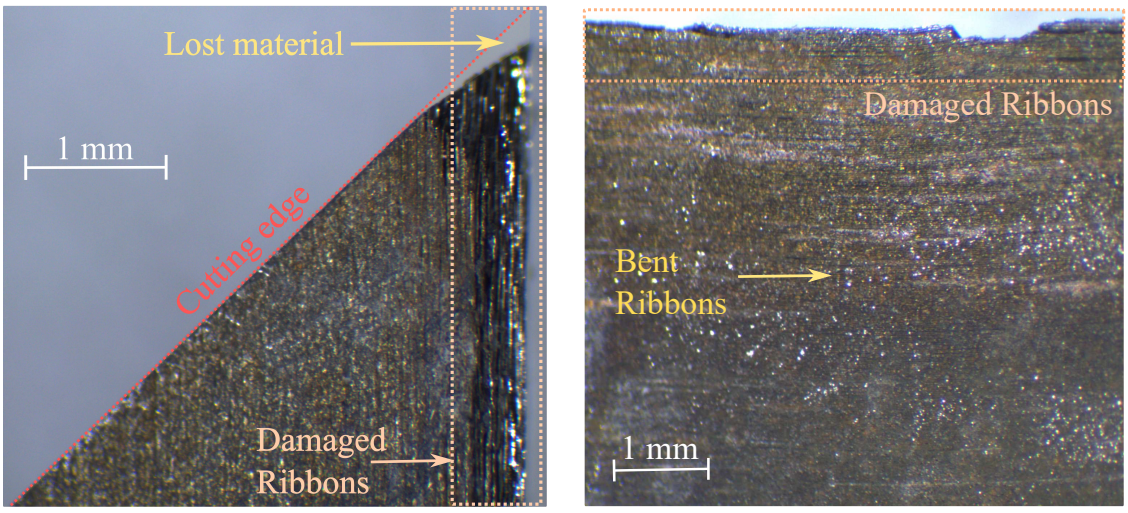

(a) (b)

Fig. 4.35 Images of the nanocrystalline ribbon core after being cut into a trapezoidal form. *a*) Cross-section *b*) Lateral face after the cut. The flaked, damaged, and bent ribbons are highlighted in the figure.

4.6.2 Core segmentation

In [17], core segmentation was introduced as a method to reduce the gap-losses in C-shaped nanocrystalline alloy inductors. Here, gap losses refer to the eddy-current losses induced in the core by the presence of the air gap between two C-shaped cores. A significant reduction of these losses was achieved by dividing the core into different segments as shown in Fig.4.36a. The eddy-current losses decrease exponentially with the number of core segments as seen in Fig. 4.36b.

Likewise, IPT cores can be segmented as shown in Fig.4.36c. The total core volume is constant, but the eddy-current loops can be reduced. For medium power levels, WPT1 and WPT2, core segmentation is not always possible since the required core thickness is less than 5 mm and it is already close to the manufacturing limits. For VACUUMSCHMELZE, the minimum width of the ribbon is 3.2 mm while it is 4 mm for AT&M and Hitachi Metals. Nonetheless, core segmentation is a viable alternative for high power IPT systems (>WPT3) that required thick cores such as the 50 kW studied in [9, 72]. These power levels are out of the scope of this dissertation. Further analysis is recommended as a topic for future work.

4.6.3 Core Slitting

In large electrical machines (generators), it is common to slit the stator-tooth laminations at both ends of the stator. Slitting reduces the eddy-current losses produce by the non-axial flux

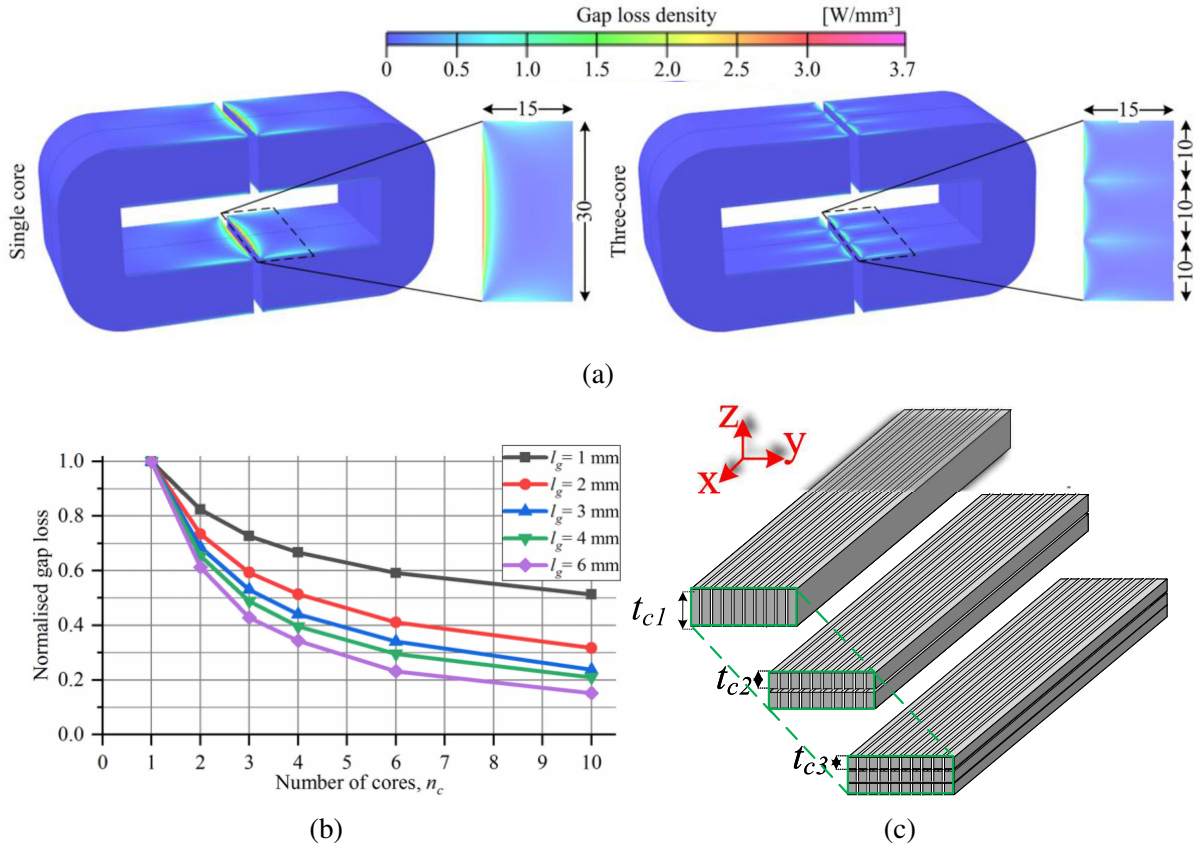

(a) (b) (c)

Fig. 4.36 Reduction of gap losses in nanocrystalline ribbon cores by segmenting the core. *a*) Gap losses in a nanocrystalline inductor for different number of segments in the core. The air gap between cores is 4 mm, $f_0 -$ 150 kHz. *b*) Normalized losses vs air gap between cores and number of core segments. *c*) Equivalent method applied to IPT cores. Here, $3 \cdot t_{c3} = 2 \cdot t_{c2} = t_{c1}$.

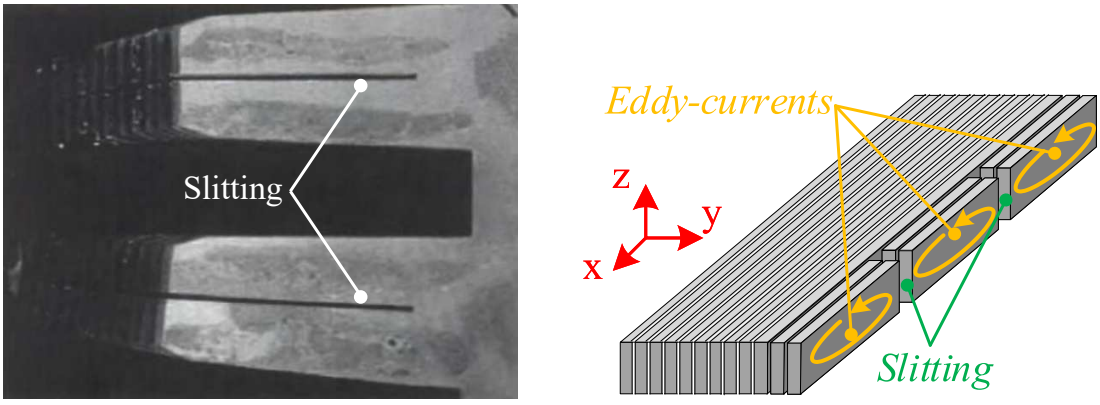

(a) (b)

Fig. 4.37 Depiction of core slitting. *a*) Core-End slitting of the core-end lamination of an electrical machine [29]. *b*) Slitting of IPT cores.

generated by the end-windings. An example of tooth-slitting is shown in Fig.4.37a [29]. This method can be applied to the lateral walls of the nanocrystalline ribbon core bars a shown in Fig.4.37b. The slit dimension has been exaggerated to ease the visualization. Slitting only applies to a portion of the bar since the ribbons in the center are not affected by the perpendicular flux. The number of slits per bar, depth of cut, and slit dimensions have an impact on the eddy-current losses. The cuts can be done parallel to the z axis (as in Fig.4.37b), parallel to the x axis, or at an angle. The former case, however, might lead to gap losses like the one seen in gapped inductors made with nanocrystalline ribbon cores as the slits are perpendicular to the main flux path. The introduction of slits can also decrease the effective permeability of the core. A quantification of this effect requires a deeper analysis and it is suggested as future work. It is worth noting that slitting the cores can lead to damage to the insulation between ribbons. A chemical etching is therefore required to ensure galvanic insulation after slitting [5]. Alternatively, several shorter cores can be manufactured and placed next to the core bar. This is equivalent to the core segmentation discussed previously.

4.6.4 Hybrid-cores: ferrite and nanocrystalline

The flux density in the core is not uniform. Higher flux density is encountered in the mid-section of the core bar, just below the flux pipe, as seen in Fig.3.15. In [59], this feature is exploited when designing the cores. The distribution of core material is adjusted according to the flux density; i.e., more material is placed below the flux pipe and less everywhere else, as seen in Fig.2.14c.

A similar strategy can be applied to pads using nanocrystalline alloy cores. Nanocrystalline alloys can be used in the mid-section of the core which is subjected to a higher flux density while ferrite can be used elsewhere. This hybrid-core can potentially lead to higher power densities without compromising efficiency, performance, or cost. Nonetheless, the mechanical robustness of the pad will still be compromised due to the brittleness of ferrite. The study of hybrid cores is not presented in this dissertation and it is suggested as a topic of future work.

4.7 Summary and Conclusions

This Chapter studied the design of IPT pads with nanocrystalline ribbon cores taking into account the anisotropic and particular properties of this material. Guidelines of design were first derived:

- For an optimal design, the core length and the percentage of the area of the pad covered by core material (A_c) ought to be maximized. Lengths between 82% and 88% of the pad's length are recommended. High values of A_c ($> 60\%$) are also suggested. As A_c increases, the losses in the core decrease.

- To limit the volume of core material, the thickness of the core can be defined as small as possible, provided that the core remains unsaturated. Slim cores help to reduce the eddy-current losses. With the current technology, the minimum core thickness commercially available is 3 to 4 mm. Hence, nanocrystalline ribbon cores are better suitable for high-power IPT systems.

- As opposed to ferrite cores where the use of core bars is advisable, core plates are recommended for IPT systems using nanocrystalline ribbon cores. Eddy-current losses increase exponentially with the separation between bars.

- The higher saturation flux density of nanocrystalline ribbon cores makes them ideal for IPT systems with small footprints, high power levels, and high power densities.

These guidelines were used in the design of an 11.1 kW WPT3/Z1 system. Ferrite and nanocrystalline ribbon cores were both tested under the same operating conditions. The main results and conclusion are:

- Compared to ferrite, the system with nanocrystalline ribbon cores yields superior magnetic performance in terms of coupling factor and mutual inductances. Similarly, lower leakage fluxes were measured. A reduction of up to 25% was achieved. Moreover, the efficiency of this system was between 1.3% and 2% higher than the system with ferrite cores. These results show that it is possible to design efficient IPT systems with nanocrystalline ribbon cores following the aforementioned guidelines. The efficiency can be further improved by using ferromagnetic shielding. The thickness of the shield should be adjusted as to not compromise the power transfer capability of the system.

- Additionally, the system showed superior thermal performance with lower thermal gradients and steady-state temperatures. Moreover, the higher saturation flux density allowed the system to operate at double its rated power while the system with ferrite cores saturated at a lower value. Thus, higher power densities can be achieved when using these cores.

The Curie temperature of nanocrystalline alloys lies around 570 °C. This value is almost twice the Curie temperature of MnZn ferrites. Thus, the operation at higher temperatures is a

clear possibility. By exploiting this advantage, IPT systems with nanocrystalline ribbon cores could operate at higher power levels and with minimum or without forced cooling. A careful evaluation is recommended for future work.

Chapter 5

Multi-frequency operation of a Double-sided LCCL compensated IPT system

In the previous chapters, it was shown that nanocrystalline ribbon cores can be used to design IPT systems with a high power density and small footprints. These highly dense systems are still expected to interoperate with other ferrite-based or even ferrite-less systems made by the same or different manufacturers. Inter-operability becomes then a clear challenge. The standard SAE J2954 was developed in an attempt to regulate and normalize IPT technology in terms of power levels, air gap tolerance, and health code compliance. However, there are several degrees of freedom when it comes to the design of an IPT system. Each pad can have a different coil topology (circular, Double-D, bipolar, etc.), coil dimensions, number of turns, compensation circuit, as well as voltage and current ratings. Thus, inter-operability of pads developed by different manufactures remains a current problem [31, 85, 49].

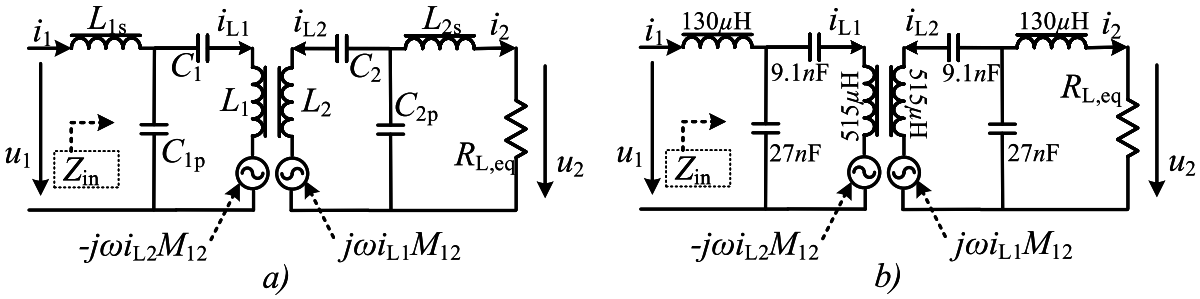

Fig. 5.1 Double-sided LCCL compensation topology (LCCL-LCCL). If $C_1 = C_2 = \infty$, this topology is referred to as LCL-LCL.

In this Chapter, a multi-frequency control strategy is presented for a double-sided LCCL compensated system. The strategy has the potential to facilitate the inter-operability of pads that were design for different voltage/current ratings or clearances between the transmitter and the receiver. Moreover, this strategy can be applied to systems with nanocrystalline cores to enhance their inter-operation capability. The Chapter begins with an analysis of the frequency response of LCL-LCL and LCCL-LCCL compensation topologies. Next, the control strategy is presented and validated via simulations and experimental results. Conclusions regarding the advantages and drawbacks of this control strategy are also presented.

5.1 LCCL-LCCL frequency response

The double-sided LCCL, also known as LCCL-LCCL, is shown in Fig.5.1.*a*. It was introduced previously in Section 2.3.5 for a fixed operating frequency f of 85 kHz. Here, the study is expanded to other operating frequencies. To understand the behavior of the system, the effective input impedance of the system, $Z_{in} = u_1/i_1$, must be analyzed. An expression for Z_{in} can be derived as shown in (5.1).

$$Z_{in}(\omega) = j\omega L_{1s} + \frac{\left(\omega L_1 - j\frac{1}{C_1\omega} - j\frac{M_{12}^2\omega^2}{\kappa}\right)}{C_{2p}\omega\left(j\omega L_1 - j\frac{1}{C_1\omega} - j\frac{1}{\omega C_{1p}} + \frac{M_{12}^2\omega^2}{\kappa}\right)} \tag{5.1}$$

where

$$\kappa = j\omega L_2 - j\frac{1}{C_2\omega} - \frac{j(R_{L,eq} + j\omega L_{2s})}{C_{2p}\omega\left(R_{L,eq} + jL_2\omega - j\frac{1}{C_{2p}\omega}\right)} \tag{5.2}$$

C_1, C_2, L_{1s}, L_{2s}, C_{1p}, and C_{2p} are the resonant tank components. They are tuned for a resonant frequency f =85 kHz ($\omega = 2\pi f$) following (5.3):

$$\omega^2 = (2\pi \cdot f)^2 = \frac{1}{L_{1s}C_{1p}} = \frac{1}{L_{2s}C_{2p}}$$
$$L_{1s} = L_1 - \frac{1}{\omega^2 C_1} \quad \text{and} \quad L_{2s} = L_2 - \frac{1}{\omega^2 C_1} \tag{5.3}$$

This way, at the resonant frequency, Z_{in} is real and a unity power factor is achieved. At any other frequency, however, Z_{in} would have both real and imaginary components depending on the operating conditions. Z_{in} depends on the equivalent load $R_{L,eq}$ and the coupling factor k. The former varies according to the battery management system (BMS) while the latter changes with the position of the pad. The effect of k and $R_{L,eq}$ in the frequency response is studied in

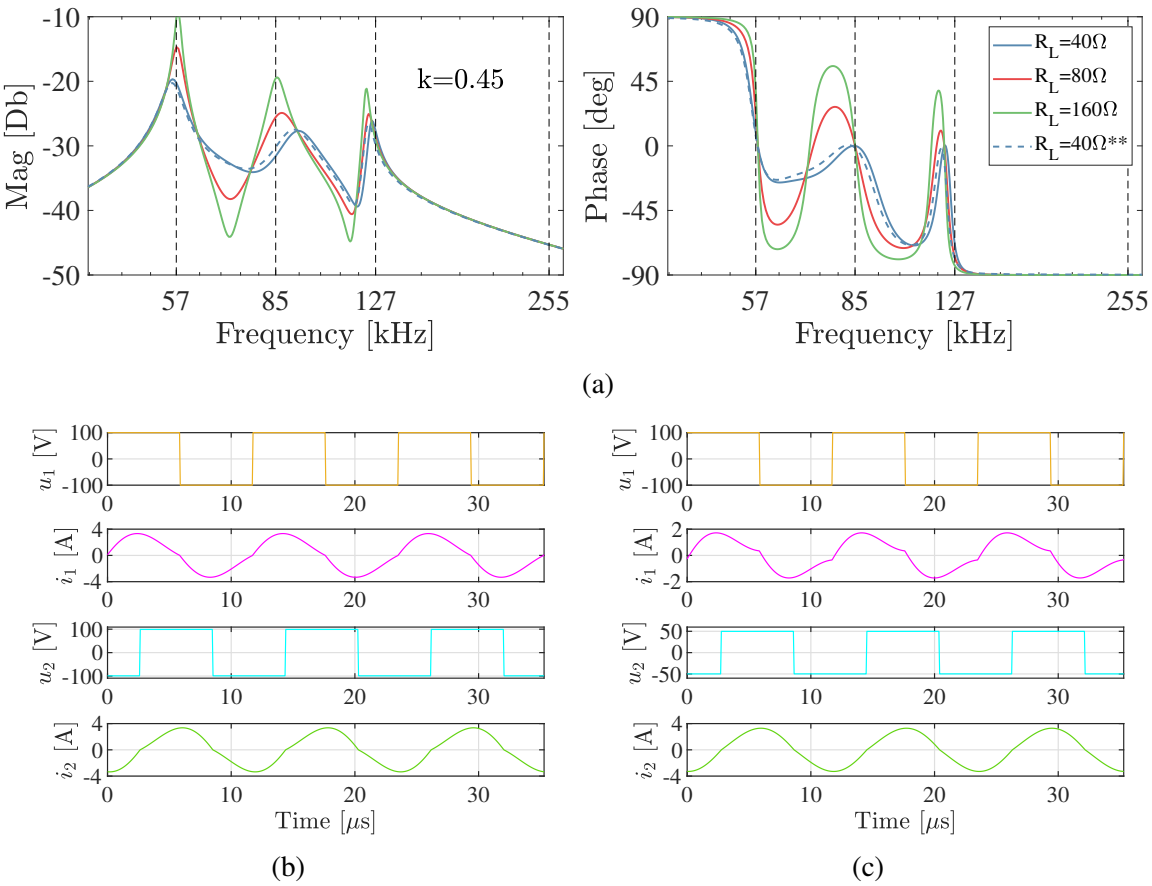

Fig. 5.2 Frequency response of an LCCL-LCCL compensated system and its operation at different loads. *a*) Frequency response of the LCCL-LCCL system shown in Fig.5.1.*b* highlighting the effect of $R_{L,eq}$ on Y_{in}. Simulation results of the primary and secondary converter current and voltages under different conditions: *b*) $R_L = 48\Omega$, $P_2 = 200$W. *c*) $R_L = 24\Omega$, $P_2 = 100$W. $k \sim 0.45$, $f = 85$kHz.

the next sub-sections. For this analysis, the input admittance $Y_{in} = 1/Z_{in}$ is considered, as opposed to Z_{in}, for sake of simplicity since Y_{in} is directly proportional to the input current. The analysis considers the DD pad tested in Chapter 3 (see Fig.3.12) and whose equivalent is depicted in Fig.5.1.*b*.

Effect of R_L on Z_{in}

Fig.5.2.*a* shows the frequency response of the input admittance, $|Y_{in}|$, for different equivalent load values $R_{L,eq}$. At f =85 kHz, $|Y_{in}|$ increases proportionally to the load $R_{L,eq}$. Thus, the power transfer is proportional to the load. This current-source behavior is typical of an IPT system with LCCL-LCCL compensation. From Fig.5.2.*a*, it is clear that LCCL-LCCL topology has two other secondary resonant frequencies: $f_{2,a}$ (57 kHz) and $f_{2,b}$ (127 kHz). The

location of these resonant frequencies changes only slightly with the load. Their magnitude, however, is directly proportional to the load, $R_{L,eq}$. For light loads, the value of $|Y_{in}|$ at the secondary resonant frequencies can be higher than that at the main resonant frequency.

Fig.5.2.*b* and Fig.5.2.*c* shows the primary and secondary converter voltages and currents for the IPT system in Fig.5.1.*b* and two different loads: 48Ω and 24Ω, respectively. As $R_{L,eq}$ decreases by 50%, so does the power transfer P_2 and the voltage u_2. This decrease is accompanied by an increment in the current harmonic content. This is because $|Y_{in}|$ at f =255 kHz (third harmonic) is almost independent of the load as seen in Fig.5.2.*a*. Consequently, higher harmonic content is expected at light loads (low $R_{L,eq}$ values). This can be seen when comparing Fig.5.2.*b* and Fig.5.2.*c*. In principle, harmonic content is not harmful to the system as the receiver side has a rectification stage. However, the harmonic content can affect the soft-switching strategy of the converters and it also radiate emissions. Current harmonics are also known to increase both coil and core losses.

Effect of k on Z_{in}

Fig.5.3.*a* shows the frequency response of the input admittance, $|Y_{in}|$, for different coupling factors. The input admittance $|Y_{in}|$ is *directly* proportional to the coupling factor at the main resonant frequency, f =85 kHz. Thus, more power is transferred to the load when the coupling factors are high. This matches the analysis presented in Section 2.3.5 and equation (2.17). Conversely, the magnitude of $|Y_{in}|$ at the second resonant frequencies is *inversely* proportional to the coupling factor. For low coupling factors, $|Y_{in}|$ at the secondary resonant frequencies can be higher than $|Y_{in}|$ at the main resonant frequency, f.

The location of the secondary frequency depends largely on the coupling factor. As k tends to zero, the secondary resonant frequencies converge to fixed frequencies that can be calculated analytically by means of (5.4):

$$f_{2,a} = f \cdot \sqrt{1 - \sqrt{\frac{1}{1 + C_{1p}/C_1}}}; \quad f_{2,b} = f \cdot \sqrt{1 + \sqrt{\frac{1}{1 + C_{1p}/C_1}}} \tag{5.4}$$

Considering f =85 kHz and the system parameters in Fig.5.1.*b*, $f_{2,a}$ and $f_{2,b}$ are approximately 60 kHz and 104 kHz, respectively. These frequencies are depicted in Fig.5.3.

Fig.5.3.*c* and Fig.5.3.*d* show the pad performance at two different coupling factors, 0.45 and 0.15, respectively. When k is reduced from 0.45 to 0.15, the power transfer decreases from 200 W to ∼68 W. Moreover, the current harmonic content is larger for the system with lower coupling. This is because the magnitude of Y_{in} at f_3 =255 kHz (third harmonic) remains

approximately constant regardless of the value of k. Thus, higher coupling factors lead to a lower current harmonic distortion. This can be seen when comparing Fig.5.3.*b* and Fig.5.3.*c*.

5.2 LCL-LCL frequency response

The LCL-LCL topology is a special case of the LCCL-LCCL. The input impedance Z_{in} can be computed from the equivalent LCL-LCL circuit shown in Fig.5.1.*a* neglecting C_1 and C_2. Z_{in} is then given by (5.5):

$$Z_{in}(\omega) = j\omega L_{1s} + \frac{\left(\omega L_1 - j\frac{M_{12}^2\omega^2}{\kappa}\right)}{C_{1p}\omega\left(j\omega L_1 - j\frac{1}{\omega C_{1p}} + \frac{M_{12}^2\omega^2}{\kappa}\right)} \tag{5.5}$$

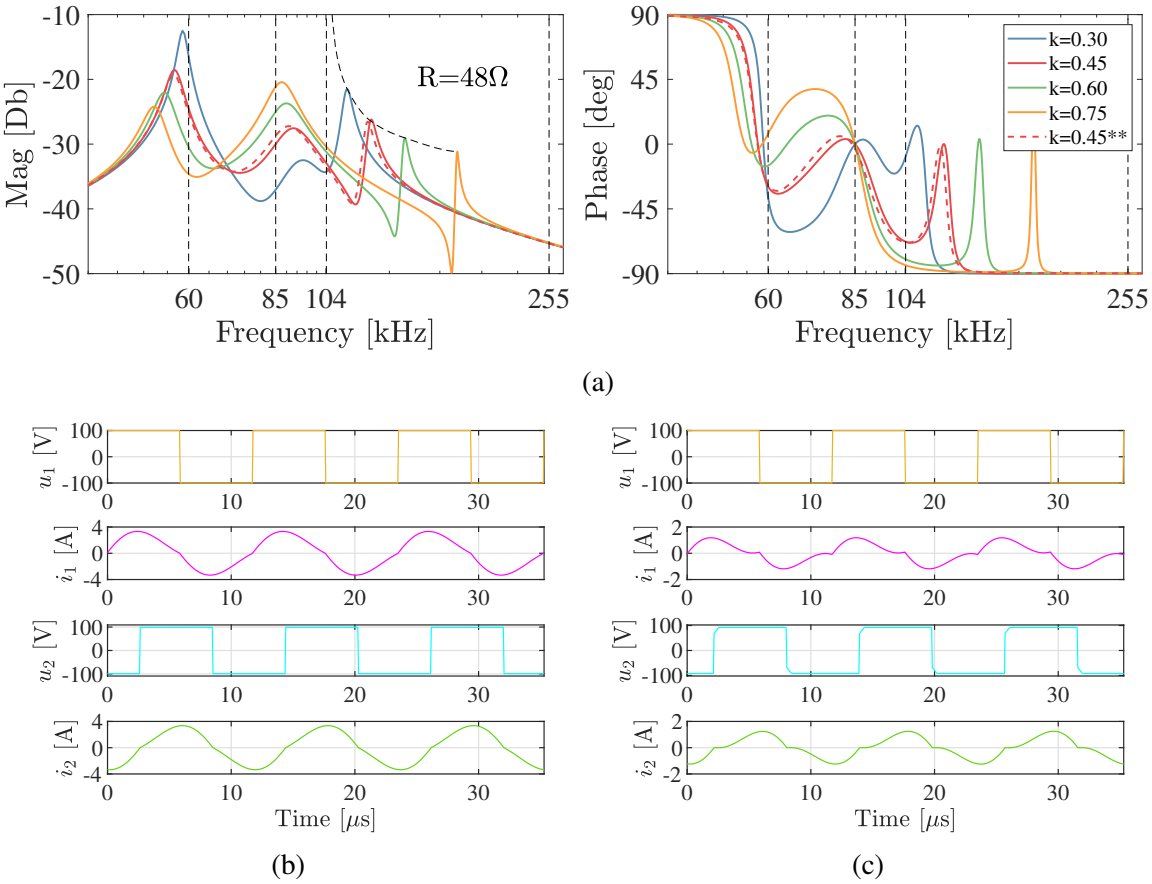

Fig. 5.3 *a*) Frequency response of the LCCL-LCCL system shown in Fig.5.1.*b* highlighting the effect of k on Y_{in}. Simulation results of the primary and secondary converter current and voltages under different conditions: *b*) $R_L = 48\Omega$, $k \sim 0.45$, $P_2 = 200$W. *c*) $R_L = 144\Omega$, $k \sim 0.15$, $P_2 = 59$W. $f = 85$kHz.

with

$$\kappa = j\omega L_2 - \frac{j(R_{L,eq} + j\omega L_{2s})}{C_{2p}\omega\left(R_{L,eq} + jL_{2s}\omega - j\frac{1}{C_{2p}\omega}\right)} \tag{5.6}$$

The components of the resonant tank, C_{1p}, C_{2p}, L_{1s}, and L_{2s} are tuned for f =85 kHz according to (5.7):

$$\omega^2 = (2\pi \cdot f)^2 = \frac{1}{L_{1s}C_{1p}} = \frac{1}{L_{2s}C_{2p}} \quad L_{1s} = L_1 \quad \text{and} \quad L_{2s} = L_2 \tag{5.7}$$

Similar to the LCCL-LCCL, the frequency response is affected by changes to the load and the coupling factor. This is discussed in the next sub-sections. Once again, the admittance Y_{in} is considered to ease the analysis.

Effect of R_L on Z_{in}

Fig.5.4.*a* shows the frequency response of the input admittance, $|Y_{in}|$, for different equivalent load values $R_{L,eq}$. The behavior of the LCL-LCL topology is similar to the LCCL-LCCL.

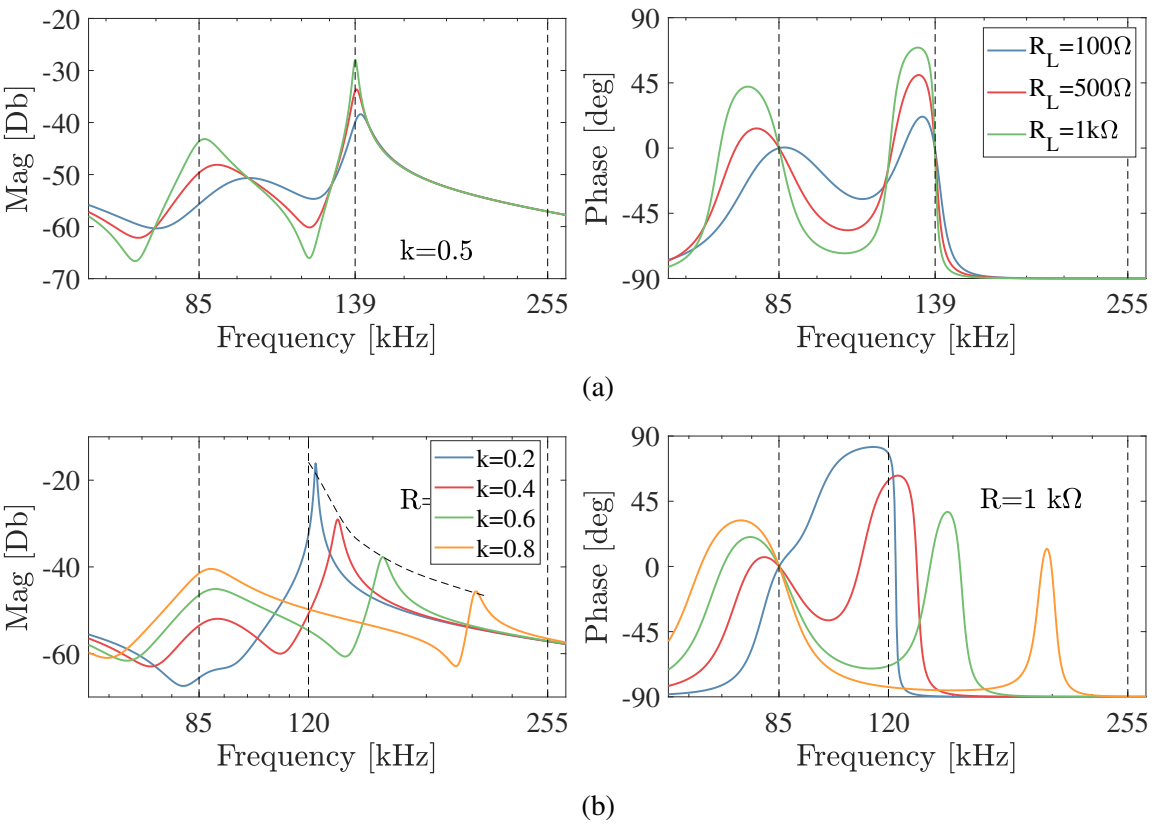

Fig. 5.4 Frequency response of the LCL-LCL system shown in Fig.5.1.*b*. *a*) Effect of $R_{L,eq}$ on Y_{in}. *b*) Effect of k on Y_{in}.

First, $|Y_{in}|$ is proportional to the load. Second, $|Y_{in}|$ at the third harmonic (255 kHz) is almost independent of the load. Thus, a higher harmonic content is expected at light loads. As opposed to the LCCL-LCCL, however, there is only one secondary resonant frequency, f_2 (139 kHz in this case). $|Y_{in}|$ at this frequency increases proportionally to the load. In some cases, particularly for light loads, Y_{in} at f_2 can be higher than at the main resonant frequency, f.

Effect of k on Z_{in}

Fig.5.4.*b* shows the frequency response of the input admittance, $|Y_{in}|$, for different coupling factors k. Y_{in} shows similar behavior as the one seen in the LCCL-LCCL topology. Y_{in} at the main resonant frequency is directly proportional to k. The opposite behavior is observed at the secondary resonant frequency f_2. The position of this secondary resonant frequency also changes with k. For low coupling factors f_2 converges to $f_1 \cdot \sqrt{2}$. For f_1 =85 kHz, f_2 is equal to 120 kHz as seen in Fig.5.4.*b*.

5.3 Summary of frequency response

From the analysis of the frequency response, the following conclusions can be drawn. First, the amplitude of the third harmonic is practically unaffected by the load or the coupling factor. As a result, current harmonics in the inverter currents are more important at light loads and low coupling factors. Second, the capability of the pad to transfer power at the main resonant frequency f is directly proportional to the coupling factor and the load, $R_{L,eq}$. Third, the LCCL-LCCL topology has secondary resonant frequencies. The capability of the pad to transfer power at these frequencies is inversely proportional to the coupling factor k. At partial load, the admittance $|Y_{in}|$ at the secondary frequencies can be higher than the one obtained at the main resonant frequency f. These features are used in the control strategy presented in the next section. The location of the secondary frequencies depends mainly on k. As k reduces, the second resonant frequencies converge to values closer to the main resonant frequency. If the parameters of the system are known, the location of these secondary resonant frequencies can be calculated using (5.4) for the LCCL-LCCL topology. Moreover, one can design the system to ensure that the secondary resonant frequencies lie on a particular frequency range. For the LCL-LCL topology, only one secondary resonant frequency exists. This frequency converges to $(f \cdot \sqrt{2})$ as the coupling factor tends to zero.

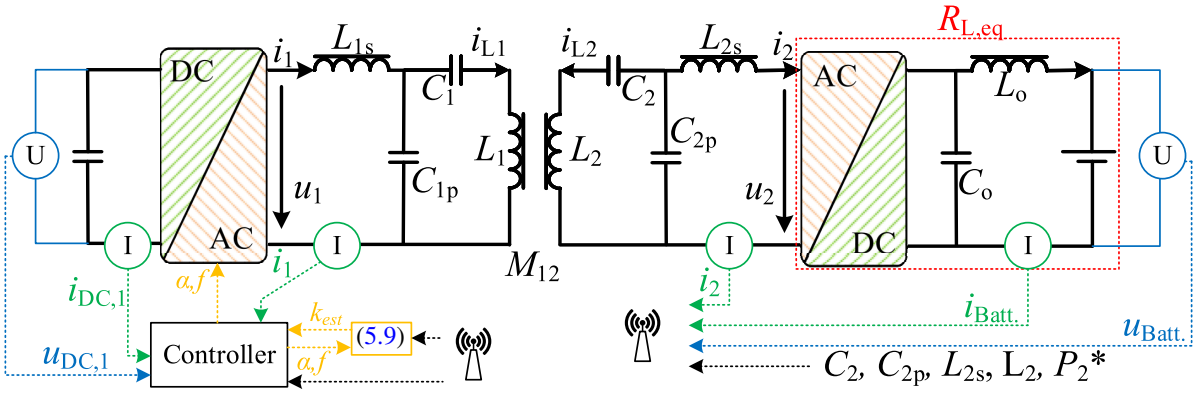

Fig. 5.5 Illustration of the multi-frequency control Strategy. C_o and L_o are the filter inductance and capacitance of the battery.

5.4 Control Strategy

The power transfer equation at the main resonant frequency f for an LCL-LCL or LCCL-LCCL compensated pad is given by (5.8):

$$P_2 = \frac{u_1 \cdot u_2 \cdot \sin(\theta)}{\omega} \frac{M_{12}}{L_{1s} L_{2s}} \tag{5.8}$$

where θ is the phase of the voltage imposed by the converter (usually 90°). From (5.8), it is clear that the maximum power transferred to the load is compromised for low values of M_{12}. This occurs when the pads are misaligned, the clearance between pads (air gap) increases, or when pads of different design (number of turns, size, etc.) are used. To increase the power transfer, one can increase the DC-link voltage; however, this voltage is usually limited by the rating of the converter. A viable solution, inspired by the analysis of the frequency response presented in the previous sections, is to utilize the secondary resonant frequencies. The capacity of an LCCL-LCCL IPT system to transmit power at these frequencies is inversely proportional to the coupling factor. Thus, for certain operating conditions, the operation at these resonant frequencies can be beneficial. Operation at the secondary resonant frequencies is also a viable solution for partial load provided that the magnitude of Y_{in} at f_2 is higher than it is at the primary frequency f. For these cases, operating at the second resonant frequency can lead to lower current harmonics and higher quality factors ($Q = \omega L_1 / R_{coil}$). A multi-frequency control strategy that takes into account these considerations is presented in this section. The control strategy is shown in Fig.5.5.

A simple system without an impedance matching stage is considered to demonstrate the advantages of multi-frequency operation. The normal operation of the system at the primary resonant frequency is as follows. First, the secondary pad communicates the power set-point

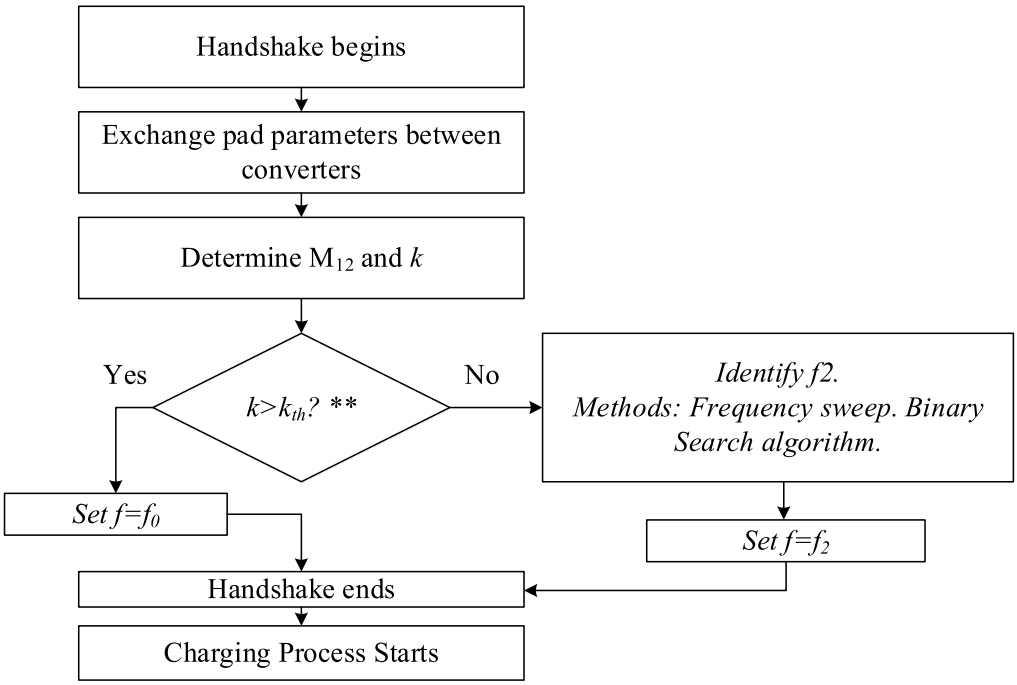

Fig. 5.6 Flow diagram of the handshake protocol required before the beginning of the power transfer for the multi-frequency control strategy.

(P_2*) as well as the system parameters (C_2, C_{2p}, L_{2s}, and L_2) to the primary pad. The primary converter adjusts the AC voltage u_1 according to the required power P_2*. This can be done by adjusting the firing angles in the primary converter (see Fig.2.22) or by controlling the DC-link voltage on the transmitter side.

The same principle of operation can be applied if the pad were to operate at a second resonant frequency. To determine when to operate at f or f_2, a handshake protocol is required before the start of the charging process. An exemplary handshake protocol is shown in Fig.5.6. First, the mutual inductance M_{12} and coupling factor k are estimated using a predefined sequence of test pulses along with measurements of i_2. This methodology of estimation of k is standard in IPT systems [11]. M_{12} is calculated using (5.9).

$$M_{12} \approx \frac{\pi}{4} \cdot |i_2| \cdot \frac{L_{1s} \cdot L_{2s}}{u_{DC,1} \cos(\alpha)} \tag{5.9}$$

where α defines the firing angle of the converter. With the information of M_{12}, k, P_2*, and $R_{L,eq}$, the controller can determine the frequency of operation. In this case, the coupling factor k_{th} is used as a threshold. For values of k lower than k_{th}, the secondary resonant frequencies are used. A threshold for the load can be also determined. If the operation at the secondary resonant frequencies is required, the controller will then identify their location and proceed with the normal operation.

Since the impedance Z_{in} changes significantly with the frequency, empirical methods are required to locate the secondary resonant frequencies. To locate these frequencies, two features can be used. First, at a resonant frequency, $|Y_{in}|$ is at a local maximum. Thus, finding the resonant frequency entails locating this maximum. For this, only the amplitude of the converter current needs to be measured. This can be done with a simple circuit such as the one shown in Fig.5.7.*a*. Second, at the resonant frequencies, the voltage and current waveforms are in phase. Thus, a zero-crossing circuit can be used to estimate the phase of the converter current with respect to the voltage. An exemplary circuit that achieves this is shown

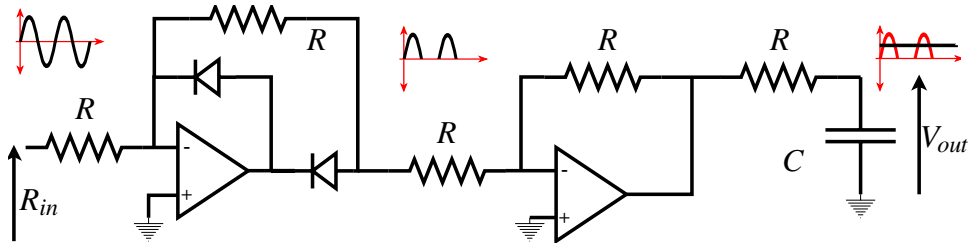

(a)

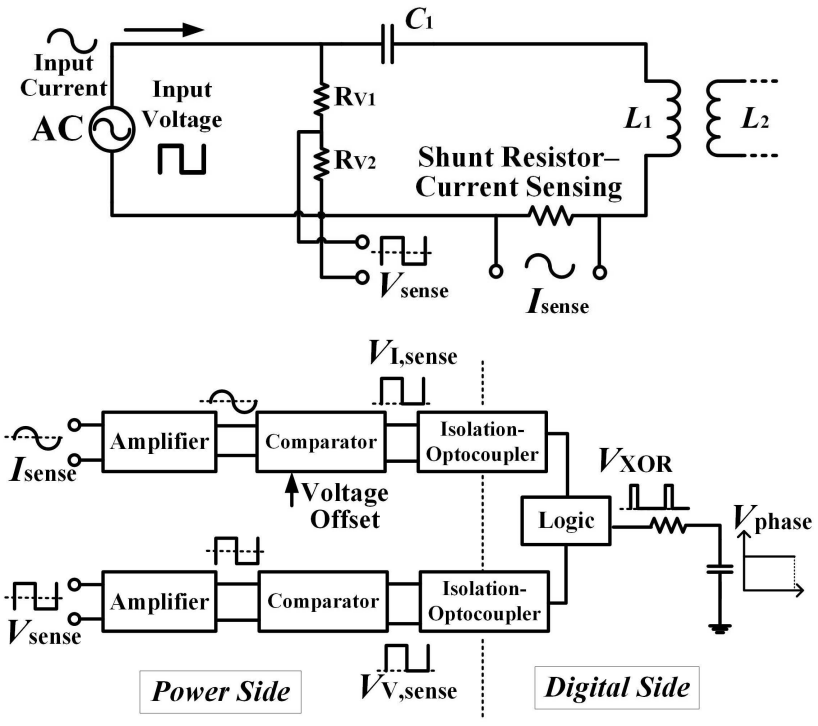

(b)

Fig. 5.7 Exemplary signal conditioning circuits for measuring the current magnitude and phase. *a*) The AC voltage generated by a current transducer is rectified and filtered. Only the magnitude is measured. *b*) Signal processing to estimate the phase difference between the converter current and voltage waveforms.

in Fig.5.7.*b* [52]. This method, however, can be more difficult to implement, particularly due to the noisy signals. Regardless of the strategy, a searching algorithm, like the binary search, is required to find the secondary resonant frequencies. While a frequency sweep scans all frequency, a binary search, also known as half-interval search, dissects the frequency space in two, evaluates them, and disregards one. This process continues until the desired frequency is found. Accurate initialization points for the searching algorithm can be found using (5.1). However, this can be mathematical/computational intensive. Alternatively, the initial points can be also estimated using (5.4) with less accuracy. Equation (5.4) is simpler and relies only on the capacitance values of the primary pad.

Once the secondary frequencies are located, the charging begins and power flow continues as usual: adjusting the voltage magnitude. Changes in the load or pad position can shift the secondary resonant frequencies. In this case, a tracking algorithm is necessary, similar to the Maximum Power Point Tracking (MPPT) algorithm used in solar PV systems. Dynamic tracking of the secondary frequencies is not presented in this dissertation and it is suggested as future work. Simulation and experimental results are shown in the next section to validate the proposed control strategy.

5.5 Simulation and Experimental Results

The pad presented in Chapter 3 is tested at two different coupling factors: $k = 0.45$ and $k = 0.15$. The parameters of the system are shown in Fig.5.1*b*). These coupling factors correspond to air gaps of 100 mm and 250 mm respectively. Such large changes to the coupling could result from paring transmitters and receiver pads of different classes (Z1, Z2, or Z3), power levels, or manufacturers. Three different operating modes are considered. Table 5.1 list the most important parameters for comparison. For all the operating modes, the battery voltage is set to 100 V. The maximum voltage in the converter is also limited to 100 V.

1. **Normal operation,** $k = 0.45$**,** f =85 kHz**:** The first mode, referred to as *normal operation*, is shown in Fig.5.8.*a*. The transmitter DC-link voltage is 100 V and the coupling

Table 5.1 Performance of an IPT system at three different operating points under the multi-frequency control strategy.

	Z* [mm]	k	Freq. [Hz]	$u_{1,DC}$ [V]	$R_{L,eq}$ [Ω]	$P_{DC,1}$ [W]	$P_{DC,2}$ [W]	η_{DC-DC} [%]	$P_{AC,1}$ [W]	$P_{AC,2}$ [W]	η_{AC-AC} [%]	$i_{1,pk}$ [A]	$i_{2,pk}$ [A]
1)	103	0.45	85	100	48	220	205	93.3	217	208	96.0	3.4	3.3
2)	250	0.15	85	100	144	73	66.9	91.5	70.6	67.2	95.2	1.0	1.1
3)	250	0.15	108	48	48	277	197	71.3	265	201	75.96	9.4	3.2

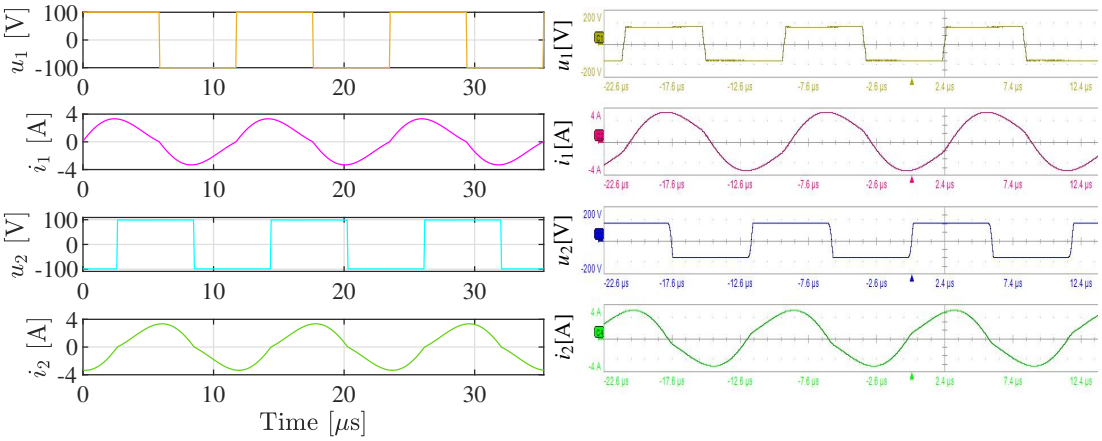

(a) *Normal Operation.* (Left) Simulation (right) Measurements.

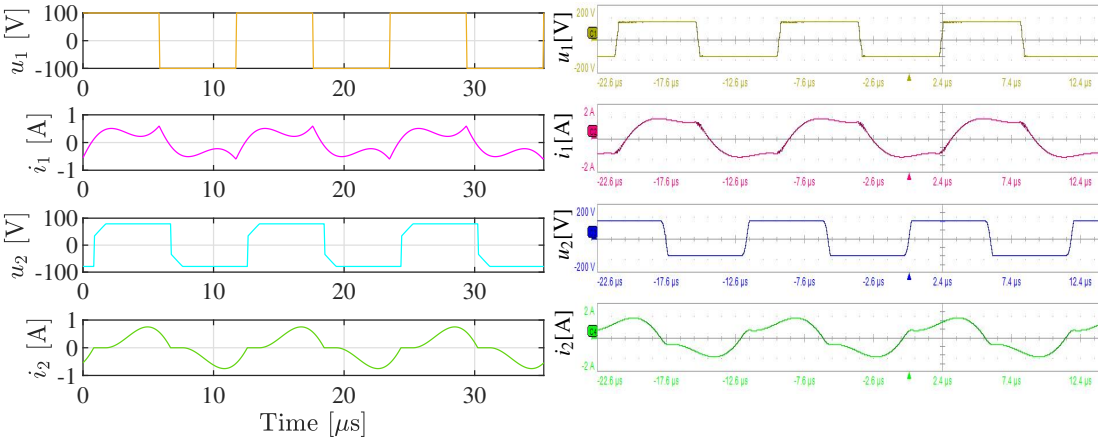

(b) *Low-k operation.* (Left) Simulation (right) Measurements.

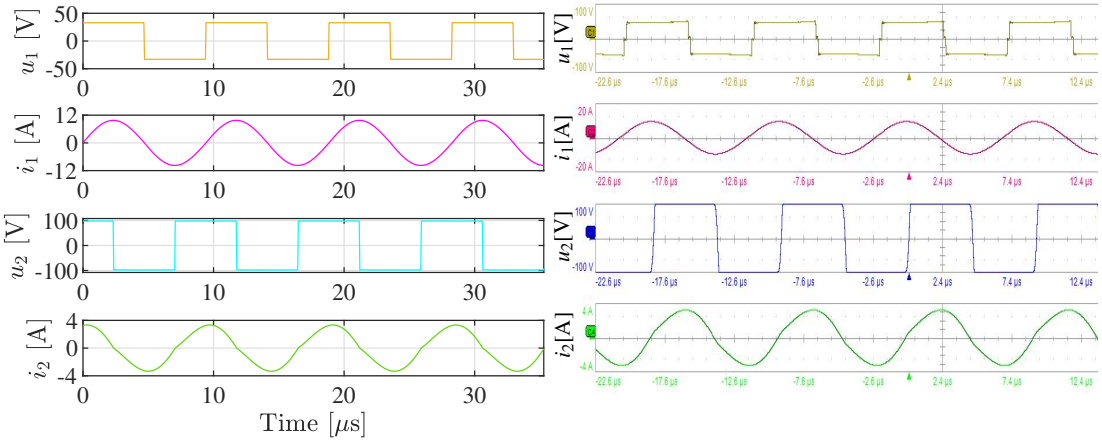

(c) *Low-k-f_2 operation.* (Left) Simulation (right) Measurements.

Fig. 5.8 Experimental validation of the multi-frequency control strategy. Three different operation modes ares tested. *a*) $R_L = 48\Omega$, $k = 0.45$, $f = 85$kHz,$P_2 = 200$W. *b*) $R_L = 144\Omega$, $k \sim 0.15$, $f = 85$kHz,$P_2 = 68$W. *c*) $R_L = 48\Omega$, $k = 0.15$, $f* = 106$kHz ($f_{exp} = 108.1$kHz),$P_2 = 200$W.

factor is 0.45. The pad transmits approximately 200 W at 85 kHz. The currents have a low harmonic content.

The converter currents i_1 and i_2 are almost the same. This is because the transmitter and receiver pads are practically identical, and the DC-link bus and battery voltages are the same (100 V). As a result, the system operates at the maximum AC efficiency since the load matching factor is optimum (see Section 2). An AC efficiency (without considering converter losses) of 96% is achieved.

2. **Low-k operation,** $k = 0.15$**,** f =85 kHz**:** In the second operating mode, the air gap is increased which reduces the coupling factor to 0.15. The increase in the air gap also changes the self-inductances of the pads: L_1 and L_2. As a result, the primary resonant frequency is no longer at 85 kHz. The power factor is, therefore, no longer unity when the system is operated at 85 kHz. The current waveform is also affected as the equivalent impedance is now partially capacitive. Furthermore, the lower coupling factor implies an increase in the harmonic content of the current as seen in Fig.5.8.*b*.

   The power transfer capability of the pad is also diminished due to the lower coupling factor. At 85 kHz, the simulation estimates that the maximum power transfer is only 68 W at the maximum DC-link voltage (100 V). In practice, only 59 W are transferred to the load when the primary converter is at its rated voltage. The difference is attributed to the coil, core, and converter losses which are not perfectly accounted for in the simulation.

   The power transfer efficiency drops to 95%. The drop in efficiency is due to the lower coupling factor. The load, however, is still close to the optimum load matching factor at which the maximum efficiency is achieved. This is demonstrated by the fact that the converter currents and voltages are approximately the same.

3. **Low-k-**f_2 **operation,** $k = 0.15$**,** $f = f_2$**:** In this mode, the secondary resonant frequency $f_{2,b}$ is used to increase the power transfer capability of the system. First, a frequency sweep is performed. From (5.1), the secondary resonant frequency $f_{2,b}$ was calculated as 106 kHz. This frequency is used as a starting point for the searching algorithm. The secondary resonant frequency was found to be 108.1 kHz.

   The magnitude of Y_{in} at the secondary frequency $f_{2,b}$ is larger than that at f_0. Thus, for the same DC-link voltage, the power transfer capability of the pad increases. In the simulation, a DC-link voltage of 33 V is enough to provide the required 200 W to the load. In practice, a slightly higher voltage was required, 40 V. The extra required voltage is necessary to compensate for the losses in the pad.

Apart from improving the power transfer capability of the pad. Operating at $f_{2,b}$ reduces the third harmonic content of the current as seen when comparing Fig.5.8.*b* to Fig.5.8.*c*. This facilitates the implementation of soft-switching techniques. The system can be operated at a frequency slightly higher than $f_{2,b}$ to ensure ZVS.

As seen in Table 5.1, the current in the primary converter is almost 3 times higher than that of the secondary side. As a result, the optimum load matching point is no longer sustained. As discussed in Chapter 2, the efficiency drops when operating at sub-optimal load matching factors. An efficiency of 76% was measured. It is worth noting that this effect is not particular to this control strategy but arises from the operation at off-rated conditions. This is explained more clearly in the next section.

Operation with an impedance matching circuit

Table 5.2 compares the operation of the LCCL-compensated system under different scenarios. The first case, against which all other cases are compared, corresponds to the operation at rated conditions: $k = 0.45$. For all the other cases, the coupling factor is lower: 0.15. Case 2) corresponds to the one analyzed in the previous section: operation without an impedance matching circuit at the rated frequency. The lack of an impedance matching circuit restricts the power transfer to approximately $P_2/3$. However, the load matching factor is kept at its optimal as the currents and voltages are the same for both the transmitter and the receiver side. Hence, high efficiency is achieved.

An impedance matching circuit is added at the receiver side in the Case 3). With this, the equivalent resistance $R_{L,eq}$ can be adjusted to allow the transfer of the rated power P_2. As a result, the secondary DC-link voltage and the coil current ($i_{L,2}$) triple. Thus, the load matching factor is sub-optimal which yields a lower efficiency. The losses are concentrated in the secondary coil as the current is 3 times the rated one. The currents in the primary side, on the other hand, are the same as in the rated case 1).

Table 5.2 Simplified comparison of the operation of the LCCL system

#	$u_{DC,1}$	$i_{1,rms}$	$i_{L1,rms}$	k	$i_{L2,rms}$	$i_{2,rms}$	$u_{DC,2}$	$R_{L,eq}$	P_2	γ	$Freq.$
1)	U_{max}	i	i_L	0.45	i_L	i	$U_{batt.}$	R_L	P_2	Opt.	f_1
2)	U_{max}	$i/3$	i_L	0.15	i_L	$i/3$	$U_{batt.}$	$3 \cdot R_L$	$P_2/3$	Opt.	f_1
3)	U_{max}	i	i_L	0.15	$3 \cdot i_L$	$i/3$	$3 \cdot U_{batt.}$	$9 \cdot R_L$	P_2	Sub-opt.	f_1
4)	$U_{max}/3$	$3 \cdot i$	$2.3 \cdot i_L$	0.15	$1.3 \cdot i_L$	i	$U_{batt.}$	R_L	P_2	Sub-opt.	f_2

i =3.14 A i_L = 1.7 A U_{max} =100 V $U_{batt.}$ =100 V R_L =48 Ω P_2 =200 W

Case 4), on the other hand, presents the operation of the system at the secondary resonant frequency. As discussed in the previous section, the rated power P_2 can be transferred without the need for an impedance matching circuit. Similar to the case 3), however, the load matching factor γ is sub-optimal. This is evidenced by the difference between the currents in the primary and secondary circuits. As opposed to the case 3), nonetheless, the losses are concentrated on the primary rather than the secondary circuits. This is favorable as losses in the stationary ground pad can be more easily handle since the size and the weight of this pad are of less importance. Last, since an impedance matching circuit is not required, its associated losses are omitted.

Operation at the secondary resonant frequencies is also possible with an impedance matching circuit at the secondary side. The added degree of freedom can be used to improve the load matching factor. This analysis is not presented in this thesis and it is suggested as future work.

5.6 Considerations for Multi-frequency operation

The multi-frequency operation could facilitate the integration and the interoperability of IPT pads with different designs and power levels or chargers placed on EVs with different chassis heights. The harmonic content can also be improved which facilitates the implementation of soft-switching techniques. Two important features, however, must be considered when designing such systems. The higher power transferred achievable with this methodology implies that higher currents will circulate through the coils and compensation elements. Thus, the voltage and current rating of these components must be designed carefully considering the critical operating points that exert the highest stress in the components. Moreover, since the magnitude of the gain of the admittance $|Y_{in}|$ at the secondary frequencies can be large, de-rating of the DC-link voltage or a closed-loop current control is required to avoid over-currents. Finally, it is worth remembering that the secondary resonant frequencies change slightly with the load but largely with the coupling factor. Thus, this control strategy is not recommended for systems in which the mutual coupling changes frequently during the charging process like in dynamic charging. For static charging, the coupling factor does not change during operation. This eases the implementation of this strategy.

5.7 Summary and Conclusions

In this chapter, a review of the state-of-the-art frequency response of LCL and LCCL compensation topologies is presented. Based on the multi-resonant performance of these topologies, a multi-frequency controls strategy is suggested. The most important conclusions are:

- LCL and LCCL compensation topologies have more than one resonant frequency. These frequencies shift slightly with the load but largely with the change of coupling. As the coupling reduces, the resonant frequencies converge to values that can be determined analytically.
- For LCL or LCCL compensated systems, light loads and low coupling factors result in currents with high harmonic content which can reduce the system's efficiency and restrict soft-switching operation.
- Operating the system at the secondary resonant frequency can improve the power transfer capability of the system under off-rated conditions (lower coupling factor). Thus, more power can be transferred without using an impedance matching circuit. Moreover, this control strategy can reduce the harmonic content of the converter currents.
- Multi-frequency control can facilitate the inter-operability of pads of different sizes and power levels of EV's with different chassis heights.
- Since the input impedance Y_{in} can be large, the inverter current limits may be exceeded. This needs to be considered during the design and operation of the system.

The control strategy presented here is a proof-of-concept and requires further analysis. For instance, the optimum design of an LCCL-LCCL pad intended purposely for the operation at two different frequencies is required. Moreover, the dynamic tracking of the secondary resonant frequencies is another topic for further research. Finally, an impedance matching circuit at the secondary side can be used to improve the load matching factor and efficiency. This analysis is not presented in this thesis and it is also suggested as future work.

Chapter 6

Conclusions and Future Directions

Inductive power transfer (IPT) is a key technology to accelerate the adoption of electric vehicles. First, it increases safety by limiting user interaction with high-voltage galvanic terminals. Second, IPT technology allows for automation of the charging process. This not only increases the user's comfort but also allows for vehicles-to-grid (V2G) and opportunity-charging schemes. Through V2G, the battery of every EV works as a storage unit for the grid, facilitating peak-shaving and the integration of renewable generation. Opportunity-charging schemes, on the other hand, can reduce the range anxiety of EV users, reduce the depth-of-discharge of batteries, and increase their lifespan. The work presented in this thesis had the objective of enhancing the state-of-the-art of this technology by addressing some of the remaining challenges. In particular, this thesis focuses on the improvement of the magnetic performance of the charging pads to increase their power density, efficiency, and reliability. The following sections summarize the work presented in this thesis and suggest directions for future work.

6.1 Summary and Conclusions

In recent years, the improvement of the magnetic performance of IPT systems has received a lot of attention from industry and academia. Different coil topologies for single-phase and three-phase systems have been proposed – DD, bipolar, tripolar, 3-phase DD, etc. Different shielding materials and methods (reflection winding, aluminum/nanocrystalline shielding) have been also introduced. Likewise, the magnetic core has been the focus of attention. Most IPT systems use MnZn as a core material. This material presents several drawbacks when used in IPT systems. First, its permeability and saturation flux density are both relatively low when compared to other ferromagnetic materials. Higher permeabilities are desired to improve the coupling factor and reduce the leakage flux. At the same time, higher saturation flux densities are required to increase the volumetric and gravimetric power densities. Second, ferrite is

brittle, particularly when manufactured as pieces with large footprints and small thicknesses. This reduces the reliability of the system particularly when the system is exposed to harsh environmental conditions. Finally, the magnetic properties of ferrite change drastically with temperature. This stresses the requirements of the cooling system and hinders the design of high-power-dense systems and their reliability.

The optimization of the ferrite core has been studied by different researchers. The use of polymers along with ferrite cores has also been proposed to reduce the amount of ferrite. However, in most cases, the designs are constrained by the brittleness and saturation flux density of this material. Ferrite-less or coreless designs have been also investigated in recent years. These pads can achieve adequate performance at the expense of higher VA ratings. In this thesis, the use of nanocrystalline ribbon cores as cores of IPT systems is presented. Nanocrystalline alloys have several properties that make them ideal for IPT applications. First, higher permeabilities can be achieved, up to 100 times higher than the one achieved with ferrites. Moreover, the saturation flux density of these materials is up to three times that of ferrite. Additionally, these materials are metallic, malleable, and mechanical more robust than ceramic ferrite cores. Finally, the Curie temperature of these materials is around 570 °C and hence they can operate at high temperatures.

The analysis of nanocrystalline core began in Chapter 3 with the modeling of IPT systems using nanocrystalline ribbon and ferrite cores. The modeling of nanocrystalline ribbon cores was not a trivial task due to the drastic ratio between the dimension of the domains. The ribbon thickness is in the micrometer range while the dimension of the IPT system can be up to 80 cm for some designs. Homogenization methods were used to simulate the laminated nanocrystalline ribbon cores as a single unit. For this, the electromagnetic properties of the core had to be defined as tensors with different values on every axis. Lower conductivity and permeability values were defined in the axis perpendicular to the ribbon. Moreover, saturation was also considered which resulted in non-linear FEM simulations for which the meshing become a crucial element. For a base of comparison, a typical IPT system with 4 segregated core bars was considered during the FEM analysis. Ferrite and nanocrystalline ribbon cores were tested and compared. The results show that the higher permeability of the nanocrystalline alloys improves the magnetic performance of the pad but only marginally. This is because the air gap between pads dominates the reluctance of the magnetic circuit formed by the transmitter and receiver pads. Improvements between 5% to 10% are expected depending on the air gap. Due to the anisotropic character of the nanocrystalline ribbon cores, the flux density in the core is nonuniform and it concentrates at the lateral faces of the core bars. The flux entering these faces also produces eddy-current losses which first, reduce the magnetic performance of the pad, and second, cause severe losses in the system.

A test rig was built to test the nanocrystalline cores. The test rig included dedicated SiC-based power electronics, compensation circuits, and measuring equipment. The experimental results validated the simulation results. Higher-self and mutual inductance values were achieved with the nanocrystalline ribbon cores. However, its improvement was minimum (5%). The efficiency of the pad with nanocrystalline cores was measured as 88% while the one with ferrite core was measured as 97%. In general, nanocrystalline ribbon cores have lower hysteresis losses. However, the flux entering the lateral walls of the core increases the flux density in these regions and the hysteresis losses. These losses along with the eddy-current losses are the reason for the lower efficiency values. According to the simulations, and validated later through thermal image testing, the losses are concentrated on the lateral faces of the core bars. The rest of the bar (majority) showed lower losses and lower flux density values. Since the saturation flux density of the nanocrystalline ribbon cores is large (1.25T) higher power densities can be achieved. However, to makes use of this potential, the losses produced by the eddy-currents ought to be mitigated. This was analyzed more deeply in Chapter 4.

To reduce the eddy-current losses, different methods were first proposed: 1) the modification of the core geometry, 2) the optimum design of the core, and 3) the use of hybrid (ferrite and nanocrystalline) core geometries as well as ferromagnetic shielding. Core slitting and the modification of the core cross-section were quickly discarded due to the difficulty of manufacturing nanocrystalline ribbon cores of unusual cross-sections or reshaping the core after construction. Although the core bars are mechanically more robust (higher yield strength) compared to ferrite (ceramic), machining the bars after construction produces flaking and jeopardizes the integrity of the insulation between ribbons. As an alternative method, the core design process was carefully analyzed to determine guidelines that considered the anisotropic properties of the nanocrystalline ribbon cores into account. First, the effect of the dimensions of the core (length, width, thickness, and the number of core bars) on the power transfer capability of the pad (P_{su}) and the maximum flux density within the core (B_{max}) was studied. The analysis shows that the length of the core and the percentage of the pad's area covered by core material (A_c) are keys to achieve higher values of P_{su}. P_{su} is also improved by using more core bars but only for low values of A_c. For larger values of A_c, the number of cores used has less importance. On the other hand, the thickness of the core (t_c) was found to be critical in reducing B_{max} but its impact on P_{su} was found to be less important. Thus, t_c can be adjusted during the last stage of design to ensure the core remains unsaturated. A Pareto-front was found between the volume of the core material and P_{su}. Contrary to what was expected, P_{su} remains fairly constant and only decays for very low volumes of the core material. Thus, higher core utilization factors can be achieved by selecting a core design at the knee point of the Pareto-front. Designs at this point are however constrained by the saturation

point of the core material. For pads with small footprints, especially, designs at the knee of the Pareto-front are only achievable with materials that possess high saturation flux density such as nanocrystalline ribbon cores. A second study was done in which the effect of the core dimension on the hysteresis and eddy-current losses were analyzed. The study revealed that increasing A_c permits a reduction of the core loss. Likewise, the use of slimmer cores also helps to reduce eddy-current losses. These analyses were used to determine guidelines for the design of nanocrystalline ribbon cores.

For IPT systems, long and monolithic magnetic cores without air gaps are advantageous; particularly for polarized IPT pad designs where the mainstream magnetic flux is conducted along with the length of the core. A length between 80% and 88% of the pad's length is recommended. To reduce eddy-current losses, the core ought to cover a large portion of the pad's area. Full coverage of the pad's flux-pipe is recommended. The core thickness can be reduced when the coverage is increased to reduce the core volume and eddy-current losses. The core thickness, however, must be adjusted to prevent saturation. Commonly, the minimum width of the ribbon commercially available for core production is between three to four millimeters, depending on the manufacturer. Thus, nanocrystalline ribbon cores with vertically-aligned ribbons are better suitable for high-power IPT systems. The design guidelines can be also used for ferrite cores; however, ferrite cores show different dimensional limitations. It is difficult to make ferrite cores with large footprints, particularly when the ratios of length-to-thickness and width-to-thickness are large. Thus, multi-piece cores a more viable solution. Nonetheless, undesirable air gaps between pieces are inevitable. On the positive side, since the eddy-currents are not a significant issue for ferrite cores, the percentage of the pad's area covered by core material (A_c) can be relaxed as compared to the cores made with nanocrystalline ribbon cores. Thus, the design process is different for nanocrystalline ribbon and ferrites cores.

These guidelines were put into practice in the design of a 11.1 kW pad with a footprint of 420 mm$\times$210 mm. Simulation results showed that using nanocrystalline ribbon cores, superior magnetic performance and efficiency can be achieved. This was validated experimentally. The pads with nanocrystalline ribbon cores improved the coupling factor by 11% and the mutual inductance by 23% compared to ferrite cores. The improvement was slightly larger than expected from the simulations due to the air gaps between ferrite tiles that made up the core. Even when closely packed, the air gaps between tiles are unavoidable due to manufacturing tolerances. These gaps reduce the overall permeability and the magnet performance of the pad. Better performance can be achieved with larger ferrite pieces; however, manufacturing ferrite cores with large footprints is difficult as breakage can occur during fabrication due to the thermal gradients. Moreover, larger pieces can more easily break during handling. The intersection between ferrite tiles is prone to hot spots and localized saturation. Hot spots can

be reduced by increasing the separation between tiles at the expense of magnetic performance. Nanocrystalline ribbon cores, on the other hand, can be constructed as long bars. Thus, no air gaps are included in the flux path. Hence, superior magnetic and thermal performance can be obtained.

Apart from the superior magnetic performance, the pads with nanocrystalline ribbon cores also achieved higher efficiencies compared to those with ferrite cores. A 2% higher efficiency was achieved for the same operating conditions. The lower losses are attributed to the higher coupling factor and lower hysteresis losses of the nanocrystalline ribbon cores. This shows that high efficiency can be achieved with this material. However, these results also show that an adequate design process, different from the one used for ferrite cores, is critical to take advantage of the superior electromagnetic properties of this material. The higher efficiency of the pad yielded lower core temperatures in steady-state. Along the y-axis, slightly higher temperatures were obtained in the center of the pad and the sides of the bar, where the flux concentration and eddy-currents are larger. The temperature distribution at the sides of the core can be improved by using ferromagnetic shielding. Shielding can also improve the efficiency of the system. Along the ribbon length, on the other hand, the temperature distribution was relatively uniform. This is due to the high thermal conductivity of this material. On the other hand, the temperature distribution in the ferrite cores was less homogeneous. Large temperature gradients were observed in the core, generated by the hot spots between tiles. A better temperature performance can be achieved by increasing the air gap between tiles to reduce the hot spots. This however proved to be detrimental to the magnetic performance of the pad.

The performance of the pad to temperature variations was also studied. For both materials, temperature increments reduce the mutual inductance between pads. This change was lower for the pad with nanocrystalline ribbon cores; i.e., these cores are more robust to temperature variations. Regarding efficiency, ferrite and nanocrystalline ribbon cores exhibit opposing behaviors. In the case of ferrite cores, the power losses decrease with the temperature. However, this reduction only holds until approximately 100 °C. For higher temperatures, hysteresis loss increase once again. Contrarily, for the nanocrystalline ribbon cores, the losses increase monotonically with temperature. The rate of increment is moderate which ensures that the reduction of efficiency is minimum. Even that 100 °C (optimal temperature for the pad with ferrite cores), the efficiency of the pad using nanocrystalline ribbon cores was 1.26% higher than that of the pad with ferrite cores. This shows that the performance of nanocrystalline ribbon cores at high temperatures ($\geq$100 °C) is superior. This conclusion is supported by the fact that the saturation flux density of ferrite decays drastically with the temperature. For most ferrites, it halves between 100 °C and 150 °C. The saturation point of nanocrystalline ribbon cores is two

to three times larger than that of ferrite. As a result, more power can be transferred between pads for the same core volume; i.e., higher power densities can be achieved. This was validated experimentally. Furthermore, the saturation flux density versus temperature decreases at a slower rate than in ferrites. Thus, nanocrystalline cores can operate at higher temperatures without compromising majorly the performance of the pad or its reliability.

The results obtained from Chapter 3 and 4 show that nanocrystalline ribbon cores can be effectively used in IPT applications. The analysis presented in Chapter 4 shows that the vertically-oriented nanocrystalline ribbon cores are particularly important in the design of pads with smaller footprints, high power levels, and high power densities. The smaller footprints and superior magnetic performance reduce the leakage flux. Up to 25% lower leakage fluxes were measured when using these cores as opposed to ferrite cores. This eases the compliance of safety regulations which in turn accelerates the adoption of IPT systems. Moreover, pads using nanocrystalline ribbon cores achieve higher efficiencies and power densities. Also, superior performance at high temperatures is attainable. This facilitates the design of systems with high power densities and relaxes the requirements of the cooling system. The design and simulation methods presented in this thesis can be used in the further analysis of these cores. Suggested directions for future research are presented in the next section.

Finally, a minor contribution was also presented in Chapter 5 for IPT systems operating with LCL-LCL or LCCL-LCCL compensation circuits. These systems are known for having more than one resonant frequency. These secondary resonant frequencies can be designed to be within the desired frequency range (e.g., 70-100 kHz). When the pads become misaligned, the capability of the system to transfer power at the main resonant frequency decreases. At the same time, the amount of power that can be transferred at the secondary resonant frequencies increases. A control system that takes advantage of this phenomenon is presented in this thesis. This control can improve the power transfer capability of the pad at different air gaps between Tx and Rx and misalignments. Moreover, it can facilitate the interoperability of pads from different manufacturers. Experimental results validated this control strategy.

6.2 Future Work

Future direction for research are listed below:

- **Analysis of the thermal performance of nanocrystalline ribbon cores at high temperatures ($\geq$200 °C):** The Curie temperature of the nanocrystalline alloys is around 570 °C. Thus, in principle, pads with nanocrystalline ribbon cores could operate at very high temperatures. This can be beneficial for systems with high power ratings and densities. The maximum temperature in the pad is restricted by the temperature rating of

the binder used between ribbons, winding insulation, and fixtures used to hold the components in place. Nonetheless, operation above 200 °C is not unrealistic. Ferrite cores cannot operate at these temperatures due to their lower Curie temperature. With the increasing temperature, copper and core losses increase. A careful analysis of IPT systems with nanocrystalline ribbon cores operating at high temperatures is therefore required to evaluate the efficiency, power transfer capability, and reliability of the system at these operating conditions. For this, a thermal chamber is required to guarantee measurement accuracy and uniform core temperatures.

- **Optimization of the core utilization factor:** In this thesis, the performance of nanocrystalline ribbon cores in the IPT system was studied. However, it is important to recognize that nanocrystalline ribbon cores are more costly than ferrite ones. In this thesis, the cost was not considered as the focus was on the optimization of the pad performance. Thus, different studies are still pending. First, methods to reduce the required volume of core material without compromising the performance of the pad are necessary. The core volume is directly correlated to the cost, size, and weight of the pad. Alternatively, the design of the core can be also optimized considering cost and performance. A compromise can be found for every particular application. In the same direction, an analysis of the cost of cores in mass production can be carried out. To date, the production of nanocrystalline ribbon cores has been limited to specific applications. This technology has been optimized for the production of U and toroidal cores but not for bars such as the ones needed in IPT systems. For this reason, the production of bespoke nanocrystalline ribbon cores is expensive. However, this cost is expected to drop significantly if the core bars are produced in large quantities. An analysis of this cost reduction can shine a light on the applicability of nanocrystalline cores. If the cost reduction is large and the amount of core material per pad can be optimized, nanocrystalline cores can be adopted for most IPT applications. Otherwise, their applicability will be restricted to applications where high power density, reliability, and robustness to harsh environmental conditions are more important than cost.

- **Hybrid cores (ferrite + nanocrystalline ribbon cores):** The mid-section of the core, below the flux pipe, is the region of the core with higher flux density. The rest of the core remains at relatively lower flux densities. One of the main features of nanocrystalline ribbon cores is their higher saturation flux density. Thus, nanocrystalline ribbon cores can be used in the mid-section while ferrite can be used elsewhere. This hybrid structure can help to reduce the cost of the core. Moreover, as shown in Chapter 4, by placing ferrite strategically, the nanocrystalline ribbon cores can be shielded which translates into

lower core losses. The optimum location, geometry, and composition of these hybrid cores require an in-depth analysis.

- **Horizontally-oriented nanocrystalline ribbons cores:** In this thesis, the ribbons were oriented vertically (perpendicular to the shield). This orientation is beneficial for two reasons. The majority of the flux entering the bar is perpendicular to the shield. Thus, by placing the ribbons vertically, the flux can travel parallel to the ribbon, reducing the formation of eddy-currents. Also, by placing the ribbons vertically, the thermal conductivity in the z-axis is high. Thus, the heat produced by the core losses can be transferred more easily to the shield which helps spread the heat and improve the thermal performance of the system. Nonetheless, cores with vertically oriented ribbons are more difficult to manufacture. Moreover, the minimum thickness of the core is limited to 3-4 mm, depending on the manufacturer. Using horizontally oriented ribbons, slimmer cores can be more easily constructed. To reduce the production of eddy-current losses, flaked ribbons can be used. A first attempted of this topology was presented in [87]. Here, slimmer cores were constructed which yielded adequate efficiencies (>96%). Nonetheless, the thermal performance of this system was poor due to the low thermal conductivity of this structure, particularly in the z-axis. Methods to improve the thermal performance of these pads and the optimal design of these cores are two very interesting research topics.

- **Optimization of the multi-frequency control strategy:** The control strategy presented in Chapter 5 is a proof-of-concept and requires further analysis. First, LCL or LCCL-compensated pads are usually designed to operate at the main resonant frequency. The design methodologies found in the literature seek to enhance the power transfer capability of the pad at this frequency while reducing it for the other secondary resonant frequencies. Therefore, the optimum design of an LCL or LCCL compensated pad intended purposely for the operation at two different frequencies is an interesting topic of research.

  In this thesis, a method to estimate the location of the secondary frequencies was described. However, the dynamic tracking of the resonant frequencies when the load or coupling factor change was not presented. This is could also be further explored. Finally, in Chapter 5, an impedance matching circuit at the secondary side is suggested as a possible method to improve the load matching factor and efficiency of the system when operated with the proposed control strategy. This analysis is not presented in this thesis and it is also suggested as future work.

6.3 List of Publications during Ph.D. program

- D. E. Gaona and T. Long, "Feasibility Analysis of Nanocrystalline Cores for Polarize and Non-Polarized IPT Charging Pads," 2019 IEEE Applied Power Electronics Conference and Exposition (APEC), Anaheim, CA, USA, 2019, pp. 1539-1546. doi: 10.1109/APEC.2019.8722317
- D. E. Gaona, S. Ghosh and T. Long, "Embedded compensation for DDQ/Bipolar-Q IPT Charging Pads," 2019 IEEE Energy Conversion Congress and Exposition (ECCE), Baltimore, MD, USA, 2019, pp. 551-556. doi: 10.1109/ECCE.2019.8913244
- D. E. Gaona, S. Ghosh, and T. Long, "Feasibility Study of Nanocrystalline-Ribbon Cores for Polarized Inductive Power Transfer Pads," in IEEE Transactions on Power Electronics, vol. 35, no. 7, pp. 6799-6809, July 2020. doi: 10.1109/TPEL.2019.2957774
- S. Ghosh, D. Gaona, Y. Siwakoti and T. Long, "Synchronous Combined Cuk-SEPIC Converter for Single Phase Transformerless Solar Inverter," 2020 IEEE Applied Power Electronics Conference and Exposition (APEC), New Orleans, LA, USA, 2020, pp. 3225-3231. doi: 10.1109/APEC39645.2020.9124353
- D. E. Gaona, H. El Khatib, T. Long, and M. Saur, "Analysis of Implementation Methodologies of Deadbeat Direct-Torque and Flux Control (DB-DTFC) for IPMSMs in Stationary and Rotatory Reference Frames," 2020 IEEE Energy Conversion Congress and Exposition (ECCE), Detroit, MI, USA, 2020, pp. 6071-6078.
- D. E. Gaona, H. El Khatib, T. Long, and M. Saur, "Overmodulation Strategy for Deadbeat-Flux and Torque Control of IPMSM with Flux Trajectory Control in the Stationary Reference Frame," 2020 IEEE Energy Conversion Congress and Exposition (ECCE), Detroit, MI, USA, 2020, pp. 6087-6095. doi: 10.1109/ ECCE44975.2020.9236331
- C. Jiang, D. E. Gaona, Y. Shen, H. Zhao, K. T. Chau, and T. Long, "Low-Frequency Medium Power Capacitor-Free Self-Resonant Wireless Power Transfer," in IEEE Transactions on Industrial Electronics. doi: 10.1109/TIE.2020.3034867
- D. E. Gaona and T. Long, "Design Considerations for High-power Density IPT Pads using Nanocrystalline Ribbon Cores," 2020 IEEE Wireless Power Week (WOW), Korea, 2020.
- D. E. Gaona-Erazo, C. Jiang and T. Long, "Highly Efficient 11.1 kW Wireless Power Transfer Utilizing Nanocrystalline Ribbon Cores," in IEEE Transactions on Power Electronics. doi: 10.1109/TPEL.2021.3064902

References

[1] Advanced Propulsion Centre UK (2017a). Electric machines roadmap. Technical report, UK.

[2] Advanced Propulsion Centre UK (2017b). Electrical energy storage roadmap. Technical report, UK.

[3] Advanced Propulsion Centre UK (2017c). Power electronics roadmap. Technical report, UK.

[4] Agency, I. E. (2019). Global ev outlook 2019. scaling up the transition to eletric mobility,. Technical report.

[5] ATM (2017). Antainano nanocrystalline products. Technical report, Beijing, China.

[6] Beddingfield, R. B., Bhattacharya, S., and Ohodnicki, P. (2019). Shielding of leakage flux induced losses in high power, medium frequency transformers. In *2019 IEEE Energy Conversion Congress and Exposition (ECCE)*, pages 4154–4161.

[7] Bermudez, A., Gomez, D., and Salgado, P. (2008). Eddy-current losses in laminated cores and the computation of an equivalent conductivity. *IEEE Transactions on Magnetics*, 44(12):4730–4738.

[8] Bosshard, R. (2015). *Multi-objective optimization of inductive power transfer systems for EV charging*. PhD thesis, ETH Zurich.

[9] Bosshard, R. (2016). Comprehensive evaluation of rectangular and double-d coil geometry for 50 kw/85 khz ipt system. *IEEE Journal of Emerging and Selected Topics in Power Electronics*, 4(4):1406–1415.

[10] Bosshard, R., Iruretagoyena, U., and Kolar, J. W. (2016). Comprehensive evaluation of rectangular and double-d coil geometry for 50 kw/85 khz ipt system. *IEEE Journal of Emerging and Selected Topics in Power Electronics*, 4(4):1406–1415.

[11] Bosshard, R. and Kolar, J. W. (2016). Inductive power transfer for electric vehicle charging: Technical challenges and tradeoffs. *IEEE Power Electronics Magazine*, 3(3):22–30.

[12] Bosshard, R., Kolar, J. W., Mühlethaler, J., Stevanović, I., Wunsch, B., and Canales, F. (2014). Modeling and eta/alpha-pareto optimization of inductive power transfer coils for electric vehicles. *IEEE Journal of Emerging and Selected Topics in Power Electronics*, 3(1):50–64.

[13] Bosshard, R., Kolar, J. W., Mühlethaler, J., Stevanovic, I., Wunsch, B., and Canales, F. (2015). The η-α-pareto front of inductive power transfer coils. *IECON 2012 - 38th Annual Conference on IEEE Industrial Electronics Society*, 3(1):50–64.

[14] Boys, J. and Covic, G. (2017). Current distribution and thermal regulation in inductive power transfer coupling structures.

[15] Budhia, M., Boys, J. T., Covic, G. A., and Huang, C. Y. (2013). Development of a single-sided flux magnetic coupler for electric vehicle ipt charging systems. *IEEE Transactions on Industrial Electronics*, 60(1):318–328.

[16] Budhia, M., Covic, G. A., and Boys, J. T. (2011). Design and optimization of circular magnetic structures for lumped inductive power transfer systems. *IEEE Transactions on Power Electronics*, 26(11):3096–3108.

[17] Calderon-Lopez, G., Wang, Y., and Forsyth, A. J. (2019). Mitigation of gap losses in nanocrystalline tape-wound cores. *IEEE Transactions on Power Electronics*, 34(5):4656–4664.

[18] Chem, C. W. (2012). Magnetism and metallurgy of soft magnetic materials. *Burlington: Elsevier Science.*

[19] Covic, G. A. and Boys, J. T. (2013). Modern trends in inductive power transfer for transportation applications. *IEEE Journal of Emerging and Selected Topics in Power Electronics*, 1(1):28–41.

[20] Davies, H. A. and Gibbs, M. R. J. (2007). *Amorphous alloys*. Wiley.

[21] Deepak Bhalla, D. S. (2012). American journal of materials science. *Journal of Alloys and Compounds*.

[22] Delgado, A., Salinas, G., Rodriguez, J., Oliver, J. A., and Cobos, J. A. (2018). Finite element modelling of litz wire conductors and compound magnetic materials based on magnetic nano-particles by means of equivalent homogeneous materials for wireless power transfer system. In *2018 IEEE 19th Workshop on Control and Modeling for Power Electronics (COMPEL)*, pages 1–5.

[23] Diekhans, T. and De Doncker, R. W. (2015). A dual-side controlled inductive power transfer system optimized for large coupling factor variations and partial load. *IEEE Transactions on Power Electronics*, 30(11):6320–6328.

[24] Feng, H., Tavakoli, R., Onar, O. C., and Pantic, Z. (2020). Advances in high-power wireless charging systems: Overview and design considerations. *IEEE Transactions on Transportation Electrification*, 6(3):886–919.

[25] Fletcher, J., Williams, B., and Mahmoud, M. (2005). Airgap fringing flux reduction in inductors using open-circuit copper screens. *IEE Proceedings - Electric Power Applications*, 152(4):990–996.

[26] Füzer, J., Dobák, S., and Kollár, P. (2015). Magnetization dynamics of fecunbsib soft magnetic ribbons and derived powder cores. *Journal of Alloys and Compounds*, 628:335–342.

[27] Gaona, D., Ghosh, S., and Long, T. (2020). Feasibility study of nanocrystalline-ribbon cores for polarized inductive power transfer pads. *IEEE Transactions on Power Electronics*, 35(7):6799–6809.

[28] Gaona, D. E., Ghosh, S., and Long, T. (2019). Embedded compensation for ddq/bipolar-q ipt charging pads. In *2019 IEEE Energy Conversion Congress and Exposition (ECCE)*, pages 551–556.

[29] Geoff Klempner, I. K. (2018). *Handbook of Large Turbo-Generator Operation and Maintenance*. John Wiley and Sons.

[30] Geselowtiz, D. B., Hoang, Q. T. N., and Gaumond, R. P. (1992). The effects of metals on a transcutaneous energy transmission system. *IEEE Transactions on Biomedical Engineering*, 39(9):928–934.

[31] Hatchavanich, N., Sangswang, A., and Naetiladdanon, S. (2016). Operation region of lcl resonant inverter for inductive power transfer application. In *2016 13th International Conference on Electrical Engineering/Electronics, Computer, Telecommunications and Information Technology (ECTI-CON)*, pages 1–6.

[32] Herzer, G. (2007). *Soft magnetic materials — nanocrystalline alloys*. Wiley.

[33] Hitachi (2007). Nanocrystalline fe-based soft magnetic material with high saturation flux density and low core loss. Technical report.

[34] Hitachi (2016). Nanocrystalline soft magnetic material finemet. Technical report.

[35] Hollaus, K., Huber, M., Schöberl, J., and Hamberger, P. (2012). A linear fem benchmark for the homogenization of the eddy currents in laminated media in 3d. *IFAC Proceedings Volumes*, 45(2):1190–1194.

[36] Hu, A. P. (2001). *Selected Resonant Converters for IPT supplies*. PhD thesis, University of Auckland, New Zealand.

[37] Hurley, William G.; Wöfle, W. H. (2013). *Transformers and inductors for power electronics. Theory, design and applications*. Wiley-Blackwell, 2 edition.

[38] ICNIRP (2010). Icnirp guidelines for limiting exposure to time-varying electric and magnetic fields (1hz – 100 khz). *HEALTH PHYSICS 99(6):818-836; 2010*.

[39] IEEE (2019). Ieee approved draft standard for safety levels with respect to human exposure to electric, magnetic and electromagnetic fields, 0 hz to 300 ghz. *IEEE PC95.1/D3.5, October 2018*, pages 1–312.

[40] J.T. Boys, G. A. C. (2011). Ipt fact sheet series: no.1 basic concepts. *Department of Electrical Engineering. Auckland University*.

[41] J.Teillet, S. J. B. H. (2000). Microstructural study of nanocrystalline fe–(cu–nb)–si–b ribbons obtained by a nitriding thermochemical treatment. *Journal of Magnetism and Magnetic Materials*.

[42] Kalra, G. R., Pearce, M. G. S., Kim, S., Thrimawithana, D. J., and Covic, G. A. (2019). Measuring the q-factor of ipt magnetic couplers. In *2019 IEEE PELS Workshop on Emerging Technologies: Wireless Power Transfer (WoW)*, pages 34–38.

[43] Kim, J., Kim, J., Kong, S., Kim, H., Suh, I., Suh, N. P., Cho, D., Kim, J., and Ahn, S. (2013). Coil design and shielding methods for a magnetic resonant wireless power transfer system. *Proceedings of the IEEE*, 101(6):1332–1342.

[44] Kim, S., Covic, G. A., and Boys, J. T. (2016). Analysis on tripolar pad for inductive power transfer systems. In *2016 IEEE PELS Workshop on Emerging Technologies: Wireless Power Transfer (WoW)*, pages 15–20.

[45] Kim, S., Zaheer, A., Covic, G., and Boys, J. (2014). Tripolar pad for inductive power transfer systems. In *IECON 2014 - 40th Annual Conference of the IEEE Industrial Electronics Society*, pages 3066–3072.

[46] Knecht, O. and Kolar, J. W. (2017). Comparative evaluation of ipt resonant circuit topologies for wireless power supplies of implantable mechanical circulatory support systems. In *2017 IEEE Applied Power Electronics Conference and Exposition (APEC)*, pages 3271–3278. IEEE.

[47] Kolar, J. W. (2019). Future challenges for research and teaching in power electronics. *1st Conference Power Electronics UK: Underpinning Research.*

[48] L. Gonzalez-Legarreta, e. a. (2016). Magnetoimpedance effect in nanocrystalline fe73.5cu1nb3si13.5b9 single-layer and bilayer ribbons. *Journal of Alloys and Compounds*.

[49] Li, M., Yao, G., Zhou, L., and Yin, Z. (2016). Harmonic analysis of bidirectional lcl-ipt system. In *2016 IEEE 2nd Annual Southern Power Electronics Conference (SPEC)*, pages 1–5.

[50] Lin, F. Y., Covic, G. A., and Boys, J. T. (2015). Evaluation of magnetic pad sizes and topologies for electric vehicle charging. *IEEE Transactions on Power Electronics*, 30(11):6391–6407.

[51] Lin, F. Y., Kim, S., Covic, G. A., and Boys, J. T. (2017). Effective coupling factors for series and parallel tuned secondaries in ipt systems using bipolar primary pads. *IEEE Transactions on Transportation Electrification*, 3(2):434–444.

[52] Liu, N. (2016). *Design of a universal inductive charging system for electric vehicles*. PhD thesis, Georgia Institute of Technology, USA.

[53] Lucian Petrescu, e. (2019). Magnetic properties of manganese-zinc soft ferrite ceramic for high frequency applications. *MDPI Journal of Material*.

[54] Madawala, U. K. and Thrimawithana, D. J. (2011). A bidirectional inductive power interface for electric vehicles in v2g systems. *IEEE Transactions on Industrial Electronics*, 58(10):4789–4796.

[55] Magnetics (2018). Designing with magnetic cores at high temperatures. Technical report.

[56] Mallinson, J. (1973). One-sided fluxes – a magnetic curiosity? *IEEE Transactions on Magnetics*, 9(4):678–682.

[57] McLyman, C. W. T. (2016). *Transformer and inductor design handbook*. CRC press.

[58] Mohammad, M. and Choi, S. (2017). Core design and optimization for better misalignment tolerance and higher range of wireless charging of phev. In *IEEE Transaction on Transportation Electrification*, pages 1350–1356.

[59] Mohammad, M. and Choi, S. (2018). Optimization of ferrite core to reduce the core loss in double-d pad of wireless charging system for electric vehicles. In *2018 IEEE Applied Power Electronics Conference and Exposition (APEC)*, pages 1350–1356. IEEE.

[60] Mohammad, M., Choi, S., and Elbuluk, M. E. (2019). Loss minimization design of ferrite core in a dd-coil-based high-power wireless charging system for electrical vehicle application. *IEEE Transactions on Transportation Electrification*, 5(4):957–967.

[61] Moses, A. J. (2007). *Advanced soft magnetic materials for power applications*. Wiley.

[62] Mühlethaler, J. (2012). *Modeling and multi-objective optimization of inductive power components*. PhD thesis, ETH Zurich.

[63] Muramatsu, K., Okitsu, T., Fujitsu, H., and Shimanoe, F. (2004). Method of nonlinear magnetic field analysis taking into account eddy current in laminated core. *IEEE Transactions on Magnetics*, 40(2):896–899.

[64] Papamanolis, P., Guillod, T., Krismer, F., and Kolar, J. W. (2020). Transient calorimetric measurement of ferrite core losses. In *2020 IEEE Applied Power Electronics Conference and Exposition (APEC)*, pages 195–201.

[65] Pearce, M. G. S. (2020). *Inductive Power Transfer Magnetics for Roadways*. PhD thesis, University of Auckland, New Zealand.

[66] Pearce, M. G. S., Covic, G. A., and Boys, J. T. (2019a). Passive reflection winding for ferrite-less double d topology for roadway ipt applications. In *2019 IEEE Energy Conversion Congress and Exposition (ECCE)*, pages 1202–1209.

[67] Pearce, M. G. S., Covic, G. A., and Boys, J. T. (2019b). Robust ferrite-less double d topology for roadway ipt applications. *IEEE Transactions on Power Electronics*, 34(7):6062–6075.

[68] Pearce, M. G. S., O'Sullivan, M. J., Carretero, C., Covic, G. A., and Boys, J. T. (2019c). Optimising ferrite-less pad reflection winding with a multi-objective genetic algorithm. In *2019 IEEE PELS Workshop on Emerging Technologies: Wireless Power Transfer (WoW)*, pages 1–6.

[69] Rasekh, N. and Mirsalim, M. (2018). Analysis of a compact and efficient ddq pad integrated to the lcc compensation topology for ipt. In *2018 9th Annual Power Electronics, Drives Systems and Technologies Conference (PEDSTC)*, pages 26–29.

[70] Reilly, P. (2014). Human exposure standards in the frequency range 1 hz to 100 khz: the case for adoption of the ieee standard. *Health Phys.*, 107(4):343–350.

[71] Research, A. M. (2018). Wireless electric vehicle charging market by power source (3 - <11 kw, 11 - 50 kw and >50 kw), installation (home and commercial), distribution channel (oems and aftermarket), and vehicle type (battery electric vehicles (bev), plug - in hybrid electric vehicle (hev) and commercial electric vehicles): Global opportunity analysis and industry forecast, 2018 - 2025. Technical report.

[72] Schneider, J. (2016). Wireless power transfer for light-duty plug-in/electric vehicles and alignment methodology. *SAE International J2954 Taskforce*.

[73] Steigerwald, R. L. (1988). A comparison of half-bridge resonant converter topologies. *IEEE Transactions on Power Electronics*, 3(2):174–182.

[74] T. M. Fisher, K. B. Farley, Y. G. e. a. (2014). Electric vehicle wireless charging technology: A state-of-the-art review of magnetic coupling systems. *IEEE Wireless Power Transfer*, 1(2):87–96.

[75] TDK (2017). Ferrites and accessories siferrit material n87. Technical report.

[76] Tejeda, A., Carretero, C., Boys, J. T., and Covic, G. A. (2017). Ferrite-less circular pad with controlled flux cancelation for ev wireless charging. *IEEE Transactions on Power Electronics*, 32(11):8349–8359.

[77] Tesla (2017). Model s datasheet. Technical report, USA.

[78] Trevisan, R. and Costanzo, A. (2014). State-of-the-art of contactless energy transfer (cet) systems: design rules and applications. *Wireless Power Transfer*, 1(1):1020.

[79] Vacuumschmelze (2019). Vitroperm® vp 800 / 500. Technical report.

[80] Wang, C.-S., Covic, G. A., and Stielau, O. H. (2004). Investigating an lcl load resonant inverter for inductive power transfer applications. *IEEE Transactions on Power Electronics*, 19(4):995–1002.

[81] Wang, J., Lin, H., Huang, Y., and Sun, X. (2011). A new formulation of anisotropic equivalent conductivity in laminations. *IEEE Transactions on Magnetics*, 47(5):1378–1381.

[82] Wang, Y. (2015). *Modelling and Characterisation of Losses in Nanocrystalline Cores*. PhD thesis, University of Manchester.

[83] Wang, Y., Calderon-Lopez, G., and Forsyth, A. J. (2017). High-frequency gap losses in nanocrystalline cores. *IEEE Transactions on Power Electronics*, 32(6):4683–4690.

[84] Watanabe, T. and Yamamichi, S. (2012). A novel u-shaped magnetic shield for perpendicular mram. In *2012 IEEE 62nd Electronic Components and Technology Conference*, pages 920–925.

[85] Weihan Li, Han Zhao, Tianze Kan, and Mi, C. (2015). Inter-operability considerations of the double-sided lcc compensated wireless charger for electric vehicle and plug-in hybrid electric vehicle applications. In *2015 IEEE PELS Workshop on Emerging Technologies: Wireless Power (2015 WoW)*, pages 1–6.

[86] WiTricity (2017). Drive datasheet. Technical report.

[87] Xiong, M., Wei, X., Huang, Y., Luo, Z., and Dai, H. (2020). Research on novel flexible high-saturation nanocrystalline cores for wireless charging systems of electric vehicles. *IEEE Transactions on Industrial Electronics*, pages 1–1.

[88] Y. Yoshizawa, S. O. and Yamauchi, K. (1988). New iron based soft magnetic alloys composed of ultrafine grain structure. *Journal of Applied Physics*, 64(10):6044–6046.

[89] Yilmaz, T., Hasan, N., Zane, R., and Pantic, Z. (2017). Multi-objective optimization of circular magnetic couplers for wireless power transfer applications. *IEEE Transactions on Magnetics*, 53(8):1–12.

[90] Yoshizawa, Y. (1999). Magnetic properties and microstructure of nanocrystalline fe-based alloys. *Journal of Metastable and Nanocrystalline Materials*, 1:51–62.

[91] Zaheer, A., Kacprzak, D., and Covic, G. A. (2012). A bipolar receiver pad in a lumped ipt system for electric vehicle charging applications. In *2012 IEEE Energy Conversion Congress and Exposition (ECCE)*, pages 283–290.

[92] Zhao, L., Ruddell, S., Thrimawithana, D. J., Madawala, U. K., and Hu, P. A. (2017a). A hybrid wireless charging system with ddq pads for dynamic charging of evs. In *2017 IEEE PELS Workshop on Emerging Technologies: Wireless Power Transfer (WoW)*, pages 1–6.

[93] Zhao, L., Thrimawithana, D. J., and Madawala, U. K. (2017b). Hybrid bidirectional wireless ev charging system tolerant to pad misalignment. *IEEE Transactions on Industrial Electronics*, 64(9):7079–7086.

[94] Zhao, L., Thrimawithana, D. J., Madawala, U. K., Hu, P., and Mi, C. C. (2018). A misalignment tolerant series-hybrid wireless ev charging system with integrated magnetics. *IEEE Transactions on Power Electronics*, pages 1–1.

[95] Zhao, L., Thrimawithana, D. J., Madawala, U. K., and Hu, P. A. (2017c). A bi-directional wireless power system with integrated magnetics. In *2017 IEEE Southern Power Electronics Conference (SPEC)*, pages 1–6.

[96] Ziske1, J., Neubert, H., and Disselnkoetter, R. (2014). Modeling of anisotropic laminated magnetic cores using homogenization approaches. In *2014 COMSOL Conference in Cambridge*.

Appendix A

PCB Design

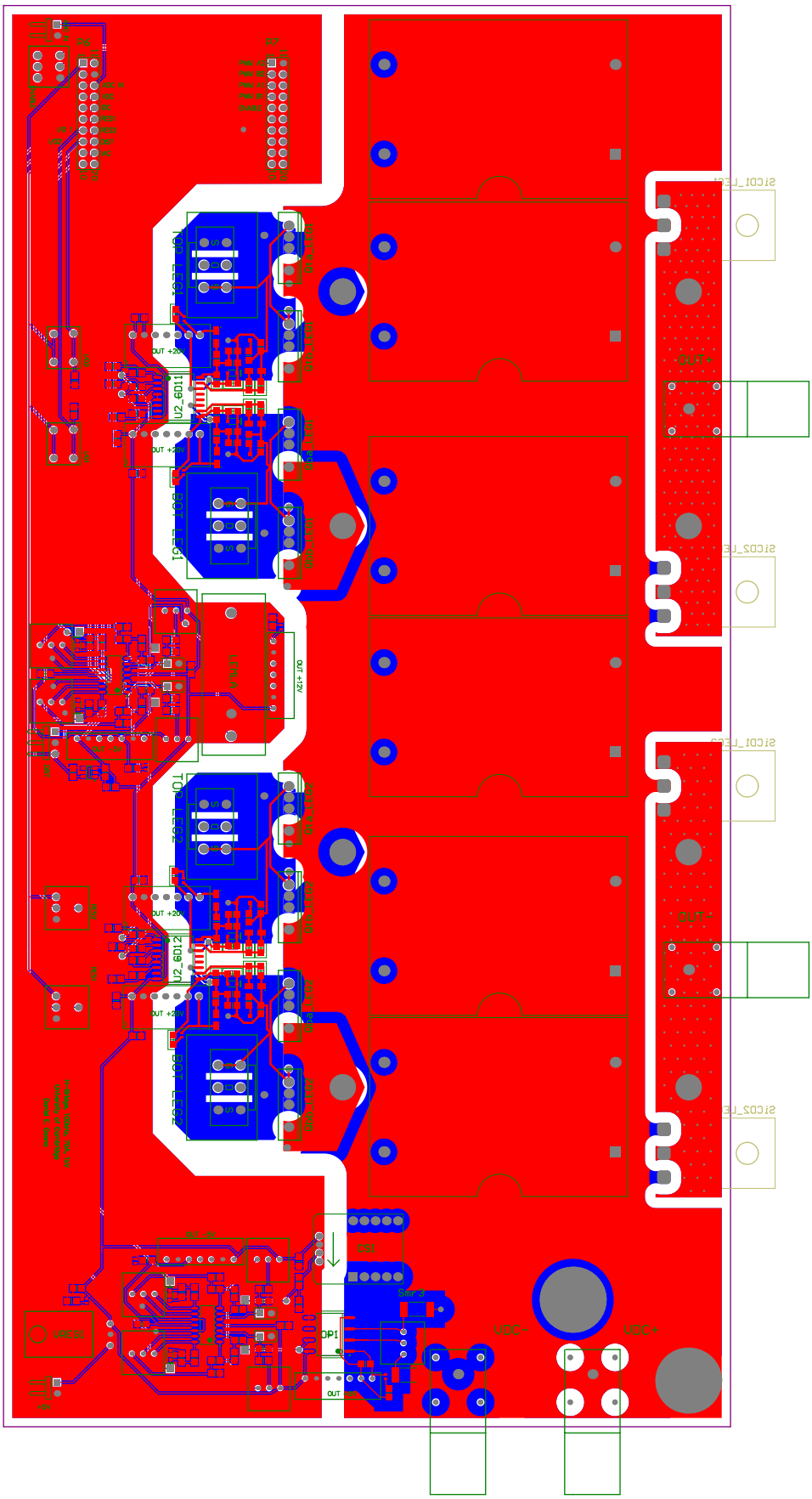

Fig. A.1 PCB Design, Top Layer.

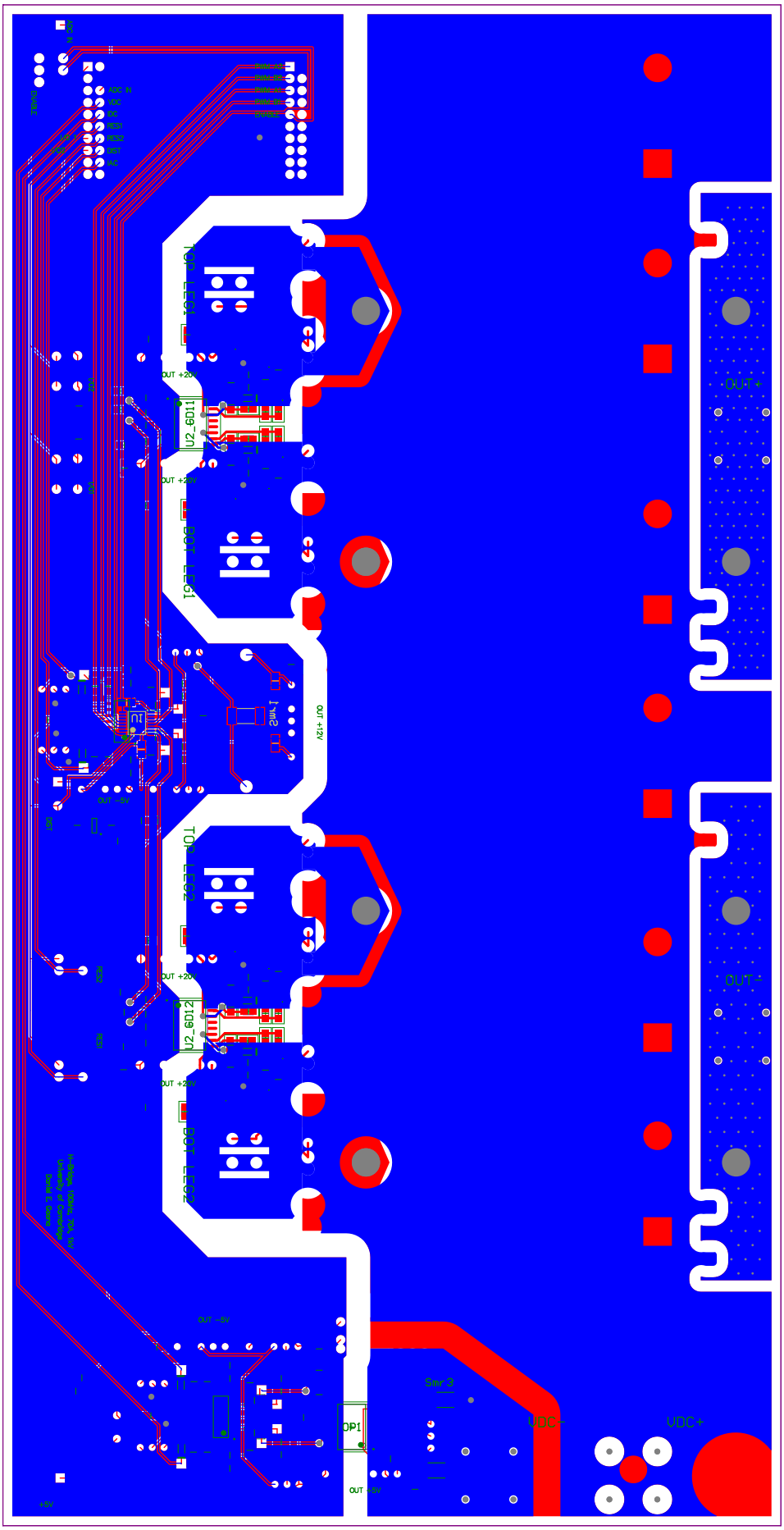

Fig. A.2 PCB Design, Bottom Layer.

Appendix B

Core Design for Circular Pads

Optimum Core and coil Position

- For circular pads without shield, P_{su} increases with the coil mean radius as seen in Fig.B.1a. In fact, P_{su} reaches its maximum when the coil outer radius matches the pad radius r_{pad}. Even higher P_{su} can be achieved with longer cores.
- For shielded pads and small cores, the coil position that maximizes P_{su} depends on the core length l_c and number of turns N as seen in Fig.B.1b and Fig. B.1c. For larger cores ($l_c \geq 60\% l_{pad}$), P_{su} reaches a maximum when the coil mean radius is $\sim 70\%$ of the pad radius. This is independent of the number of turns.
- For fixed coil mean radius r_{mean} and l_c, the power transfer P_{su} increases linearly with the number of turns N, as seen in Fig.B.1e. P_{su} increases linearly as opposed to quadratic since r_{mean} is kept constant. Any increase in N results is smaller inner coil radius r_{inner}, and therefore lower inductace.
- For a fixed coil mean radius r_{mean} and N, P_{su} increases with the core length, as seen in Fig.B.1f. The rate of increase decays for larger l_c ($\geq$70 % of the pad radius). Effective utilization of ferrite should consider values of l_c between 70% and 85% of the pad radius. Longer coils bring only a marginal improvement in the performance of the pad. Moreover, longer rectangular bars cannot be easily accommodated within the pad.

Thus, two heuristic rules for pad design are determined: 1) the coil center should be located at $\sim 67\%$ of the pad radius and 2) the length of core bars should be between 70 and 85% of the pad radius.

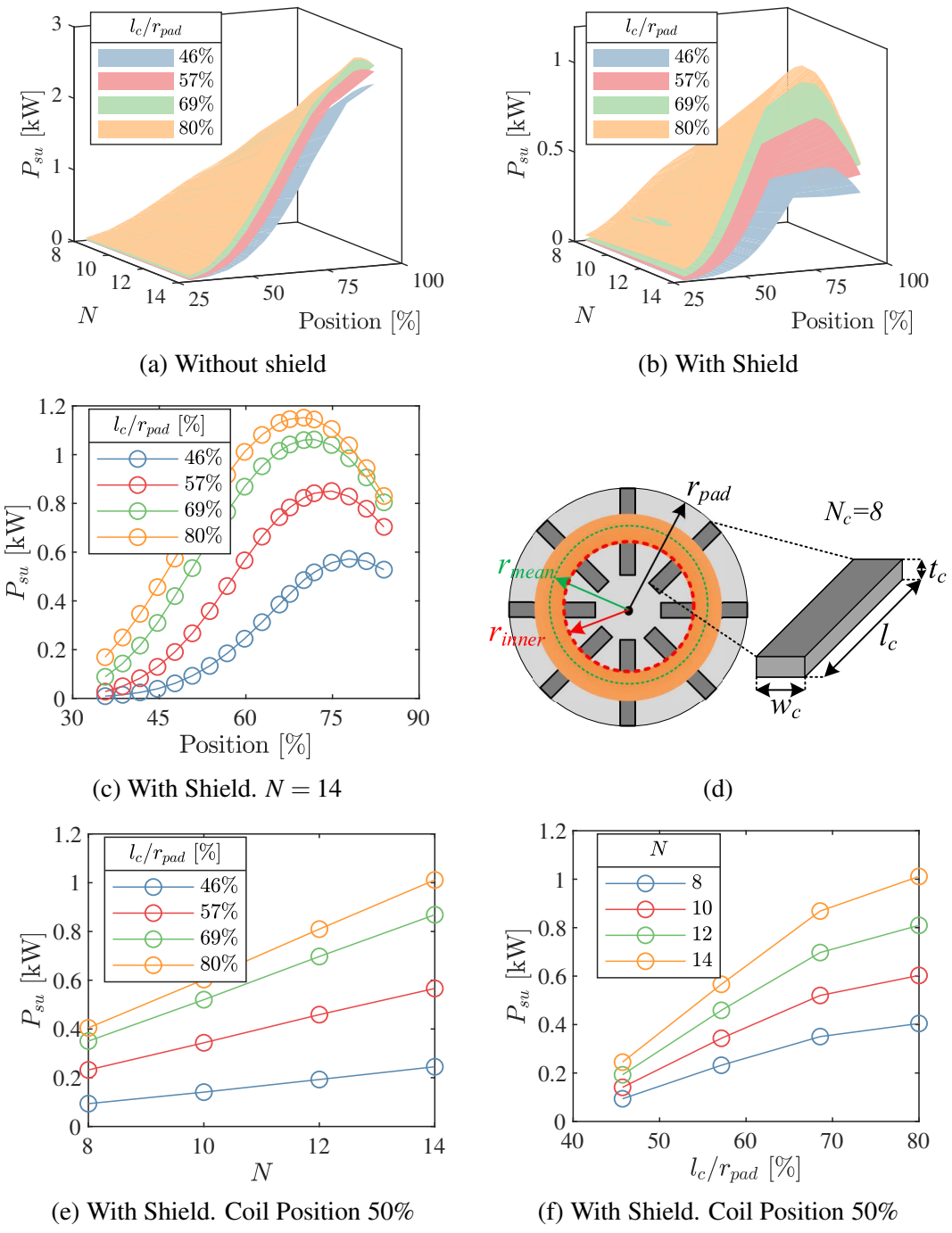

(a) Without shield

(b) With Shield

(c) With Shield. $N = 14$

(d)

(e) With Shield. Coil Position 50%

(f) With Shield. Coil Position 50%

Fig. B.1 Power transfer capability P_{su} of a circular pad for different core lengths l_c, number of turns N, and coil position. The latter is defined as a location of the mean coil radius with respect to the pad radius. The core length is also normalized with respect to the pad radius r_pad. Pad radius: r_{pad} =175 mm. $i_{1,rms} = 23$A. f_0 =85 kHz.

Optimum Core Dimensions

The power transfer capability of the pad P_{su}, the maximum flux density in the core B_{max}, and the core losses P_{loss} depend on the volume and dimension of the core bars. Fig.B.2 shows the

effect of each core dimensions (core length l_c, width w_c, thickness t_c, number of cores N_c). As opposed to w_c, the percentage of area covered by the core A_c% is presented as a metric. The main findings are listed below:

- B_{max} and P_{loss} are inversely proportional to the volume of core material, as seen in Fig.B.2c. P_{su} increases with the volume of core material. However, for a given core volume, different core dimension lead to higher or lower P_{su} values, as seen in Fig.B.2a.
- Increasing l_c, A_c, or t_c result in higher P_{su} but the rate of increase is different. l_c has the biggest impact on P_{su} followed by A_c and t_c.
- Increasing t_c improves P_{su} only slightly but reduces B_{max} and P_{loss} considerably. Increasing l_c or A_c does not reduce B_{max} and P_{loss} considerably.

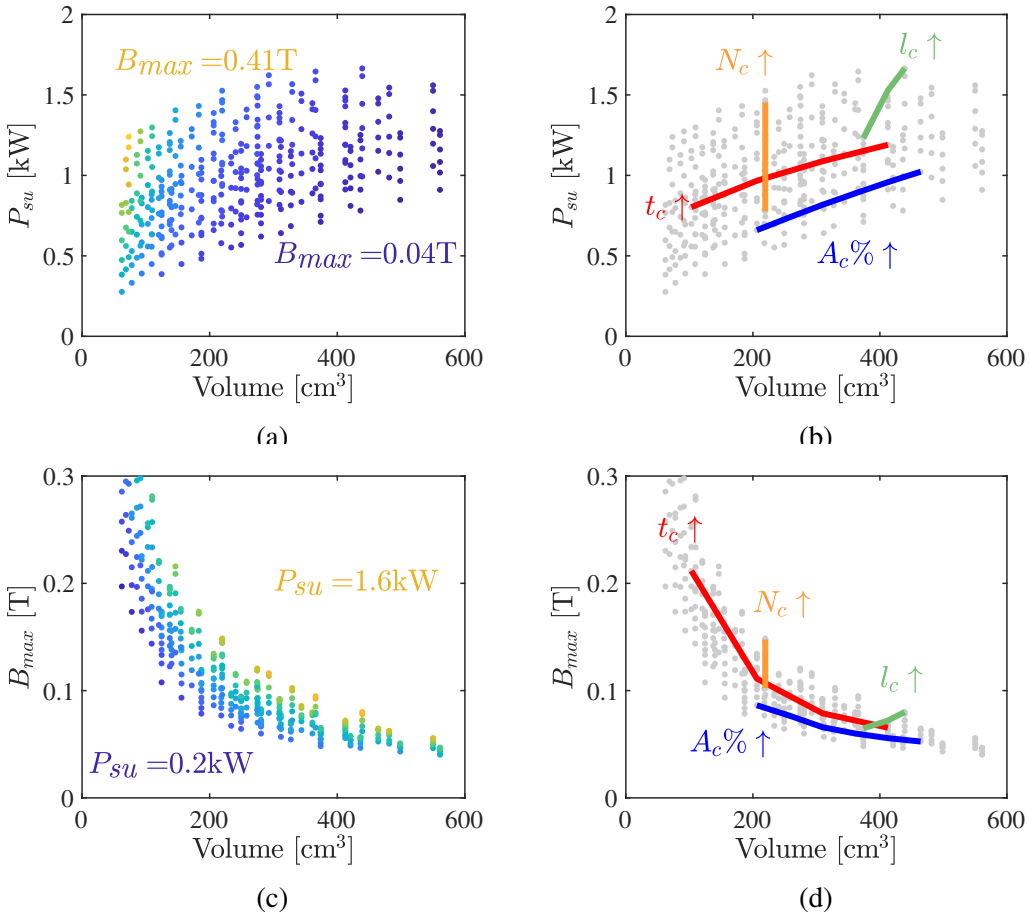

Fig. B.2 Power transfer capability P_{su}, maximum flux density in the core B_{max}, and core losses P_{loss} versus volume of core material for different values of l_c, w_c, and N_c. $N = 12$. Pad radius: r_{pad} =175 mm. $i_{1,rms} = 23$A. f_0 =85 kHz.

- For the same core volume, P_{su} and B_{max} increase both with N_c. This is due to the lower reluctance obtained with a more symmetric core placement.

From Fig.B.2, guidelines for design can be obtained. An optimal core design should lay on the envelope of the Fig.B.2a. The envelope corresponds to design with large cores, a relatively high number of cores. Considering the analysis in Section B, a length between 80% to 90% of the pad radius must be considered. The core width can be increased to obtain more than 60% of the are covered by core material. Finally, the core thickness can be designed last as it has the lowest impact on P_{su}. Thus, t_c can be adjusted to ensure ensure B_{max} remains below the saturation flux density B_{sat}. It can be further increased to reduce core losses.